Observational constraints on the influence of active galactic nuclei on the evolution of galaxies

CHRISTOPHER MARK HARRISON

Observational constraints on the influence of active galactic nuclei on the evolution of galaxies

Christopher Mark Harrison

Abstract

At the centre of every massive galaxy there resides a super-massive black hole that grew during periods of active galactic nuclei (AGN) activity. Current theoretical models of galaxy evolution invoke AGN-driven galaxy-scale feedback processes (e.g., the expulsion of gas through outflows) in order to reproduce many of the fundamental properties of galaxies and the intergalactic medium. This thesis uses observations to test some of the predictions of these feedback processes. I present integral field unit observations of AGN host galaxies to trace their ionised gas kinematics. The targets are eight high-redshift ($z = 1.4 - 3.4$) ultra-luminous infrared galaxies, that are representative of rapidly evolving distant galaxies, and sixteen $z < 0.2$ luminous AGN, that were selected from a parent sample of ≈24,000 sources to be representative of the overall population. In both samples I identify galaxy-wide outflows (i.e., over kiloparsec scales), calculate their properties (e.g., mass outflow rates and energetics) and show that they are broadly consistent with theoretical predictions. I find that ionised outflows are common in $z < 0.2$ luminous AGN and are consistently extended over kiloparsec scales (in $\geq 70\%$ of cases). I also use far-infrared *Herschel* data of X-ray detected $z = 1$–3 AGN to test the prediction that luminous AGN shut down star formation in their host galaxies. Using stacking techniques I show that, on average, X-ray detected AGN over a wide range of luminosities (i.e., $L_{2-8\,\mathrm{keV}} \approx 10^{42-45}\,\mathrm{erg\,s^{-1}}$) have star formation rates that are consistent with non-active galaxies. This may imply that luminous AGN do not impact upon the star formation in their host galaxies. Overall, this thesis demonstrates that energetic galaxy-wide outflows are prevalent in AGN host galaxies; however, it also demonstrates that we still lack *direct* observational evidence that luminous AGN are suppressing star formation in their host galaxies.

Observational constraints on the influence of active galactic nuclei on the evolution of galaxies

Christopher Mark Harrison

A thesis presented in accordance with the regulations for admittance to the degree of Doctor of Philosophy

Extragalactic Astronomy
Department of Physics
University of Durham
United Kingdom

April 2014

Dedicated to

Mum and Dad

Declaration

The work described in this thesis was undertaken between October 2010 and April 2014 while the author was a research student under the supervision of Prof. David M. Alexander in the Department of Physics at the University of Durham. No part of this thesis has been submitted for any other degree at the University of Durham or any other university.

Portions of this work have appeared in the following papers:

- *Chapter 3:* C. M. Harrison, D. M. Alexander, A. M. Swinbank, I. Smail, S. Alaghband-Zadeh, F. E. Bauer, S. C. Chapman, A. Del Moro, R. C. Hickox, R. J. Ivison, K. Menendez-Delmestre, J. R. Mullaney, N. P. H. Nesvadba, 2012, MNRAS, 426, 1073: **Energetic galaxy-wide outflows in high-redshift ultra-luminous infrared galaxies hosting AGN activity**

- *Chapter 4:* C. M. Harrison, D. M. Alexander, J. R. Mullaney, A. M. Swinbank, 2014, MNRAS, 441, 3306: **Kiloparsec-scale outflows are prevalent among luminous AGN: outflows and feedback in the context of the overall AGN population**

- *Chapter 5:* C. M. Harrison, D. M. Alexander, J. R. Mullaney, D. Coia, V. Charmandaris, E. Daddi, H. Dannerbauer, K. Dasyra, A. Del Moro, M. Dickinson, R. C. Hickox, R. J. Ivison, J. Kartaltepe, E. Le Floc'h, R. Leiton, B. Magnelli, P. Popesso, E. Rovilos, D. Rosario, A. M. Swinbank, 2012, ApJL, 760:L15: **No clear submillimetre signature of suppressed star formation among X-ray luminous AGN**

The work described in Chapters 3–5 was performed in collaboration with others (listed above). Chapter 3 is based on the results of observing proposals led by D. M. Alexander and S. Alaghband-Zadeh. Chapter 4 is based on the results of observing proposals led by J. R. Mullaney and the author. The author has carried out all of the data reduction and analysis in this work with the following exceptions: (1) the data reduction of the SINFONI data in Chapter 3 (carried out by S. Alaghband-Zadeh); (2) the spectral energy distribution analysis in Chapter 3 (carried out by A. Del Moro); (3) the reduction of the *Herschel* images used in Chapter 5 (carried out by A. M. Swinbank) and (4) the reduction of the radio data shown in Figure 6.1 (carried out by A. P. Thomson). All of the text has been written by the author.

In addition to the work presented in this thesis, the author has also either worked on, or been involved in, the following work during the period of their PhD:

- C. M. Harrison, 2014, Proceedings of the International Astronomical Union, Symposium 304, Cambridge Journals: **The impact of AGN on their host galaxies**

- A. M. Swinbank, J. M. Simpson, Ian Smail, C. M. Harrison, J. Hodge, A. Karim, F. Walter, D. M. Alexander, W. Brandt, C. de Breuck, E. de Cunha, S. C. Chapman, K. E. K Coppin, A. L. R. Danielson, H. Dannerbauer, R. J. Ivison, T. R. Greve, K. K. Knudsen, C. Lagos, E. Schinnerer, A. Thomson, J. L. Wardlow, A. Weiss, P. van der Werf, 2014, MNRAS, 438, 1267: **An ALMA Survey of Sub-millimetre Galaxies in the Extended Chandra Deep Field South: The Far-Infrared Properties of SMGs**

- E. Rovilos, I. Georgantopoulos, A. Akylas, J. Aird, D. M. Alexander, A. Comastri, A. Del Moro, P. Gandhi, A. Georgakakis, C. M. Harrison, J. R. Mullaney, 2014, MNRAS, 438, 494: **A wide search for obscured Active Galactic Nuclei using XMM-Newton and WISE**

- J. R. Mullaney, D. M. Alexander, S. Fine, A. D. Goulding, C. M. Harrison, R. C. Hickox, 2013, MNRAS, 433, 622: **Narrow-line region gas kinematics of 24,264 optically-selected AGN: the radio connection**

- B. D. Lehmer, A. B. Lucy, D. M. Alexander, P. N. Best, J. E. Geach, C. M. Harrison, A. E. Hornschemeier, Y. Matsuda, J. R. Mullaney, Ian Smail, D. Sobral, A. M. Swinbank, 2013, ApJL, 765, 87: **Concurrent supermassive black hole and galaxy growth in z=2.23 Hα emitters: a 100ks Chandra observation of 2QZ Cluster 1004+00 and comparisons with C-COSMOS**

- J. M. Simpson, Ian Smail, A. M. Swinbank, D. M. Alexander, R. Auld, M. Baes, D. G. Bonfield, D. L. Clements, A. Cooray, K. E. K. Coppin, A. L. R. Danielson, A. Dariush, L. Dunne, G. de Zotti, C. M. Harrison, R. Hopwood, C. Hoyos, E. Ibar, R. J. Ivison, M. J. Jarvis, A. Lapi, S. J. Maddox, M. J. Page, D. A. Riechers, E. Valiante, P. P van der Werf, 2012, MNRAS, 426, 3201: **The evolutionary connection between QSOs and SMGs: molecular gas in far-infrared luminous QSOs at z$\approx$2.5**

- S. Alaghband-Zadeh, S. C. Chapman, A. M. Swinbank, Ian Smail, C. M. Harrison, D. M. Alexander, C. M. Casey, R. Dave, D. Narayanan, Y. Tamura, H. Umehata, 2012, MNRAS, 424, 2232: **Integral field spectroscopy of z=2.0-2.7 submillimetre galaxies: gas morphologies and kinematics**

Acknowledgements

There are many people to thank who have helped, in a variety of ways, to get my thesis into this finished state. I consider myself extremely lucky to have had Dave Alexander as my supervisor, with his infectious enthusiasm for extragalactic astronomy. Throughout the last three and a half years he has provided me with excellent advice and created a number of fantastic opportunities for me to progress as a researcher. I am very appreciative of his supervising style that has allowed me to explore my own ideas, whilst drawing upon his own experience and expertise to guide me in the right direction.

There are numerous post-docs and staff who have assisted me in my training and producing the research that is presented in this thesis. Ian Smail, Alastair Edge, John Stott, Alasdair Thomson, Agnese Del Moro and all of the co-authors on my papers have been particularly helpful. A special thanks to Mark Swinbank and Jim Mullaney who have invested considerable time into teaching me a range of skills, answering my stream of questions and coping with my irritatingly fastidious work ethic.

It has been a delight to work surrounded by my office mates, both past and present, and my other fellow PhD students within the department. It is not possible to name them all here; however, I must acknowledge my long-standing office-mate Alice Danielson, who is not only a great scientist but also has an unrivalled ability to inspire joy, enthusiasm and a love for astronomy into everybody she meets. Any department will be lucky to have her.

I am grateful to my whole family, who always provide me with a huge amount of encouragement. In particular, I will never find sufficient words to fully express my gratitude to my parents, who have given me their unrelenting support throughout my entire life. Finally, I feel truly blessed to have Lucy as my wife. She has shown an unbelievable amount of care, support and patience during my time as a PhD student. Lucy, I love you dearly, and now as promised, it is time for a holiday.

Contents

List of Tables **xi**

List of Figures **xii**

1 Introduction **1**

1.1 Overview 1

1.2 A brief history of the discovery of galaxies and AGN 2

1.3 AGN structure and multi-wavelength emission 4

1.4 The census of AGN activity 12

1.5 The co-evolution of BH and galaxy growth 17

1.6 The influence of AGN on the evolution of galaxies 23

1.7 Thesis overview 31

2 Integral field spectroscopy **34**

2.1 Introduction 34

2.2 Integral field spectroscopy 35

2.3 The instruments used in this thesis 37

2.4 Data reduction 39

3 Energetic galaxy-wide outflows in high-z ULIRGs hosting AGN activity **42**

3.1 Motivation 43

3.2 Introduction 43

3.3 Observations and data reduction 44

3.4 Star-formation rates and AGN luminosities 50

3.5 Analysis and results 52

3.6 Discussion 66
3.7 Conclusions 79
3.8 Notes on individual sources 85

4 Kiloparsec scale outflows are prevalent in luminous AGN: outflows and feedback in the context of the overall AGN population 95
4.1 Motivation 96
4.2 Introduction 96
4.3 Targets, observations and data reduction 97
4.4 Velocity definitions and spatially resolved kinematics 111
4.5 Results 120
4.6 Discussion 135
4.7 Conclusions 146
4.8 Notes on individual sources 149

5 No submillimetre signature of star formation suppression among X-ray luminous AGN 175
5.1 Motivation 175
5.2 Introduction 176
5.3 Catalogues and data 177
5.4 Measuring average star formation rates 180
5.5 Results and discussion 182

6 Conclusions and future work 187
6.1 Summary of the presented work 187
6.2 Overall summary and outstanding issues 190
6.3 Ongoing and Future Work 190
6.4 Final remarks 200

Bibliography 203

Appendix 224

A AGN emission lines: some relevant information and applications 224

A.1 Forbidden emission lines 224

A.2 Permitted emission lines 226

A.3 BPT diagram 228

A.4 Gas masses, mass outflow rates and energy injection rates 228

B Assumed cosmology 232

B.1 The model 232

B.2 Cosmic time and distances 233

C Acronyms 236

List of Tables

2.1 Summary of the IFS instruments used in this thesis 39

3.1 The radio positions, redshifts, radio luminosities and the details of the observations for the AGN-ULIRG IFU targets 46

3.2 Infrared photometric data, SFRs and AGN luminosities for the AGN-ULIRG IFU targets 82

3.3 The properties of the galaxy-integrated [O III] emission-line profiles shown in Fig. 3.3 83

3.4 The properties of the [O III] and Hβ emission-line profiles extracted from the sub-regions shown in Figure 3.5 84

4.1 Positions and redshifts for the type 2 AGN in our IFU sample 100

4.2 SF and AGN properties for the type 2 AGN in our IFU sample 106

4.3 WISE and IRAS fluxes for the type 2 AGN in our IFU sample 107

4.4 Velocity values and sizes from our IFU data of the type 2 AGN in our IFU sample 125

5.1 The mean redshifts and mean SFRs of X-ray detected AGN in the CDF-N, CDF-S and COSMOS fields for different L_X bins 179

List of Figures

1.1 The unified AGN model 5
1.2 Schematic diagram of an AGN SED 7
1.3 BPT diagram of $z < 0.4$ SDSS sources 11
1.4 Cosmic SFR and mass accretion rate density 18
1.5 sSFR and SFR as a function of redshift for X-ray detected AGN. 20
1.6 $M_{\rm BH}$ versus $M_{\rm bulge}$ for local classical bulges and elliptical galaxies 22
1.7 Schematic diagram to show how SF and AGN activity could impact upon one other 24
1.8 Schematic diagram to illustrate the two main modes of AGN feedback . . 26
1.9 Illustration of the epochs covered by the observations in this thesis 33
2.1 Schematic diagram of an IFU data cube 36
2.2 Summary of the main techniques of IFS 37
3.1 FWHM versus [O III]λ5007 luminosity and FWHM versus 1.4 GHz luminosity for the AGN-ULIRG IFU targets. 47
3.2 The IR SEDs for the AGN-ULIRG IFU targets 50
3.3 Galaxy-integrated spectra for the AGN-ULIRGs around the [O III]λλ4959, 5007 emission-line doublet 54
3.4 FWHM, velocity and surface brightness maps for the AGN-ULIRGs . . . 56
3.4 continued. 57
3.5 Maps of the AGN-ULIRGs, colour-coded to highlight regions dominated by narrow or broad [O III] emission lines 59
3.5 continued. 60
3.6 Velocity-distance profiles for the AGN-ULIRGs 62
3.6 continued. 63

3.6 continued. 64
3.7 A comparison of the emission-line widths of the AGN-ULIRGs in this work and ULIRGs form the literature 67
3.8 The projected spatial-extent of the broad [O III] emission-line regions against velocity offset with tracks to indicate model-derived outflow kinetic energy rates 70
3.9 A schematic diagram to illustrate a possible interpretation of the observations of the broad [O III] emission lines 73
3.10 A comparison between the estimated coupling efficiencies required to power the outflows observed from the AGN activity and the star formation activity in the AGN-ULIRGs 77
3.11 [O III] emission-line velocity offset versus FWHM with tracks to indicate the escape velocities for a representative galaxy and dark matter halo . . . 78
3.12 *HST* imaging of SMM J1636+4057, overlaid with contours to indicate the spatial distribution of molecular gas (CO), narrow [O III] emission, broad [O III] emission and Hα emission 91
4.1 [O III] FWHM versus [O III] luminosity and radio luminosity for our type 2 AGN IFU targets compared to the overall $z < 0.2$ AGN population 98
4.2 Histograms of [O III] FWHM and radio luminosity of our type 2 AGN IFU targets compared to the overall $z < 0.2$ AGN population 99
4.3 IR SEDs for our type 2 AGN IFU targets 105
4.4 Illustration of the different non-parametric velocity definitions used in this chapter 112
4.5 Our IFU data for an example type 2 AGN in our IFU sample (SDSS J1010+1413): velocity maps and [O III] emission-line profiles extracted from multiple spatial regions across the data cube. 118
4.6 Velocity-distance profiles and SDSS image from an example type 2 AGN (J1010+1413) in our IFU sample. 119
4.7 The [O III] peak signal-to-noise ratio maps for all sixteen type 2 AGN in our sample. 123
4.8 Line-width maps for all sixteen type 2 AGN in our sample. 127

4.9 Line-width and maximum velocity versus [O III] luminosity and radio luminosity for our type 2 AGN IFU sample and comparison samples. . . . 131
4.10 Line-width and maximum velocity versus IR luminosity from SF, AGN luminosity and q_{IR} for our type 2 AGN IFU targets and the comparison samples. 138
4.11 The ratio of outflow kinetic energy rates to the AGN luminosity, SF luminosity and radio jet power for our type 2 AGN IFU targets. 141
4.12 Momentum rates of the outflows in our type 2 AGN IFU targets compared to the SF luminosity and AGN luminosity. 144
4.13 Same as Figure 4.5 and Figure 4.6 but for SDSS J0945+1737 160
4.14 Same as Figure 4.5 and Figure 4.6 but for SDSS J0958+1439 161
4.15 Same as Figure 4.5 and Figure 4.6 but for SDSS J1000+1242 162
4.16 Same as Figure 4.5 and Figure 4.6 but for SDSS J1010+0612 163
4.17 Same as Figure 4.5 and Figure 4.6 but for SDSS J1100+0846 164
4.18 Same as Figure 4.5 and Figure 4.6 but for SDSS J1125+1239 165
4.19 Same as Figure 4.5 and Figure 4.6 but for SDSS J1130+1301 166
4.20 Same as Figure 4.5 and Figure 4.6 but for SDSS J1216+1417 167
4.21 Same as Figure 4.5 and Figure 4.6 but for SDSS J1316+1753 168
4.22 Same as Figure 4.5 and Figure 4.6 but for SDSS J1338+1503 169
4.23 Same as Figure 4.5 and Figure 4.6 but for SDSS J1339+1425 170
4.24 Same as Figure 4.5 and Figure 4.6 but for SDSS J1355+1300 171
4.25 Same as Figure 4.5 and Figure 4.6 but for SDSS J1356+1026 172
4.26 Same as Figure 4.5 and Figure 4.6 but for SDSS J1430+1339 173
4.27 Same as Figure 4.5 and Figure 4.6 but for SDSS J1504+0151. 174
5.1 L_X versus redshift for X-ray AGN detected in the CDF-S, CDF-N and COSMOS fields 178
5.2 Mean SFR versus L_X for AGN with spectroscopic redshifts in the CDF-N field 182
5.3 Mean SFR versus L_X for AGN in the CDF-N, CDF-S and COSMOS fields 183
6.1 HST image of J1430+1339 with JVLA 5 GHz radio data overlaid 193
6.2 CO(1-0) emission-line profiles for two type 2 AGN 195

6.3 A comparison of the [O III] emission-line profiles of AGN and H II galaxies 198
6.4 An illustration of the epochs covered by the observations in this thesis and those of future programmes 199
6.5 A snap-shot from a preliminary EAGLE run of a galaxy undergoing an AGN-driven outflow 201
A.1 Diagram of the O III electron sub-shells 225
A.2 [O III] energy-level diagram 227

CHAPTER 1

Introduction

1.1 Overview

Just over a century has passed since the first observations of active galactic nuclei (AGN) were recorded. As AGN continued to be discovered over the following years it became clear that they were among the most powerful energy sources in the Universe and we now know that they are extremely luminous over the whole electromagnetic spectrum. For many decades these energetic phenomenon, residing at the centre of galaxies, were largely considered rare, yet fascinating, objects to study in their own right. However, over the last quarter of a century or so, high-quality observations and theoretical work have moved AGN to the forefront of extragalactic astronomy research. Observations have now shown us that all massive galaxies are likely to have hosted AGN activity during their lifetimes. Furthermore, theoretical work now suggests that AGN activity has a profound influence on the evolution of its host galaxy and the larger scale environment that it resides in. However, placing *observational constraints* on the influence of AGN on the evolution of galaxies remains an open area of research, with many outstanding questions. This thesis uses a variety of observational techniques to address these questions and to test theoretical predictions. Introductory material, specific to the topic being investigated, is provided at the beginning of individual science chapters. The aims of this first chapter are to provide: (1) a (very) short history of the discovery of galaxies and AGN; (2) a summary of the key properties and observations of AGN, which are thereafter referred to throughout this thesis; (3) a brief review of the current research on *the influence of active galactic nuclei on the evolution of galaxies*.

1.2 A brief history of the discovery of galaxies and AGN

1.2.1 Galaxies

Extragalactic astronomy is not yet a century old, despite the fact that several extragalactic objects (i.e., galaxies outside of our own Milky Way) had been unknowingly catalogued, along with other "nebulous objects", as far back as the 1780s (Messier 1781; Herschel 1786). Furthermore, whilst Thomas Wright had speculated that some of these nebulae could be distant groups of stars, outside of our own Milky Way, in the eighteenth century, it wasn't until the early twentieth century that their extragalactic nature was confirmed. Early use of spectroscopy showed that "spiral nebulae" (the spiral shape of some nebulae was noted by Rosse 1850) were composed of stars (e.g., Huggins & Miller 1864; Scheiner 1899) with larger radial velocities than any other known astronomical objects (Slipher 1915, 1917a); however, it was by exploiting the tight luminosity-period relationship of Cepheid variable stars that lead to the definitive proof that these stellar systems are indeed separate from the Milky Way (i.e., they are extragalactic; Hubble 1925, 1929). It quickly became apparent that the Universe was full of "extragalactic nebulae" (i.e., galaxies), which exhibit a rich and diverse range of shapes and sizes (Hubble 1926). Largely thanks to the launch of the *Hubble Space Telescope (HST)* in 1990 we now know that the Universe is home to around 100 billion galaxies (this is roughly the number of Olympic-sized swimming pools that it would take to cover the surface of the Earth four-times over!). The ultimate goal for extragalactic astronomers is to understand how all of these galaxies form and evolve. Reviewing the full extent of the current knowledge of galaxy formation and evolution is way beyond the realms of this introduction. Instead the following sections focus on the fascinating objects residing at the centre of galaxies (i.e., active galactic nuclei) and the role that they are believed to play in galaxy evolution.

1.2.2 Active Galactic Nuclei

The first recorded observational evidence for the existence of (what are now referred to as) active galactic nuclei came from Edward A. Fath in 1908 who was obtaining spectra of star clusters and "spiral nebulae" at the Lick Observatory (Fath 1909). Fath noted that the spectrum of the object called NGC 1068, which was not yet known to be extragalactic

(see previous section), exhibited strong emission lines; however, it was not until almost a decade later that the interesting features of the spectrum (with the unusually strong and broad high-excitation emission-line profiles) received proper attention (Slipher 1917b). Twenty five years later, the seminal work of Carl Seyfert presented analyses on the spectra of six of the twelve galaxies that had been identified as having equivalent nuclear spectra to that of NGC 1068 (Seyfert 1943). Consequently, similar objects are now called "Seyfert galaxies". Two classes of Seyfert galaxy were eventually established: (1) "type 1", where the permitted emission lines are significantly broader than the forbidden emission lines and (2) "type 2", where the permitted lines and forbidden lines are of the same width (Weedman 1970; Khachikian & Weedman 1971).[1] Over the following three decades, since Seyfert (1943), the number of identified Seyfert galaxies increased dramatically and further study revealed the unusual nature of these objects: they have exceptionally compact and bright nuclear regions, and have a variable ultra violet to optical continuum, in addition to their unusually strong and broad emission lines (an early review is given by Weedman 1977). All of these observations were suggestive of a very compact powerful energy source at the centre of these galaxies.

Independently of the optical studies discussed above, during the 1960s, radio astronomers discovered a class of extremely bright radio sources that appeared to be associated with optical point sources (e.g., Matthews & Sandage 1963). These "quasi-stellar radio sources" (shortened to quasars),[2] turned out to have very high redshifts (z), given their considerable brightness (i.e., $z \gtrsim 0.1$; e.g., Schmidt 1963; Greenstein 1963; see Appendix B for how redshift relates to distance). Although it was a controversial idea for many years (e.g., see Weedman 1976, 1977), it eventually became apparent that these quasars were distant, more luminous versions of Seyfert galaxies. Around the same time, it was also discovered that luminous non-thermal radio emission, in the form of collimated jets and large extended structures (up to megaparsec scales), were associated with the nuclear regions of several galaxies in the nearby Universe (e.g., Baade & Minkowski

[1]The lines typically used were the permitted line Hβ and the forbidden line [O III]λ5007. Further discussion on emission lines in AGN is provided in Section 1.3.3 and Appendix A.

[2]It is now common practice to use the term "quasar" to refer to the most luminous AGN in the Universe (i.e., bolometric luminosities of $L_{\rm AGN} \gtrsim 10^{45}\,{\rm erg\,s^{-1}}$; see Section 1.3.4), irrespective of their radio properties. Throughout this thesis the term quasar is used as a generic term to refer to very luminous AGN.

1954; Burbridge 1963). Collectively powerful radio galaxies, quasars and Seyfert galaxies are now referred to as "active galactic nuclei" (AGN), due to the luminous emission produced at the nuclei of these objects. Furthermore, these different observational classes of AGN, including the difference between Seyfert type 1 and type 2, have been unified using a single physical model (described in Section 1.3). There are now many other observational classifications of objects that are considered to be AGN; however, because they are not the focus of this thesis they are not reviewed here (see e.g., Antonucci 1993; Urry & Padovani 1995; Tadhunter 2008).

During the continuing discovery of AGN, it became apparent that a massive, extremely compact, powerful energy source, with the ability to form highly collimated jets was required to explain their observational characteristics. The source of this energy was heavily debated for a long time (see e.g., Saslaw 1974); however, the prevailing idea was that of mass accretion onto a supermassive black hole (BH)[3] (e.g., Salpeter 1964; Zeldovich & Novikov 1964; Lynden-Bell 1969; Rees 1984). A variety of evidence lead to this consesus view. Evidence for the existence of "massive dark objects" (MDOs), in the inner regions of galaxies in the local Universe was established through the collective work of many studies using the dynamical modelling of stars, emission-line gas and molecular masers (e.g., Sargent et al. 1978; Tonry 1984; Dressler & Richstone 1988; Harms et al. 1994; Miyoshi et al. 1995; see review in Kormendy & Richstone 1995). Furthermore, a comparison of the mass density of MDOs to the estimated total energy produced by AGN across cosmic time, has been used to show that these objects most likely grew through luminous mass-accretion events with a $\approx 10\%$ efficiency of mass-to-energy conversion (see Section 1.3.1; e.g., Soltan 1982; Marconi et al. 2004). It is now almost universally accepted that MDOs are BHs that grew through mass accretion events, during which they would have been visible as AGN. With over 80 confirmed BHs residing in local galaxies, combined with a huge amount of observational evidence from galaxy and AGN studies, it is now believed that BHs are (probably) residing inside of all massive galaxies and consequently that all of these galaxies undergo AGN activity during their lifetime (see re-

[3]Throughout this thesis only "supermassive" black holes are referred to; i.e., those with a mass in the range $\approx 10^5$–10^{10} $M_\odot$. This is in contrast to stellar mass BHs that have masses $\approx$ 2–20 $M_\odot$ (e.g., McClintock & Remillard 2006).

view by Kormendy & Ho 2013). In summary, AGN were once considered rare and exotic objects but they are now believed to represent a universal episode in the evolution of all massive galaxies.

1.3 AGN structure and multi-wavelength emission

To assist with the understanding of the different methods of AGN identification used in this thesis, it is useful to briefly outline the currently most accepted model of the physical structure of AGN (see Fig. 1.1) and to highlight the corresponding features observed in their spectral energy distributions (SEDs; see Fig. 1.2) and spectra. It is also useful to introduce the favoured "unified" model of AGN (Antonucci 1993, Urry & Padovani 1995) that can be used to explain both the different observational classes of AGN (e.g., type 1 versus type 2 Seyferts; see Fig. 1.1). Whilst this model does not account for all observational characteristics of AGN, and recent work has suggested small modifications are required (e.g., Nenkova et al. 2008; Elvis 2012; Bianchi et al. 2012), the major aspects of the model are still widely accepted and it is sufficient for the demonstrative purposes required here. This section uses the standard AGN physical model and unified model as a basis to describe some of the key features of AGN spectra and continuum SEDs; however, it should be noted that the exact physical processes that result in the observed emission of AGN is a topic of ongoing research and a full overview cannot be given here (instead see e.g., Koratkar & Blaes 1999; Polletta et al. 2000; Laor & Behar 2008; Vasudevan & Fabian 2009; Done et al. 2012).

1.3.1 The growing BH

The standard physical model of an AGN (Fig. 1.1) starts with a central BH that is growing via mass accretion. The accretion luminosity is given by,

$$L_{\rm acc} = \eta \dot{M} c^2 \tag{1.3.1}$$

where η is the mass-energy efficiency conversion (typically estimated to be ≈ 0.1, but is dependent on the spin of the BH with an expected range of $\eta = 0.05$–0.42; e.g., Kerr

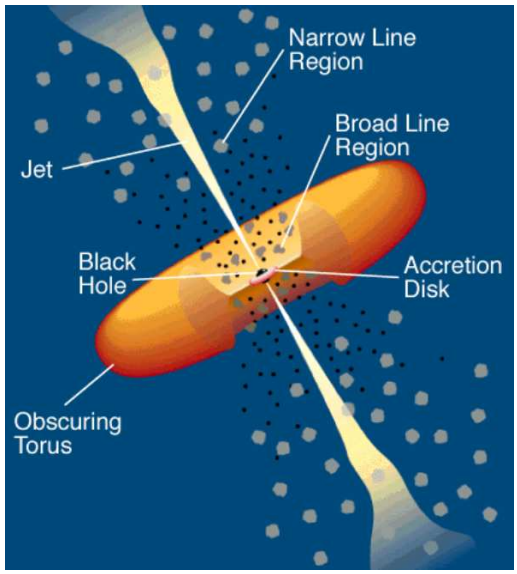

Figure 1.1: A schematic diagram (adapted from Urry & Padovani 1995) of the currently most accepted model of the structure of AGN. Surrounding the central BH is an accretion disk that resides inside a geometrically thick and optically thick dusty structure called the "torus". Above and below the accretion disk is a hot corona. Two distinct emission-line regions are present: (1) the broad-line region (BLR) that is under the gravitational influence of the BH and (2) the narrow-line region (NLR) that is extended over much larger scales. Radio jets may also be launched from close to the accretion disk. The "unified model" of AGN implies that, along certain lines of sight, obscuration by the dusty torus will prevent the optical emission from the accretion disk and BLR from being observable. In contrast, observing emission from the NLR, torus and radio jets is less dependent on the line of sight.

1963; Thorne 1974) and $\dot{M}$ is the mass accretion rate. A theoretical upper limit on $L_{\rm acc}$ can be calculated assuming accretion of fully ionised hydrogen onto a BH of mass $M_{\rm BH}$, when the force of gravity is equal to the radiation pressure from the accretion luminosity. This upper-limit is called the "Eddington luminosity" and has the value

$$L_{\rm Edd} = \frac{4\pi G M_{\rm BH} m_p c}{\sigma_T} \quad (1.3.2)$$

$$\approx 1.3 \times 10^{38} (M_{\rm BH}/\,{\rm M}_\odot)\,{\rm erg\,s^{-1}} \quad (1.3.3)$$

where m_p is the proton mass, c is the speed of light, G is the gravitational constant and σ_T is the Thomson cross-section for an electron. The ratio of the observed accretion luminosity to the Eddington luminosity (called the "Eddington ratio"; $\lambda_{\rm Edd}$) is a useful measure for comparing BH accretion rates over a wide range of BH masses

$$\lambda_{\rm Edd} = L_{\rm acc}/L_{\rm Edd} \quad (1.3.4)$$

The term "high-accretion" rate AGN is often used to refer to sources with high values of $\lambda_{\rm Edd}$ (i.e., $\lambda_{\rm Edd} \gtrsim 0.1$). The value of $L_{\rm acc}$ used in Equation 1.3.4 is assumed to be the *radiative* bolometric output of the AGN (i.e., $L_{\rm AGN}$; see Section 1.3.5); however, it should be noted that another definition of Eddington ratio uses the combined radiative and mechanical output of the AGN (discussed more in Section 1.4.5; also see Best & Heckman 2012).

1.3.2 AGN standard model and broad-band continuum SEDs

The standard AGN physical model (Fig. 1.1) is a good starting point to understand the broad-band continuum SEDs of AGN. Figure 1.2 shows a schematic representation of an AGN SED from radio frequencies to hard X-rays. The figure shows the various physical components (discussed below) that are thought to make up the overall observed SEDs of AGN; however, it should be noted that the relative contribution of these components can vary dramatically for different types of AGN. The focus of this thesis, and therefore this discussion, is on high-accretion rate AGN that emit most of their energy radiatively (sometimes called "radiatively efficient", "radiative mode" or, when referring to

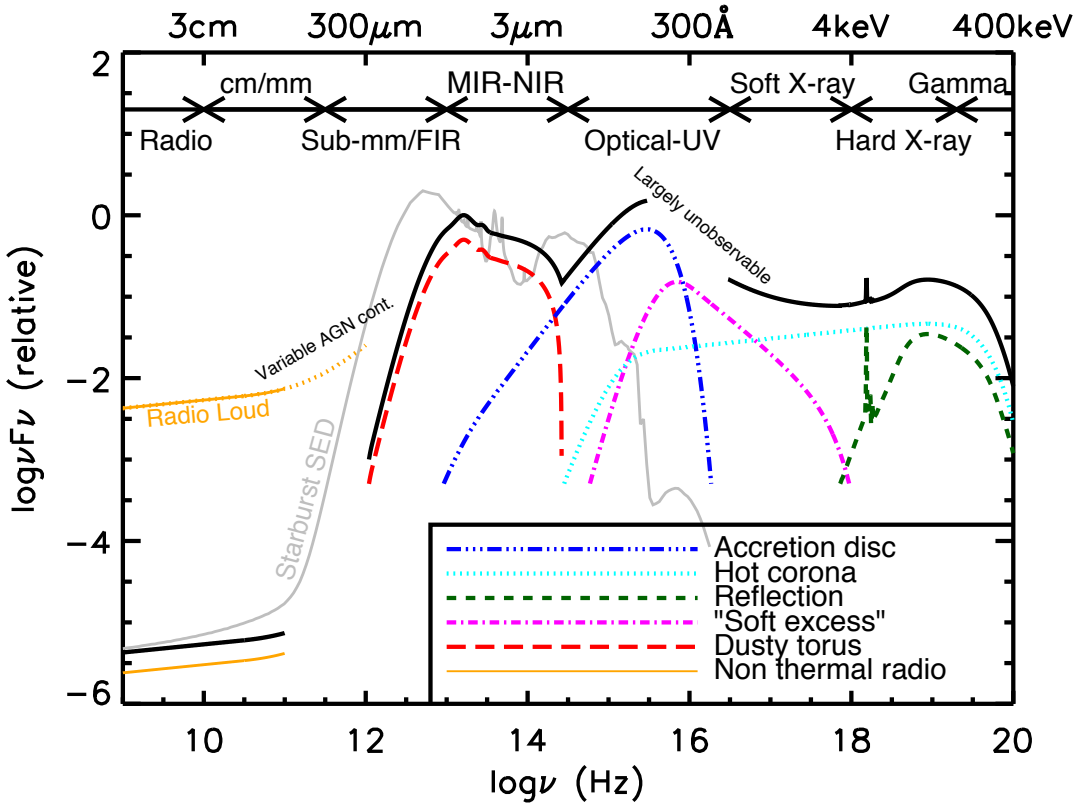

Figure 1.2: A schematic representation of an AGN SED, loosely based on the observed SEDs of radio-quiet quasars (e.g., Elvis et al. 1994; Richards et al. 2006a). The black solid curve represents the total SED and the various coloured curves (with an arbitrary offset) represent the individual components (see Section 1.3.2). The SED of an AGN in the mm–FIR regime is uncertain; however, it is widely believed to have a minimal contribution (to an overall galaxy SED) compared to star formation, except in the most intrinsically luminous quasars and powerful radio-loud AGN. The primary emission from the AGN accretion disk peaks in the UV region. Radio-loud AGN have radio emission that can be several orders of magnitude higher than radio-quiet AGN (shown with the labelled orange line). Also shown is an example radio–UV SED of a starburst galaxy (grey curve; the SED is of M82 taken from the GRASIL library; Silva et al. 1998).

radio galaxies, "high excitation"; see review in Heckman & Best 2014) and that are radio quiet.[4] This thesis does not focus on radiatively-inefficient AGN (sometimes called "low excitation", "radio mode" or "jet mode") that emit the majority of their energy mechanically through radio jets (e.g., Merloni & Heinz 2007; McNamara & Nulsen 2012; Best & Heckman 2012; Heckman & Best 2014).

The standard AGN model has a BH surrounded by an accretion disk (Fig. 1.1). If it is assumed that this accretion disk is optically thick (e.g., Shakura & Sunyaev 1973),[5] the resulting continuum spectrum would be thermal with a black-body temperature of $\approx 2 \times 10^5$ K that peaks in the ultra violet (UV; $\approx$10–400 nm) for a "typical" AGN (i.e., with $M_{\rm BH} \approx 10^8\,{\rm M}_\odot$; $\lambda_{\rm Edd} \approx 0.1$). Indeed, AGN are often observed to have a peak in their optical–UV continuum that is referred to as the "big blue bump" (Fig. 1.2). Unfortunately, the majority of the bolometric luminosity of an AGN is thought to be in the UV, which is a region of the electromagnetic spectrum that can not easily be observed from Earth. Around the accretion disk there is thought to be an optically thin corona where the photons produced at the accretion disk undergo Compton up-scattering to produce the power-law spectrum of high-energy X-rays that are observed in AGN (Fig. 1.2). These X-ray photons may also reflect off the torus (see below) and/or the accretion disk to produce an additional "reflection" component in the X-ray region (e.g., George & Fabian 1991; see Fig. 1.2). Additionally, at soft X-ray frequencies, there is often emission observed at a level above that expected from simple accretion disk models, that is referred to as a "soft excess"

[4] There are multiple definitions of "radio-quiet" AGN (as opposed to radio-loud AGN) used throughout the literature and it is therefore useful to clarify this term here. Historically, radio-loud AGN are defined as those where the ratio of 5 GHz radio luminosity (L_ν[5GHz]) to B-band optical luminosity (L_ν[B]) is much higher than average (i.e., $L_\nu[5{\rm GHz}]/L_\nu[{\rm B}] > 10$; Kellermann et al. 1989; also see Xu et al. 1999 for a definition using optical emission lines). The term "radio loud" is also sometimes used interchangeably with "radio AGN" where AGN dominate the radio emission over star formation (see Best & Heckman 2012 and references there-in). Additionally, "radio loud" is often used as a generic term to describe AGN that are particularly luminous at radio wavelengths (e.g., $L_{1.4{\rm GHz}} \gtrsim 10^{25}\,{\rm W\,Hz^{-1}}$). In this thesis, "radio loud" is used to refer to sources with exceptionally high radio luminosities where the luminosity is almost certainly dominated by the AGN and "radio quiet" refers to more typical radio luminosities of $L_{1.4{\rm GHz}} \lesssim 10^{24-25}\,{\rm W\,Hz^{-1}}$. The term "high-excitation" (opposite to "low-excitation") radio AGN is used to refer to radio-identified AGN that also look like AGN based on various optical emission-line diagnostics (see Best & Heckman 2012 and references there-in; also see Section 1.4.5). Finally, "radio excess" AGN are defined as AGN where there is significant radio emission above that expected from star formation alone (e.g., Roy & Norris 1997; Donley et al. 2005; Del Moro et al. 2013) that could imply radio emission from an AGN.

[5] The assumption of an optically thick accretion disk may only be valid for radiatively-efficient AGN that are the focus of this thesis (see e.g., Yuan & Narayan 2014; Heckman & Best 2014 and references there-in).

component. The origin of this soft excess emission is a topic of active research (see Done et al. 2012 and references there-in).

According to the unified model, surrounding the inner regions of an AGN is a geometrically thick and optically thick dusty region, with an inner radius set by the dust sublimation temperature. In the standard model, this region has a torus shape (Fig. 1.1); however, the geometry of this structure is the subject of ongoing research and is now widely believed to be clumpy (e.g., Hönig et al. 2006; Nenkova et al. 2008). The dust in this region will be heated by absorbing the photons from the accretion disk (making the accretion disk unobservable along some lines-of-sight) and consequently this dust will re-emit thermal radiation in the infrared (IR; i.e., $\approx$ 1–1000 μm; e.g., Pier & Krolik 1992, Rowan-Robinson 1995; Polletta et al. 2000; see Fig. 1.2).[6] Although the exact form of the IR emission for an AGN varies from source to source, the peak in this torus component seems to be around $\lambda \approx$ 20–50 μm and has a steep fall-off at longer wavelengths (e.g., Schartmann et al. 2008; Nenkova et al. 2008; Mullaney et al. 2011; Fig. 1.2). In the sub-mm/FIR frequency range it is generally thought that, for the majority of AGN, the emission is dominated by thermal emission from cooler dust heated by the star formation in the host galaxy (e.g., Alexander et al. 2005; Mullaney et al. 2011; see review in Lutz 2014) with a minimal contribution from the AGN itself (Fig. 1.2). However, the contribution to the heating from the most luminous quasars and in radio-loud AGN can be non-negligible, particularly at $\lesssim$ 70 μm, and for some of the most radio-luminous AGN non-thermal emission could also be present in this part of the SED (e.g., Willott et al. 2002; Polletta et al. 2000; Tadhunter et al. 2007; Dicken et al. 2009, 2010; Hill & Shanks 2011).

The SEDs of AGN at radio frequencies are extremely diverse, with a variety of spectral slopes and several orders of magnitude difference in the radio luminosities from radio-loud compared to radio-quiet AGN (e.g., Kellermann et al. 1989; Elvis et al. 1994; Fig. 1.2). The radio emission in radio-loud AGN originates from relativistic jets, launched close to the accretion disk (Fig. 1.1), as well as emission from extended radio structures. In radio-quiet AGN the radio emission is usually more compact, and the process (or pro-

[6] It should be noted that in a fraction of radio-loud AGN the mid-IR emission may have a significant non-thermal contribution (e.g., Dicken et al. 2008).

cesses) that produce this emission is less certain, with possible contributions from supernovae, compact radio jets and a corona close to the accretion disk (see e.g., Smith et al. 1998; Polletta et al. 2000; Laor & Behar 2008; and references there-in).

1.3.3 AGN standard model and the emission-line regions

The previous sub-section discussed the origin of the multi-wavelength continuum emission from an AGN (Fig. 1.2). In this sub-section the origins of the luminous emission lines observed in the spectra of AGN are briefly discussed. Some more specific details on the production mechanisms of emission lines in AGN are provided in Appendix A.

UV photons produced at the accretion disk are thought to excite dense (i.e., electron densities $n_e \gtrsim 10^8$ cm^{-3}; Osterbrock & Ferland 2006) high velocity gas clouds that are under the direct gravitational influence of the BH. This results in the production of extremely broad permitted emission lines (typically FWHM$\approx 10^3$–10^4 km s^{-1}; see Fig. 1.3). The region where these broad lines are produced is called the *broad-line region* (BLR; Fig. 1.1) and has a size-scale of light-days to light-months (e.g., Peterson et al. 2004). Forbidden emission lines are not observed in this region due to these lines being collisionally de-excited before they can de-excite by the emission of a photon (see Appendix A for more details). The presence or absence of broad permitted emission lines in the spectra of AGN results in the optical classifications of type 1 and type 2 respectively (as mentioned in Section 1.2.2). For type 2 AGN, the unified model states that no permitted emission lines are observed that are considerably broader than the observed forbidden lines because the line-of-sight to the BLR is obscured from view by the torus (Fig. 1.1).

Ionising photons that escape the central regions of the AGN can ionise gas in low-density regions that extend beyond the inner BLR (with electron densities $n_e \lesssim 10^6$ cm^{-3}; Osterbrock & Ferland 2006; see Fig. 1.1). Here the emission lines produced have narrower widths (i.e., $250 \lesssim$ FWHM $\lesssim 2000$ km s^{-1}) and this region is referred to as the *narrow-line region* (NLR; Fig. 1.1). Unlike the BLR both permitted lines and forbidden lines are produced in the NLR, which can extend over large scales (i.e., $\approx 10^2$–10^4 pc; e.g., Walker 1968; Wampler et al. 1975; Wilson & Heckman 1985; Boroson et al. 1985; Stockton & MacKenty 1987; Osterbrock 1989; Tadhunter & Tsvetanov 1989; Bennert et al. 2002; Greene et al. 2011).

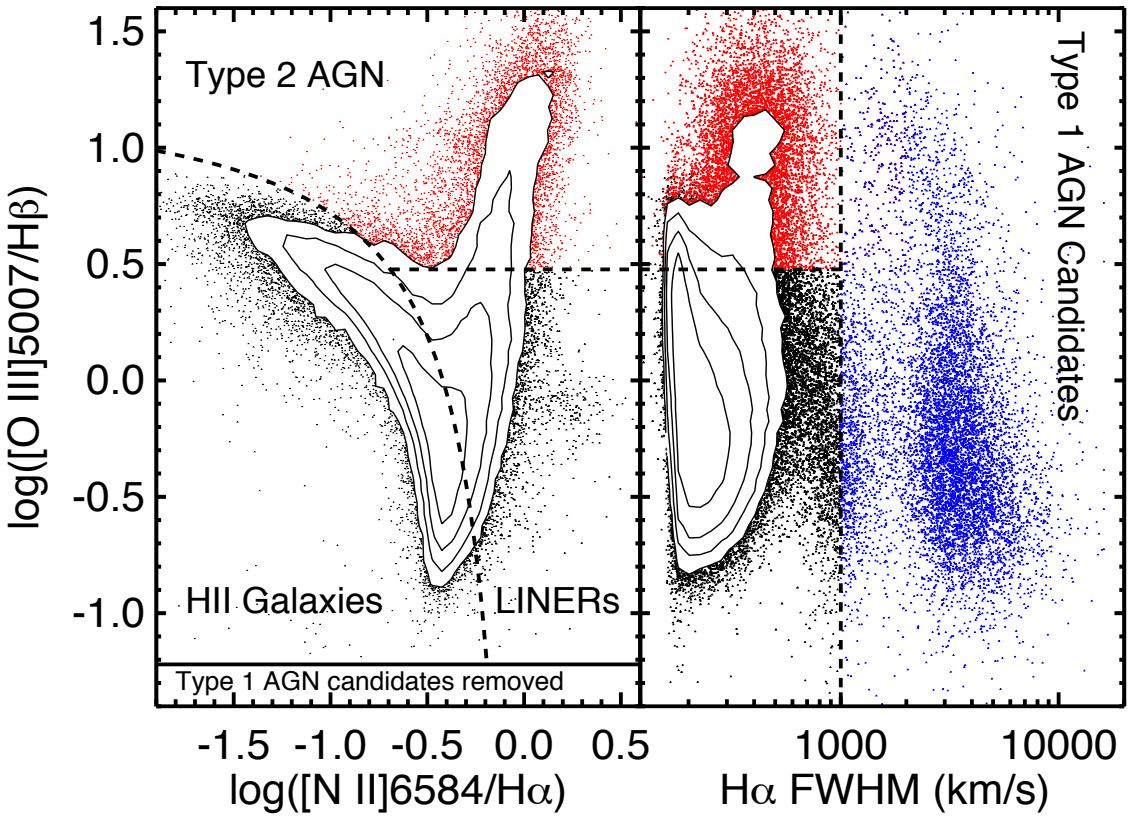

Figure 1.3: Plots to highlight typical optical emission-line diagnostics used to identify AGN (adapted version of Fig. 1 in Mullaney et al. 2013). All data shown are taken from the SDSS DR7 database for extragalactic sources with $z < 0.4$. *Left:* Emission-line flux ratios of [O III]λ5007/Hβ versus [N II]λ6584/Hα for sources with $\mathrm{FWHM_{H\alpha}} < 1000\,\mathrm{km\,s^{-1}}$. The dashed lines are taken from Ho et al. (1997a) and Kauffmann et al. (2003) to identify different source classifications (i.e., Type 2 AGN [shown in red]; LINERS and H II galaxies [shown in black]). *Right:* [O III]λ5007/Hβ versus $\mathrm{FWHM_{H\alpha}}$. Broad Hα emission-line profiles (i.e., $\mathrm{FWHM_{H\alpha}} \gtrsim 1000\,\mathrm{km\,s^{-1}}$) may indicate the presence of BLR (see Section 1.3.3). It is possible for reasonably broad emission lines (i.e., $1000\,\mathrm{km\,s^{-1}} \lesssim \mathrm{FWHM} \lesssim 2000\,\mathrm{km\,s^{-1}}$) to be produced in the NLR due to outflows (see Section 1.6.2) therefore care needs to be taken when classifying AGN with these "intermediate" line widths (e.g., Mullaney et al. 2013).

1.3.4 Bolometric luminosities

It is a common situation, as is the case in this thesis, that AGN only have measurements in a limited range of continuum wavebands and/or emission lines, whilst what is often desired is a bolometric luminosity (i.e., the total accretion luminosity that primarily emits in the optical–UV; Equation 1.3.1; see Fig. 1.2). Therefore, using template AGN, wavelength-dependent bolometric correction factors (BC_λ) need to be applied to calculate the total accretion luminosity ($L_{\rm AGN}$; e.g., Elvis et al. 1994; Hopkins et al. 2007; Richards et al. 2006a; Lusso et al. 2010) from a single continuum waveband or emission-line luminosity (L_λ), following,

$$L_{\rm AGN} = L_\lambda BC_\lambda. \tag{1.3.5}$$

It is important to note that the measured luminosities are often from re-processed emission (e.g., the infrared emission from the torus; see Figure 1.2) rather than the primary emission of the AGN accretion disk. Furthermore, bolometric corrections are empirical measurements from samples of AGN, therefore they assume an "average" relative strength of the different physical components that produce the overall SEDs (see Fig. 1.2).

1.4 The census of AGN activity

The previous section described how AGN emit strongly across the whole range of the electromagnetic spectrum, with distinctive features in their continua (see Fig. 1.2) and spectra. It is possible to build up large samples of AGN, using a variety of observations, by exploiting these features. In this thesis a variety of approaches are used to identify AGN activity and it is therefore useful to briefly summarise different methods and describe some of their advantages and disadvantages. In addition, in this section, it is discussed how different AGN selection methods could preferentially identify AGN with different accretion properties, host galaxies properties and environments.

1.4.1 Optical/UV surveys

The optical/UV SEDs of AGN and starburst galaxies are noticeably different (e.g., see Fig. 1.2). Therefore, for several decades, colour diagnostics have been applied to the ob-

jects detected in photometric surveys to identify AGN (Schmidt & Green 1983; Boyle et al. 1990; Richards et al. 2001). However, these methods are generally limited to the most luminous AGN (i.e., quasars) where the optical emission is unambiguously AGN-like with little-to-no contamination from stellar emission. In contrast, optical spectroscopic surveys (e.g., the Sloan Digital Sky Survey; SDSS; York et al. 2000 and the 2dF Galaxy Redshift Survey; 2dFGRS; Colless et al. 2001) have revolutionised the study of AGN in the local Universe by identifying tens of thousands of AGN at low redshifts across a broad range of intrinsic luminosities (e.g., Ho et al. 1997b; Kauffmann et al. 2003; Schneider et al. 2005; Pâris et al. 2012). These studies make use of optical emission lines, either through the identification of extremely luminous or broad profiles (i.e., FWHM $\gtrsim$1000 km s^{-1}) or through emission-line ratio diagnostics (e.g., the "BPT" diagram; Baldwin et al. 1981; Fig. 1.3). These emission-line ratio diagnostics make use of the varying production of different emission-line species produced under the radiation field from an AGN, when compared to those produced under the radiation field from starlight (i.e., H II regions). The presence of strong high-excitation emission lines (e.g., [Ne V] or particularly luminous [O III]) in the spectra of a galaxy, indicates a "harder" ionising continuum (i.e., out to higher energies) than seen from stars, and therefore is likely to imply AGN activity (see Fig. 1.2 and Fig 1.3; also see Appendix A). Emission lines are used to identify AGN in Chapter 3 and Chapter 4 of this thesis.

Emission-line ratio diagnostics (using narrow emission lines, e.g., Fig. 1.3) have proven to be successful at identifying AGN over a range of luminosities and, under the unified model, these methods are not dependent on the line-of-sight to the accretion disk (e.g., see Fig. 1.1). These diagnostic tools are well-calibrated and used extensively to identify AGN at low redshift (i.e., $z \lesssim 0.4$); however, beyond $z \gtrsim 0.4$, the observed wavelengths of the key emission-lines (see Fig. 1.3) are redshifted into the near-IR (NIR) and it is only recently that it has become possible to begin large systematic spectroscopic surveys in this wavelength range due to the successful commissioning of high-quality NIR multi-object spectrographs (e.g., FMOS; Kimura et al. 2010; MOSFIRE; McLean et al. 2010; MMIRS; McLeod et al. 2012; KMOS; Sharples et al. 2013). Futhermore, re-calibrating these emission-line ratio diagnostic tools to be applicable for observations of galaxies at higher redshifts is an open area of research (e.g., Juneau et al. 2011; Kewley et al. 2013).

Aside from the redshift limitations, the main disadvantage of this AGN identification approach is that it requires targeted spectroscopic follow-up observations of galaxies that were previously identified in photometric surveys, making it difficult to create a complete and unbiased sample of AGN.

1.4.2 X-ray surveys

From the early-days of X-ray observations, AGN have been found to be luminous X-ray emitters (Elvis et al. 1978) with distinctive spectral shapes (see Section 1.3.2 and Fig. 1.2). X-rays surveys are a successful method for identifying AGN; at luminosities of $L_{2-10\mathrm{keV}} \gtrsim 10^{42}\,\mathrm{erg\,s^{-1}}$ AGN dominate X-ray detections (over e.g., star formation, X-ray binaries and hot gas) and at all luminosities other sources of X-rays can be isolated on the basis of different spectral slopes and X-ray–to–optical flux ratios (e.g., O'Sullivan et al. 2001; Steffen et al. 2006; Persic & Rephaeli 2007; Lehmer et al. 2010; Wang et al. 2013). Consequently, deep blank-field X-ray surveys (e.g., Brandt et al. 2001; Giacconi et al. 2002; Alexander et al. 2003a; Luo et al. 2008; Xue et al. 2011) have provided what are arguably the most uniform samples of luminous AGN to-date, particularly at high redshift (see review by Treister & Urry 2012). Chapter 5 of this thesis makes use of deep X-ray surveys to study a large sample of distant AGN.

X-ray photons (in particular those of higher energies; i.e., $\gtrsim$2 keV) are much less sensitive to obscuration compared to optical and UV photons, which means that they can be used to observe AGN even when there is substantial material along the line of sight (e.g., Mushotzky et al. 2000; Tozzi et al. 2006) and therefore they are reasonably insensitive to inclination effects (see Fig. 1.1). However, X-ray surveys still miss the most heavily obscured sources (particularly at high column densities $N_H \gtrsim 10^{24}\,\mathrm{cm^{-2}}$; e.g., Treister et al. 2004; Daddi et al. 2007b; Alexander et al. 2008a). Additionally, AGN have a wide range in levels of obscuration making it very challenging to obtain the *intrinsic* luminosities without data from a broad energy range (e.g., Lansbury et al. 2014). Furthermore, X-rays from AGN do not trace the majority of the accretion disk luminosity (see Fig. 1.2); therefore, there is uncertainty in the bolometric luminosities derived from X-ray fluxes over a small energy range and using average bolometric correction factors (Section 1.3.4).

1.4.3 Infrared surveys

As described in Section 1.3.2, luminous IR emission will be emitted from warm dust that has been heated by AGN (see Fig. 1.2); therefore, observations in the IR waveband can provide useful data to identify AGN. Both star formation and AGN activity heat dust and therefore both produce infrared emission; however, the SEDs produced from these two processes are reasonably distinct (e.g., Polletta et al. 2000; Mullaney et al. 2011; see Fig. 1.2; although see caveats below). This means that mid-IR (MIR) to NIR colour diagnostics can be used to identify AGN and these methods have been used on the data from several IR photometric surveys (e.g., Lacy et al. 2004; Stern et al. 2005, 2012; Donley et al. 2008, 2012; Hickox et al. 2007; Jarrett et al. 2011; Mateos et al. 2012). MIR spectroscopy is another successful method of identifying AGN due to the characteristic continuum and the presence of high-excitation emission lines produced in this wavelength range (e.g. Weedman et al. 2005; Goulding & Alexander 2009); however, MIR spectroscopy is not used in this thesis.

Based on the unified model, IR selection of AGN should be reasonably insensitive to orientation effects as the dust emission should be visible from all viewing angles (Section 1.3.2; Fig. 1.2). This means that IR methods can be used to identify AGN which are missed by even the deepest X-ray surveys, presumably because even the X-rays are unable to penetrate the obscuring material (e.g., Donley et al. 2008, 2012; see Fig. 1.1). IR detection methods can also be used to identify AGN across a wide-range of redshifts (e.g., Kirkpatrick et al. 2013). However, IR-colour selected samples of AGN are non-uniform because in galaxies undergoing significant amounts of star formation, the IR emission due to the AGN can be diluted by the thermal emission from dust heated by the star formation (e.g., Cardamone et al. 2008; Assef et al. 2013; also see Kirkpatrick et al. 2013; Fig. 1.2). A more promising avenue is multi-component SED fitting to photometric data from multiple bands at MIR–FIR wavelengths, during which the emission from star formation and AGN activity can be de-coupled (e.g., Mullaney et al. 2011). Chapter 3 and Chapter 4 make use of photometric data from IR surveys to perform SED fitting and consequently to measure AGN luminosities by de-coupling the emission due to star formation from that due to AGN activity.

1.4.4 Radio surveys

AGN can be luminous radio emitters due to a number of different physical processes (see Section 1.3.2). Consequently, radio surveys (across a wide range of frequencies) have been used for decades to build up samples of AGN (e.g., Laing et al. 1983; Wall & Peacock 1985; Becker et al. 1995; Rengelink et al. 1997; Condon et al. 1998; Bock et al. 1999). Radio surveys are particularly effective at building up samples of radiatively-inefficient (aka "low excitation" or "jet mode"), radio-luminous AGN that are not easily identified using other methods (e.g., Heckman & Best 2014). Furthermore, on the basis of the "unified model", if the radio emission is produced on scales beyond the central regions (as will be the case for extended radio jets), the identification of this radio emission should be independent of the orientation of the AGN with respect to the line of sight (see Fig. 1.1). This thesis focuses on the radiatively efficient, radio-quiet AGN population where the origin of the radio emission can be ambiguous and can easily be dominated by star formation processes (see Section 1.3.2). Consequently, this thesis does not make use of radio surveys to identify AGN. However, radio data are used, in combination with SED fitting, to classify some of the sources as "radio excess" AGN in Chapter 4. These "radio excess" AGN are those that have levels of radio emission significantly above that expected to be produced by the star formation that is occurring in their host galaxies (e.g., Roy & Norris 1997; Donley et al. 2005; Del Moro et al. 2013) and may indicate radio emission due to an AGN is present.

1.4.5 The AGN demography

In the previous subsections some of the main techniques used to build up large samples of AGN were described. This sub-section briefly addresses how AGN selected using different techniques may (or may not) represent different source populations. This is particularly important for the later discussion on the impact of AGN on the evolution of galaxies (Section 1.6) because AGN residing in different host galaxies and environments may play very different roles in the evolution of galaxies

It has been shown that there is a reasonable overlap between X-ray/IR and optically selected AGN (albeit with the caveats outlined in the previous sub-sections), whilst radio

AGN are less frequently detected with other identification methods (e.g., Hickox et al. 2009; Trump et al. 2009; see review by Alexander & Hickox 2012 for more details). Additionally, AGN selected in X-ray, optical and IR surveys tend to reside in galaxies reasonably uniformly over a large mass range (predominantly over $M_{\star} \approx 10^{9}$–10^{12} $M_{\odot}$) that often have on-going star formation and are located in a wide range of environments (e.g., Kauffmann et al. 2003; Akiyama 2005; Hickox et al. 2009, 2011; Silverman et al. 2009; Xue et al. 2010; Mullaney et al. 2012a; Rosario et al. 2013). In contrast, the fraction of galaxies that host radio-identified AGN appears to be a strong function of mass, with the highest fractions in the most massive galaxies (i.e., $M_{\star} > 10^{11}$ $M_{\odot}$) that have old stellar populations and reside inside the most massive dark matter halos (i.e., $M_{\rm DM} \approx 10^{13-14}$ $M_{\odot}$; e.g., Yee & Green 1987; Best et al. 2005; Kauffmann et al. 2008; Shen et al. 2009; Hickox et al. 2009, 2011; Tasse et al. 2008; Smolčić et al. 2011; Goulding et al. 2014). Furthermore, radio AGN appear to be predominantly radiatively inefficient with low Eddington ratios (i.e., $\lambda_{\rm Edd} \lesssim 10^{-2}$) whilst AGN selected at other wavelengths have higher Eddington ratios (e.g., Ho 2002; Hickox et al. 2009; see review in Alexander & Hickox 2012). Radio AGN (where the radio emission is unambiguously from an AGN) are predominantly low-excitation sources (at least for $z \lesssim 0.3$ and for $L_{1.4\,\rm GHz} \lesssim 10^{26}$ W Hz^{-1}; Heckman & Best 2014) and these sources drive the results found for radio-identified AGN described above; however, high-excitation radio AGN appear to have host-galaxy properties (e.g., colours) and Eddington ratios more in line with the "radiatively efficient" AGN identified at other wavelengths (e.g., Hardcastle et al. 2007, Smolčić 2009; Best & Heckman 2012; see review in Heckman & Best 2014).

In summary, this thesis focuses on radio-quiet AGN selected at optical and X-ray wavelengths that, as discussed above, appear to reside inside a wide range of environments and host galaxies. In particular, the focus is on luminous AGN (i.e., $L_{\rm AGN} \gtrsim 10^{43}$ erg s^{-1}) that reside inside reasonably massive galaxies ($M_{\star} \approx 10^{10}$–$10^{12}$ $M_{\odot}$) and, as described below, are likely to represent the sources where the majority of BH growth occurs.

1.5 The co-evolution of BH and galaxy growth

There are several observational and theoretical results that imply BH growth and galaxy growth are intimately connected, which seems incredible because there are nine orders of magnitude difference in the physical size scale of a BH and its host galaxy (equivalent to the difference between the size of a coin and the Earth!). This section explores three observational results that imply that BH growth and galaxy growth are linked: (1) the cosmic evolution of BH growth and star formation look very similar; (2) most BH growth occurs in star-forming galaxies; (3) BH masses correlate with galaxy bulge mass and velocity dispersion. Section 1.6 explores theoretical and observational results that may imply that AGN activity (i.e., BH growth) can *directly* impact upon the evolution of their host galaxies.

1.5.1 The cosmic space density of BH growth and star formation are similar

Several pieces of observational evidence suggest that the most rapid BH growth and star formation occurred at high redshift (i.e., $z \approx 1$–3). Firstly, the average Eddington ratios of local AGN imply growth times larger than the age of the Universe and therefore these BHs must have grown much more rapidly in the past (e.g., Heckman et al. 2004; Ho 2008). Secondly, observations show that quasars (with the highest mass-accretion rates) were significantly more numerous at $z \gtrsim 1$ than at $z \lesssim 1$ (e.g., Schmidt & Green 1983; Hewett et al. 1993; Boyle et al. 2000; Richards et al. 2006b). Thirdly, the cosmic space density of BH growth peaks at $z \approx 1$–2 (Fig. 1.4) and over half of the integrated BH growth occurred around these redshifts or higher (e.g., Ueda et al. 2003; Marconi et al. 2004; Hopkins et al. 2007; Shankar et al. 2009; Aird et al. 2010), with the majority of BH growth occurring in AGN with luminosities of $L_{\rm AGN} \approx 10^{44}$–$10^{46}\,{\rm erg\,s^{-1}}$ (e.g., see review by Alexander & Hickox 2012). Similarly to quasars, the peak space density of the most intensely star-forming galaxies is at $z \approx 2$ (Chapman et al. 2005; Wardlow et al. 2011; Simpson et al. 2013b), with the peak in cosmic star formation density occurring at the same epoch (Fig. 1.4; e.g., Madau et al. 1996; Lilly et al. 1999; see review in Madau & Dickinson 2014). Studies of local galaxies have also suggested that massive

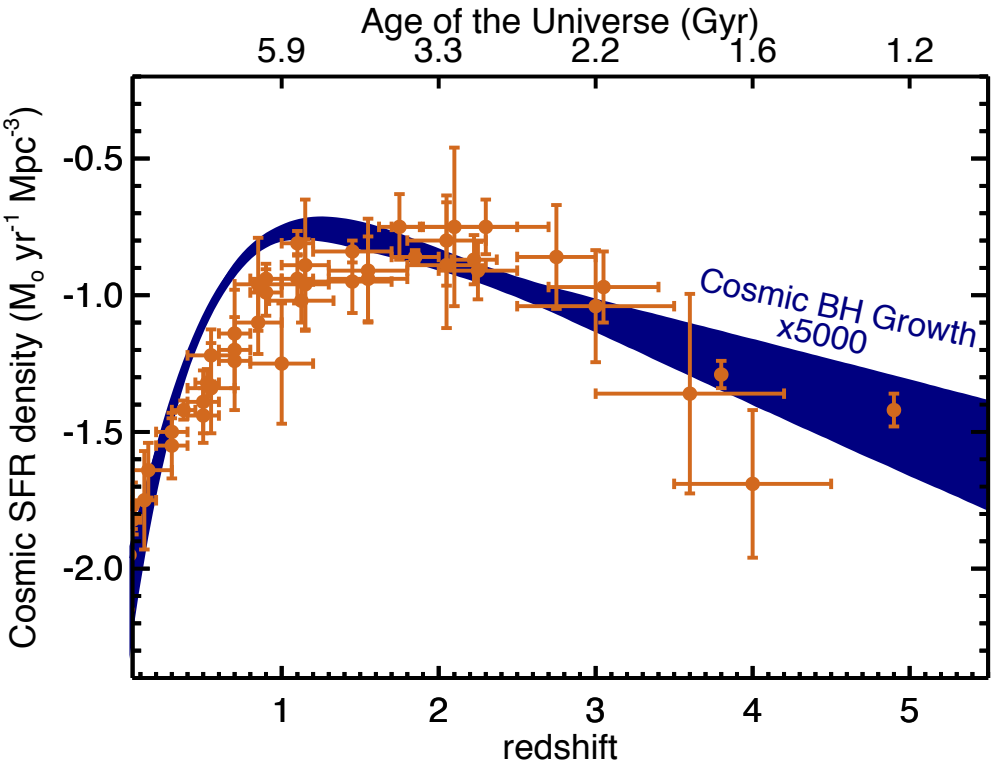

Figure 1.4: Volume averaged cosmic SFR density as a function of redshift, where the data points are from the compilation by Madau & Dickinson 2014 (see references there-in). Also shown is a representative model to the observed evolution of cosmic BH growth (i.e., mass accretion density; blue shaded region) scaled by ≈ 5000 taken from Aird et al. (2010). The peak in the density of BH growth and star formation occurred at similar epochs (i.e., $z \approx 1$–3) and both decline towards lower redshift.

galaxies (i.e., $M_\star \gtrsim 10^{10-11}$ M$_\odot$) formed the bulk of their stars at high redshift ($z \gtrsim 1$–2; e.g., Heavens et al. 2004; Pérez-González et al. 2008). As demonstrated in Figure 1.4, the cosmic SFR density and cosmic BH growth show remarkably similar evolution with redshift. However, while this result shows that BH growth (i.e., AGN activity) and star formation evolved in a similar manner, this only provides indirect evidence that they might be causally connected.

1.5.2 Most BH growth occurs in star-forming galaxies

Radiatively luminous AGN (i.e., those primarily identified at optical, X-ray and infrared wavelengths; see Section 1.4) are preferentially located in galaxies with on-going star formation (Kauffmann et al. 2003; Alexander et al. 2005; Xue et al. 2010; Rafferty et al. 2011; Mainieri et al. 2011; Mullaney et al. 2012a; Alonso-Herrero et al. 2012; Rosario et al. 2013). Since the launch of the *Herschel* satellite, the study of the star-formation rates (SFRs) of AGN has increased greatly, largely because the far-infrared wavelength regime observed (i.e., $\lambda = 70 - 500 \mu m$) arguably provides the most reliable SFR tracer in luminous AGN (e.g., Mullaney et al. 2011). These studies have shown that, on average, the SFRs of X-ray selected AGN with moderate luminosities (i.e., $L_{2-10\mathrm{keV}} \approx 10^{42} - 10^{44}$ erg) are consistent with galaxies of the same mass and redshift that do not host AGN (e.g., Fig. 1.5; Mainieri et al. 2011; Santini et al. 2012; Mullaney et al. 2012a; Rovilos et al. 2012; Rosario et al. 2013). The SFRs of the most luminous AGN (i.e., $L_{2-10\mathrm{keV}} \gtrsim 10^{44}$ erg s^{-1}) is a more controversial issue and is discussed in Section 1.6.

It is useful to compare the SFRs of AGN host galaxies to star-forming galaxies that do not host an AGN. Star-forming galaxies (out to $z \approx 2$), have specific SFRs (sSFRs; i.e., SFR divided by stellar mass) that increase in a well-defined form with redshift, with a reasonably small scatter (a factor of ≈2–3; Fig. 1.5; e.g., Noeske et al. 2007; Daddi et al. 2007a; Rodighiero et al. 2010; Elbaz et al. 2011; see review in Lutz 2014). This evolutionary track has been dubbed the "main sequence of star formation" and it has been suggested that most star formation occurs on the main sequence (e.g., Noeske et al. 2007; Rodighiero et al. 2011). In this work the physical implications (or lack thereof) of this main sequence are not discussed; however, it provides a useful benchmark to compare AGN to the overall star-forming population of galaxies. The crucial result is

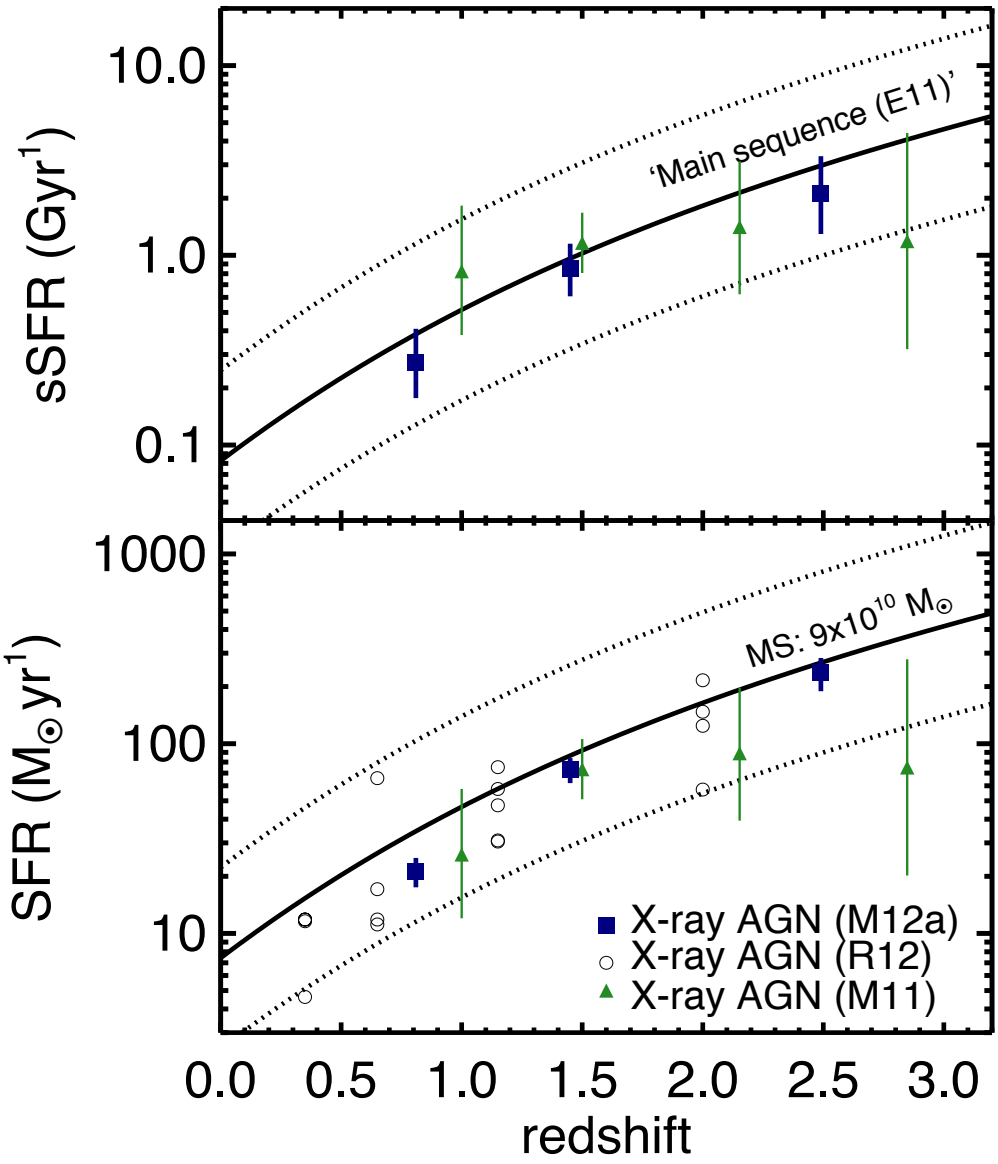

Figure 1.5: *Upper:* Average sSFR as a function of redshift for X-ray detected AGN (Mullaney et al. 2012a; M12a; Mainieri et al. 2011; M11). The solid curve shows the average evolution of sSFR found for star forming galaxies (i.e., the "main sequence"; Elbaz et al. 2011; E11), and the dotted curves show 3× above and below this curve (representative of the scatter). *Lower:* Average SFR as a function of redshift for X-ray detected AGN from M11, M12a and Rosario et al. (2012) (R12; SFRs from various X-ray bins are shown).* The solid curve represents the "main sequence of star formation" (E11) for a 9×10^{10} M$_\odot$ galaxy (the average mass of the X-ray AGN in M12a) and the dotted curves are 3× above and below this. On average, X-ray AGN have the same average sSFRs, and trace the same evolution as, non-AGN star-forming galaxies.

*For the R12 data points, the centre of each redshift bin is assumed (actual values are not provided in the paper). To match the method of M12a a conversion of $+0.2$ dex from $\nu L_\nu[60\,\mu\mathrm{m}]$ to $L_{8-1000\mu\mathrm{m}}$ was assumed (this is typical for the SEDs of star forming galaxies; e.g., Chary & Elbaz 2001; Kirkpatrick et al. 2013) and the relationship of Kennicutt (1998) to calculate the SFRs.

that, on average, AGN appear to trace this main sequence of star formation at least for moderate luminosity AGN (i.e., $L_{2-10\mathrm{keV}} \approx 10^{42} - 10^{44}$ erg; e.g., Mullaney et al. 2012a; see Fig. 1.5).

The results described above imply that the bulk of BH growth has occurred in star-forming galaxies, and that AGN activity goes hand-in-hand with the formation of stars. However, these results do not directly imply a direct causal relationship between these two processes. Furthermore, the observational results presented here may only apply for radiatively efficient AGN with moderate luminosities (i.e., $L_{2-10\mathrm{keV}} \approx 10^{42}$–$10^{44}\,\mathrm{erg\,s^{-1}}$; see Section 1.4). Radiatively inefficient (radio) AGN reside in galaxies that have lower star formation rates, compared to the AGN discussed above (e.g., see review in Heckman & Best 2014). In addition, the host galaxy properties of the most luminous AGN in the Universe (i.e., $L_{2-10\mathrm{keV}} \gtrsim 10^{44}\,\mathrm{erg\,s^{-1}}$) is a more controversial issue, and is a key-component of this thesis; the discussion of these sources is deferred to Section 1.6.

1.5.3 BH masses are related to galaxy bulge properties

The most quoted pieces of observational evidence to argue that BH growth and galaxy growth are intimately connected, are probably the relationships between BH masses and the properties of their host galaxy bulges (or "spheroids") in local systems. BH masses are found to be proportional to the luminosity and ("equivalently") masses of their host galaxy bulges (e.g., Dressler 1989; Kormendy 1993; Magorrian et al. 1998; Marconi & Hunt 2003; Häring & Rix 2004; Gültekin et al. 2009)[7] and a tight relationship is also found between BH masses and the velocity dispersion of the bulge (e.g., Ferrarese & Merritt 2000; Gebhardt et al. 2000; Tremaine et al. 2002; Gültekin et al. 2009). The term "bulge" here refers to both classical bulges and elliptical galaxies (see Kormendy & Ho 2013). It should be noted that, at least in the local Universe, BH masses do not appear to correlate well with pseudobulges or galaxy disks (e.g., Greene et al. 2008, 2010; Ho 2008; Kormendy et al. 2011; see Kormendy & Ho 2013 for a comprehensive review).

[7]Measuring a bulge mass is notoriously more difficult than measuring their luminosity. Whilst it should be possible to convert between luminosity and mass in bulges (as the stars dominate both the mass and the luminosity), the appropriate choice of conversion is not trivial (see Kormendy & Ho 2013 for a discussion of this in relation to BH–bulge mass relationships).

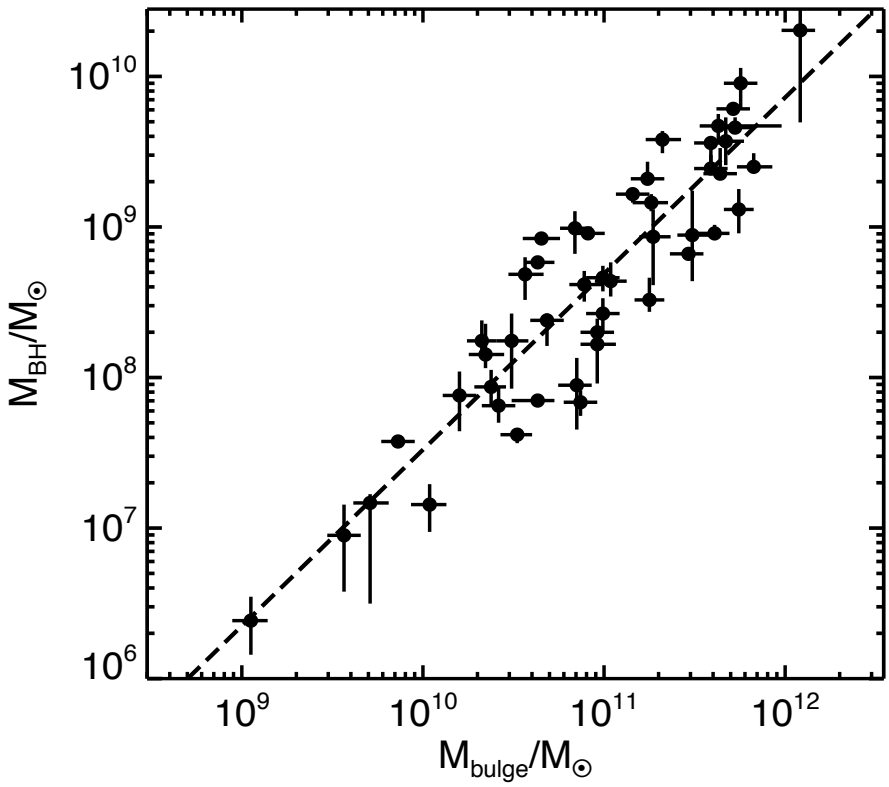

Figure 1.6: BH mass ($M_{\rm BH}$) versus bulge mass ($M_{\rm bulge}$) for the classical bulges and ellipticals used to derive the relationship between these quantities (Equation 1.5.6 [dashed line]; Kormendy & Ho 2013 and references there-in).

Figure 1.6 shows the BH–bulge mass relationship, containing data on classical bulges and ellipticals compiled from the literature (Kormendy & Ho 2013 and references there-in). This relationship is almost linear, with BH masses ($M_{\rm BH}$) containing around 0.2–0.8% of the mass of their host bulges ($M_{\rm bulge}$) and can be parametrised in the form:

$$\frac{M_{\rm BH}}{10^{8}\,{\rm M}_{\odot}} = \left(4.9^{+0.6}_{-0.5}\right)\left(\frac{M_{\rm bulge}}{10^{11}\,{\rm M}_{\odot}}\right)^{1.17\pm0.08}. \tag{1.5.6}$$

The remarkable implications of this relationship (Equation 1.5.6; derived in Kormendy & Ho 2013) include: (1) a universal method to calculate the masses of BHs residing in classical bulges or ellipticals using "easy" to measure quantities (i.e., bulge luminosity or velocity dispersion); and (2) the potential interpretation of a causal link between BH growth and the formation of classical bulges and ellipticals that forged this tight relationship.

Whilst the relationship observed in Figure 1.6 is well calibrated locally, overcoming the observational challenges of accurately measuring $M_{\rm BH}$ and $M_{\rm bulge}$ in distant galaxies is an ongoing area of research. Early indications suggest a possible evolution with redshift, where BH growth preceded or outpaced the growth of bulges, and additionally that the relationship has become tighter over time (McLure et al. 2006; Merloni et al. 2010; Bennert et al. 2011; see review in Kormendy & Ho 2013; but see Lauer et al. 2007 for possible observational biases). Finally, another interesting independent result that is useful to mention here is that, when averaging the AGN luminosities and SFRs over large populations of star forming galaxies, the estimated ratio of mass accretion rates to star formation rates comes out as $\approx 0.1\%$ out to high redshifts (Heckman et al. 2004; Rafferty et al. 2011; Mullaney et al. 2012b; Chen et al. 2013), which is remarkably close to the observed ratio of $M_{\rm BH}/M_{\rm bulge}$ in local galaxies (Fig. 1.6). Although speculative, this result could imply that, on average, BHs and galaxies have grown at the required rate to be on the local $M_{\rm BH}$–$M_{\rm bulge}$ relationship over the last $\approx$10 Gyrs. However, these results do not tell us what sets this ratio, and additionally they consider the *total* galaxy growth, not just the growth of galaxy bulges and ellipticals that drive the $M_{\rm BH}$–$M_{\rm bulge}$ relationship (Fig. 1.6).

The $M_{\rm BH}$–$M_{\rm bulge}$ relationship described here is often used as observational evidence that there must be a direct interplay between AGN activity (i.e., the build up of BH mass) and star formation (i.e., the build up of stellar mass).[8] Searching for observational evidence of a direct interplay between AGN activity and star formation is the focus of this thesis.

1.6 The influence of AGN on the evolution of galaxies

The previous section summarised some of the observational evidence that AGN activity and star formation are coeval, and stated that the observed $M_{\rm BH}$–$M_{\rm bulge}$ relationship provides indirect evidence that these two processes may somehow be regulated (at least during the formation of classical bulges and ellipticals). Fundamentally, the rates of star

[8] It has also been suggested that the $M_{\rm BH}$–$M_{\rm bulge}$ relationship may be a natural consequence of repeated mergers (e.g., Peng 2007; Jahnke & Macciò 2011)

formation and BH growth (i.e., AGN activity) in galaxies will be down to the balance between "feeding" (i.e., a supply of cold gas) and "feedback" (i.e., the prevention of the cold gas supply). A simple explanation for the co-evolution of star formation and BH growth and the observed relationships between galaxies and BHs, is that they grow from a common fuel supply. However, both star formation and AGN activity are known to be a source of energy and momentum (due to radiation pressure and the expulsion of material through winds or jets). If these winds, jets or radiation pressure are able of significantly suppress the supply of cold gas they will be the cause of negative "feedback" (see Fig. 1.7). Furthermore, theoretical work on galaxy formation has shown than such feedback processes are an integral part of the evolution of galaxies (see below). However, understanding the details of how, when and where these feedback processes occur is an ongoing challenge of extragalactic astronomy. Most relevant for this thesis, is an understanding of *AGN* feedback, which is an area of active research from both an observational and theoretical perspective (as shown by the large number of recent reviews that cover the topic: Cattaneo et al. 2009; Alexander & Hickox 2012; McNamara & Nulsen 2012; Fabian 2012; Kormendy & Ho 2013; Heckman & Best 2014). This section provides an overview of some of the theoretical and observational research on AGN feedback.

1.6.1 Matching models to observations: AGN to the rescue

AGN are incredible energy sources. During the growth of a BH, huge amounts of energy can be liberated. For example, the energy released to build a BH with mass $M_{\rm BH} = 10^8\,{\rm M}_\odot$ (via mass accretion) would correspond to $E_{\rm BH} \approx 10^{61}$ erg, assuming $E = 0.1 M_{\rm BH} c^2$ (i.e., a mass-to-energy conversion of 10%; see Section 1.2.2). This total accretion energy is two-to-three orders of magnitude higher than the binding energy of the galaxy bulge in which this BH is likely to reside (i.e., $E_{\rm BE} \approx 10^{58}$ erg)[9] and is likely to be comparable to, or higher than, the thermal energy of the gas in the dark matter halo in which this galaxy resides (e.g., Bower et al. 2008). Therefore, if even a small fraction (i.e., $\approx$0.1–1%) of the accretion energy could couple to the gas over 0.1–1000 kpc scales, growing BHs have the potential to regulate their own growth and the growth of their host galaxies, by pre-

[9]The binding energy of $E_{\rm BE} \approx 10^{58}$ erg is obtained assuming $M_{\rm bulge} = 3 \times 10^{10}\,{\rm M}_\odot$ (following Equation 1.5.6) and $E_{\rm BE} \approx M_{\rm bulge}\sigma^2$ with $\sigma \approx 200\,{\rm km\,s^{-1}}$.

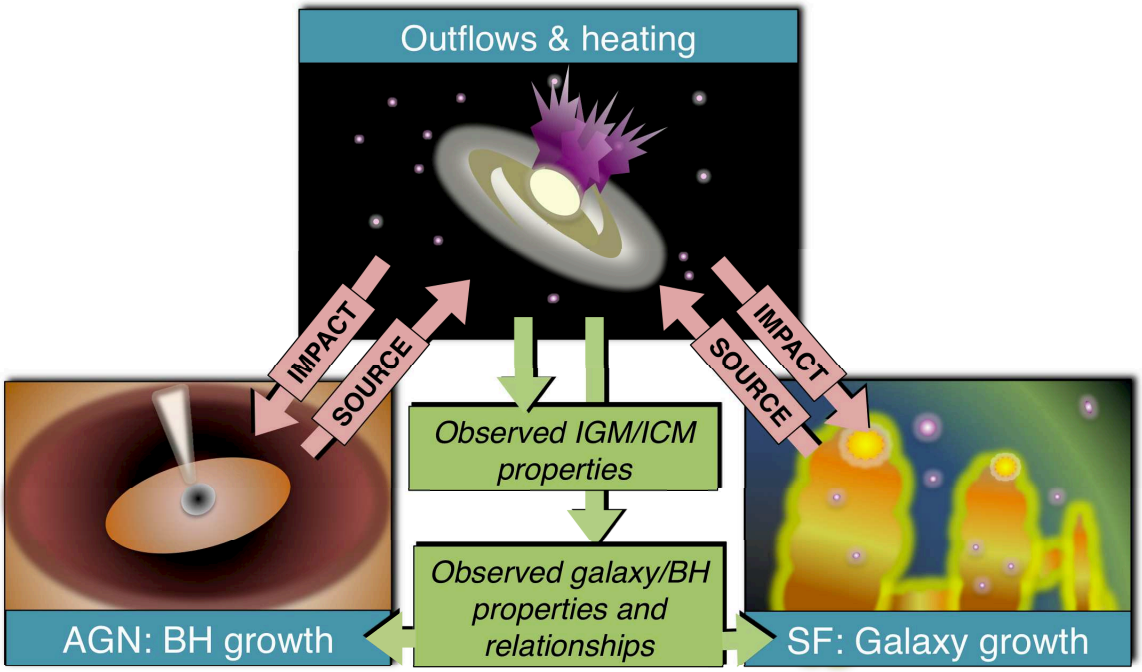

Figure 1.7: A schematic diagram to illustrate how AGN activity (BH growth) and star formation (galaxy growth) could be connected. If either one of these processes injects energy or momentum into their surroundings (i.e., provides the *source* of heating or outflows) future AGN activity and star formation could be enhanced or suppressed (i.e., the *impact*). The overall results of these processes could affect the observed properties of galaxies, BHs and the gas in the larger scale environment (i.e., the IGM and the ICM). The influence of AGN activity (i.e., AGN as the *source*) on the evolution of galaxies (i.e., constraining what *impact* they have) is the focus of this thesis.

venting the supply of cold gas (i.e., by becoming a "feedback" mechanism; see above) as well as impact upon the properties of the gas in the larger scale environment by injecting material and/or energy into this gas. Indeed, theoretical models of galaxy formation have found it necessary to implement AGN feedback mechanisms, to successfully reproduce many of the fundamental properties of galaxies, the intracluster medium (ICM) and the intergalactic medium (IGM; e.g., Silk & Rees 1998; Churazov et al. 2005; Bower et al. 2006; Hopkins et al. 2006; McCarthy et al. 2010; Gaspari et al. 2011). Some specific examples of this are given below.

One of the most famous and significant theoretical results on the potential role of AGN in galaxy evolution comes from semi-analytical models, which are unable to reproduce the cut-off at the bright end of the galaxy luminosity function without energy injection from accreting BHs (e.g., Bower et al. 2006; Croton et al. 2006; Somerville et al. 2008). In these models low-accretion rate AGN, located in the quasi-hydrostatic halos of massive galaxies, efficiently suppress the cooling of hot gas through the so-called "maintenance-mode" (also known as the "radio mode" or "hot halo mode"; Fig. 1.8). During this mode of feedback, the rate at which hot gas in the galaxy halos is able to cool and collapse onto the host galaxy (where it would ultimately trigger star formation and AGN activity), is maintained at a low level. This method of feedback has also been used to explain other observables such as the rates of gas cooling in galaxy clusters, the colour bi-modality of galaxies, the evolution of the cosmic star formation density and the steep X-ray luminosity-temperature (i.e., $L_{\rm X}$-$T_{\rm X}$) relationship seen in galaxy groups and clusters (e.g., Quilis et al. 2001; Churazov et al. 2002; Peterson et al. 2003; Bower et al. 2006, 2008; Croton et al. 2006; Bower et al. 2008; Puchwein et al. 2008; McCarthy et al. 2010).

Observational evidence for AGN heating the gas in massive halos, is found through combining X-ray and radio imaging of clusters where cavities in the X-ray emitting gas, indicating the prevention of cooling, are observed to be spatially co-incident with radio emission (e.g., Boehringer et al. 1993; Carilli et al. 1994; Rizza et al. 2000; McNamara et al. 2000; Hlavacek-Larrondo et al. 2013). Mechanical energy from the AGN, in the form of jets, inflates these cavities and is capable of exceeding the X-ray luminosities of their cooling atmospheres (e.g., Bîrzan et al. 2008; Cavagnolo et al. 2010; see McNamara

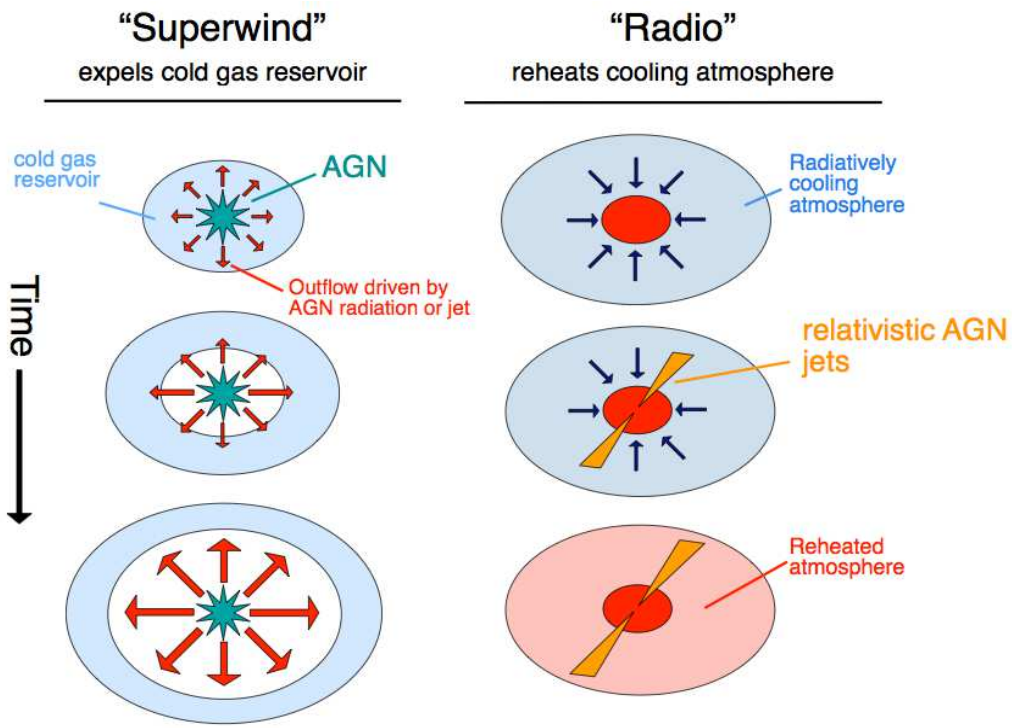

Figure 1.8: Schematic diagram to illustrate the two main modes of AGN feedback described in this thesis (taken from Alexander & Hickox 2012; also see Bower et al. 2012). Other names for the "superwind" mode are "quasar mode" and "starburst mode". Other names for the "radio mode" are "maintenance mode" and "hot-halo mode".

& Nulsen 2012 for a review). Indeed, the rates of cooling and heating (inferred from X-ray and radio observations respectively) in radio-luminous AGN appear to be in relatively close balance in clusters (e.g. Bîrzan et al. 2004; Dunn & Fabian 2008) and potentially even in groups and massive elliptical galaxies out to $z \approx 1$ (Best et al. 2006; Smolčić et al. 2009; Danielson et al. 2012; Simpson et al. 2013a).

The "maintenance-mode" of feedback, discussed above, is thought to be most efficient in the most massive halos, at late times and during periods of low BH accretion rates. The objects that are responsible for this type of feedback are likely to be the low-excitation radio AGN discussed in Section 1.4.5 (e.g., Churazov et al. 2005; Bower et al. 2006; McCarthy et al. 2011). In contrast, a more rapid/catastrophic form of interaction between AGN and their host galaxies (sometimes dubbed the "quasar mode", "superwind mode" or "starburst mode"; see Fig. 1.8) is proposed during periods of rapid accretion (e.g., Silk & Rees 1998). Therefore, the objects that are predicted to be responsible for this type of feedback are the radiatively-efficient AGN described in Section 1.4.5, where the majority

of BH growth occurred (Section 1.5). To reproduce many fundamental observables of massive galaxies and BHs, theoretical models that invoke this form of feedback typically require $\approx 0.5-15\%$ of the accretion energy to couple to the cold gas within the host galaxy and to expel this gas through outflows which ultimately results in the shut-down or suppression of future BH growth and star formation (e.g., Benson et al. 2003; Granato et al. 2004; Di Matteo et al. 2005; Springel et al. 2005; Hopkins et al. 2006, 2008; Booth & Schaye 2010; Hopkins & Elvis 2010; Debuhr et al. 2012). In addition, analytical models have used the idea of galaxy-scale outflows, initially launched by AGN, to explain the $M_{\rm BH}$–$M_{\rm bulge}$ relationship (i.e., Fig. 1.6; e.g., Fabian 1999; Granato et al. 2004; Murray et al. 2005; King et al. 2011; Faucher-Giguère & Quataert 2012; see reviews in Alexander & Hickox 2012 and Fabian 2012). While this form of feedback has been predicted to be effective at producing high mass outflow rates, shutting down rapid star formation episodes and producing many observables, several studies suggest that the "maintenance-mode" of feedback is still required, for example, to successfully reproduce the galaxy luminosity function (Gabor et al. 2011; McCarthy et al. 2011; Bower et al. 2012).

In addition to the potential affects of AGN feedback described above, AGN-driven outflows (in addition to supernovae and stellar winds) may be required to unbind gas from their host galaxies to fully explain the chemical enrichment of the ICM and IGM (e.g., Borgani et al. 2008; Wiersma et al. 2009; Fabjan et al. 2010; Ciotti et al. 2010). It has also been proposed that, in some cases, AGN driven outflows could induce *positive* feedback by triggering star formation episodes through induced pressure in cold gas reservoirs (e.g., Nayakshin & Zubovas 2012; Ishibashi & Fabian 2012; Silk 2013). Furthermore, *star formation* occurring in galaxy nuclei may *enhance* the level of AGN activity by driving gas towards the BH (via stellar winds); however, in contrast this star formation could *reduce* the level of AGN activity by preventing gas from reaching the BH (e.g., Wada & Norman 2002; Schartmann et al. 2009; Hobbs et al. 2011; see review by Alexander & Hickox 2012). Overall a complex picture emerges, where star formation and AGN activity could be linked by either one of these processes injecting energy and momentum into their surrounding gas and consequently enhancing or suppressing one or both of these processes (as summarised in the schematic diagram in Fig. 1.7).

Galaxy formation models have proven to be very successful at reproducing the *global*

observed properties of galaxies, the ICM and the IGM. However, they often rely on diverse, simplified and artificial prescriptions when implementing AGN feedback, in particular it is not well established how the accretion energy couples to the gas to drive outflows. Observations are required to constrain the details of how, when and where these processes actually occur. This thesis studies luminous AGN (i.e., those that may be responsible for "quasar mode" feedback), searching for observational evidence that: (1) they are driving galaxy-wide outflows (i.e., the potential mechanism for AGN to influence the evolution of their host galaxies) and (2) they impact upon on the evolution of their host galaxies by suppressing star formation. The following two subsections review previous observational work that covers these two areas.

1.6.2 Outflows

While there is little doubt that star formation processes (e.g., stellar winds and supernovae) drive galaxy-wide outflows (e.g., Heckman et al. 1990; Lehnert & Heckman 1996; Swinbank et al. 2009; Genzel et al. 2011; Newman et al. 2012; Bradshaw et al. 2013; see review in Veilleux et al. 2005) and are an integral part of galaxy evolution (e.g., Dalla Vecchia & Schaye 2008; Hopkins et al. 2013a), it is believed that AGN activity is required to drive the highest velocity outflows and are particularly important for the evolution of the most massive galaxies (e.g., Benson et al. 2003; McCarthy et al. 2011; Hopkins et al. 2013b; Zubovas & King 2014; see Section 1.6.1). AGN-driven outflows are initially launched from the accretion disk or dusty torus surrounding the BH, either in the form of a radio jet/lobe or a radiatively-driven wind. It is thought that these jets or winds then sweep up gas in the ISM resulting in kpc-scale "outflows" (e.g., Springel et al. 2005; King 2005; Di Matteo et al. 2005; Hopkins et al. 2006; Faucher-Giguère & Quataert 2012; Debuhr et al. 2012).

Observationally, AGN-driven winds are known to be prevalent in luminous AGN at low and high redshift: X-ray and UV absorption-line spectroscopy reveal high-velocity winds of up to $v \approx 0.1c$ (e.g., Reeves et al. 2003; Blustin et al. 2003; Reeves et al. 2003; Trump et al. 2006; Gibson et al. 2009; Tombesi et al. 2010; Gofford et al. 2011; Page et al. 2011) and may be a ubiquitous property of all luminous AGN (Ganguly & Brotherton 2008). However, these high-velocity winds are most likely to be produced close to the

accretion disk ($<$ 1 pc scale; e.g., Crenshaw et al. 2003; Tombesi et al. 2012; see Fig. 1.1). For these winds to have a global effect on the host galaxy, they must couple to the ISM and drive the gas over galaxy-wide ($\approx$ 1–10 kpc) scales. To test the impact of AGN-driven outflows on the formation and evolution of galaxies, it is therefore necessary to search for kpc-scale energetic outflows.

Spatially resolved spectroscopy provides a particularly direct method to search for and characterise kpc-scale outflows. Such observations of low-redshift AGN have identified kpc-scale outflows in ionised, atomic and molecular gas (e.g., Holt et al. 2008; Feruglio et al. 2010; Fu & Stockton 2009; Rupke & Veilleux 2011; Alatalo et al. 2011; Westmoquette et al. 2012; Veilleux et al. 2013; Rupke & Veilleux 2013; Liu et al. 2013b). At high redshift, most observations have concentrated on searching for galaxy-wide outflows of ionised gas (e.g., Nesvadba et al. 2006, 2007a, 2008; Cano-Díaz et al. 2012), largely because this is the most practical gas phase to observe at these redshifts with current facilities. Since this thesis studies galaxy-wide ionised outflows of AGN at both low redshifts ($z < 0.2$) and high redshifts ($z = 1.4$–3.4), the remainder of this sub-section explains the main observational techniques used to identify galaxy-wide ionised outflows and reviews the previous work that has used these methods.

Observations of galaxy-wide ionised outflows

A diagnostic that is commonly used to identify outflowing ionised gas over large scales is broad (i.e., emission-line widths exceeding that expected from galaxy dynamics), asymmetric and high-velocity [O III]λ5007 emission-line profiles. As a forbidden transition the [O III]λ5007 emission line cannot be produced in the high-density sub-parsec scales of AGN BLRs, making it a good tracer of the kinematics in the NLR, and can be observed over parsecs to tens of kiloparsecs (see Section 1.3.3 and Appendix A for more details). The [O III]λ5007 emission line has long been used to identify outflowing ionised gas in small samples of local and low-redshift AGN (e.g., Weedman 1970; Stockton 1976; Veron 1981; Heckman et al. 1981, 1984; Feldman et al. 1982; Vrtilek 1985; Whittle 1985; Whittle et al. 1988; Veilleux 1991; Veilleux et al. 1995; Boroson & Green 1992; Nelson & Whittle 1996); however, the small sample sizes makes it difficult to know how representative these observations are of the overall AGN population. More recently, large

systemic spectroscopic surveys (e.g., SDSS; York et al. 2000) have enabled the study of NLR kinematics in hundreds to tens of thousands of AGN (e.g., Boroson 2005; Greene & Ho 2005; Komossa et al. 2008; Zhang et al. 2011; Wang et al. 2011; Mullaney et al. 2013) to constrain both the ubiquity of these outflow features and study them as a function of key AGN properties. However, these studies have used one-dimensional spectra and therefore provide no insight on the spatial extent or structure of the outflows. To obtain spatial information of these outflows requires spatially resolved spectroscopy.

Both longslit and integral-field unit (IFU) observations of local and low-redshift AGN ($z \lesssim 0.4$), have identified disturbed and high-velocity ionised gas over kiloparsec scales (e.g., McCarthy et al. 1996; Villar-Martín et al. 1999; Colina et al. 1999; Tadhunter et al. 2001; Holt et al. 2008; Lipari et al. 2009a,b; Fu & Stockton 2009; Humphrey et al. 2010; Greene et al. 2011; Rupke & Veilleux 2011, 2013; Westmoquette et al. 2012; Husemann et al. 2013; Liu et al. 2013b). Several of these studies have revealed considerable masses of outflowing gas with velocities higher than the host galaxy escape velocity, in apparent agreement with basic predictions from galaxy formation models. However, a key limitation of these studies is that it is often difficult to place the observations into the context of the overall AGN and galaxy populations as the samples are small, inhomogeneous and/or only represent the most extreme AGN or star-forming systems in the Universe. This limitation is addressed in this thesis by searching for and characterising kpc-scale outflows by using IFU observations of $z < 0.2$ AGN drawn from a well constrained parent population of optically identified AGN (Chapter 4; Harrison et al. 2014).

At high redshift, where accretion-related outflows are predicted to be most prevalent (e.g., Di Matteo et al. 2005; King 2005), IFU observations of high-redshift radio galaxies (HzRGs, at $z \approx 2$–3; Nesvadba et al. 2006, 2008) have showed that kpc-scale energetic outflows are present in at least a fraction of the high-redshift galaxy population. With implied velocities of greater than a few hundred $\mathrm{km\,s^{-1}}$ these outflows could potentially drive gas out of the host galaxy, inhibiting future BH growth and star formation. Additionally, IFU observations of the [O III] and Hα emission lines in a high-redshift quasar also reveal similar outflow signatures (Cano-Díaz et al. 2012; also see Maiolino et al. 2012 for observations of the [C II] emission in another high-redshift quasar). Due to the small number of the high-redshift AGN studied with IFUs, the prevalence and significance of

such galaxy-wide outflows remains poorly constrained. This limitation is addressed in this thesis by performing similar IFU observations of eight $z = 1.4$–3.4 radio-quiet AGN hosted in star-forming galaxies (Chapter 3; Harrison et al. 2012a). Importantly, the targets are much more representative of the high-redshift AGN population than HzRGs; the radio luminosities of our targets (i.e., $L_{1.4\,\mathrm{GHz}} = 10^{24}$–$10^{25}\,\mathrm{W\,Hz^{-1}}$) imply a space density of $\Phi \approx 10^{-5}\,\mathrm{Mpc^{-3}}$ compared to $\Phi \lesssim 10^{-8}\,\mathrm{Mpc^{-3}}$ for HzRGs (e.g., Willott et al. 1998; Simpson et al. 2012).

1.6.3 The SFRs of luminous AGN

The previous sub-section explored the observational evidence for outflows in galaxies that host luminous AGN activity. However, just *detecting* outflows in AGN does not provide any evidence that AGN have a long-term impact on the evolution of their host galaxies. As discussed in Section 1.6.1 many theoretical models predict that the most luminous AGN suppress the star formation in their host galaxies. An obvious test of this prediction is to measure the SFRs of the host galaxies of luminous AGN.

In Section 1.5.2, several pieces of observational work on the SFRs of AGN were described. The general consensus presented was that, on average, galaxies hosting moderate luminosity AGN (i.e., $L_{2-10\,\mathrm{keV}} \approx 10^{42-44}\,\mathrm{erg\,s^{-1}}$; or equivalently $L_{\mathrm{AGN}} \approx 10^{43-45}\,\mathrm{erg\,s^{-1}}$) have SFRs that are consistent with those of galaxies lacking AGN but with similar masses and redshifts (also see Fig. 1.5). However, the literature presents different results for the average SFRs of galaxies that host the most luminous AGN (i.e., $L_{\mathrm{AGN}} \gtrsim 10^{45}\,\mathrm{erg\,s^{-1}}$) with all possible options claimed: (1) the SFRs are *consistent* with galaxies that do not host AGN (at least for $z \approx 1$–2.5; e.g., Rosario et al. 2012); (2) the SFRs are *enhanced* compared to galaxies that host less luminous (or no) AGN (e.g., Lutz et al. 2010; Rovilos et al. 2012) and (3) the SFRs are *suppressed* compared to galaxies that host less luminous (or no) AGN (Page et al. 2012). The last of these three cases could be taken as observational evidence that luminous AGN have a direct influence on their host galaxies by suppressing star formation. Understanding the discrepancies between these results is important if we are to make a comparison to theoretical predictions. In this thesis the difference between these studies is investigated and a solution is presented in Chapter 5 (Harrison et al. 2012b).

1.7 Thesis overview

The overall aim of this thesis is to place observational constraints on the influence of AGN on the evolution of galaxies. This is achieved using two main strategies: (1) searching for and characterising galaxy-wide ionised outflows (a potential mechanism for an AGN to influence its host galaxy) by using IFU observations, and (2) searching for evidence that luminous AGN suppress star formation by using FIR photometric data to measure the SFRs of AGN host galaxies. Additionally SED fitting methods have been developed to explore the AGN luminosities and the SFRs of the targets with IFU observations. A brief outline of the content of each chapter in this thesis is provided below. The redshift ranges that the main observing programmes cover are illustrated in Figure 1.9.

- **Chapter 2:** This chapter gives a summary of integral field spectroscopy (the major observational technique used in this thesis) and an overview of the different instruments used in this thesis.

- **Chapter 3:** This chapter uses IFU observations to search for and to characterise galaxy-wide ionised outflows in eight $z = 1.4$–3.4 ultra-luminous infrared galaxies (ULIRGs; $L_{8-1000\mu\mathrm{m}} > 10^{12}$ L$_{\odot}$) that host AGN activity. These galaxies are undergoing both rapid BH growth and star formation and therefore are key objects for studying the connection between AGN activity and star formation. A key development of this investigation is that it almost doubled the number of high-redshift AGN with IFU observations of this type. Additionally, the targets are radio-quiet and consequently they are much more representative of the AGN population than the radio-loud AGN that had been the focus of most of the similar previous work. The work presented here is an important test of theoretical predictions that suggest that ULIRGs hosting luminous AGN activity represent a key evolutionary phase and that these galaxies should host AGN-driven outflows capable of expelling significant fractions of gas. This work is published in Harrison et al. (2012a).

- **Chapter 4:** This chapter presents IFU observations of sixteen $z < 0.2$ type 2 AGN to search for and characterise galaxy-wide outflows. This work is an important progression on the work presented in the previous chapter and other work in the literature. The main advantage of this work is that the targets are selected from a well

constrained parent sample of $\approx 24,000$ AGN, which means that the observations can be placed into the context of the overall AGN population. Outflow velocities, sizes and morphologies are measured and these properties are explored as a function of the AGN and host galaxy properties (e.g., SFR and $L_{\rm AGN}$). Mass outflow rates, energetics and momentum rates are estimated and compared to theoretical predictions. This work is published in Harrison et al. (2014).

- **Chapter 5:** This chapter uses *Herschel* photometric data to investigate the average SFRs of AGN as a function of X-ray luminosity. Earlier published work had provided contradictory results on the SFRs of the most luminous AGN (i.e., $L_{2-10\rm keV} \gtrsim 10^{44}\,{\rm erg\,s^{-1}}$). In particular a result presented in *Nature* claimed evidence of SFR suppression, in apparent contradiction with most earlier work. The work in this chapter presents the reasons for these contradictory results and therefore provides a clearer picture of the average SFRs of luminous AGN. This work is published in Harrison et al. (2012b).

- **Chapter 6:** This chapter provides an overall summary of the work presented in this thesis along with the outstanding questions that are yet to be fully answered. An overview is given of the observational projects that have either started, or that are planned, to address some of the outstanding questions. Some of the initial new results from these programmes are also shown.

- **Appendices:** In Appendix A some relevant information and applications of the emission lines used in this thesis is provided. In Appendix B the assumed cosmological model is briefly described. Finally, Appendix C provides a list of the acronyms used in this thesis along with their definitions.

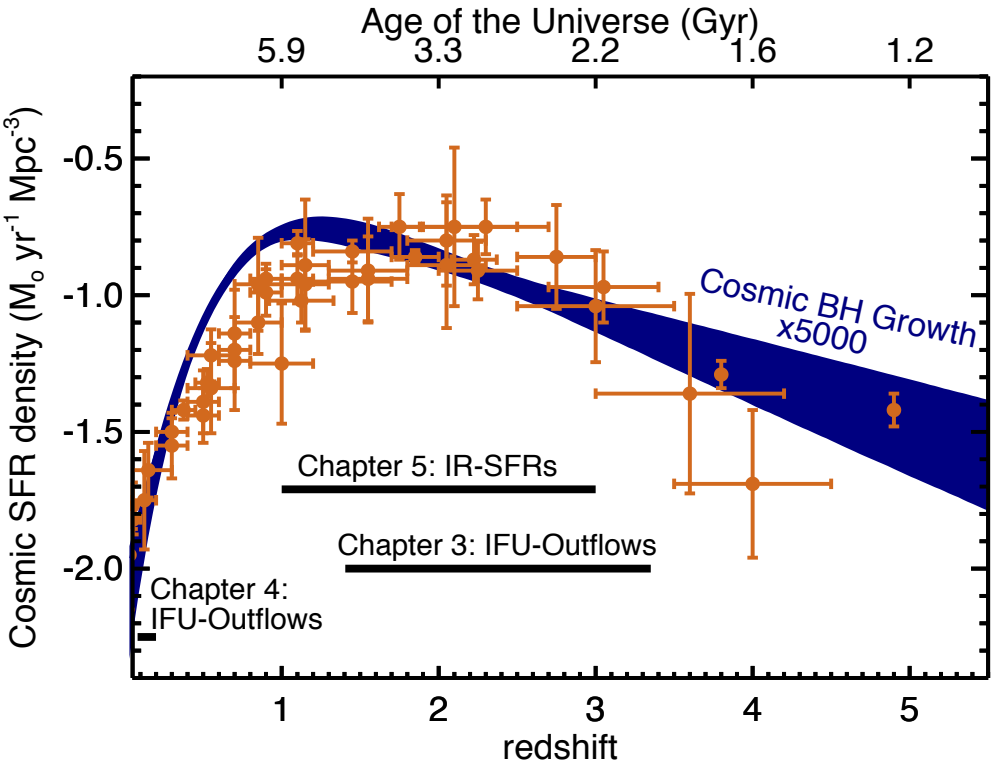

Figure 1.9: Same as Figure 1.4 but with the addition of solid lines to illustrate the redshift ranges covered by the main observing programmes presented in this thesis. In Chapter 3, IFU observations are presented of AGN that have redshifts (i.e., $z = 1.4$–3.4) that cover the peak of the cosmic SFR density. IFU observations of low redshift AGN ($z < 0.2$) are presented in Chapter 4. The low redshift observations have the advantage of increased signal-to-noise and spatial resolution and, crucially, a much better understanding of the parent population from which the targets were drawn. Chapter 5 presents SFR measurements of luminous AGN that have redshifts covering the peak epochs of cosmic star formation and BH growth. To test predictions of galaxy evolution models it is investigated if the most luminous AGN are suppressing the star formation in their host galaxies.

CHAPTER 2

Integral field spectroscopy

The bulk of this thesis is based on spatially resolved spectroscopy data that were obtained using an observational technique called integral field spectroscopy. These data are used to trace the ionised gas kinematics over kiloparsec scales in the objects studied in Chapter 3 and Chapter 4. This chapter gives brief details of how integral field spectroscopy works, the instruments used in this thesis and the basic steps required to reduce integral field spectroscopy data.

2.1 Introduction

With traditional astronomical spectroscopy a single spectrum is obtained for the source that is being observed. However, most extragalactic sources are spatially extended on the sky and therefore it is often desirable to spatially resolve the spectra. In *long-slit* spectroscopy the light from a source is passed through a slit, and then it is the image of this slit that gets dispersed. This has the advantage of providing spatial information in the direction along the slit. However, if you are interested in characterising the spectra for the full source, there are two main disadvantages with long-slit spectroscopy: (1) you only obtain a spectrum of the light that actually passes through the slit (i.e., all other light is lost); (2) all of the spatial information perpendicular to the slit is lost. If the target has a large angular size on the sky (either intrinsically or due to poor seeing), it can be time consuming to undertake the multiple observations required to obtain spectra for the full source. *Integral field spectroscopy* (IFS) provides the solution.

2.2 Integral field spectroscopy

IFS is an observational technique that provides three dimensional information of the target being observed. The instruments used are called integral field spectrographs and they produce data in the form of data cubes. These data cubes consist of two spatial dimensions (i.e., [x, y] or [RA, DEC]) and a wavelength dimension (i.e., λ; see Fig. 2.1). Figure 2.1 is a schematic diagram that demonstrates that, with these data, it is possible to obtain images of the target in different wavelength slices and also to obtain spectra at every spatial pixel. These data can thus be used for several different types of analyses, a few examples of which are: (1) creating emission-line images; (2) tracing the velocity structure of emission and absorption lines across the target; (3) measuring emission-line flux ratios across the target. Common scientific experiments that are performed with IFS data of extragalactic objects include: (1) measuring the dynamical structures of gas and stars; (2) spatially resolving stellar populations; (3) measuring the spatial distribution of on-going star formation; (4) searching for and characterising outflowing or inflowing gas.

IFS is performed with an integral field spectrograph in the optical or infrared wavebands. These instruments consist of an integral field unit (IFU), which samples the light into multiple spatial components, and a spectrograph, which disperse the light. IFUs sample the light by using lenslets, fibres or slicing mirrors. Figure 2.2 illustrates the main methods of IFUs, and they are summarised below.

- *Lenslets arrays* can be used to format the image into several points of light that are then dispersed by the spectrograph. The dispersed light is angled to avoid excessive overlap between the spectra.

- *Fibres* can be used either on their own or in combination with a lenslet array. This technique uses a bundle of optical fibres to sample the image directly or the fibres can be placed behind a lenslet array. The light from the fibres is then aligned to create a "pseudoslit" that is passed to the spectrograph.

- An *image slicer* uses segmented mirrors to split the image into horizontal stripes that are sent in slightly different directions. A second set of mirrors then formats these slices on top of each other into a "pseudoslit" that is then passed to the spectrograph.

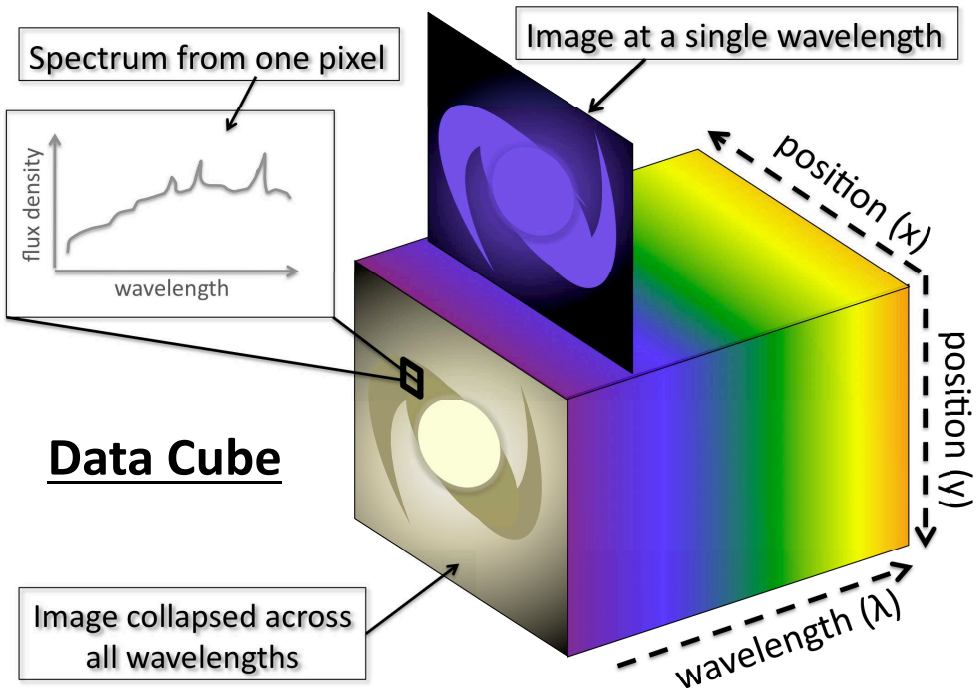

Figure 2.1: Schematic diagram of a data cube. A data cube provides information in three dimensions: two spatial dimensions (i.e., an image in [x,y]) and a third dimension of wavelength. It is therefore possible to obtain an image of the target at a single wavelength or collapsed over wavelength slices. Furthermore, at every spatial pixel of the datacube a spectrum can be extracted.

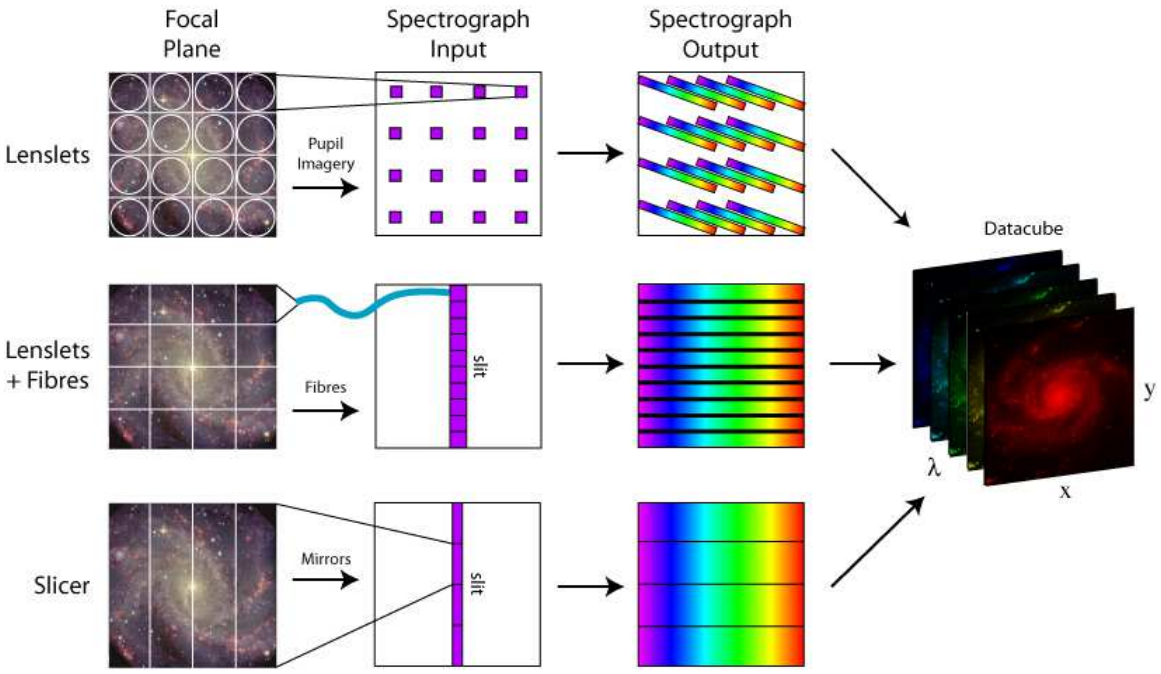

Figure 2.2: A diagram of the main techniques used in IFS. An IFU samples the light from the focal plane using different techniques (lenslets, lenslets plus fibres and an image slicer are shown here) and then sends the light to a spectrograph to be dispersed. The spectrograph output can then be formatted into a datacube (see Fig. 2.1) during the data reduction process. *Image Credit: M. Westmoquette; adapted from Allington-Smith & Content (1998).*

The formatted light (using the above methods) is collimated and dispersed by the spectrograph before being recorded by the detector. The final output image consists of multiple lines of spectra, corresponding to different positions in the original image (see Fig. 2.2). Each individual spectrum can then be reformatted into the three-dimensional data cube (Fig. 2.1) during the data reduction process.

2.3 The instruments used in this thesis

Three different integral field spectrographs are used in this thesis: (1) The IFU mode of the Gemini Multi-object Spectrograph (GMOS; Allington-Smith et al. 2002) installed on the Gemini-South telescope in Chile; (2) The Near-Infrared Integral Field Spectrometer (NIFS; McGregor et al. 2003) installed on Gemini-North in Hawaii; (3) The Spectrograph for INtegral Field Observations in the Near Infrared (SINFONI; Eisenhauer et al. 2003) on the Very Large Telescope (VLT) in Chile. This sub-section gives a brief overview of each instrument and their properties are summarised in Table 2.1.

- **SINFONI** is a near-infrared spectrograph which uses an image slicer IFU. The IFU contains 32 slices with three choices of slit height, leading to different pixel scales and fields-of-view (see Table 2.1). In Chapter 3 of this thesis we use SINFONI with slit heights of 250 mas which results in a $8'' \times 8''$ field-of-view. There are four gratings available (J, H, K, H+K) giving an overall wavelength coverage of 1.1–2.45 μm. In Chapter 3 of this thesis we use the H+K grating, which has a spectral resolution of $\lambda/\Delta\lambda \approx 1500$.

- **NIFS** is a near-infrared spectrograph which uses an image slicer IFU. There are 29 individual slices with a height of 103 mas. There are four gratings (Z, J, H, K) giving an overall wavelength coverage of 0.94–2.40 μm. In Chapter 3 of this thesis we use NIFS with the J, H and K filters which provide spectral resolutions of $\lambda/\Delta\lambda \approx 5300$–$6000$.

- **GMOS** is a multi-purpose optical instrument that can be used for imaging and spectroscopy. For this thesis we make use of the IFU inside the instrument that makes it into an integral field spectrograph. A lenslet array of 1500 elements is used to slice the image into small components. 1000 elements are used to observe the target field and 500 elements are used to simultaneously observe a blank sky field $\approx$1 arcmin away from the target field. Each lenslet is coupled to a fibre that takes the sliced components to the spectrograph in the form of two "pseudoslits". In "two-slit mode" (i.e., using both pseudoslits) the full field-of-view is sent to the detector (i.e., $5'' \times 7''$). In "one-slit mode" only half of the field-of-view is recorded; however, the extra space on the detector is used to increase the recorded spectral coverage. A variety of gratings are available with different spectral resolutions that are optimised for either blue or red wavelengths. In Chapter 4 we use the GMOS IFU in one-slit mode with the B1200 grating, which has a spectral resolution of $\lambda/\Delta\lambda \approx 3700$.

SUMMARY OF IFS INSTRUMENTS USED IN THIS THESIS

Name	Design	Pixel scale (milli-arcsec)	Field of view (arcsec)	Wavelength coverage (μm)	Resolution
NIFS	Image slicer	103×40	3×3	0.94–2.40	≈5000–6000
GMOS†	Fibre+lenslet	200	5×7	0.36–0.94	≈600–4400
SINFONI⋆	Image slicer	125×250	8×8	1.10–2.45	≈1500–4000
		50×100	3×3		
		12.5×25	0.8×0.8		

Table 2.1: A summary of the properties of the different integral field spectrographs used in this thesis.
† We use GMOS in "one-slit" mode that provides a field-of-view of 5×3.5 arcsec.
⋆ SINFONI has three different options for spatial sampling and they are all listed here; however, in this thesis we only use the 8×8 arcsec field-of-view.

2.4 Data reduction

The final image produced by an IFS is in the form of several rows of spectra each corresponding to a different position in the target field (see Fig. 2.2). Just like with traditional spectroscopy these spectra must undergo several calibration steps before they can be used for scientific analyses. The details of the data reduction for the individual instruments are provided in Chapter 3 and Chapter 4; however, a brief outline of the mains steps is given here.

Firstly, sky images or "frames" are subtracted from the science frames. Sky frames are observations of a blank-sky field using exactly the same set-up and exposure times as the science observations. This sky subtraction is required because the background sky has a non-zero brightness in the optical and infrared wavebands. Of particular trouble are the large number of infrared emission lines produced by molecules in the atmosphere that need to be removed by this sky-subtraction process. The sky-subtracted science frames must then undergo a series of calibration steps. The steps of calibration are required to correct for imperfections in the telescope and instrument response and also convert the recorded data into physical units (i.e., flux density and wavelength). Several calibration frames are required to perform these steps and they are listed below.

- Bias frames are zero second exposures taken with the detector's shutter closed. These frames can be used to correct for a non-zero "bias" and/or hot pixels on the

detector.

- Dark frames are images taken with the detector's shutter closed. Several are taken to produce a set of dark frames with exposure lengths to match all of the other calibration and science frames. These dark frames can be used to correct all of the other frames for the average "dark current" (due to thermal excitation) produced during an exposure.

- Flat-field frames are images taken when the detector is illuminated with a uniform source of non-dispersed light. The process of "flat fielding" uses these frames to correct for the non-uniform response of the detector frames due to spatial variations in the sensitivity of the detector or anomalies in the optical path. In the case of IFS this can be done for each slice individually.

- Arc frames are images of the dispersed light from an arc-lamp with a well known set of spectral lines (e.g., Neon and Argon lamps). These frames are used to create the wavelength solution for the science images (i.e., assign a wavelength to each of the pixels in the dispersion direction). These frames can also be used to correct for any spectral curvature on the science frame.

- Ronchi mask frames are images of a grid of perfectly arranged slits or rulings. These frames can be used to correct for any spatial distortions in the images.

After the calibration process the sky-subtracted science frames (see Fig. 2.2) will have been corrected for the telescope and instrument imperfections and have a good wavelength solution. The datacube now needs to be constructed by extracting each row of spectra on the frame, and placing them into the appropriate spatial position (see Fig. 2.1). Finally, each spectrum needs to be flux calibrated. This is done using observations of "standard stars" that are observed and calibrated in the same manner to the science targets. The chosen stars have well known intrinsic luminosities and spectra in the wavelength bands being observed and their spectra have few features beyond the continuum. The standard star observations are used to create a model of the correction between observed intensity units (i.e., counts) and flux density units as a function of wavelength. This model is then applied to each spatial pixel of the science data cube. Standard stars can also be used to

correct for telluric absorption by the atmosphere which can be particularly troublesome in the infrared waveband.

CHAPTER 3

Energetic galaxy-wide outflows in high-z ULIRGs hosting AGN activity

Abstract

We present integral field spectroscopy observations, covering the [O III]$\lambda\lambda$4959, 5007 emission-line doublet of eight high-redshift ($z = 1.4$–3.4) ultra-luminous infrared galaxies (ULIRGs) that host active galactic nuclei (AGN) activity, including known sub-millimetre luminous galaxies (SMGs). The targets have radio luminosities that are typical of high-redshift ULIRGs ($L_{1.4\mathrm{GHz}} = 10^{24}$–$10^{25}\,\mathrm{W\,Hz^{-1}}$) and therefore are not radio-loud AGN. We de-couple kinematic components due to the galaxy dynamics and mergers from those due to outflows. We find evidence in the four most luminous systems ($L_{[\mathrm{O\ III}]} \gtrsim 10^{43}\,\mathrm{erg\,s^{-1}}$) for the signatures of large-scale energetic outflows: extremely broad [O III] emission (FWHM $\approx$ 700–1400 km s^{-1}) across $\approx$ 4–15 kpc, with high velocity offsets from the systemic redshifts (up to $\approx 850\,\mathrm{km\,s^{-1}}$). The four less luminous systems have lower quality data, displaying weaker evidence for spatially extended outflows. We estimate that these outflows are potentially depositing energy into their host galaxies at considerable rates ($\dot{E} \approx 10^{43}$–$10^{45}\,\mathrm{erg\,s^{-1}}$); however, due to the lack of constraints on the density of the outflowing material and the structure of the outflow, these estimates should be taken as illustrative only. Based on the measured maximum velocities ($v_{\mathrm{max}} \approx$ 400-1400 km s^{-1}) the outflows observed are likely to unbind some fraction of the gas from their host galaxies, but are unlikely to completely remove gas from the galaxy haloes. By using a combination of energetic arguments and a comparison to ULIRGs without clear evidence for AGN activity, we show that the AGN activity could be the dominant power source for driving the observed outflows, although star formation may also play a significant role in some of the sources.

3.1 Motivation

Section 1.6 of this thesis described how galaxy-wide AGN-driven outflows are predicted to be an integral part of the evolution of massive galaxies. These outflows are predicted to be particularly prevalent at high redshift (see Section 1.6). Previous to the work presented in this chapter, IFU observations of a handful of high-redshift AGN had identified powerful galaxy-wide outflows that have the potential to unbind gas from their host galaxies. However, the sources that were observed are predominantly radio-loud AGN that make up the minority of the high-redshift AGN population (see Section 1.6.2). The work presented in this chapter uses IFU observations of high-redshift *radio-quiet* AGN, to search for and characterise galaxy-wide outflows. A general introduction to this research is in Section 1.6, whilst in this chapter we only give a short introduction to the research that is specific to the observations presented here. The subsequent sections of this chapter (Section 3.3 onwards) have been published, as written here, in Harrison et al. (2012a).

3.2 Introduction

Potentially the best place to search for AGN-driven outflows is within high-redshift far-IR (FIR; $\lambda = 8$–$1000\,\mu$m) luminous galaxies with $L_{\rm FIR} > 10^{12}\,{\rm L}_{\odot}$ (Ultra-Luminous Infra-Red Galaxies - ULIRGs), such as sub-millimetre galaxies (SMGs). These systems are the most intensely star-forming galaxies known with star formation rates (SFRs) of $\gtrsim$100–$1000\,{\rm M}_{\odot}\,{\rm yr}^{-1}$ and are thought to represent a rapid star-forming phase that every massive galaxy goes through (e.g., Swinbank et al. 2006; Tacconi et al. 2008). They have a peak space density at $z \approx 2$–2.5 (Chapman et al. 2004, 2005; Wardlow et al. 2011; Simpson et al. 2013b) which roughly coincides with the peak epoch of BH growth (e.g., Cattaneo & Bernardi 2003; Hopkins et al. 2007; Silverman et al. 2008). Using optical, mid-infrared and X-ray diagnostics, high-redshift ULIRGs are found to have emission dominated by starburst activity with $\approx$ 20–30% of SMGs also revealing significant AGN activity (e.g., Alexander et al. 2003b, 2005, 2008b; Chapman et al. 2005; Ivison et al. 2010a; Rafferty et al. 2011; Wang et al. 2013). Indeed, clustering analysis of SMGs and quasars supports the idea that starburst and AGN activity occur in the same systems (Hickox et al. 2012) and that SMGs may evolve into massive elliptical galaxies by the present day (see also

Simpson et al. 2013b). Therefore, high-redshift ULIRGs that host AGN activity could be in transition from a star-formation dominated to an AGN dominated phase (also see e.g., Sanders et al. 1988). This transition phase, which is potentially facilitated by kpc-scale outflows, is an evolutionary period required by many models (e.g., Silk & Rees 1998; Springel et al. 2005; Di Matteo et al. 2005; Hopkins et al. 2006, 2008; see Alexander & Hickox 2012 for a review).

In this chapter we present Gemini-North Near-Infrared Integral Field Spectrometer (NIFS) and VLT Spectrograph for Integral Field Observations in the Near Infrared (SINFONI) IFU observations of $z \approx 2$ ULIRGs with known optical AGN activity. These sources have radio luminosities ($L_{1.4\mathrm{GHz}} = 10^{24}$–$10^{25}\,\mathrm{W\,Hz^{-1}}$) typical of high-$z$ ULIRGs and can therefore be considered to be radio-quiet AGN. In Section 3.3 we give the details of the IFU observations and data reduction, in Section 3.4 we derive star formation rates and AGN luminosities for the targets using SED fitting, in Section 3.5 we present the analysis and results, in Section 3.6 we discuss the results and their implications for galaxy evolution models and in Section 3.7 we give our conclusions. We provide background information and detailed results on individual sources in Section 3.8. We have adopted $H_0 = 71\,\mathrm{km\,s^{-1}}$, $\Omega_M = 0.27$ and $\Omega_\Lambda = 0.73$ throughout; in this cosmology, $1''$ corresponds to 8.5 kpc at $z = 2.0$.

3.3 Observations and data reduction

3.3.1 Target selection

For this study we selected ten radio-detected $z = 1.4$–3.4 star-forming galaxies that host AGN activity to study their spatially resolved dynamics. The sample consists of eight SMGs (labelled 'SMM' with 850 μm flux densities $S_{850} > 4$ mJy) and two sources that are undetected at 850 μm (labelled 'RG'). We will collectively refer to the sample as high-redshift ULIRGs throughout. We detected [O III] emission in eight of the sources (see Section 4 for details). All our detected sources are [O III] luminous ($L_{[\mathrm{O\,III}]}$=10^{42}–$10^{44}\,\mathrm{erg\,s^{-1}}$), and have high [N II]/Hα and [O III]/Hβ emission-line ratios, or an AGN-dominated continuum, indicating the presence of AGN activity (e.g., Kewley et al. 2006), with most of the sources having additional observational evidence for AGN activity (see

Table 3.1 for details); see Section 3.8 for background information on the individual sources. We provide details of the target selection below.

Seven of our targets are selected from Takata et al. (2006) who presented near-IR spectroscopy around the redshifted [O III]$\lambda\lambda$4959,5007 emission-line doublet of 22 high-redshift ULIRGs. In order to select sources that might contain AGN-driven outflows, we chose seven targets with broad (FWHM $\gtrsim 700\,\mathrm{km\,s^{-1}}$) and bright ($F_{[\mathrm{OIII}]} \gtrsim$ few $\times\ 10^{-16}$ erg s^{-1}) [O III] emission. We also include in our sample three, $z \approx 2$–2.5 ULIRGs selected from Alaghband-Zadeh et al. (2012) which were identified as hosting AGN activity on the basis of their rest-frame optical emission-line ratios. These targets were initially selected on the basis of their Hα luminosities and are therefore not pre-selected to have luminous and broad [O III] emission. One of the sources was presented in a pilot study (SMM J1237+6203; Alexander et al. 2010) and we present the whole sample here.

Details of our observations and the targets' 1.4 GHz flux densities, obtained from the literature, are provided in Table 3.1. The 1.4 GHz radio luminosities ($L_{1.4\mathrm{GHz}}$) are calculated using Equation (2) from Alexander et al. (2003b), with the 1.4 GHz flux densities shown here and an assumed spectral index of α=0.8.[1] We estimate AGN luminosities for our sources using the SED fitting procedures outlined in Section 3.4 and these values are provided in Table 3.2.

Although this sample is heterogeneous, it is more representative of the overall AGN population than previous IFU studies searching for AGN-driven outflows in high-redshift radio galaxies (with $L_{1.4\mathrm{GHz}} \gtrsim 10^{27}\,\mathrm{W\,Hz^{-1}}$; e.g., Nesvadba et al. 2008). For example, the radio luminosities of our sources ($L_{1.4\mathrm{GHz}}$=10^{24}–$10^{25}\,\mathrm{W\,Hz^{-1}}$) imply a space density of $\Phi \approx 10^{-5}\,\mathrm{Mpc^{-3}}$ compared to $\Phi \lesssim 10^{-8}\ \mathrm{Mpc^{-3}}$ for high-redshift radio galaxies (Fig. 3.1; Simpson et al. 2012; Willott et al. 1998). This is important if we are to understand the prevalence of AGN-driven outflows in high-redshift galaxies. In Fig. 3.1 we compare the integrated [O III] properties and radio luminosities of our sample with low- and high-redshift AGN.

[1] This value is approximately the mean value for radio-identified SMGs with an observed range of roughly α=0.2–1.5, which includes AGN (Ibar et al. 2010). Here we define a spectral index α such that flux density, S_ν, and frequency, ν, are related by $S_\nu \propto \nu^{-\alpha}$.

GEMINI-NORTH NIFS AND VLT SINFONI OBSERVATIONS

ID	Source	R. A. (J2000)	Dec (J2000)	$z_{[OIII]}$	$S_{1.4}$ (μJy)	$L_{1.4GHz}$ (10^{24} W Hz^{-1})	AGN	t_{exp} (ks)	Average seeing ($''$)	(kpc)	Instrument	Quality
(1)	(2)	(3)	(4)	(5)	(6)	(7)	(8)	(9)	(10)	(11)	(12)	(13)
1	SMM J0217−0503	02:17:38.68	−05:03:39.5	2.021	207±16	5.0	O	4.8	0.47	4.0	S	1
2	SMM J0302+0006	03:02:27.73	+00:06:53.5	1.405	217±9	2.2	O,M?	11.4	0.42	3.6	N	2
3	RG J0302+0010	03:02:58.94	+00:10:16.3	2.239	55±10	1.7	O,U	9.6	0.38	3.2	N	1
4	RG J0332−2732	03:32:56.75	−27:32:06.3	2.315	160±20	5.3	O	2.4	0.53	4.4	S	1
5	SMM J0943+4700*	09:43:04.08	+47:00:16.2	3.351	60	4.7	O,U,M	14.4	0.42	3.2	N	1
6	SMM J1235+6215	12:35:49.41	+62:15:36.9	2.199	93±6	2.8	O,X,M?	7.8	0.45	3.8	N	2
7	SMM J1237+6203	12:37:15.97	+62:03:23.1	2.075	179±9	4.6	X,U,B	7.8	0.30	2.5	N	1
8	SMM J1636+4057	16:36:50.43	+40:57:34.5	2.385	242±11	8.7	O,U,M,B	13.2	0.33	2.7	N	1
9	SMM J2217+0010	22:17:37.39	+00:10:25.1	(2.610)	179±19	7.9	O,M	3.6	0.40	3.2	N	3
10	SMM J2217+0017	22:17:42.25	+00:17:02.0	(2.278)	114±27	3.7	O	9.6	0.56	4.7	S	3

Table 3.1: NOTES: Column (1): Source ID. Column (2): Source name. Columns (3)–(4): The co-ordinates corresponding to the radio positions from: Ledlow et al. (2002); Swinbank et al. (2004); Chapman et al. (2005); Miller et al. (2008); Morrison et al. (2010); Ivison et al. (2011); Arumugam et al. (in prep); R. J. Ivison (priv. comm). Column (5) The redshifts based on the narrow [O III] emission lines using the galaxy-integrated spectra presented in Fig. 3.3. For SMM J2217+0010 and SMM J2217+0017 we do not detect [O III] and we therefore quote the Hα redshift from Takata et al. (2006) and Alaghband-Zadeh et al. (2012), respectively. Column (6): Radio flux densities taken from the same references as for the radio positions. Column (7): Rest-frame radio luminosities using the standard *k*-correction and a spectral index of α=0.8. Column (8): Evidence for AGN activity in the sources on the basis of: O: optical emission-line ratios (Swinbank et al. 2004; Takata et al. 2006; Alaghband-Zadeh et al. 2012; this work); M: excess in the mid-infrared continuum from infrared spectra (Valiante et al. 2007; Menéndez-Delmestre et al. 2009; the evidence for IR-AGN activity in the sources with a "?" is tentative); U: rest-frame UV spectral signatures (Ledlow et al. 2002; Smail et al. 2003; Chapman et al. 2004; Chapman et al. 2005); X: X-ray observations (Alexander et al. 2005); B: Broad-line AGN (Swinbank et al. 2005; Coppin et al. 2008; see Section 3.8 for more details on the classifications of individual sources). Column (9): The total on-source exposure times for the data presented here. Columns (10)–(11): The average seeing for the observations, based on standard star observations. Column (12): The instrument used for the observations, either SINFONI (S) or NIFS (N). Column (13) A data quality flag as follows: 1: data which have sufficiently high signal-to-noise ratios to study the spatially resolved kinematics; 2. data with lower signal-to-noise ratios and limited spatially resolved information; 3. undetected in [O III]λ5007 in this study. * For SMM J0943+4700 we observed the radio counter-part H6 (Ledlow et al. 2002) and the 1.4 GHz flux density has been corrected for an amplification factor of 1.2 (Cowie et al. 2002).

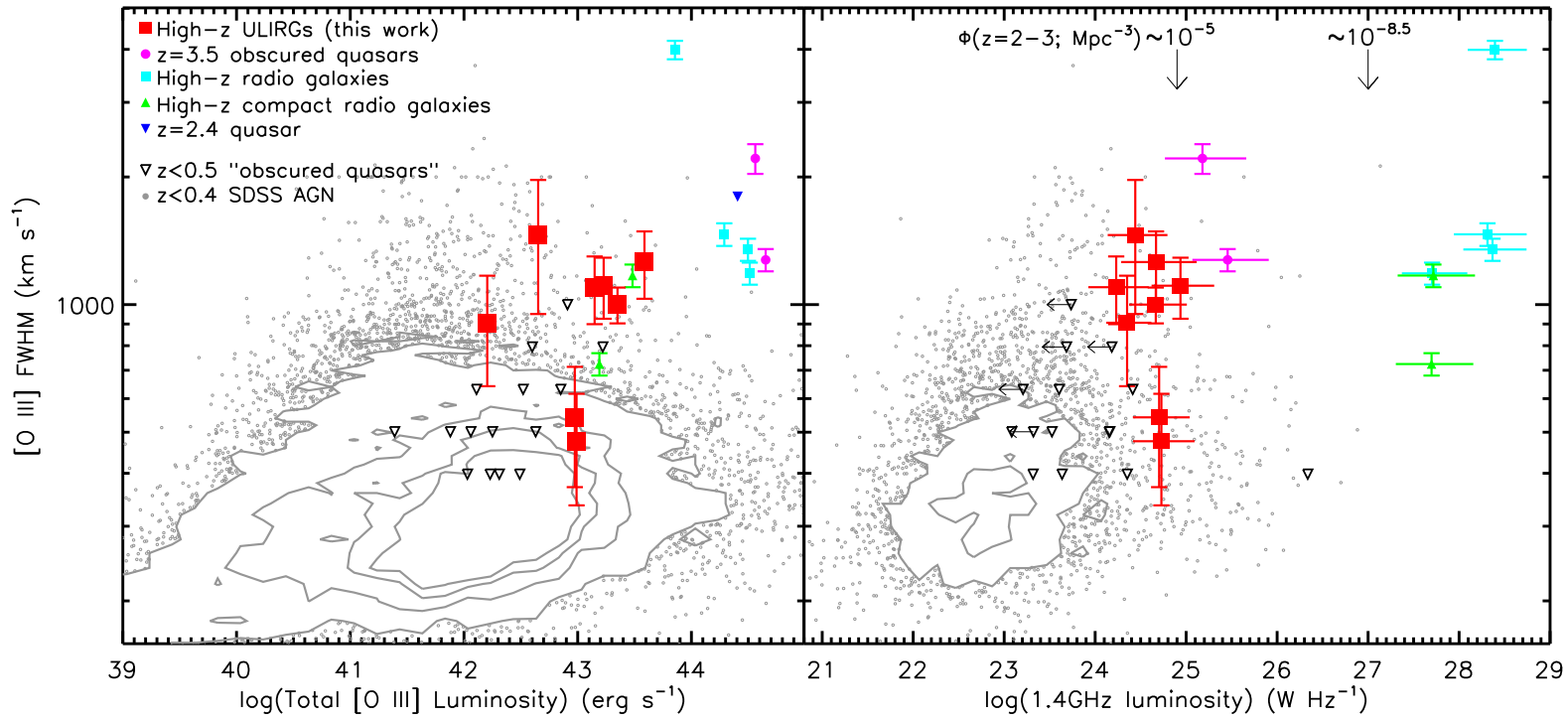

Figure 3.1: FWHM versus total [O III]λ5007 luminosity (*left*) and FWHM verses 1.4 GHz luminosity (*right*) for our eight [O III] detected targets. Shown for comparison are low redshift (z <0.4) AGN from the Sloan Digital Sky Survey (Mullaney et al. 2013) and $z < 0.5$ obscured quasars with long-slit data (Greene et al. 2011). Also shown are other high-redshift sources with IFU data: $z \approx 2$–3 radio galaxies (Nesvadba et al. 2006, 2008), compact radio galaxies (Nesvadba et al. 2007a), $z \approx 3.5$ obscured quasars (Nesvadba et al. 2011) and a z=2.4 quasar (Cano-Díaz et al. 2012). Our targets have very broad [O III] emission, comparable with high-redshift radio galaxies but having 3–4 orders of magnitude lower radio luminosities such that they are ≈3 orders of magnitude more common at z ≈2–3. When the [O III] profile is decomposed into multiple components, the FWHMs of the broadest components have been plotted. All rest-frame radio luminosities are calculated using the standard k-correction, on the basis of their measured 1.4 GHz flux densities. Radio spectral indices are taken to be α=0.8; however, the horizontal error bars indicate the range of luminosities using spectral indices in the range α=0.2–1.5. The arrows in the right panel correspond to space densities of $\Phi \approx 10^{-5}$ Mpc^{-3} (Simpson et al. 2012) and $\Phi \approx 10^{-8.5}$ Mpc^{-3} (Willott et al. 1998) from the radio luminosity function at $z \approx 2.5$.

3.3.2 Gemini-North NIFS observations

Seven of the sources in our sample (those selected from Takata et al. 2006) were observed using Gemini-North NIFS (Table 3.1). The NIFS IFU uses an image slicer to reimage a 3.0×3.0 arcsec field into 29 slices of width $0.103''$ with a pixel scale of $0.04''$ along the slices. The dispersed spectra from the slices are reformatted on the detector to provide two-dimensional spectro-imaging. Depending on the target redshift, we used the $J-$, $H-$ or $K-$band grisms to ensure that we cover the rest-frame [O III]$\lambda\lambda$4959,5007 emission-line doublet. These grisms have an approximate spectral resolutions of $\lambda/\Delta\lambda \approx$ 6040, 5290 and 5290, respectively (FWHM $\approx$ 2, 3, 4 Å, or $\Delta v \approx 50$, 57, 57 $\mathrm{km\,s^{-1}}$). For our analysis we measured the instrumental dispersion more accurately, by measuring the widths of several bright sky-lines close to the observed wavelengths of the emission lines for the observations of each source. We found that the uncertainties in the instrumental dispersion (by measuring the scatter from the widths of several sky-lines) to be insignificant ($\approx 5\%$) compared to the uncertainties from our fitting procedures. We consequently do not include the uncertainties on the instrumental resolution in our measurements. These observations were taken between 2008 March 25 and May 19 and 2009 August 5 and December 30. All observations were taken in $<0.5''$ seeing.

The observations were performed using repetitions of the standard ABBA configuration in which we chopped either $6''$ to blank sky or, if the source was compact (emission-line region $<1.5''$), we chopped within the IFU. Individual exposures were 600s. Final on-source exposure times and seeing measurements, calculated using the corresponding standard star observations, are shown in Table 3.1.

We reduced the data with the Gemini IRAF NIFS pipeline which includes sky subtraction, wavelength calibration, and flat fielding. Attempts to remove residual OH sky emission lines were made using the sky-subtraction techniques described in Davies (2007). We further corrected for variations in the night sky emission by masking the source (when clearly detected) and taking a median of each pixel-column and consequently subtracting the (empty sky) background separately from each wavelength.

3.3.3 VLT/SINFONI observations

Three of the sources in our sample were observed using VLT/SINFONI (Table 3.1). The full details of these SINFONI observations are given in Alaghband-Zadeh et al. (2012) with only basic information given here. We used the widest available field-of-view, 8.0×8.0 arcsec, which is divided into 32 slices of width $0.25''$ with a pixel scale $0.125''$ along the slices . The *H*+*K* grating was used, which gives an approximate resolution of $\lambda/\Delta\lambda \approx 1500$ (FWHM ≈ 13 Å or $\Delta v \approx 200\,\mathrm{km\,s^{-1}}$). We made accurate measurements of the instrumental dispersion for the observations for each source in the same manner as outlined for the NIFS observations in the previous section. Again we found the uncertainties on the instrumental dispersion to be insignificant compared to the uncertainties from our fitting procedures. The targets were chopped around quadrants of the IFU for sky subtraction. All observations were taken in $<0.6''$ seeing. Individual exposures were 600s. Final on-source exposure times and seeing measurements, calculated using the corresponding standard star observations, are shown in Table 3.1.

The data were reduced using the SINFONI ESOREX pipeline, which includes sky subtraction, wavelength calibration and flat fielding.

3.3.4 Flux calibration and stacking

Each night's data were flux calibrated separately using observations of standard stars, at a similar airmass to the target galaxies, which were reduced in the same manner as the targets. Since the [O III]$\lambda\lambda$4959,5007 emission-line doublets typically lie in regions of $> 95\%$ sky transparancy, no corrections were made for telluric absorption. To find spatial centroids for the flux-calibrated data cubes, white-light (wavelength collapsed) images around the redshifted [O III]λ5007 emission line (NIFS targets) or Hα emission line (SINFONI targets) were produced. The data cubes for which we could not measure a centroid were discarded to improve the reliability of the spatially resolved data. Data cubes were only discarded for SMM J0302+0006 (2 discarded out of the 21 observed), RG J0302+0010 (4 discarded out of 20) and SMM J1235+6215 (8 discarded out of 21). We then spatially aligned and co-added the individual data cubes to create the final mosaic, using a median with a 3σ clipping threshold to remove remaining cosmetic defects

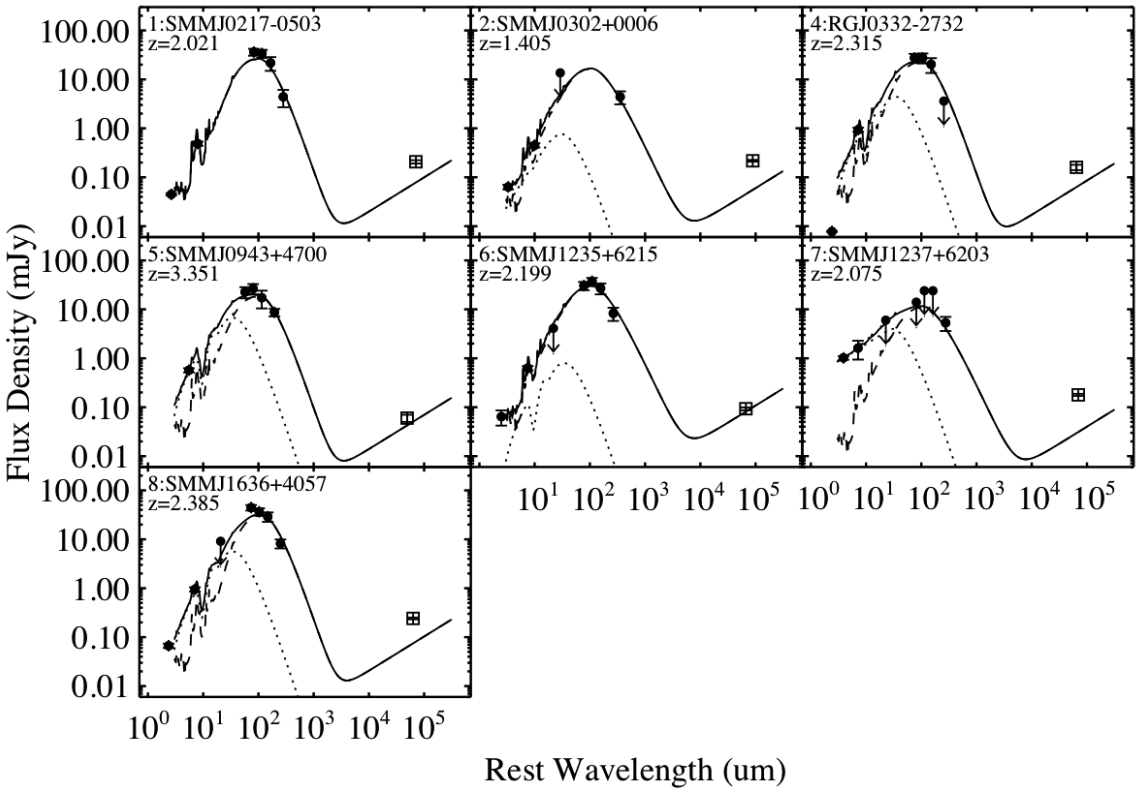

Figure 3.2: The infrared flux densities (filled circles) in the rest frame for the seven sources for which we performed SED fitting (see Section 3.4, Table 3.2 and Del Moro et al. (2013) for more details). The source RG 0302+0010 (source ID number 3) does not appear due to insufficient infrared data available. For guidance, also shown are the overall best-fit SEDs. The total SEDs are shown as solid curves, the AGN templates are shown as dotted curves and the starburst templates are shown as dashed curves. The 1.4 GHz flux densities (open squares) were not included in the SED fitting process. These SED fits were used to constrain the contributions to the infrared luminosities from AGN activity and star formation activity for each of the sources (Table 3.2).

and cosmic rays. The total on-source exposure times used in the final stacks are given in Table 3.1.

In all of the following sections, the effect of instrumental dispersion was corrected for by subtracting it in quadrature from the observed line dispersions.

3.4 Star-formation rates and AGN luminosities

To assist in the analyses of this work we need to constrain the star-formation rates and AGN luminosities of the eight [O III]-detected sources in a consistent manner. To achieve this we obtained infrared flux densities from the literature (Table 3.2) and fit these data using AGN and star-forming galaxy templates with the χ^2 minimisation spectral energy

distribution (SED) fitting procedure outlined in Del Moro et al. (2013). Briefly, we fit the infrared data using the empirical AGN template defined in Mullaney et al. (2011), allowing for A_V=0–5 mag of extinction, with each of the "SB2"–"SB5" star-forming galaxy templates; the "SB1" star-formation template did not fit the data well in any of the sources. This provides four best-fitting solutions (i.e., one for each of the four star-forming galaxy templates) with minimum χ^2 solutions. We used these solutions to find the star-formation rates and AGN luminosities for each of the sources using the methods described below. The infrared data points and the overall best-fit solutions are shown in Fig. 3.2.

We found convincing evidence for both star formation and AGN activity at infrared wavelengths for all of the sources except for RG J0302+0010 (for which there is insufficient infrared data available) and SMM J0217−0503, which had no significant AGN component providing only an upper limit on the AGN infrared luminosity. The AGN components in SMM J0943+4700 and SMM J1237+6203 were found to be particularly bright and dominated the mid-infrared emission; the SED fitting results for SMM J0943+4700 also agreed well with that found from mid-IR spectral fitting (Valiante et al. 2007) but no mid-IR spectroscopy exists for SMM J1237+6203. The AGN components for the other sources are weaker at mid-IR wavelengths. However, three of the sources have published mid-infrared spectroscopy (SMM J0302+0010, SMM J1235+6215, and SMM J1636+4057; Menéndez-Delmestre et al. 2009), and we found good agreement between the strength of the AGN component calculated from our SED-fitting procedure and the strength of the AGN derived from the mid-infrared spectroscopy.

We used the SED-fitting results to calculate the infrared luminosities of the star-formation components ($L_{\rm IR,SF}$; integrated over 8-1000μm) and consequently calculated star formation rates following Kennicutt (1998); see Table 3.2. This was achieved by taking the mean luminosity of the best-fitting solutions that used the four star-formation templates described above. The quoted uncertainties in the star-formation luminosity and star-formation rates are the average of the difference between these mean values and the models with the highest and lowest values. We found that all of the sources have $L_{\rm IR,SF} > 10^{12}\,{\rm L}_{\odot}$, confirming that they are ULIRGs with SFRs in the range ≈300–1400 $\rm M_{\odot}\,yr^{-1}$. For the source RG J0302+0010 we estimated the infrared luminosity using the radio-infrared relationship for star-forming galaxies (e.g., Helou et al. 1985) with

$q = 2.1$, which is a typical value for high-redshift ULIRGs (Kovács et al. 2006). For this source we take the value of $L_{\rm IR,SF}$ as an upper limit because the AGN will be contributing some unknown fraction of the radio luminosity (e.g., see Fig. 3.2 which shows that some of the sources have excess radio emission relative to that expected from star-formation alone; also see Del Moro et al. 2013).

To determine the bolometric AGN luminosities for each source we first calculated the AGN continuum luminosity [rest-frame $\nu L_\nu(6\mu{\rm m})$] by taking the average AGN contribution to the 6μm flux of the four models described above. These average infrared AGN luminosities are then converted into AGN bolometric luminosities using the 6μm-to-2–10 keV luminosity relationship found for AGN (conversion factor of $\approx$0.3; Lutz et al. 2004) and the 2–10 keV-to-bolometric luminosity ratio in Elvis et al. (1994) (conversion factor of $\approx$25; see Table 3.2). This overall correction factor of 7.5 that we apply to convert between between $\nu L_\nu(6\mu{\rm m})$ and AGN bolometric luminosity is in excellent agreement with the correction factor of $\approx 8\pm 2$ found by Richards et al. (2006a) from their mean SED of SDSS quasars. We found that the two sources with the largest fractional uncertainties on their SED-derived AGN luminosities are also those which only have tentative evidence for IR-AGN activity in their mid-infrared spectra (see Table 3.2). However, we compared all the SED-derived AGN bolometric luminosities to those predicted using the measured [O III] luminosities and the locally derived relationship of Heckman et al. (2004) ($L_{\rm AGN}$=3500$L_{\rm [OIII]}$). We found that the $L_{\rm [OIII]}$ derived AGN luminosities are on average a factor of $\approx$ 2.5 higher than the SED derived values, with a remarkably small scatter (all sources have a factor of 2.5 ± 1.5), giving evidence that (1) our derived AGN bolometric luminosities are reasonable, and (2) the [O III] luminosities are dominated by AGN activity. To predict the AGN luminosity for the source RG J0302+0010, for which we were unable to perform the SED fitting, we therefore take the $L_{\rm [OIII]}$ derived AGN luminosity and divide by a factor of 2.5 (see Table 3.2).

3.5 Analysis and results

We have studied the galaxy-integrated and spatially resolved properties of the [O III]$\lambda\lambda$4959,5007 emission-line doublet in our sample. Of the ten sources in our sample,

six have spatially extended [O III] emission, two have lower quality [O III] data and limited spatially-resolved information and two were undetected in [O III] (see Table 3.1). In this section we provide the details of our analyses and give an overview of the results of the sample as a whole. We give specific results for individual sources in Section 3.8. In this section we first describe the galaxy-integrated properties of the eight [O III] detected targets before providing a detailed analysis of the kinematics for the six spatially resolved sources. We defer discussion of the results and their implications for galaxy evolution to Section 3.6.

3.5.1 Galaxy-integrated spectra

In Fig. 3.3 we show the galaxy-integrated spectra around the [O III]λλ4959,5007 emission-line doublet for the eight sources with detected [O III] emission. The two sources that have an [O III] flux below our detection threshold (SMM J2217+0010 and SMM J2217+0017; see Section 3.8) are not shown. The spectra were created by integrating over the full spatial extent of the observed [O III] line emission; i.e., the aperture sizes to create the spectra were chosen by increasing the sizes until the [O III] fluxes reached a maximum.

To fit the emission-line profiles we employed a χ^2 minimisation procedure, down-weighting at the positions of the strongest sky lines. We fit the [O III]λλ4959, 5007 emission-line doublet with Gaussian components using a fixed wavelength separation. The intensity ratio was fixed at [O III]λ4959/[O III]λ5007=0.33 (e.g., Dimitrijević et al. 2007) and the width of the [O III]λ4959 line was fixed to be the same as the [O III]λ5007 line. In several cases the emission-line profiles are complex, with the presence of asymmetric wings. To characterise this complexity, we first fit a single Gaussian profile followed by a double Gaussian profile, only accepting the double Gaussian profile if it resulted in a significant improvement ($\Delta\chi^2 > 25 \sim 5\sigma$). In one source, SMM J1636+4057, we find evidence for a third Gaussian component at +1350 km s^{-1} from the narrow component; we confidently attribute this to [O III] as there are other emission lines found at the same velocity as this component (Smail et al. 2003; also see Section 3.8). Uncertainties on the parameters are calculated by perturbing one parameter at a time, allowing the others to find their optimum values, until the χ^2 value increases by 1. The mean of these upper and lower uncertainties are quoted throughout. The parameters for all of the fits

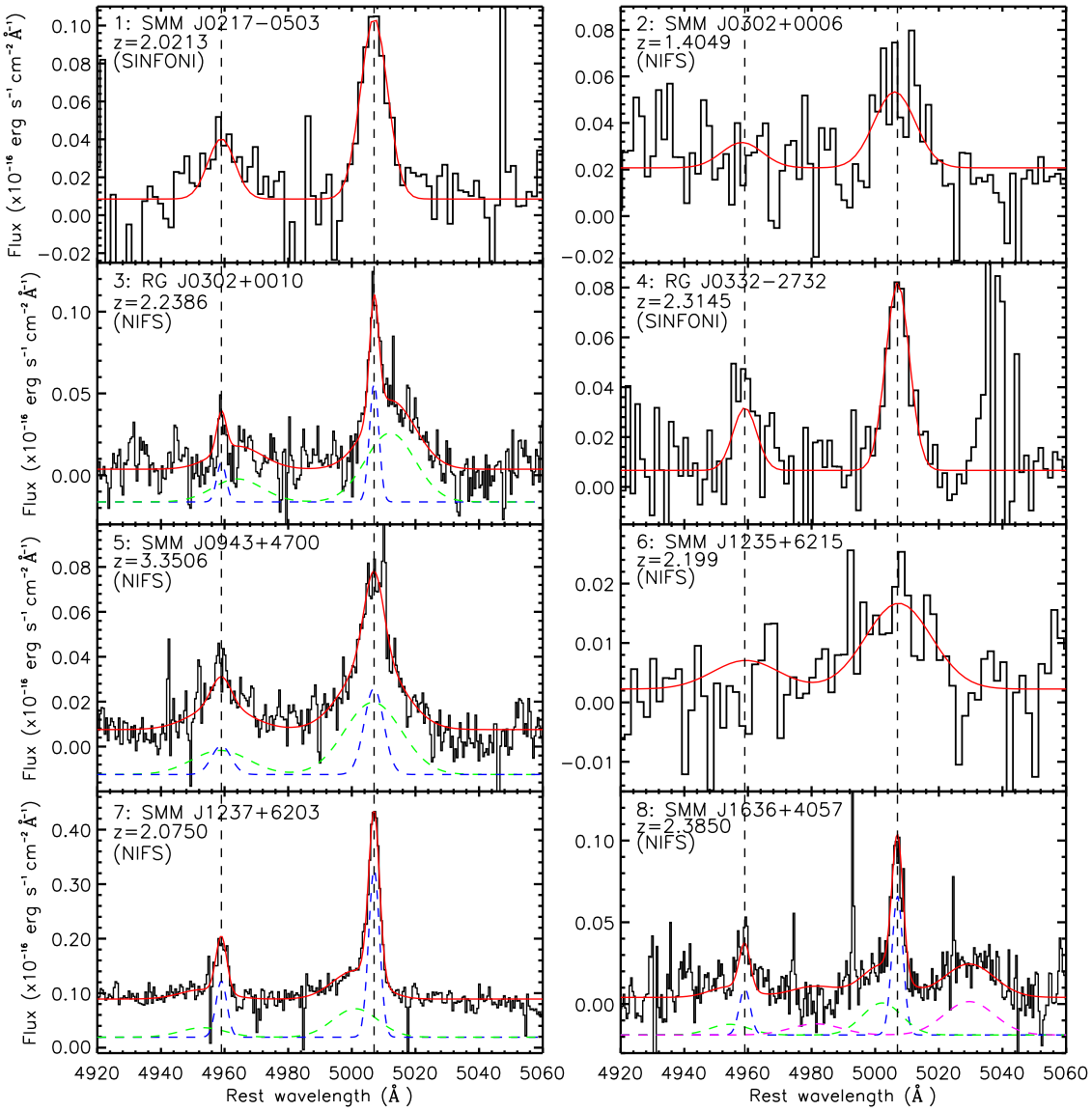

Figure 3.3: Galaxy-integrated spectra, shifted to the rest-frame, around the [O III]λλ4959,5007 emission-line doublet. A large variety in the [O III] emission-line profiles is found, with both blueshifted and redshifted extremely broad (FWHM≈900–1500 km s^{-1}) emission-line components, in addition to narrow emission-line components. Of particular note is SMM J1636+4057 which exhibits two broad components separated by ≈1700 km s^{-1}, one blueshifted and one redshifted with respect to the narrow component (see Section 3.8 for details). The dashed curves show the individual Gaussian components (with an arbitrary flux offset) of the fits when two or three components are required. The solid curves show the best fitting overall emission-line profiles. The vertical dashed lines show the rest-frame wavelengths of redshifted [O III]λ4959 and [O III]λ5007 based on the redshift of the narrowest Gaussian component. The spectra for SMM J0302+0006 and SMM 1235+6215 are of lower signal-to-noise than the other spectra and have been binned by a factor of four for clarity. The parameters of the emission-line fits and their uncertainties are given in Table 3.3.

and their uncertainties are given in Table 3.3. We note that the true absolute uncertainties on the flux measurements will be a factor of ≈2–3 higher, due to unknown uncertainties on the absolute flux calibrations. We note that there are some discrepancies between the fluxes shown here and those given in Takata et al. (2006) and Alexander et al. (2010). We attribute this to the more reliable flux calibration procedures used in our work.

In Fig. 3.3 it can be seen that the [O III] emission-line profiles are diverse across the sample, with both narrow (FWHM ≈ few hundred $\mathrm{km\,s^{-1}}$) and broad components (FWHM≈900–1500 $\mathrm{km\,s^{-1}}$) which can be blueshifted and/or redshifted with respect to the narrow emission ($-350 \lesssim \Delta v \lesssim 1350\,\mathrm{km\,s^{-1}}$). We will discuss in Section 3.6.1 that the narrow [O III] components are likely to be tracing the host galaxy dynamics and merger remnants, while the broad components are most likely due to energetic outflows (see Section 3.8 for a discussion on individual objects). We will also argue that the observed diversity across the sample is due to a combination of orientation and obscuration effects.

The four sources for which we were able to decompose the line profiles into multiple Gaussian components are those which have the highest flux and consequently highest signal-to-noise (Table 3.3). It is possible that the other four detected sources also have both narrow and broad emission-line components, but we were unable to decompose them in these spectra due to their lower signal-to-noise ratios. For example, in one source (SMM J0217−0503), we identify a broad [O III] component in a sub-region of the IFU datacube that is not identified in the galaxy-integrated spectrum (Section 3.5.3).

In the following sections we discuss the spatially resolved properties of all of the [O III] detected sources except SMM J0302+0006 and SMM J1235+6215.
SMM J0302+0006 is spatially unresolved in our data while SMM J1235+6215 only displays tentative evidence for extended emission (see Section 3.8 for further details on these two sources). Due to the low signal-to-noise ratios of the data for these two sources it is difficult to determine if they are intrinsically compact or if any extended emission lies below our detection threshold. We do not discuss these two sources any further in this section.

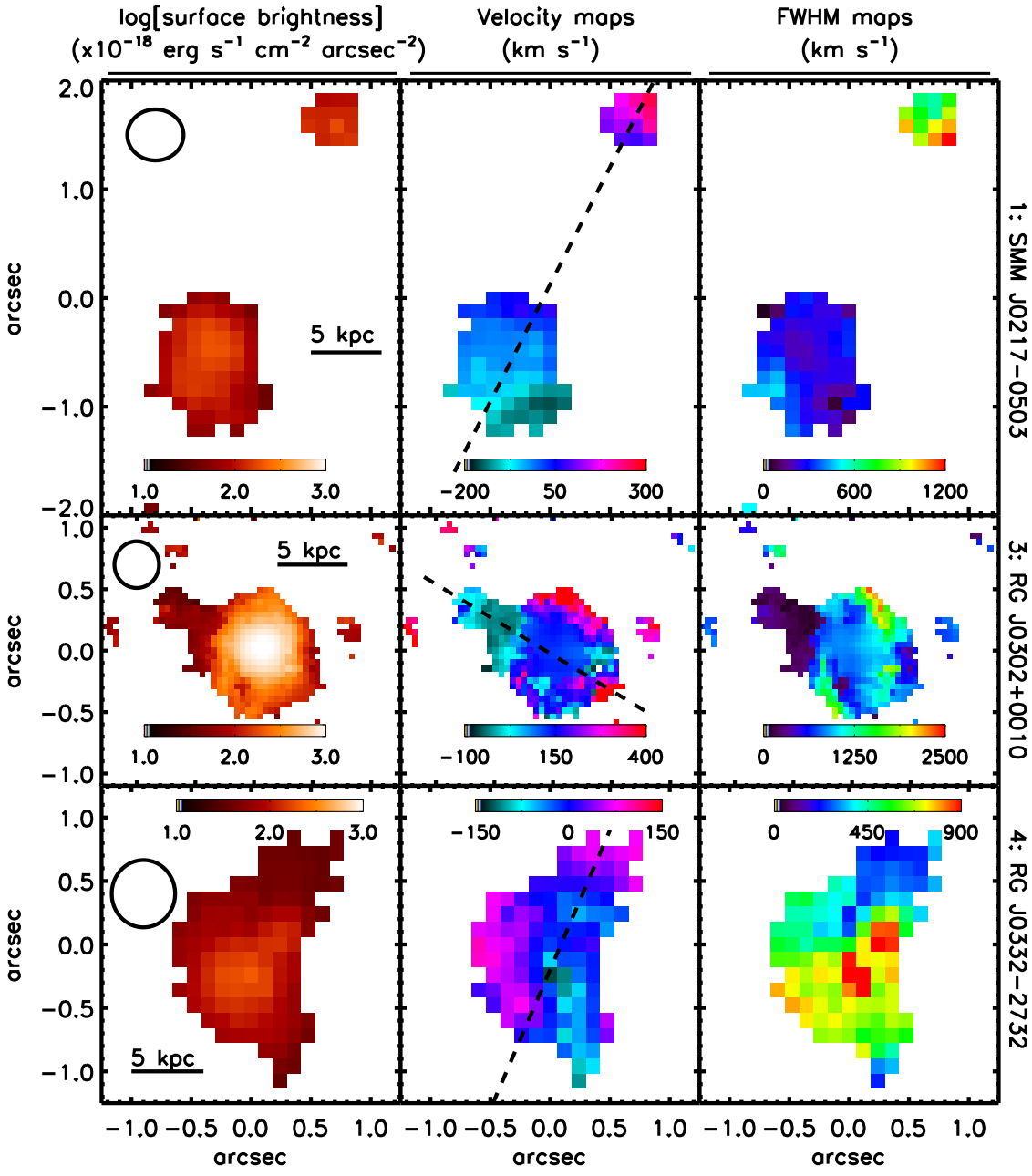

Figure 3.4: [O III] flux, velocity and FWHM fields, from fitting single Gaussian components to individual pixels for our six sources with spatially resolved emission. The [O III] emission is evidently very diverse and complex with large velocity offsets (up to $\approx 1700\,\mathrm{km\,s^{-1}}$) and regions of both narrow (FWHM $\approx$ few $100\,\mathrm{km\,s^{-1}}$) and broad (FWHM ≈ 700–$2500\,\mathrm{km\,s^{-1}}$) emission-line components. We attribute the narrow emission to galaxy dynamics and merger remnants and the broad emission to energetic outflows. Zero velocity is defined at the redshift of the narrowest component shown in the galaxy-integrated spectra (Fig. 3.3). No corrections have been made for unknown orientation effects or dust extinction. The open circles denote the average seeing disc during the observations of each target and the solid bars indicate 5 kpc in extent. The dashed lines show the axes through which we produced the velocity and FWHM profiles shown in Fig. 3.6. North is up and east is left in all panels.

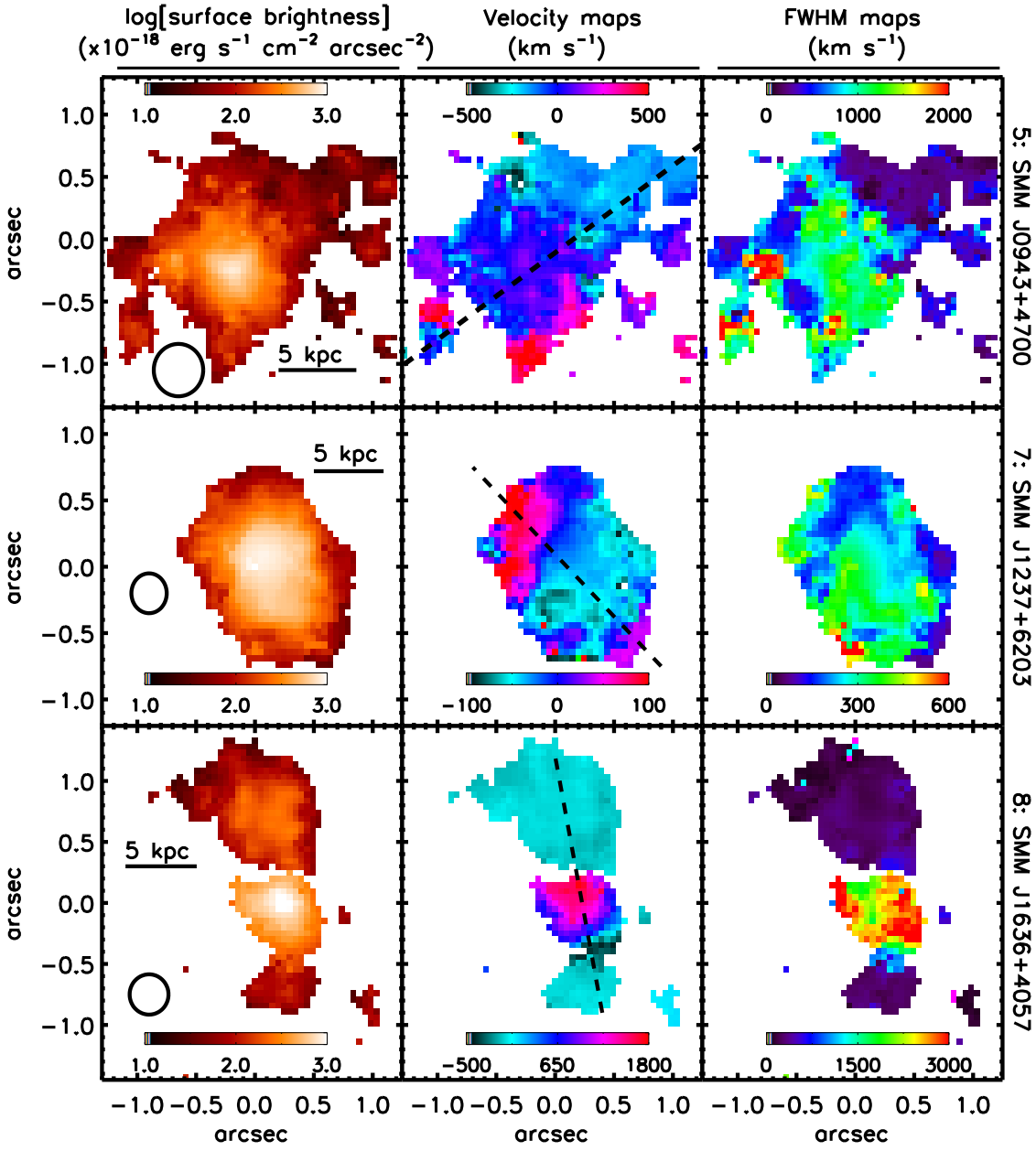

Figure 3.4: continued.

3.5.2 Surface brightness, velocity and FWHM maps

In Fig. 3.4 we show surface brightness maps, velocity fields and FWHM maps for the six sources for which we were able to spatially resolve the [O III] emission. These maps were produced using a adaptive binning technique such that the high surface brightness regions are averaged over smaller regions than the outer low surface brightness regions. We do this by taking a mean spectrum over 3×3 spatial pixels, increasing to 5×5 pixels (maximum for SINFONI data) and ultimately to 7×7 pixels (maximum for NIFS data) if the signal was too low to produce a sufficiently high χ^2 improvement in a continuum+emission-line fit over a simple continuum fit ($\Delta\chi^2 > 16$; equivalent to $\approx 4\sigma$). The continuum level was taken to be the median of line-free continuum in the vicinity of the emission lines. When this criterion is met, we fit the [O III]$\lambda\lambda$4959,5007 emission-line doublet with a single-Gaussian profile, allowing the normalisation, width and central wavelength to vary. We defined zero velocity at the central wavelength of the narrowest Gaussian component in the galaxy-integrated spectra.

The flux maps in Fig. 3.4 show that the observed emission-line regions of these sources are diverse and irregular, with at least two sources showing spatially distinct emission-line regions, indicating multiple interacting or merging systems. The [O III] emission is observed to be extended up to $\approx$20 kpc. The velocity fields and FWHM maps in Fig. 3.4 show that there are regions dominated by narrow [O III] emission ($\approx$ few hundred km s^{-1}) with modest velocity gradients ($\Delta v \lesssim 200$ km s^{-1}). There are also regions which are kinematically chaotic, extended up to 15 kpc in spatial extent, with extreme widths ($700 \lesssim$ FWHM $\lesssim 2500$ km s^{-1}) and large velocity offsets (Δv up to $\approx$1700 km s^{-1}).

The velocity fields and FWHM maps in Fig. 3.4 were created using single Gaussian components and do not separately trace the broad and narrow [O III] emission line components observed in the galaxy-integrated spectra (Fig. 3.3). Instead they roughly trace the brightest [O III] kinematic component. For example, we will show that although the source SMM J1237+6203 looks to have fairly quiescent kinematics in Fig. 3.4, the extremely broad and high-velocity [O III] component seen in the galaxy-integrated spectrum (FWHM$\approx$1000 km s^{-1}; $\Delta v \approx -350$ km s^{-1}; Fig. 3.3) is found over the central 5–8 kpc (see also Alexander et al. 2010). In the following sections, we therefore use further analysis methods to give a more complete description of the kinematics of these sources.

3.5.3 Regions dominated by narrow and broad emission lines

In Fig. 3.5 we show spatially-integrated spectra from regions dominated by broad or narrow emission lines. To produce these spectra we took our [O III] FWHM maps (Fig. 3.4) and integrated the spectra over the pixels that have FWHM$<500\,\mathrm{km\,s^{-1}}$ (narrow [O III]) and those that have FWHM$>500\,\mathrm{km\,s^{-1}}$ (broad [O III]). We do not do this for SMM J1237+6203 as there are too few pixels that contain emission lines with FWHM$>500\,\mathrm{km\,s^{-1}}$. For this source the narrow component of the [O III] emission line seen in Fig. 3.4 dominates the whole of the velocity and FWHM maps. The value of $500\,\mathrm{km\,s^{-1}}$ was motivated by the maximum line-widths generally expected from galaxy dynamics and merger remnants in high-redshift ULIRGs (see Section 3.6.1; Alaghband-Zadeh et al. 2012). We fit the spectra using the same method as the galaxy-integrated spectra (see Section 3.5.1) and provide all of the parameters of the fits and their uncertainties in Table 3.4. We also fit any observed Hβ emission in these regions using a single Gaussian profile and give the parameters and their uncertainties in Table 3.4. When no Hβ emission lines were detected we use the standard deviation of the emission-line free continuum and the FWHM of the [O III] emission-line components to derive 3σ upper limits on the flux.

By comparing the spatially-integrated spectra from the regions shown in Fig. 3.5 with the galaxy-integrated spectra shown in Fig. 3.3 we are able to locate the different kinematic components in the galaxies. For example, in the majority of the sources there is narrow emission (FWHM$\approx$ a few $100\,\mathrm{km\,s^{-1}}$) extended over the full spatial extent of the emission-line regions (up to $\approx$20 kpc). The regions dominated by the broadest emission lines (Fig. 3.5) are also the regions where the [O III] emission peaks in surface brightness and the [O III]/Hβ ratios are the largest (log([O III]/Hβ)$>$0.6; see Table 3.4), indicating excitation dominated by AGN activity in these regions (e.g., Kewley et al. 2006). Further evidence for the broad emission lines being associated with AGN activity is found in the source SMM J0217−0503, which is comprised of two separate systems, and the broad emission line is only observed in the system that is identified as hosting AGN activity by Alaghband-Zadeh et al. (2012) (also see Section 3.8). In addition, SMM J1636+4057 displays two broad [O III] components which are co-spatial with the Hα broad-line region of the AGN (Menéndez-Delmestre et al. 2013; see Section 3.8).

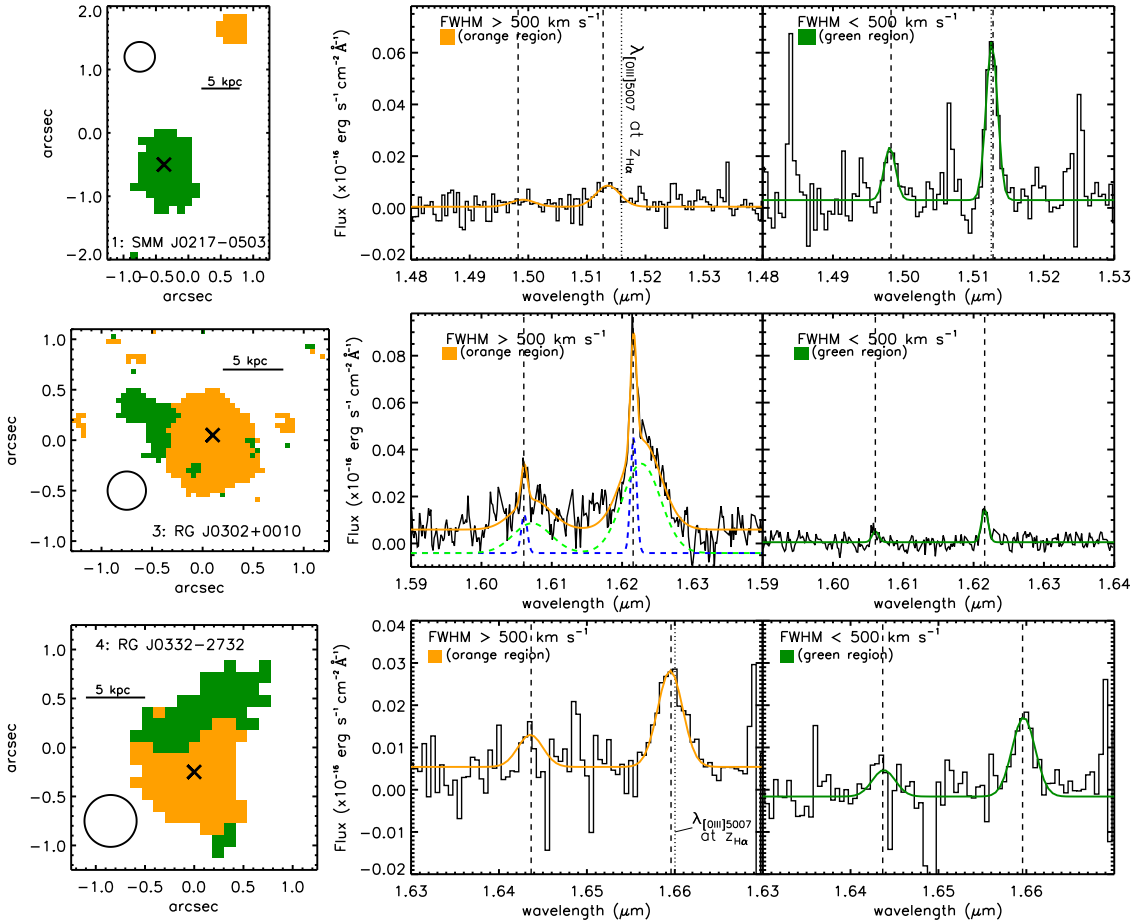

Figure 3.5: *Left:* Maps of our spatially resolved sources colour-coded to separate regions dominated by narrow [O III] emission lines (green: FWHM $< 500\,\mathrm{km\,s^{-1}}$) or broad [O III] emission-lines (orange: FWHM $> 500\,\mathrm{km\,s^{-1}}$) determined from the FWHM maps shown in Fig. 3.4. For the source SMM J1237+6203 the narrow component dominates the [O III] flux throughout and therefore we are unable to define the separate spatial regions using this method (see Section 3.5.3 for details). The narrow emission lines are observed over the largest extents but the broad emission lines are still observed in extended regions (≈4–15 kpc). The open circles denote the average seeing discs during the observations, the solid bars indicate 5 kpc in extent and the crosses indicate the peak in [O III] surface brightness. North is up and east is left. *Middle and Right:* The spatially-integrated spectra around the [O III]λλ4959, 5007 emission-line doublet extracted from the regions indicated in the left panels. The central regions exhibit complex emission-line profiles. The dashed curves show the individual Gaussian components (with an arbitrary flux shift) of the fits when two components were required. The solid curves show the best fitting overall emission-line profiles; the parameters and their uncertainties are shown in Table 3.4. The vertical dashed lines shows the centroids of the [O III]λλ4959,5007 narrow line components in the galaxy-integrated spectra (Fig. 3.3). The vertical dotted lines for SMM J0217−0503 and RG J0332−2732 show the expected position of [O III] given the redshift of the Hα emission-line from the same spatial region (Alaghband-Zadeh priv. comm.). For the source SMM J1636+4057 the vertical dotted line indicates the expected wavelength of the [O III]5007 line using the redshift of the Hα broad-line region (Swinbank et al. 2005).

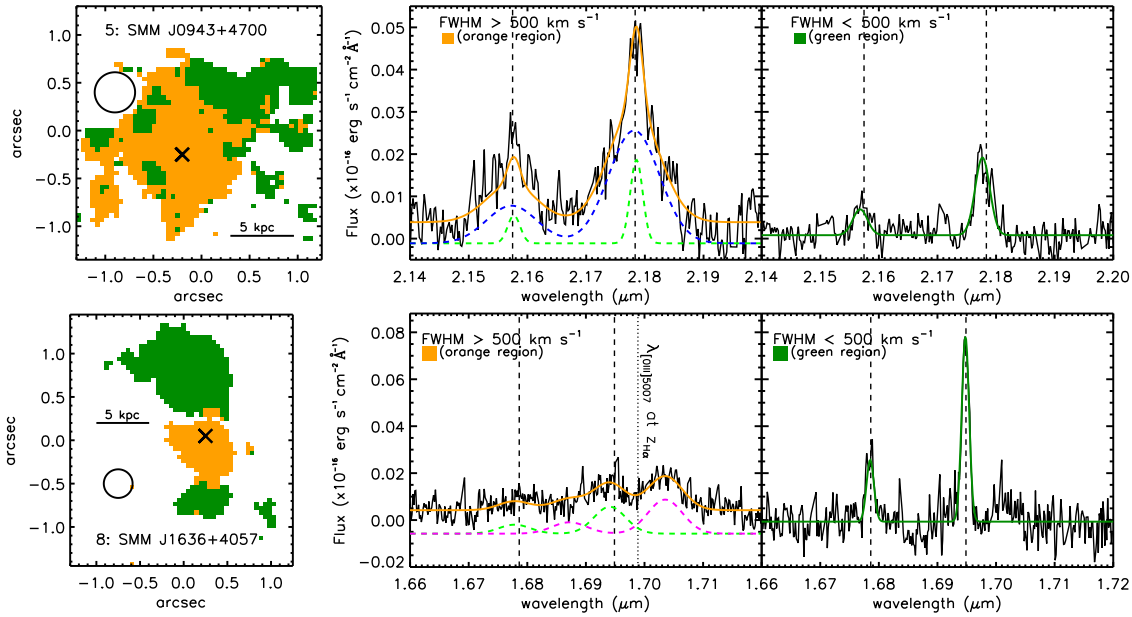

Figure 3.5: continued.

3.5.4 Velocity profiles

To further quantify the [O III] velocity structure and spatial extents of the different kinematic components in our sample we created velocity and FWHM profiles for each of the six spatially resolved sources and show them in Fig. 3.6. To produce these profiles we first repeated the pixel-by-pixel fitting routine outlined in Section 3.5.2 with the addition of allowing a second Gaussian component to be fit at each pixel, if this resulted in a significant improvement ($\Delta\chi^2 > 16$; equivalent to $\gtrsim 4\sigma$) over a single Gaussian component. Only two of the sources (RG J0302+0010 and SMM J1237+6203) had sufficiently bright narrow and broad [O III] emission-line components to de-compose the profiles using this method. For these two sources we took these double-Gaussian component FWHM and velocity maps and took a running median of all the pixels orthogonal to a vector through the most extended emission (see dashed lines in Fig. 3.4). For the other four spatially resolved sources (SMM J0217−0503; RG J0332−2732; SMM J0943+4700 and SMM J1636+4057) we used the single-Gaussian component FWHM and velocity maps shown in Fig. 3.4. For the sources SMM J0217−0503 and RG J0332−2732 we also plot the relative velocities of the Hα emission, extracted from the regions shown in Fig. 3.5, on these velocity profiles. For the source SMM J1636+4057 we plot the [O III] FWHM and velocity offset values from the spectra extracted from the broad [O III] region (Fig. 3.5)

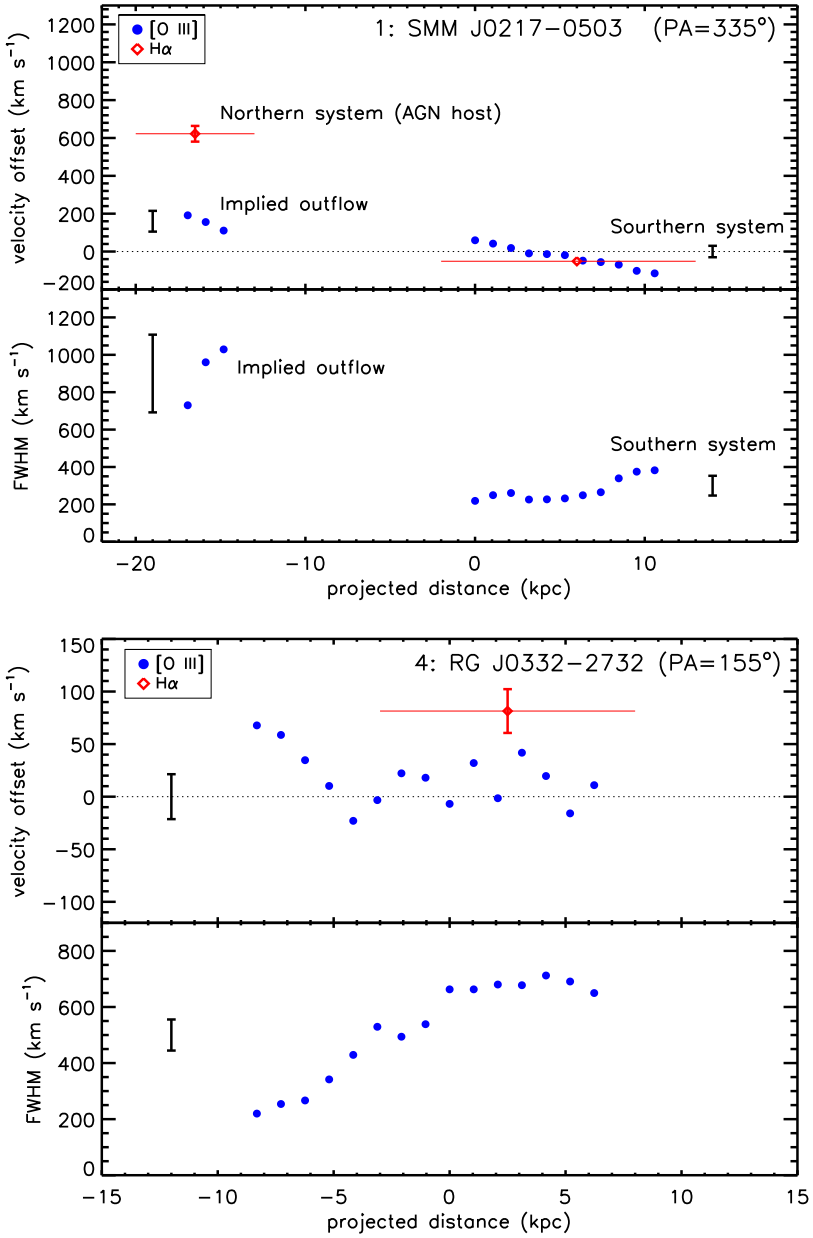

Figure 3.6: A velocity and FWHM profile of the [O III] emission lines for our six spatially resolved sources, along vectors at the angles indicated in the upper-right of each panel (see Section 3.5.4 for how these were produced). When it was possible to de-couple the [O III] emission-line profiles into two components we have shown these as filled circles (narrow) and open squares (broad). In some cases Hα data and CO(1–0) data are plotted, taken from the literature (Swinbank et al. 2005; Ivison et al. 2011; Alaghband-Zadeh et al. 2012; Menéndez-Delmestre et al. 2013). The data points for the broad [O III] components for the source SMM J1636+4057 are taken from the fits to the spectra shown in Fig. 3.5. In all cases there are underlying narrow [O III] emission lines (FWHM $\approx$ few hundred km s^{-1}) with small velocity gradients ($\Delta v \lesssim$200 km s^{-1}) which we associate with galaxy dynamics and merger remnants. Broad [O III] emission lines (FWHM$\approx$700–1400 km s^{-1}) are offset from these galaxy kinematics which we interpret as energetic outflows. The error bars are representative 1σ uncertainties for the [O III] measurements. The horizontal solid lines indicate the approximate uncertainties in the spatial positions of the measurements when applicable. The dotted lines indicate zero velocity using the redshift of the narrowest [O III] components in the galaxy-integrated spectra (Fig. 3.3).

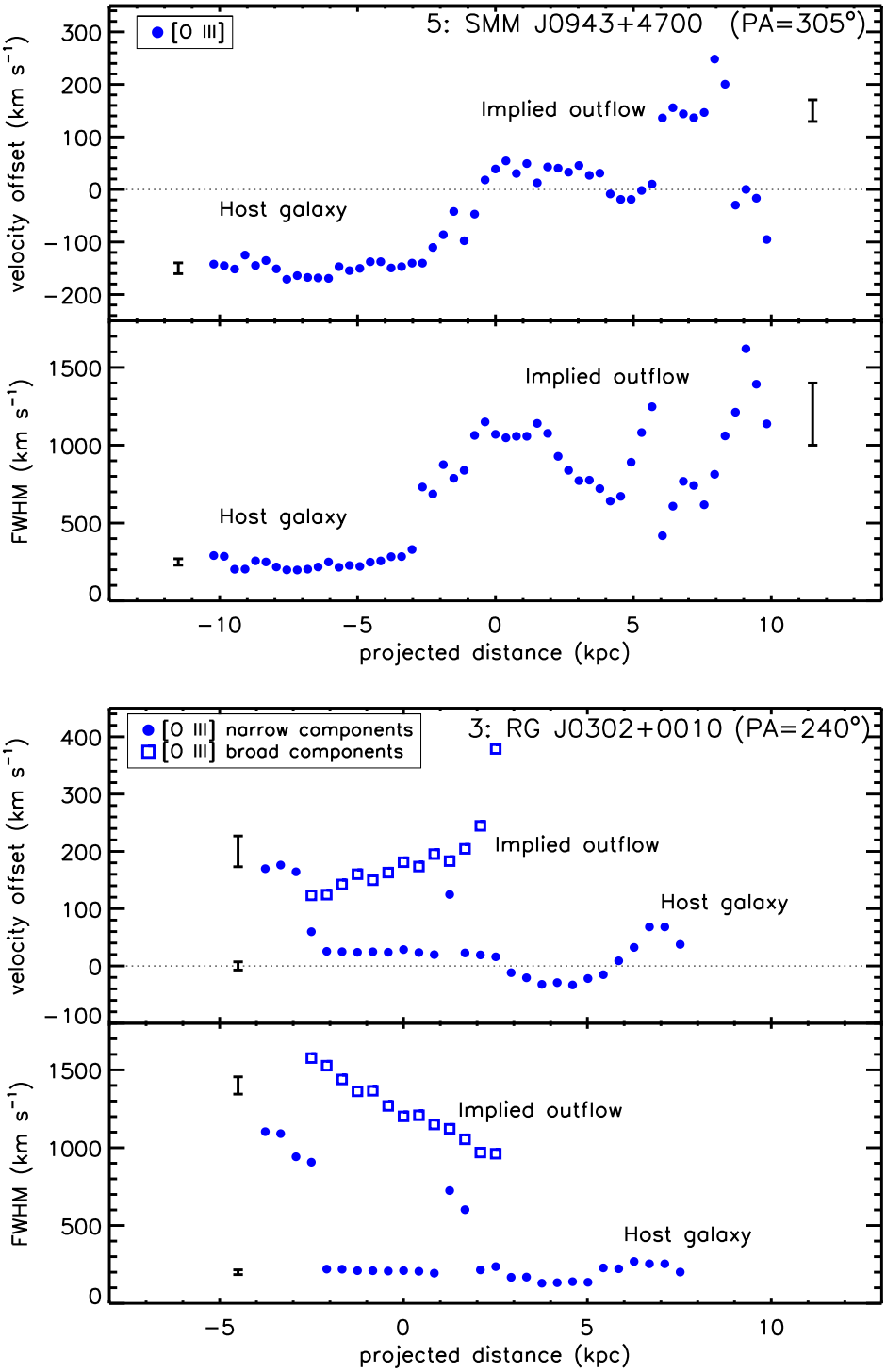

Figure 3.6: continued.

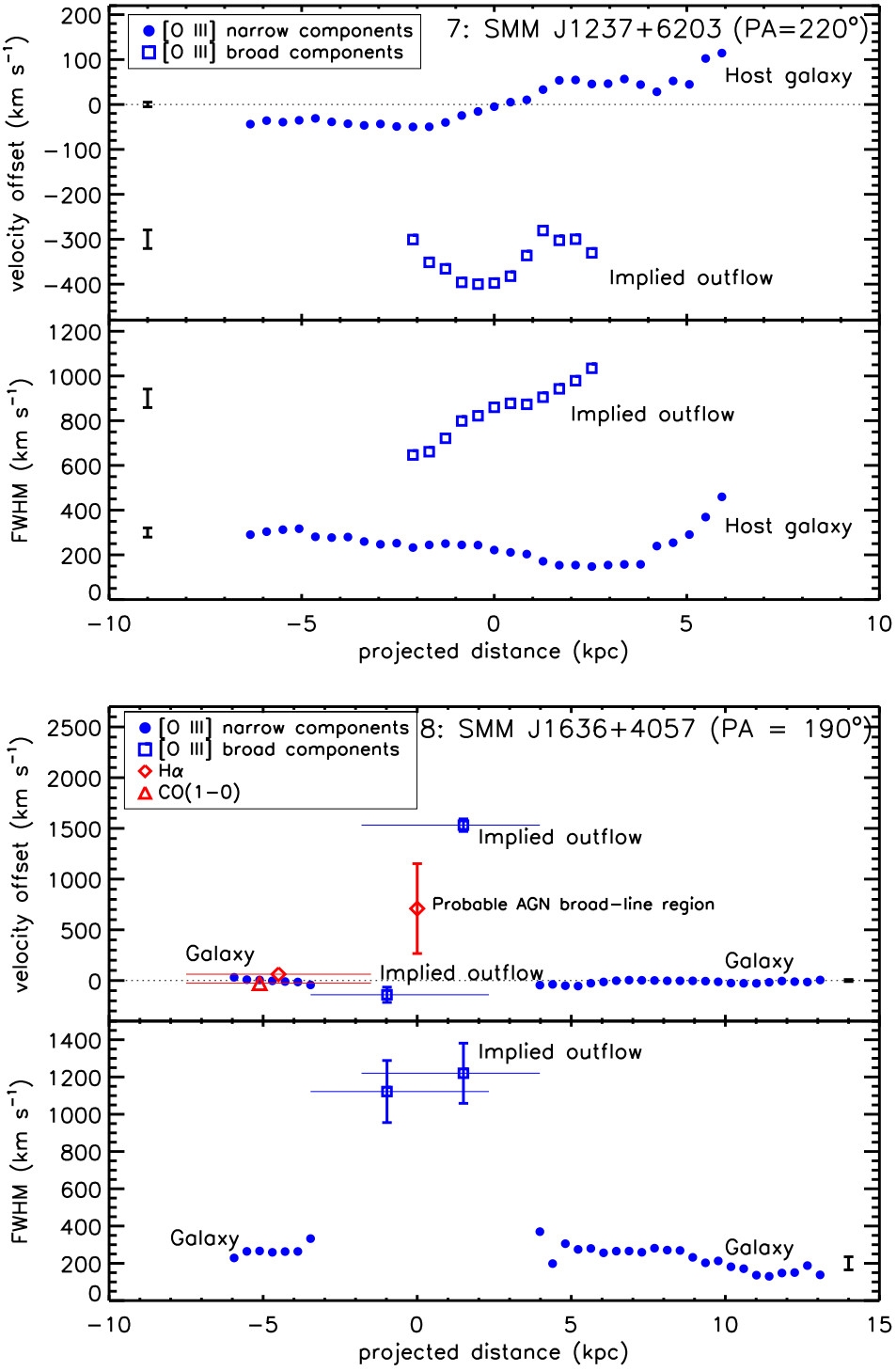

Figure 3.6: continued.

and Hα and CO(1–0) data from the literature (Swinbank et al. 2005; Ivison et al. 2011; Menéndez-Delmestre et al. 2013; see Section 3.8 for more details).

Fig. 3.6 enables us to separately trace the kinematics of the narrow (FWHM ≈ a few hundred $\mathrm{km\,s^{-1}}$) and broad (FWHM ≈700-1400 $\mathrm{km\,s^{-1}}$) [O III] emission-line components. The narrow emission lines have small velocity gradients ($\Delta v \lesssim 200\,\mathrm{km\,s^{-1}}$) and appear to be at roughly the same velocity as the Hα emission and molecular gas, when these data are available for comparison. In contrast, the broad components are offset from the narrow emission by $|\Delta v| \approx$150–1400 $\mathrm{km\,s^{-1}}$ and are found over ≈4–15 kpc in observed linear extent (except SMM J0217−0503 for which the broad emission is spatially unresolved; ≤4 kpc). The source RG J0332−2732 has emission that is not clearly separated into broad and narrow components; however, we note that the emission is broadest (FWHM≈700 $\mathrm{km\,s^{-1}}$) in the brightest central region. The source SMM J0217−0503 consists of two separate systems, which are indicated in Fig. 3.6. In the northern system we do not observe any narrow emission lines; however, the [O III] emission has a large velocity offset from the peak in the Hα emission ($\Delta v = -460 \pm 60\,\mathrm{km\,s^{-1}}$; see Section 3.8 for further details). Of particular note is the source SMM 1636+4057 for which the broad components are found at $v \approx \pm 850\,\mathrm{km\,s^{-1}}$ from the systemic velocity of the the Hα broad-line region of the AGN (Swinbank et al. 2005; Menéndez-Delmestre et al. 2013; see Section 3.8).

Due to the large uncertainties in the velocity offsets and FWHM of the broad [O III] components, we do not interpret their kinematic structure any further than quoting their spatial extent and velocity offsets from the systemic redshifts. However, we did perform tests to ensure that the broad emission lines are truly spatially extended and that the observed extents are not just the result of intrinsically compact regions being extended by the seeing during our observations. Following Alexander et al. (2010) we did this by extracting spectra from different regions and we found velocity structure in the broad emission lines, confirming that they are spatially extended (see Section 3.8 for details on individual sources).

For the remainder of this work we quote the spatial extent of the broad [O III] emission as the extent of the broad [O III] regions shown in Fig. 3.5 (see Table 3.4). These values are consistent, within the quoted uncertainties, with spatial extents of the broad [O III]

emission found in the velocity profiles shown in Fig 3.6. The source SMM J1237+6203 does not appear in Fig. 3.5 (see Section 3.5.3); therefore, we take the spatial extent from Fig. 3.6 ($\approx$5 kpc) which is conservative based on the 4–8 kpc extent found by Alexander et al. (2010) for this source. The quoted spatial extents are likely to be lower limits as they are not corrected for orientation and low surface brightness broad [O III] emission will not be detected by our fitting procedures (described in Section 3.5.2). We define the velocity offsets of the broad emission lines from the systemic, as the velocity differences between the broad and narrow [O III] emission lines in the spectra extracted from the broad [O III] regions (see Fig. 3.5 and Table 3.4). For SMM J0217$-$0503 and RG J0332$-$2732 we use the velocity offset to the narrow Hα emission, as no narrow [O III] emission is observed. For SMM 1636+4057 we use half of the velocity offset between the two broad components, which is also consistent with the offset between each component and the velocity of the Hα broad-line region (see Section 3.8).

3.6 Discussion

Our IFU observations of eight $z = 1.4-3.4$ ULIRGs that host AGN activity have revealed extreme gas kinematics with very broad [O III] emission (FWHM$\approx$700–1400 km s^{-1}), extended up to 15 kpc and with high-velocity offsets, up to $\approx$850 km s^{-1}. We have also identified narrow [O III] emission lines with moderate widths and velocity gradients (FWHM$\lesssim$500 km s^{-1}; $\Delta v \lesssim$200 km s^{-1}) over the full extent of the observed emission-line regions (up to $\approx$ 20 kpc). In the following discussion, we focus on the six sources for which we have high-quality spatially-resolved data and show that the narrow emission lines are consistent with tracing galaxy-dynamics and mergers, while the broadest emission lines are consistent with being predominantly due to energetic outflows. We then go on to discuss the impact that these outflows could be having on the future growth of the central BHs and host galaxies and the implications of these results for the formation of massive galaxies.

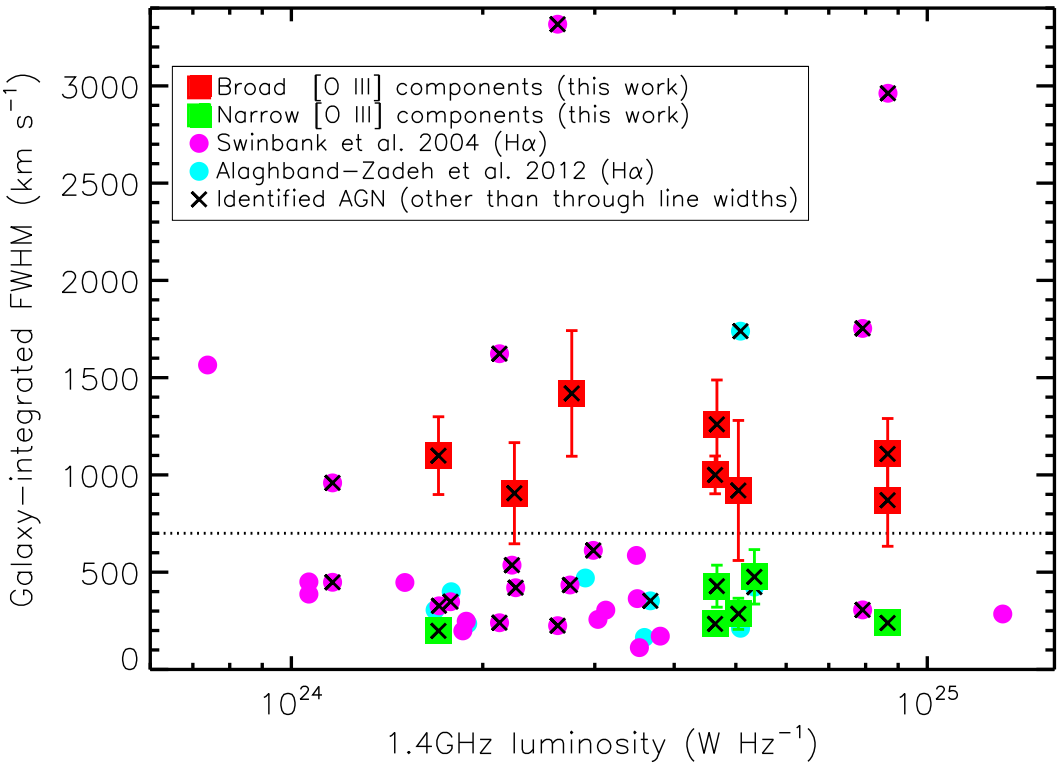

Figure 3.7: The [O III] FWHM from the galaxy-integrated spectra of our eight [O III] detected targets and high-redshift ULIRGs from the literature versus 1.4 GHz radio luminosity. Both broad components (FWHM$\gtrsim$700 km s^{-1}; dashed line) and narrow components of the profile fits have been plotted (see Table 3.3). For SMM J0217−0503 we have plotted the northern and southern systems separately (see Table 3.4). We also plot the galaxy integrated Hα FWHMs from other high-redshift ULIRGs with similar radio luminosities (Swinbank et al. 2004; Alaghband-Zadeh et al. 2012). The sources that are identified as AGN (using methods not based on emission-lines widths), have been highlighted (see Section 3.6.1 for details). The non-AGN ULIRGs have FWHMs that lie below $\approx$700 km s^{-1}. The narrow [O III] components of our sample are consistent with the emission-lines widths from non-AGN ULIRGs and presumably trace galaxy dynamics and mergers while the broadest components appear to be constrained to the AGN host galaxies and are likely to be tracing AGN-driven outflows.

3.6.1 Tracing galaxy dynamics, mergers and outflows

In six of our sources we find an extended [O III] emission-line region (up to ≈20 kpc; Fig. 3.4), which are often found in gas-rich systems containing luminous AGN (e.g., Colina et al. 1999; Nesvadba et al. 2008; Greene et al. 2011; Villar-Martín et al. 2011b; Matsuoka 2012). The presence of these emission-line regions enables us to trace the kinematics of the ionised gas in these galaxies.

We identified narrow [O III] emission (FWHM up to a few $\times 100\,\mathrm{km\,s^{-1}}$) with irregular velocity profiles and small velocity gradients ($\Delta v \lesssim 200\,\mathrm{km\,s^{-1}}$) over the full extent of the emission-line regions (Fig. 3.4 and Fig. 3.6). The line widths and velocity offsets observed in this narrow [O III] emission are similar to the kinematics of gas found in simulated merger remnants (Cox et al. 2006). The kinematics of these narrow emission lines are also broadly consistent with other high-redshift star-forming galaxies that have similar radio-luminosities, many of which are also undergoing mergers (e.g., Swinbank et al. 2004; Nesvadba et al. 2007b; Lehnert et al. 2009; Alaghband-Zadeh et al. 2012) as well as nearby ULIRGs (e.g., Colina et al. 2005). To illustrate this, in Fig. 3.7, we compare the galaxy-integrated emission-line FWHMs of our AGN sample to the Hα emission line FWHM in other high-redshift ULIRGs from Swinbank et al. (2004) and Alaghband-Zadeh et al. (2012). We highlight sources that are identified as AGN on the basis of their emission-line flux ratios, X-ray emission, UV spectral features or their mid-infrared spectra. Fig. 3.7 shows that the narrow [O III] emission lines (FWHM$\lesssim$500 $\mathrm{km\,s^{-1}}$) in our sources are comparable to the emission-line widths of non-AGN high-redshift ULIRGs and therefore are likely to be tracing the same kinematic components seen in these sources (i.e., galaxy dynamics and mergers). The velocity structure of the emission lines seen in the IFU data of the non-AGN ULIRGs (Alaghband-Zadeh et al. 2012) are also similar to the narrow [O III] components observed here. In particular, for the two sources where there are IFU observations covering both the [O III] and Hα emission lines (SMM J0217-0503 and RG J0332-2732; this work and Alaghband-Zadeh et al. 2012) the kinematics of the narrow [O III] and Hα emission-line components are roughly consistent (e.g., see Fig. 3.5).

In contrast to the narrow emission lines, the identification of broad emission lines (FWHM$\gtrsim$700 $\mathrm{km\,s^{-1}}$) in the galaxy integrated spectra of high-redshift ULIRGs appears

to be constrained to galaxies that contain known AGN activity (Fig. 3.7).[2] This is in agreement with studies of low-redshift ULIRGs where the broadest emission lines are found in systems hosting powerful AGN activity (e.g., Veilleux et al. 1999, Zheng et al. 2002; Westmoquette et al. 2012). Although broad emission-line components may be found in non-AGN high-redshift star-forming galaxies, they are generally faint and are difficult to identify other than by stacking the spectra of multiple sources or with excellent quality data (e.g., Swinbank et al. 2004; Nesvadba et al. 2007b; Le Tiran et al. 2011). However, we note that we are basing these arguments on small samples of galaxies which are biased in their selection, and to fully address if bright and broad emission lines, such as those in our sources, are unique to galaxies hosting AGN activity, requires larger systematic samples of spectra and IFU data. In addition to comparisons with the literature, there is further evidence that the broadest emission lines are associated with AGN activity in our sample. The broadest emission lines are found to be spatially co-incident with the most likely location of the AGN in these galaxies based on very high [O III]/Hβ emission-line ratios (see Section 3.5.3). The most striking example of this is the source SMM J1636+4057 where the broadest [O III] emission lines are found to be co-spatial with the AGN, and not in the region of unobscured star formation (details in Section 3.8).

Broad and asymmetric [O III]$\lambda\lambda$4959,5007 emission-line profiles, such as those found in this work, are most commonly attributed to high-velocity outflowing gas (e.g., Heckman et al. 1981; Greene & Ho 2005; Barth et al. 2008; Nesvadba et al. 2008; Greene et al. 2011). In particular, IFU observations of local ULIRGs that host AGN activity reveal broad and spatially extended emission lines (similar to those that we observe) associated with energetic outflows (Rupke & Veilleux 2011; Westmoquette et al. 2012). On the basis of the above arguments the broadest kinematic components (FWHM$\gtrsim$700 km s^{-1}) appear to be associated with AGN activity and therefore do not appear to be the result of mergers and galaxy dynamics or even (as we will further argue below) star-formation driven outflows, and therefore AGN-driven outflows is the most natural explanation. We find convincing evidence for extended ($\gtrsim$ 4 kpc) outflows in four of our sample (RG J0302+0010;

[2]The one source from Swinbank et al. (2004) with FWHM$>$700 km s^{-1} that is not identified as an AGN (Fig. 3.7) has a complex spectrum and has not been covered by multi-wavelength observations in the literature. It is therefore not possible to rule out the presence of a significant AGN in this galaxy.

SMM J0943+4700; SMM J1237+6203 and SMM J1636+4057). The source RG J0332-2732 only has very broad [O III] emission lines in the most central regions, and the broad [O III] emission line in the source SMM J0217-0503 has a low signal-to-noise ratio and is spatially unresolved. These two sources have lower quality data than the other four spatially extended sources and the evidence for spatially-extended outflows in these objects is weaker (see Section 3.8 for further discussion on these two sources).

3.6.2 Outflow properties

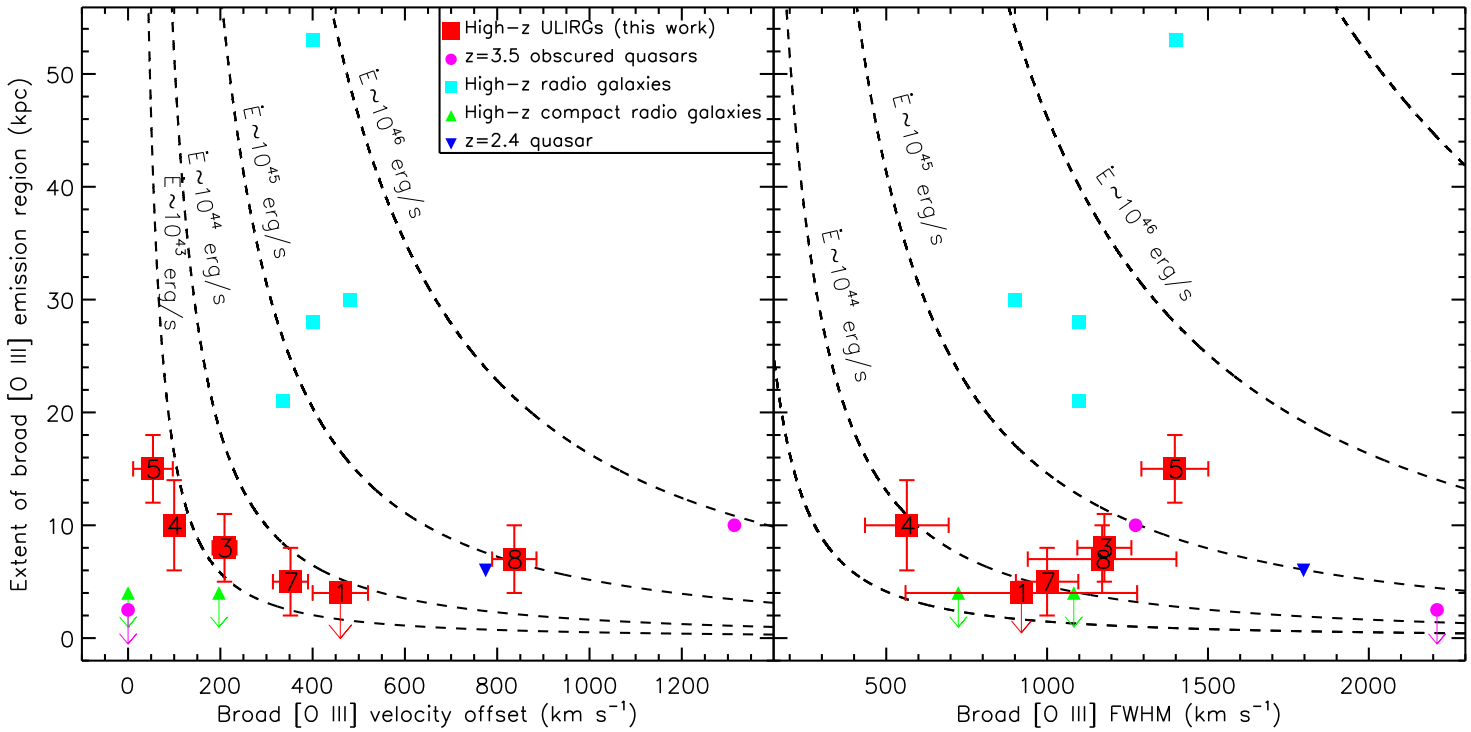

Figure 3.8: The projected spatial-extent of the broad [O III] emission-line regions against velocity offset from the systemic redshift (*left*) and FWHM (*right*) for our spatially resolved sources (see Table 3.3 and Table 3.4). The numbers inside the symbols correspond to the source IDs. Also shown are other high-redshift sources with IFU data (symbols are the same as in Fig. 3.1). If two sides of an outflow are observed, half of the velocity difference between them is used, and the average FWHM of each side. For spatially unresolved data we use the seeing disk as an upper limit of the extent. For illustrative purposes, the dashed lines show the expected energy injection rates ($\dot{E}$) using a simple outflow model (see Section 3.6.2 for details). Strong evidence for extended outflows is not confirmed for source IDs 1 and 4 (see Section 3.6.1). Despite 3–4 magnitudes difference in radio luminosities, HzRGs and high-redshift ULIRGs containing AGN activity have comparable velocity offsets and emission-line widths and are both potentially injecting energy into their host galaxies at considerable rates ($\approx 10^{43}$–10^{46} erg s^{-1}).

We can use the measured properties of the broad [O III] emission to place constraints on the outflow properties. In Fig. 3.8 we plot the observed spatial extent of the broad [O III] emission lines against the velocity offset from the systemic redshifts of the host galaxies (values are from the fits to the spectra shown in Fig. 3.5 and are provided in Table 3.4).[3] The dashed lines in Fig. 3.8 represent estimated energy injection rates which we discuss later. The broad [O III] emission-line properties ($\Delta v \approx$50–850 km s^{-1}; spatial extent ≈4–15 kpc) can be explained by the presence of an AGN-driven bi-polar outflow plus the addition of obscuring material in the host galaxy. In Fig. 3.9 we show a simple schematic diagram to attempt to explain the properties and diversity of the broad [O III] emission lines. Hydrodynamical simulations and analytical models predict that a powerful AGN-wind, launched from the central BH, could sweep up clouds of gas, resulting in an kpc-scale outflow (e.g., Debuhr et al. 2012; Zubovas & King 2012 and references therein). Galaxy-wide outflows are thought to be expanding bubbles on either side of the host galaxy, being forced into this shape by the denser material in the centre of the host-galaxy (e.g., Zubovas & King 2012; Faucher-Giguère & Quataert 2012). As we are observing the outflow through luminous [O III] emission, the *observed* properties of the outflow will also depend on the size and orientation of the AGN ionisation cones (e.g., Crenshaw et al. 2010). Multiple clouds being caught up in the bulk flow of the outflow (e.g., Zubovas & King 2012) or perturbed ionised gas would result in broad [O III] emission lines (e.g., Villar-Martín et al. 2011a). The 'near-side' of the outflow would therefore be observed as a broad and blueshifted emission line and the 'far-side' would be observed as broad and redshifted emission line (see Fig. 3.9). However, part of the outflow could be obscured by material in the host galaxy, as is likely to be the case in clumpy and dusty systems such as high-redshift ULIRGs (e.g., Ivison et al. 2007; Tacconi et al. 2008; Engel et al. 2010). High-redshift ULIRGs are kinematically disturbed, potentially resulting in a complex distribution of obscuring material, which, along with the relative orientation of the AGN, could explain why in some cases we only see either a blueshifted (i.e., when only the near-side of the outflow is observed) or redshifted broad emission line

[3] The source SMM J1237+6203 does not appear in this table. For this source we use a spatial extent of 5 kpc (see Fig. 3.6) and the FWHM and velocity offset from the galaxy-integrated spectrum (Table 3.3). See the end of Section 3.5.4 for details.

(i.e., when only the far-side of the outflow is observed; also see fig. 6 and 7 in Crenshaw et al. 2010).

The range in spatial extents and velocity offsets of the implied outflows that we observe (Fig. 3.8) can also be explained using this simple model (Fig. 3.9). The *observed* velocity offsets and *observed* spatial extents will be highly dependent on the orientation of the outflow with respect to the line of sight. If the axis of the outflow is orientated along the line of sight, high velocity offsets and a small spatial extent would be observed (e.g., this could explain the properties of SMM J1636+4057). Conversely, if the axis of the outflow is in the plane of the sky, a small velocity offset and a large spatial extent would be observed (e.g., this could explain the properties of SMM J0943+4700); see Section 3.8 for further discussion on individual sources. In contrast, the observed FWHM will be less dependent on the orientation. We emphasise that this is a very simplified model and other interpretations could also be valid. For example, the observed emission-line properties will also be dependent on the intrinsic properties of the outflow, such as their intrinsic velocity and distance travelled from the BH.

We have argued that the measured velocity offsets observed may not represent the true velocity of the outflow due to an orientation effect. We attempt to estimate corrected velocity offsets by taking the two sources which contain a known broad-line AGN (SMM J1237+6203 and SMM J1636+4057; see Section 3.8 for details). In these sources the identification of the broad-line AGN component suggests that the outflow could be primarily orientated towards us and therefore the observed velocity offset is likely to be close to the true outflow velocity. For these two sources we find that the average of FWHM/Δv is ≈ 2; reassuringly we also find a median ratio of FWHM/$\Delta v \approx 2$ for low-redshift broad-line AGN that display [O III] properties indicative of outflows (data from Mullaney et al. 2013). We therefore suggest that FWHM/2 may be an adequate approximation of the true outflow rate, although subject to large uncertainties. Using this as a diagnostic, we estimate bulk outflow velocities in the range of $\approx$300–700 km s^{-1}, which are similar to the predicted kpc-scale outflow velocities predicted by hydrodynamical simulations and analytical models of outflows ($\approx$300-1500 km s^{-1}), driven by AGN in objects with similar properties to the sources in our sample (i.e., ULIRGs, with $L_{\rm AGN} \approx 10^{46}$ erg s^{-1}; Debuhr et al. 2012; Zubovas & King 2012; Faucher-Giguère & Quataert 2012).

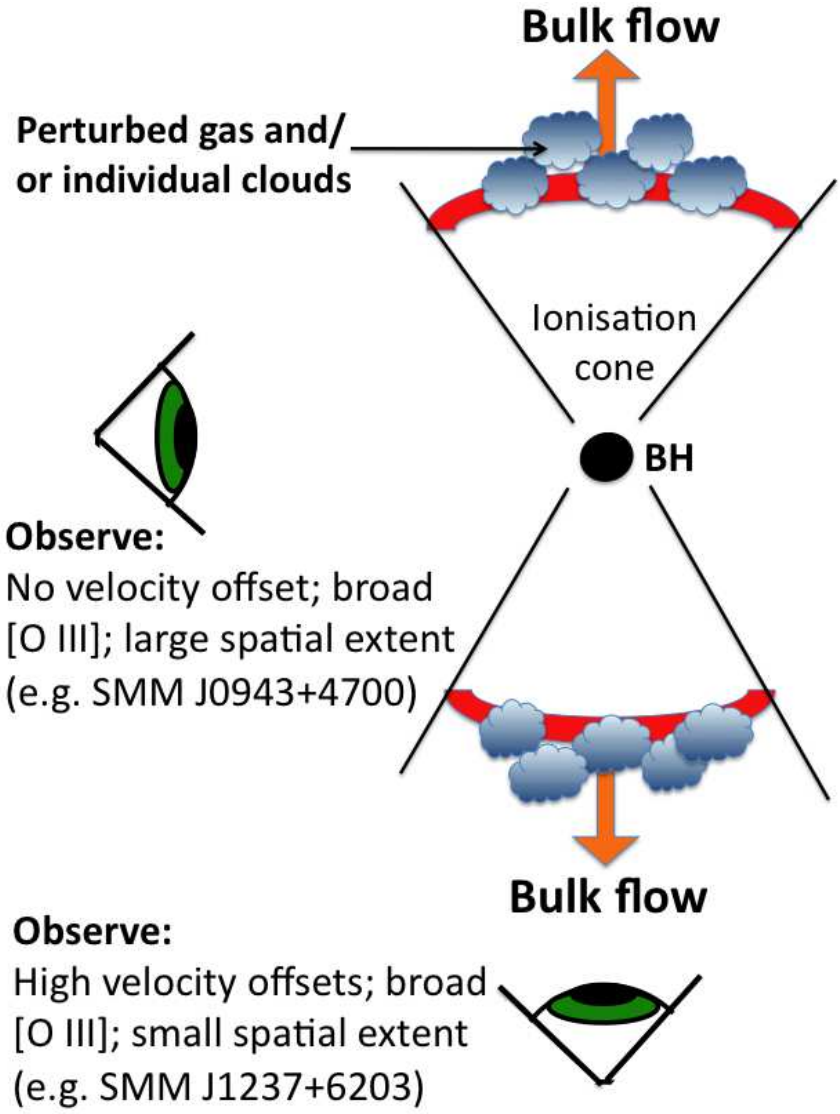

Figure 3.9: A schematic diagram to illustrate a possible interpretation of the observations of the broad [O III] emission lines. If a fast wind is initially launched around the central BH it could sweep up clouds of gas in a bi-polar outflow (as assumed by some models e.g., Debuhr et al. 2012; Zubovas & King 2012; see Section 3.6.2 for more discussion). The orientation with respect to the line of sight will determine the velocity offsets and spatial extent observed; however, broad emission lines will be always be observed. This could explain the diversity in the properties of our observations. In addition, obscuring material in the host galaxy would result in parts of the outflow not being visible which could explain why in some sources we only observe either blueshifted or redshifted broad emission lines.

Estimating outflow energy rates and determining what is powering the outflows

To attempt to quantify the impact the outflows may be having on the host galaxies we consider approaches to estimate the energy injection rates into the ISM. We do not have good constraints on the mass of the gas entrained in the outflows or on the geometry of the outflow, making such estimates uncertain. For illustrative purposes, we consider the energy injection rates assuming an energy conserving bubble into a uniform medium (e.g., Heckman et al. 1990; Veilleux et al. 2005; Nesvadba et al. 2008; and references therein) which gives the following relation:

$$\dot{E} \approx 1.5 \times 10^{46} r_{10}^2 v_{1000}^3 n_{0.5} \,\mathrm{erg\,s^{-1}}, \tag{3.6.1}$$

where r_{10} is taken to be half the extent of the observed broad [O III] emission (in units of 10 kpc) and v_{1000} are the velocity offsets in units of $1000\,\mathrm{km\,s^{-1}}$ (see Table 3.4). The ambient density (ahead of the expanding bubble), $n_{0.5}$, is in units of $0.5\,\mathrm{cm^{-3}}$ for which we have assumed $n_{0.5}$=1.[4]

In the left panel of Fig. 3.8 we plot on tracks indicating fixed energy injection rates using Equation 3.6.1. We have already discussed that the observed velocity offsets are unlikely to be representative of the intrinsic velocities and that FWHM/2 is plausibly a better estimate of the true outflow velocity. Therefore, in the right panel of Fig. 3.8 we plot the extent of the broad [O III] emission against FWHM and tracks of constant energy injection rates using Equation 3.6.1, but replacing the velocity offset with FWHM/2. For the two sources with a known broad-line AGN in this sample (SMM J1237+6203 and SMM J1636+4057) and the sources with broad-line AGN in the comparison samples (i.e. Nesvadba et al. 2006; Cano-Díaz et al. 2012), the two diagnostics for the bulk outflow

[4]This density assumption is based on the the values of $n_{0.5}$=1–4 used in e.g. Heckman et al. (1990) and Nesvadba et al. (2008). This value can be indirectly estimated from the (post-shock) electron density (see Heckman et al. 1990 and references therein for further details), derived from the [S II]λλ6171,6731 emission-line doublet which is sensitive to electron densities in the range 100-$10^5\,\mathrm{cm^{-3}}$ (Osterbrock 1989). We used a stack of the rest-frame optical spectra of the high-redshift ULIRGs from Swinbank et al. (2004) to derive a flux ratio of $R_{[\mathrm{S\,II}]} = F_{\lambda6716}/F_{\lambda6731} = 1.1 \pm 0.3$. This is consistent with the HzRGs of Nesvadba et al. 2008 who find $R_{[\mathrm{S\,II}]}$=1.0–1.1, such that the implied densities of HzRGs and high-redshift ULIRGs are similar. We therefore use the same value of $n_{0.5} = 1$ as in Nesvadba et al. (2008). Although we have no direct way of measuring $n_{0.5}$ this unknown will only vary our order-of-magnitude estimates of the energy injection rates by a factor of a few.

velocity give energy injection rates that are consistent within a factor of a few. We establish that the spatially extended outflows in these high-redshift ULIRGs are potentially injecting energy into their host galaxies at considerable rates of $\approx(0.08–3)\times10^{45}$ erg s^{-1}, where the range indicates the values for different sources. Over a typical AGN lifetime of 30 Myr (e.g., Hopkins et al. 2005b) the total energy injection would be of order $\approx(0.8–28)\times10^{59}$ ergs; however, we note that outflows could continue $\sim$10 times longer than the active time of the BH (King et al. 2011) which would increase this energy injection by another order of magnitude. These outflow energy injection rates are comparable to the typical binding energy of the host galaxies in these systems of $\approx10^{59}$ ergs (assuming a spheroid mass of $\approx10^{11}$ M$_\odot$, a velocity dispersion $\sigma\approx200$ km s^{-1} and $R_e = 4$ kpc; e.g., Binney & Tremaine 1987) and demonstrate that these outflows could unbind at least a fraction of the ISM from the host galaxies.

We next consider what could be powering the outflows based on energetic arguments. In Fig. 3.10 we compare the ratio of the outflow energy rates with the energy input rates from: (1) the radiative output of the AGN (i.e. the AGN bolometric luminosity; L_{AGN}) and (2) energy output from star formation ($\dot{E}_{SF}$). We calculate outflow energy injection rates using Equation 3.6.1, replacing v with FWHM/2 and r as half the spatial extent of the broad [O III] region (see Table 3.4; also see footnote 3). We have estimated the bolometric luminosity of the AGN using SED modelling (described in Section 3.4; values given in Table 3.2). We estimate the potential energy input from star-formation using the star formation rates from our SED modelling (Table 3.2) and assuming that the mechanical energy injection from supernovae and stellar winds would be at most $\approx7\times10^{41}(SFR/\mathrm{M}_\odot\,\mathrm{yr}^{-1})$erg s^{-1} (following Leitherer et al. 1999 and Veilleux et al. 2005).[5] We note that the assumptions made are highly idealistic, and we have not, for example, considered the case of a momentum conserving outflow. However, Nesvadba et al. (2006, 2008) follow several methods to estimate the energy injection in similar outflows in HzRGs and find that the different methods generally agree on the order of magnitude level (also see Veilleux et al. 2005 for further discussion on the energetics of outflows and

[5] If we were to follow instead Dalla Vecchia & Schaye (2008) to estimate this energy input, the values would be a factor of $\approx$2 lower. Conversely, radiation pressure from star-formation could potentially contribute a comparable amount of pressure to stellar and supernovae winds in ULIRGs (Veilleux et al. 2005). As we are considering order of magnitude estimates only, these uncertainties do not affect our conclusions.

the potential energy input from star formation and AGN activity).

Fig. 3.10 demonstrates that the radiative output of the AGN is energetically viable as the dominant power source of the outflows observed in all of these sources. Assuming the bolometric luminosity provides an estimate of the initial energy input from the AGN, so long as ≈0.2–5% of this energy can couple to the ISM, the radiative power of the AGN in these systems is large enough to drive the observed outflows. This range of coupling efficiencies is similar to the values required by many models to reproduce the properties of local massive galaxies (e.g., Springel et al. 2005; Di Matteo et al. 2005; Debuhr et al. 2012). In contrast, the required coupling efficiencies for star formation are an order of magnitude higher (≈15% to ≫100%). For the three sources with implied coupling efficiencies of ≈15–50% star formation may play a significant role; however, based on the observed properties of the broad [O III] emission presented earlier (see Section 3.6.1), and the energetic arguments presented here, we tentatively suggest that the AGN may play a dominant role in powering the outflows. Given the current quality of the available data, a more detailed analysis is not yet warranted and the values of input energetics should be used with care.

The potential fate of the outflowing gas

Based on energetic arguments we have already demonstrated that the outflows we observe are likely to unbind the gas from the host galaxies. However, many models of galaxy formation require powerful AGN-driven outflows to remove the gas completely from the host galaxy potentials to efficiently truncate star formation and remove the fuel for future accretion onto the BHs (e.g., Di Matteo et al. 2005; Hopkins et al. 2008). Will the outflowing gas we observe be able to escape the host galaxy and consequently remove the gas supply for further star formation and future accretion? In Fig. 3.11 we plot the broad [O III] velocity offset against FWHM for our spatially resolved sources and also plot other high-redshift AGN with available IFU data from the literature. By taking an estimated galaxy mass of $10^{11}\,M_{\odot}$ (typical of these sources; e.g., Engel et al. 2010; Wardlow et al. 2011; Hainline et al. 2011) the escape velocity at a distance of 4 kpc would be $v_{\rm esc} \approx 460\,{\rm km\,s^{-1}}$ (see Fig. 3.11). Considering the observed velocity offsets ($\Delta v = 50$–$850\,{\rm km\,s^{-1}}$), only the outflows in two sources (SMM J1636+4057 and SMM J0217−0503) appear likely to

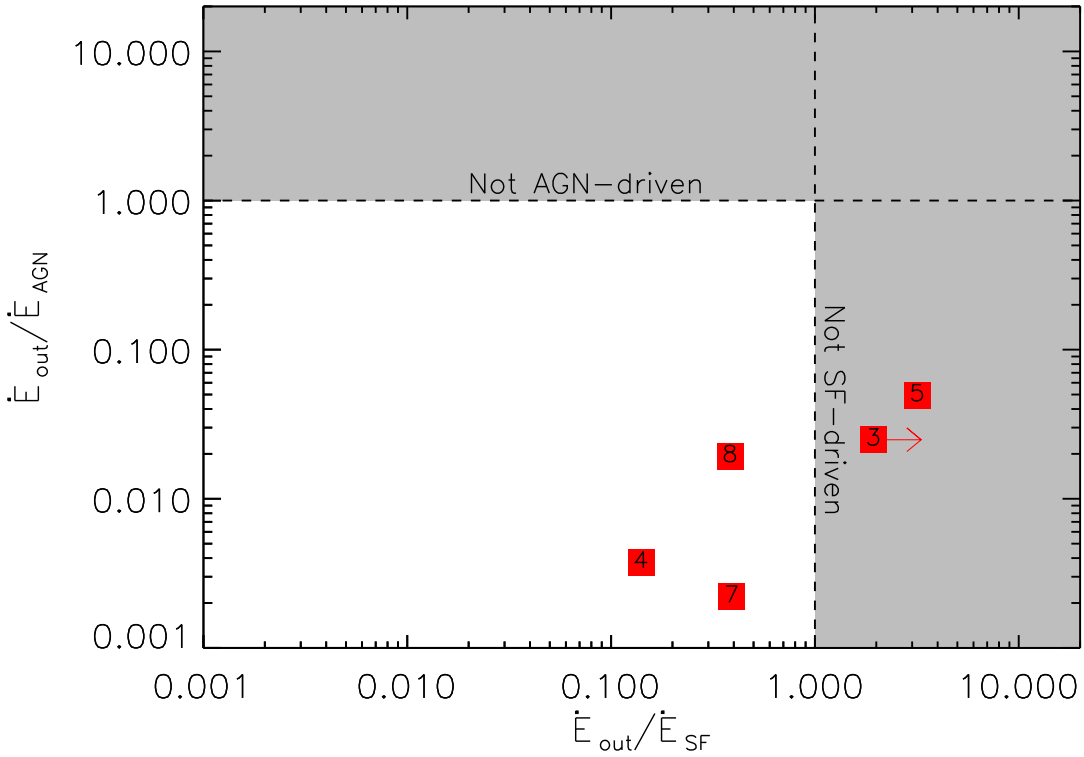

Figure 3.10: The ratio of the estimated outflow energy rate ($\dot{E}_{\rm out}$) to the derived input energy rate from AGN ($\dot{E}_{\rm AGN}$) against the ratio of the outflow energy rate to the predicted energy input rate from star formation ($\dot{E}_{\rm SF}$) for five of the six sources with spatially resolved [O III] emission. For the sixth source we only have upper limits for both $\dot{E}_{\rm AGN}$ and $\dot{E}_{\rm out}$ and therefore have no constraints on the ratio of these quantities. The numbers inside the symbols correspond to the source IDs. We note that we lack strong evidence for extended outflows for the source with ID 4 (see Section 3.6.1.) The shaded regions indicate where a >100% coupling efficiency is required between the input energy and the gas to power the outflows, effectively ruling out such an input energy mechanism. The bolometric luminosity of the AGN appears to be energetically favourable to power all the outflows requiring only ≈0.2–5% of the bolometric output to couple to the gas; however, star formation cannot be ruled out in all cases. It should be noted that the values used rely heavily on assumptions and should be taken as illustrative only. Details of the derived values that are plotted are provided in Section 3.6.2 (also see Table 3.2).

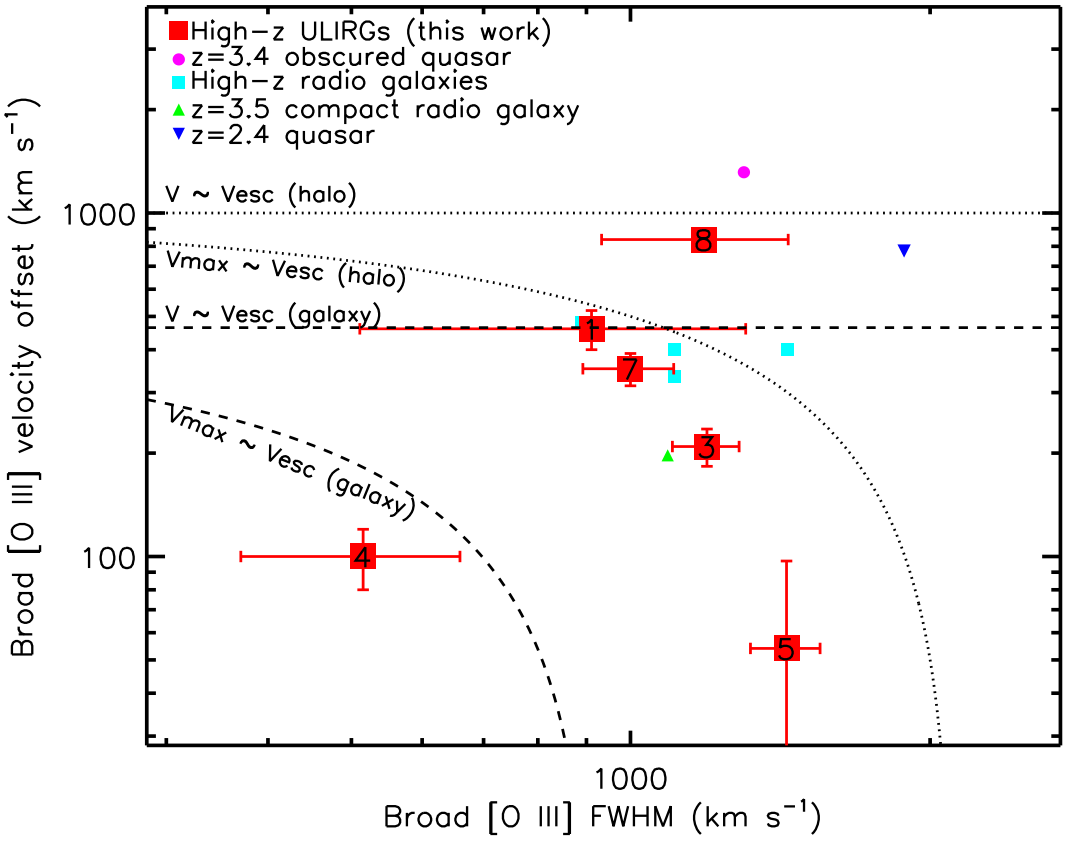

Figure 3.11: Broad [O III] emission-line velocity offset versus FWHM for the spatially resolved sources in our sample (values taken from regions of broad [O III]; see Table 3.4). Also shown are other high-redshift sources with IFU data as described in Fig. 3.1. The maximum velocities ($v_{\rm max} = |v| + \frac{1}{2}$FWHM) of the gas are potentially high enough to exceed the typical escape velocity of a typical massive galaxy (10^{11} M$_\odot$ at 4 kpc; dashed curve). However, using simplistic arguments (see Section 3.6.2) only one of our sources has a maximum outflow velocity that could potentially unbind some of the gas from a typical galaxy halo ($\approx 10^{13}$ M$_\odot$ at $\approx$4 kpc; dotted curve).

exceed this escape velocity. However, if we instead consider the the *maximum* velocities of the emission-line gas ($v_{\rm max} \approx 400$–$1400\,{\rm km\,s^{-1}}$; defined as $v_{\rm max} = |v|$+FWHM/2; i.e., Rupke et al. 2005a,b) then the outflow velocities are found to exceed the escape velocity (see dashed curve in Fig. 3.11) in all sources except RG J0332−2732, suggesting that some fraction of the gas is able to escape the host galaxy potential.

Unless the gas is completely removed from the host galaxy potential, or is unable to cool on short timescales, significant star formation and BH accretion may be able to recommence after the outflow episode. We therefore consider a simplified approach to investigate if the outflowing gas will be able to escape the dark-matter halo. Assuming a static dark matter halo with a mass of $\approx 10^{13}\,{\rm M_{\odot}}$ (expected for these sources; Hickox et al. 2012), a Navarro Frenk and White (NFW; Navarro et al. 1996) density profile, and a point mass of $\approx 10^{11}\,{\rm M_{\odot}}$ (i.e., the host galaxy), a particle initially at $\approx 4\,{\rm kpc}$ from the centre of the host galaxy would need to be travelling at $v \approx 1000\,{\rm km\,s^{-1}}$ to escape beyond the virial radius of the halo ($\approx 440\,{\rm kpc}$; M. Lovell priv. comm.; see Fig. 3.11). On the basis of this simple model, where we assume the effects of gravity only, particles travelling at $\approx$400-$800\,{\rm km\,s^{-1}}$ at $\approx 4\,{\rm kpc}$ will return to the host galaxy within a few hundred Myrs. From this analysis only one sources has a maximum outflow velocity that could potentially unbind some fraction of the gas from the dark matter halo (Fig. 3.11), which suggests that the gas in the majority of the systems may eventually cool and re-ignite another episode of AGN activity and star formation. However, it has been proposed that *quasar mode* outflows, such as those observed here, may be an effective way of expelling the gas at early times prior to a mechanical-heating dominated phase (i.e., the so-called *radio mode*), which will then efficiently prevent the gas from cooling (e.g., van de Voort et al. 2011; McCarthy et al. 2011). The outflows we observe could be a means of energetically pre-heating and ejecting gas at high redshift and therefore could be a crucial stage in the evolution of massive galaxies. In this scenario these galaxies will therefore be the progenitors of the radiatively weak, low-redshift AGN in massive galaxies which are observed to have mechanical heating that is preventing gas from cooling (Best et al. 2005, 2006; Smolčić et al. 2009; Danielson et al. 2012).

3.7 Conclusions

We have taken Gemini North/NIFS and VLT/SINFONI IFU observations around the emission-line doublet [O III]λ4959, 5007 of eight high-redshift ULIRGs that host AGN activity. Our aim was to search for broad, high-velocity and spatially extended [O III] emission as a tracer of powerful AGN-driven outflows over galaxy-wide scales that are predicted by the *quasar-mode* in galaxy evolution models. We have strong evidence that such outflows exist in at least a fraction of the high-redshift ULIRGs. Our main conclusions are the following:

1. We find narrow [O III] emission lines (FWHM≈ few hundred $\mathrm{km\,s^{-1}}$) extended over galaxy-wide scales (up to ≈20 kpc). By comparing these observations with high-redshift ULIRGs, that are also undergoing intense starbursts and mergers but do not host significant AGN activity, we show that the narrow [O III] emission lines we observe (FWHM up to a few $100\,\mathrm{km\,s^{-1}}$) are consistent with tracing host galaxy dynamics and merger remnants (Section 3.6.1).

2. In the four most luminous sources we find extremely broad [O III]λλ4959,5007 emission (FWHM≈ 700–1400 $\mathrm{km\,s^{-1}}$) with high velocity-offsets (up to ≈850 $\mathrm{km\,s^{-1}}$), extended over ≈4–15 kpc; i.e., the key signatures of galaxy-scale energetic outflows (Section 3.6.1). The other four sources exhibit broad [O III] emission but we have limited constraints on the spatial extent of the broad [O III] emission due to lower quality data.

3. We apply a simple outflow model to show that the spatially extended outflows are potentially moving through the ISM with an energy rate of $\approx(0.08\text{–}3)\times10^{45}\,\mathrm{erg\,s^{-1}}$, sufficient to unbind some of the gas from the host galaxy, and potentially disrupting future accretion and star-formation in the host galaxy (Section 3.6.2). These order of magnitude estimates are model dependent and rely on estimates of the density and therefore should be considered as illustrative only.

4. By estimating the energy injection rates from the AGN- and star formation driven-winds we find that the outflows require ≈0.2–5% of the AGN luminosity to couple to the gas, while star formation require coupling efficiencies of 15%–≫100%

(Section 3.6.2). We use a combination of energetic arguments and comparison to non-AGN systems to show that, although star formation may also play a significant role in some sources, the AGN activity is feasibly the dominant power source for driving the outflows in all sources.

5. The high maximum outflow velocities observed in these galaxies suggest that at least some fraction of the gas will be unbound from the host galaxies, but significant fractions of gas are very unlikely to be completely unbound from the galaxy haloes (Section 3.6.2).

The galaxies observed here are two to three orders of magnitude more common than the extreme high-redshift radio galaxies that are often associated with powerful AGN large-scale outflows at high redshift. We have shown that energetic large-scale outflows are present in at least a fraction of high-redshift ULIRGs that host AGN activity, which are believed to be the progenitors of today's massive elliptical galaxies. We have suggested that these outflows may be a crucial phase in the evolution of massive galaxies.

TARGET SED DATA AND DERIVED PROPERTIES

ID	Source	S_8 (μJy)	S_{24} (mJy)	S_{70} (mJy)	S_{250} (mJy)	S_{350} (mJy)	S_{500} (mJy)	S_{850} (mJy)	$L_{\rm IR,SF}$ (10^{12}L$_\odot$)	SFR (M$_\odot$ yr^{-1})	$L_{\rm AGN,SED}$ (10^{46} erg s^{-1})
(1)	(2)	(3)	(4)	(5)	(6)	(7)	(8)	(9)	(10)	(11)	(12)
1	SMM J0217–0503	44.7±2.3	0.49±0.05	-	36.3±5.8	33.9±6.3	21.7±6.8	4.4±1.7	4.5±0.8	780±160	<0.2
2	SMM J0302+0006	63.4±6.8	0.45±0.05	<13.6	-	-	-	4.4±1.3	2.0±0.3	340±50	0.14±0.09
3	RG J0302+0010	-	<0.24	-	-	-	-	<4.5	<2.1‡	<360	2.0±0.2**
4	RG J0332–2732	7.8±0.2	0.94±0.09	-	27.5±5.8	27.5±6.3	20.3±6.8	<3.6	4.9±0.9	850±120	2.2±0.4
5	SMM J0943+4700*	-	0.57±0.06	-	22.6±5.8	26.5±6.3	17.3±6.8	8.7±1.5	7.5±1.5	1300±200	5.8±0.2
6	SMM J1235+6215	64.1±22	0.63±0.06	<4.1	30.4±5.8	37.4±6.3	27.0±6.8	8.3±2.5	6.9±1.0	1200±170	0.7±0.4
7	SMM J1237+6203	(1.02±0.09)†	(1.61±0.7)†	<6.0	<14	<24	<24	5.3±1.7	2.4±0.2	430±50	5.33±0.05
8	SMM J1636+4057	66.8±6.8	0.95±0.1	<9.1	44.4±5.8	36.6±6.3	29.0±6.8	8.2±1.7	7.9±1.5	1400±200	1.9±0.6

Table 3.2: NOTES: Column (1): Source ID. Column (2): Source name. Column (3): 8μm flux densities and their uncertainties taken from: Hainline et al. (2009); Cardamone et al. (2010); or the Spitzer archive. Column (4): 24μm flux densities from: Ivison et al. (2007); Valiante et al. (2007); Menéndez-Delmestre et al. (2009); Dickinson et al. in prep; or the Spitzer archive. Uncertainties are assumed to be 10% of the measured values. Column (5): 70μm flux densities taken from Hainline et al. (2009). Columns (6)–(8): The 250μm, 350μm and 500μm flux densities. This HerMES data was accessed through the HeDaM database (http://hedam.oamp.fr) operated by CeSAM and hosted by the Laboratoire d'Astrophysique de Marseille. The uncertainties quoted are the confusion noise for each band. Column (9): 850μm flux densities and their uncertainties taken from: Cowie et al. (2002); Chapman et al. (2004); Chapman et al. (2005); Clements et al. (2008). Column (10): Derived IR luminosities (8–1000 μm) from the star formation component of the SED fitting procedures described in Section 3.4. Column (11): Star formation rates derived using the quoted $L_{\rm IR,SF}$ values and the relationship from Kennicutt (1998). Column (12): The estimated AGN bolometric luminosity calculated using the methods outlined in Section 3.4. ‡The value quoted is calculated using the radio-infrared correlation (assuming a $q = 2.1$). This is an upper limit as there will be an unknown AGN contribution to the radio flux. **This AGN bolometric luminosity is derived from the [O III] luminosity (see Section 3.4). * For SMM J0943+4700 the flux densities have been corrected for an amplification factor of 1.2. We note that the quoted flux densities will cover both radio counterparts to this source (see Section 3.8). †These are the 12μm and 22μm flux densities taken from the *Wide-field Infrared Survey Explorer* archive (Wright et al. 2010).

GALAXY-INTEGRATED [O III]λ5007 EMISSION-LINE PROPERTIES

		Component A.			Component B				
ID	Source	$z_{[OIII],A}$	FWHM$_A$ ($km\,s^{-1}$)	Flux$_A$ ($10^{-16}\,erg\,s^{-1}\,cm^{-2}$)	$z_{[OIII],B}$	FWHM$_B$ ($km\,s^{-1}$)	Flux$_B$ ($10^{-16}\,erg\,s^{-1}\,cm^{-2}$)	Δv ($km\,s^{-1}$)	Total [O III] Luminosity ($10^{42}\,erg\,s^{-1}$)
(1)	(2)	(3)	(4)	(5)	(6)	(7)	(8)	(9)	(10)
1	SMM J0217–0503	2.0213[6]	540±170	3.1±0.7	-	-	-	-	9.3
2	SMM J0302+0006	1.4049[10]	900±300	1.3±0.4	-	-	-	-	1.6
3	RG J0302+0010	2.23861[12]	200±40	0.87±0.17	2.2419[7]	1100±120	2.7±0.4	+300±60	13.9
4	RG J0332–2732	2.3145[5]	480±140	2.3±0.5	-	-	-	-	9.9
5	SMM J0943+4700⋆	3.3506[4]	430±110	1.1±0.5	3.3503[8]	1300±200	2.6±0.4	+20±60	38.4
6	SMM J1235+6215	2.199[2]	1500±500	1.2±0.4	-	-	-	-	4.5
7	SMM J1237+6203	2.07502[3]	234±10	4.1±0.2	2.0714[4]	1000±100	2.9±0.3	−350±40	22.5
8	SMM J1636+4057	2.38500[12]	240±30	1.3±0.3	2.3817[18]	900±200	1.0±0.4	−290±160	16.8
					2.4003[10]	1100±180	1.4±0.2	+1350±90	

Table 3.3: NOTES: The properties of the galaxy-integrated [O III] emission-line profiles shown in Fig. 3.3. Numbers in square brackets give the uncertainty in the last decimal place. Column (1): Source ID. Column (2): Source name. Columns (3)–(5): Properties of the narrowest Gaussian components (Component A): redshift, FWHM and flux respectively. Columns (6)–(8): Same as the previous three columns but for the broader Gaussian components (Component B). Column (9): The velocity offset between the two Gaussian components. Column (10): The total [O III] luminosity. The bottom line of the table gives the properties of the third Gaussian component which is fit to the profile of SMM J1636+4057. Flux and luminosity values are not extinction corrected. The quoted uncertainties are from the parameters of the emission-line fits. The true uncertainties on the fluxes are a factor or ≈2–3 higher, due to uncertainties in the absolute flux calibration. ⋆The flux values for SMM J0943+4700 have been corrected for an amplification factor of 1.2.

SPATIALLY INTEGRATED EMISSION-LINE PROPERTIES

		[O III] Component A.			[O III] Component B				Hβ				
ID (1)	Region (3)	$z_{[OIII],A}$ (4)	$FWHM_A$ (5)	$Flux_A$ (6)	$z_{[OIII],B}$ (7)	$FWHM_B$ (8)	$Flux_B$ (9)	Δv (10)	$z_{H\beta}$ (11)	$FWHM_{H\beta}$ (12)	$Flux_{H\beta}$ (13)	log([O III]/Hβ) (14)	Linear Extent (15)
1	BR	2.0229[11]	900±400	0.42±0.15	-	-	-	−460±60†	-	-	<0.31	>0.13	≤4
	NR	2.0209[2]	290±80	1.26±0.19	-	-	-	-	-	-	<0.34	>0.57	11±4
3	BR	2.23873[7]	180±20	0.53±0.06	2.2410[3]	1180±80	2.59±0.16	+210±30	2.2441[11]	780±170	0.34±0.10	0.97±0.13	8±3
	NR	2.23864[12]	200±30	0.17±0.02	-	-	-	-	-	-	<0.03	>0.73	6±3
4	BR	2.3143[4]	560±130	0.81±0.16	-	-	-	−100±20†	-	-	<0.20	>0.61	10±4
	NR	2.3147[4]	510±130	0.62±0.12	-	-	-	-	-	-	<0.19	>0.52	11±4
5⋆	BR	3.3511[4]	340±70	0.44±0.13	3.3503[5]	1400±100	2.41±0.17	−50±40	3.3500[7]	430±120	0.30±0.09	0.97±0.12	15±3
	NR	3.3493[2]	400±40	0.48±0.04	-	-	-	-	-	-	<0.07	>0.71	8±3
8	BR	2.3834[8]	1100±170	0.77±0.12	2.4023[7]	1220±160	1.07±0.14	+1670±100††	-	-	<0.11	>1.2	7±3
	NR	2.38481[7]	257±14	1.25±0.06	-	-	-	-	-	-	<0.11	>1.1	20±3

Table 3.4: NOTES: The properties of the [O III] and Hβ emission-line profiles extracted from the sub-regions shown in Fig. 3.5. Column (1): Source ID. Column (3): The spatial region from which the spectra are extracted, either the broad region (BR) or narrow region (NR); see Section 3.5.3. Columns (4)–(6): Properties of the narrowest [O III] Gaussian components (Component A): redshift, FWHM ($km\,s^{-1}$) and flux ($10^{-16}\,erg\,s^{-1}\,cm^{-2}$) respectively. Columns (7)–(9): Same as the previous three columns but for the broader [O III] Gaussian components (Component B). Column (10): The velocity offset ($km\,s^{-1}$) between the two Gaussian components. Columns (11)–(13): Properties of the Hβ emission lines: redshift, FWHM ($km\,s^{-1}$) and flux ($10^{-16}\,erg\,s^{-1}\,cm^{-2}$) respectively. Column (14): The logarithm of the ratio of the total [O III] and Hβ fluxes. Column (15): The approximate linear-extent, along the most extended axis, of the defined regions (kpc). We take the size of seeing disks as the uncertainty on these measurements. All flux limits are 3σ upper limits, which are calculated using the noise of the line-free continuum and the FWHM of the [O III] emission line from the same region. Flux values are not corrected for dust extinction. The quoted uncertainties are from the parameters of the emission-line fits. The true uncertainties on the fluxes will be a factor or ≈2–3 higher, due to uncertainties in the absolute flux calibration. ⋆The flux values for SMM J0943+4700 have been corrected for an amplification factor of 1.2. † These are the velocity offsets to the Hα emission in this region. †† For analysis purposes we define the velocity offset as half of this value, see Section 3.5.4 and Section 3.8 for details.

3.8 Notes on individual sources

Here we provide background notes on each source from our sample and provide some more details of our analysis on individual sources that is not required for the overall discussion given in the main text. The 1.4 GHz flux densities are provided in Table 3.1 and the infrared and sub-mm flux densities are provided in Table 3.2. All of the parameters for the profile fits to the galaxy-integrated spectra (see Fig. 3.3) and spectra extracted from different regions (see Fig. 3.5) are provided in Table 3.3 and Table 3.4 respectively.

SMM J0217-0503

This source was first identified as a sub-mm and radio source by Coppin et al. (2006) and Simpson et al. (2006) respectively. IFU emission around the Hα emission line reveal at least two merging components (Alaghband-Zadeh et al. 2012) over ≈20–25 kpc. Our IFU observations of the [O III] emission line also reveal at least two systems separated by ≈3″ (≈25 kpc; see Fig. 3.4). The northern system has broad Hα emission in the central regions (FWHM≈940 km s^{-1}; Alaghband-Zadeh et al. priv. comm.) and a high [N III]/Hα ≈1.1–1.3 ratio (Alaghband-Zadeh priv. comm). Along with our measured ratio [O III]/Hβ >1.3 this suggests that this source is most likely hosting AGN activity (e.g. Kewley et al. 2006). In Fig. 3.5 we show that the [O III] kinematics in this northern component also displays the signatures of an outflow; i.e. a broad emission line (FWHM=900±400 km s^{-1}) which has a high velocity offset from the Hα emission ($\Delta v = -460 \pm 60$ km s^{-1}; Fig. 3.6). Due to the complexity of blending between the [N II] doublet and Hα line, it is not possible to confirm if this outflowing component is also present in the Hα emission-line profile. The broad [O III] emission in this northern component is spatially unresolved (≤ 4.0 kpc) and has a modest signal-to-noise ratio such that we do not have strong evidence for a galaxy-wide outflow in this source.

The southern system has Hα emission extended over ≈10 kpc with kinematics which may be described by a rotating disk; however, the double peaked emission line and a large gradient in the [N II]/Hα ratio from east to west could also indicate that this southern system has undergone a recent merger (Alaghband-Zadeh et al. 2012). Our observations of the [O III] emission line displays a redshift, line-width and position that are only consis-

tent with the western ≈5 kpc of the Hα emission, with no [O III] detected in the eastern side. The [O III] emission is located where the [N II]/Hα ratio is lowest, suggesting a different chemical composition across the galaxy, as opposed to excitation effects (e.g., Kewley et al. 2006). These observations are consistent with the scenario that this southern system may have undergone a recent merger.

SMM J0302+0006

This sub-mm source was first detected by Webb et al. (2003). Optical and near-IR spectra show a high
[N II]/Hα =1.38±0.07 line ratio, and *Spitzer* mid-infrared spectroscopic observations show an excess in the mid-infrared continuum suggesting AGN activity (Swinbank et al. 2004; Chapman et al. 2005; Menéndez-Delmestre et al. 2009). *HST* imaging and Hα IFU data show this source contains two components separated by ≈11 kpc (Swinbank et al. 2006; Menéndez-Delmestre et al. 2013).

The galaxy-integrated [O III] emission we observe is broad (FWHM=900±300 km s^{-1}; Fig. 3.3) but is spatially unresolved ($\leq$ 3.6 kpc). However, due to the low signal-to-noise ratio of the integrated spectrum we cannot rule out the existence of low surface brightness extended emission. No Hβ emission was detected in the galaxy-integrated spectrum, with a 3σ upper limit on the flux of $F_{\mathrm{H}\beta} < 8\times10^{-17}$ erg s^{-1} cm^{-2} (assuming the line-width is the same as that measured for [O III]).

RG J0302+0010

This source was first identified by Chapman et al. (2004). This source has rest-frame UV spectroscopy that reveals strong [C IV] emission, which along with the high
[N II]/Hα=1.13±0.4 line ratio implies AGN activity (Chapman et al. 2004; Swinbank et al. 2004). Observations with long-slit spectroscopy show that the [O III] emission is broad and has an asymmetric line profile (Takata et al. 2006).

The galaxy-integrated spectrum around the [O III]λλ4959,5007 emission-line doublet reveals both a narrow and broad redshifted component (Fig. 3.3). The broad component is located in the central ≈8 kpc, where the line ratio [O III]/Hβ=9±3 implies bright AGN

activity (Fig. 3.5). We confirmed that the broad emission line was spatially extended by integrating spectra in two $0.6'' \times 0.6''$ bins, one in the north of the emission-line region and one in the south. We fit these spectra following the methods outlined in Section 3.4 and found that the broad emission line has a velocity shear of $125\pm30\,\mathrm{km\,s^{-1}}$ which is broadly consistent with the velocity gradient observed in Fig. 3.6.

The broad [O III] emission line is most likely due to an outflow with the near-side of the outflow being obscured by dust (see Section 3.6.2 for a full discussion). Blueshifted broad components are more commonly associated with outflows (e.g., Heckman et al. 1981) as opposed to the redshifted broad component we observe here. However, redshifted broad components are observed in a fraction of local AGN and can be explained by the relative orientations of the AGN and obscuring material in host galaxy (e.g., Barth et al. 2008; Crenshaw et al. 2010). In particular IFU observations of the local interacting Seyfert galaxy LEDA 135736, identify a broad, redshifted outflow associated with AGN activity, which could be a low redshift analogue of this source (Gerssen et al. 2009).

RG J0332-2732

IFU observations of this source reveals that Hα is extended over ≈10 kpc with velocity offsets of $\Delta v \lesssim 200\,\mathrm{km\,s^{-1}}$ across the galaxy. The brightest region (Fig. 3.5; Table 3.4) has a high [O III]/Hβ >4.0 line ratio, which along with the high [N II]/Hα=0.8±0.1 line ratio (Alaghband-Zadeh et al. 2012) suggests AGN activity (e.g., Kewley et al. 2006).

The [O III] emission-line kinematics (Fig. 3.4; Fig. 3.6) appear to be tracing similar kinematics to the Hα emission line (Alaghband-Zadeh et al. 2012) with similar line widths (FWHM≈200-700 $\mathrm{km\,s^{-1}}$) and velocity gradients ($\Delta v \lesssim 200\,\mathrm{km\,s^{-1}}$). The [O III] emission is more extended to the north than the Hα emission and, along with the observation that the [N II]/Hα ratio is highest in the north (Alaghband-Zadeh et al. 2012), suggests the presence of an AGN.

Unlike the majority of our sample with spatially resolved data, we are unable to fit multiple components to the emission line profile and are unable to de-couple the signatures of an outflow from the galaxy dynamics. However, we note that the emission lines in the brightest regions display very large widths (FWHM up to $\approx 700\,\mathrm{km\,s^{-1}}$; Fig. 3.6), which are broader than the narrow lines we associate with galaxy dynamics in the other

sources ($\approx$100–500 km s^{-1}; Fig. 3.7). Although not as well defined as in the other sources, we speculate that an outflow could be responsible for these large line widths.

SMM J0943+4700

This sub-mm source was first identified by Cowie et al. (2002) and is modestly lensed (amplification of 1.2). Ledlow et al. (2002) identified two radio counterparts separated by $\approx$30 kpc in projection and labelled them as H6 and H7. The latter shows narrower and fainter [O III] emission than its companion but dominates the sub-mm and CO emission, indicating that the bulk of star formation is occurring in this component (Takata et al. 2006; Valiante et al. 2007; Engel et al. 2010; Riechers et al. 2011). An excess in the mid-infrared continuum observed in *Spitzer* mid-infrared spectroscopy indicate the presence of AGN activity in this source (Valiante et al. 2007) although both H6 and H7 are covered by this spectra. H6, the source observed in our observations, has rest-frame UV emission-line widths, and line ratios indicative of a narrow-line Seyfert 1 galaxy (Ledlow et al. 2002). Additionally long-slit near-IR spectroscopy of H6 reveals [O III] emission that is broad and extended over $\approx 3''$–$4''$ (Takata et al. 2006), indicative of an outflow.

Using our IFU observations we find that the [O III] emission from this source is very extended ($\approx$20 kpc) with a complex morphology and kinematic structure (Fig. 3.4). The north-western region shows modest [O III] line-widths (FWHM=200–300 km s^{-1}) consistent with being due to galaxy dynamics and merger remnants (Fig. 3.7; see Section 3.6.1 for a discussion). In addition there is extremely broad [O III] emission (FWHM=1000–1400 km s^{-1}) extended over $\approx$15 kpc (Fig. 3.5 and Fig. 3.6), which we attribute to an energetic outflow. Despite observing modest velocity offsets between the narrow and broad [O III] emission lines ($\Delta v \leq$150 km s^{-1}; Fig. 3.6), there is clearly extremely turbulent ionised gas over a large extent. The zero velocity offset between the broad and narrow [O III] components in the spatially-integrated spectra (Fig. 3.3 and Fig. 3.5) could be explained if we are observing an outflow orientated in the plane of the sky.

SMM J1235+6215

This source was identified as a sub-mm bright galaxy by Chapman et al. (2005). Deep *Chandra* images show that it hosts a heavily obscured X-ray luminous AGN ($L_{0.5-8\mathrm{keV}}$=$10^{44.0}$ erg s^{-1}; N_{H}=10^{24} cm^{-2}; Alexander et al. 2005). An excess in the mid-infrared continuum observed in *Spitzer* mid-infrared spectroscopy further suggests the presence of AGN activity in this source (Menéndez-Delmestre et al. 2009). IFU observations reveal a bright compact ($\lesssim$3 kpc) source of broad Hα emission (FWHM $\gtrsim$1000 km s^{-1}) attributed to AGN activity and spatially offset ($\approx$0.5″) from the narrower Hα emission (FWHM $\approx$ 500–800 km s^{-1}), which is likely to be dominated by star-formation activity (Menéndez-Delmestre et al. 2013). Long-slit near-IR spectroscopy suggest that the [O III] emission is extended over $\approx$ 1″ ($\approx$8 kpc; Takata et al. 2006).

The galaxy-integrated spectrum around the [O III]$\lambda\lambda$4959,5007 emission-line doublet reveals an extremely broad emission line (FWHM=1500$\pm$500 km s^{-1}) which may suggest an outflow (Fig. 3.3). Takata et al. (2006) find that this source has extended [O III] emission over $\approx$1″. Although we find tentative evidence that the [O III] emission is marginally extended ($\approx$0.8″; 7 kpc) in our data we are unable to constrain the properties of the extended emission due to insufficient quality of data to fit the emission-line profiles.

We also detect Hβ emission, at a redshift of $z_{\mathrm{H}\beta}$=2.2031$\pm$0.0006, with a width of FWHM$_{\mathrm{H}\beta}$=500$\pm$200 km s^{-1} and flux $F_{\mathrm{H}\beta}$= 0.9$\pm$0.2$\times10^{-16}$ erg s^{-1} cm^{-2}, extended over $\approx$1″ ($\approx$8 kpc). The extremely broad [O III] emission we observe is offset from the Hβ emission $\Delta v \approx -400 \pm 200$ km s^{-1}. Although there is weak evidence for an extended outflow in this source, deeper observations are required to confirm this.

SMM J1237+6203

This source was identified as a sub-mm bright galaxy by Chapman et al. (2005). The bright optical counterpart ($R = 20.2$; Chapman et al. 2005), X-ray luminosity ($L_{0.5-8\mathrm{keV}} =$ $10^{44.3}$ erg s^{-1}; Alexander et al. 2005) and optical-near-IR spectroscopy that reveal broad emission lines (Lyα; N V; C IV; Hγ–Hα; FWHM $\approx$ 2100-2700 km s^{-1}; Chapman et al. 2005; Takata et al. 2006; Coppin et al. 2008), result in this source being classified as a broad-line quasar, with a virial BH mass of log(M_{BH})=8.2 M$_\odot$ (Alexander et al. 2008b).

IFU observations around redshifted [O III] of SMM J1237+6203 were first presented in Alexander et al. (2010), where a complete discussion of the source is provided. We note the orientation of this source in Alexander et al. (2010) is flipped in the east-west direction and the correct orientation is given in this work (Fig. 3.4). In addition we provide updated [O III] flux and luminosity measurements.

The galaxy-integrated spectrum around the [O III] emission line (Fig. 3.3) shows a bright narrow component with a prominent blue-wing. This type of profile is most commonly interpreted as being the result of an AGN-driven outflow (e.g., Heckman et al. 1981; Nesvadba et al. 2008). The velocity and FWHM profiles (Fig. 3.6) show that the narrow emission has a small velocity gradient of $\Delta v \approx 200\,\mathrm{km\,s^{-1}}$ across the galaxy and is likely to be tracing the host galaxy dynamics (also see Alexander et al. 2010). In contrast, the broad [O III] component (FWHM$\approx$1000 $\mathrm{km\,s^{-1}}$) is offset from the narrow component by $\approx -350\,\mathrm{km\,s^{-1}}$, over $\approx$5 kpc, providing strong evidence for an outflow in this region. Although the broad component is only formally fit over $\approx$5 kpc, low surface brightness broad emission exists up to $\approx$8 kpc in total extent (Alexander et al. 2010).

We also identify Hβ emission in the galaxy-integrated spectrum, with a redshift of z=2.0754[2] and flux $F_{\mathrm{H}\beta} = 1.1 \pm 0.4 \times 10^{-15}\,\mathrm{erg\,s^{-1}\,cm^{-2}}$. The width of the Hβ emission line (FWHM=2030$\pm$70 $\mathrm{km\,s^{-1}}$) indicates the presence of a broad-line region, which is consistent with that found from Hα observations of this source (Coppin et al. 2008).

SMM J1636+4057

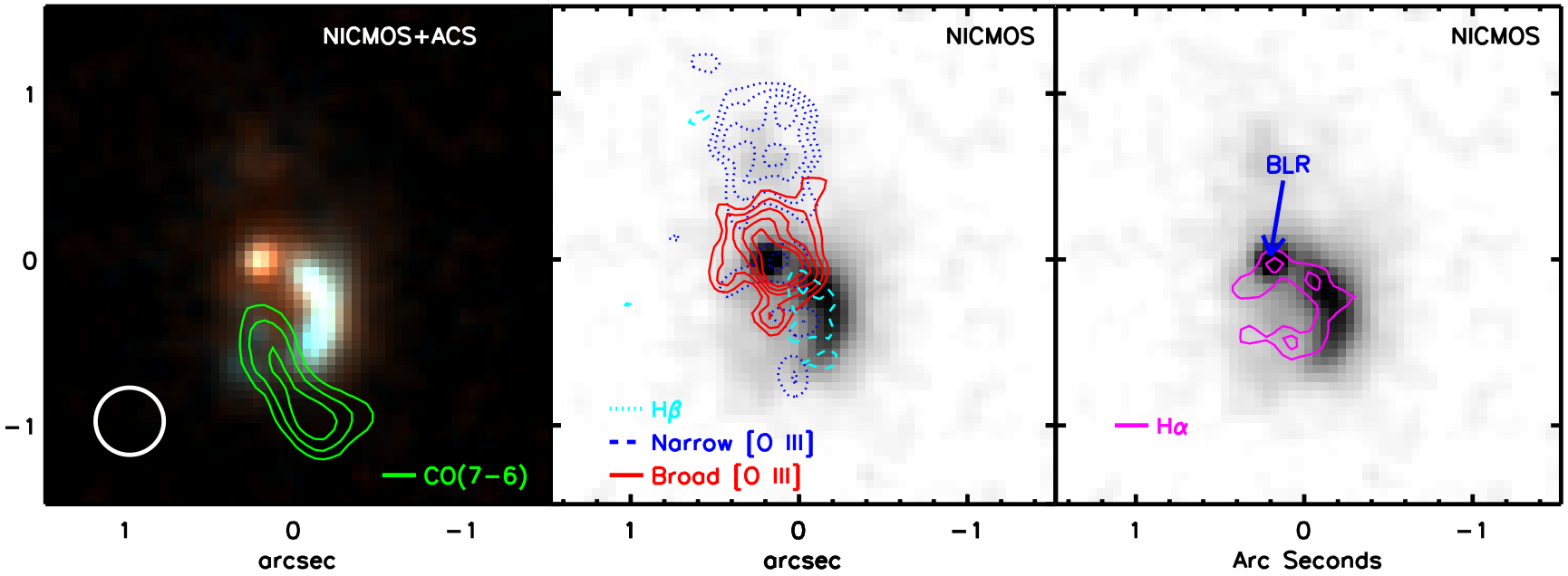

Figure 3.12: *Left:* True colour $I_{814}H_{160}$ image of SMM J1636+4057 from the *HST* ACS and NICMOS imaging (Swinbank et al. 2005). The contours denote the intensity of the velocity integrated CO(7–6) millimetre emission (Tacconi et al. 2008). The circle denotes the approximate seeing disk of our observations. *Middle: HST* NICMOS H_{160} grey-scale image with contours overlaid of narrow-band (wavelength collapsed) images from our IFU observations. The solid contours denote the extent/intensity of the broad [O III] emission, which is associated with the red continuum seen in the colour image. The dotted contours denote the extent/intensity of the narrow [O III] for which the majority is associated with faint emission observed to the north of the red continuum peak. The dashed contours denote the Hβ emission which is spatially coincident with the blue arc in the *HST* image. *Right:* The same image as in the central panel but with the contours from the IFU+adaptive optics Hα observations of Menéndez-Delmestre et al. (2013) overlaid. There is extremely broad (FWHM≈2700 km s^{-1}) unresolved Hα emission, attributed to an AGN broad line region (BLR) and narrower spatially extended emission along the blue arc, which is attributed to star formation. The field-of-view of these Hα observations did not cover the region of narrow [O III] emission seen in the north of the middle panel. North is up and east is left.

This sub-mm source was first identified by Scott et al. (2002) and Ivison et al. (2002). *Hubble Space Telescope* (*HST*) ACS and NICMOS observations reveal a complex galactic morphology with at least three merging or interacting components, covering ≈8–15 kpc in projection (Swinbank et al. 2005; see Fig. 3.12). An excess in the mid-infrared continuum observed in the *Spitzer* mid-infrared spectroscopy indicate the presence of AGN activity in this source (Menéndez-Delmestre et al. 2009). Long-slit and IFU near-IR spectroscopy reveal a broad-line AGN (broad, spatially unresolved Hα and Hβ emission with FWHM≈2000–3000 $\mathrm{km\,s^{-1}}$) and narrow Hα emission traces star-formation along the UV bright arc shown in the *HST* image (Fig. 3.12; Smail et al. 2003; Swinbank et al. 2005; Menéndez-Delmestre et al. 2013). The broad-line AGN is found at $\Delta v \approx 700\,\mathrm{km\,s^{-1}}$ from the narrow Hα emission, providing further evidence that this system is undergoing a merger. The presence of a molecular gas cloud in the southern regions of the system is shown through high and low excitation CO emission-line gas (Tacconi et al. 2008; Engel et al. 2010; Ivison et al. 2011). Previous long-slit observations show that the [O III] emission is kinematically complex and spatially extended (≈1–2″) with broad components (FWHM $\lesssim 2000\,\mathrm{km\,s^{-1}}$; Smail et al. 2003; Takata et al. 2006), providing initial evidence for an energetic outflow.

Our galaxy-integrated spectrum around the [O III]λλ4959,5007 emission-line doublet (Fig. 3.3) reveals a prominent narrow component and two broad components separated by $\Delta v = 1700 \pm 100\,\mathrm{km\,s^{-1}}$. We are confident that the broad redshifted emission line is also from [O III] as Smail et al. (2003) also identify [Ne V] and N V emission lines at approximately this velocity.

In Fig. 3.4 we show that the [O III] emission-line morphology, velocity field and FWHM map from our IFU observations. Narrow [O III] emission ($100 \lesssim$ FWHM $\lesssim 500$ $\mathrm{km\,s^{-1}}$) is extended over ≈1″ (≈8 kpc) to the north of the peak in surface brightness, associated with faint infrared emission in the *HST* image, and fainter narrow emission is observed ≈1″ to the south; this is consistent with the long-slit observations of Smail et al. (2003) (also see Fig. 3.12). The redshift of this narrow [O III] emission is consistent with the molecular gas and Hα arc and therefore is likely to be tracing merger remnants and galaxy dynamics (e.g., Fig. 3.6). We also detect faint Hβ emission that is spatially coincident with the star-forming arc (Fig. 3.12).

The two broad [O III] emission-line components (FWHM$\approx$1200 km s^{-1}) are spatially coincident with the broad Hα emission line (Fig. 3.5 and Fig. 3.12) and are moderately spatially extended ($\approx$0.8″; $\approx$7 kpc). We verified that the broad emission lines were intrinsically spatially extended by extracting spectra from two $0.6'' \times 0.6''$ bins; one in the north and one in the south of the observed broad [O III] region. We found that that the ratio of the two broad components changed from north to south. The redshifted broad component dominates in the north and the blueshifted broad component dominates in the south, which is also demonstrated in the velocity map of this source (Fig. 3.4). The broad [O III] components are offset from the broad Hα emission line by $\Delta v \approx \pm 850$km s^{-1} (Fig. 3.6; Swinbank et al. 2005), indicating that we are observing both sides of an outflow (e.g., Nesvadba et al. 2008). To verify that the broad Hα is due to a true broad-line region, as opposed to dynamics in the host galaxy, we attempted to re-fit the spectrum of Swinbank et al. (2005) with a narrow-line Gaussian component plus two additional Gaussian components with the same redshifts and line-widths of the broad [O III] emission lines (e.g., similar to the methods used by Cano-Díaz et al. 2012 and Mullaney et al. 2013). We found that this did not adequately describe the Hα emission-line profile and an additional broad component is still required (with FWHM$\approx$2700 km s^{-1} and $z = 2.393 \pm 0.005$; consistent with Swinbank et al. 2005) providing strong evidence of a true AGN broad-line region.

The outflow we observe is spatially coincident with the AGN in this source, and no outflow is observed in the region of unobscured star-formation (the UV bright arc). We conclude that the broad [O III] emission lines we see is likely to be due to a bi-polar AGN-driven outflow with $v \approx \pm 850$ km s^{-1}.

SMM J2217+0010

This source was first identified by Smail et al. (2004) and Chapman et al. (2005). An excess in the mid-infrared continuum observed in the *Spitzer* mid-infrared spectroscopy suggests the presence of AGN activity in this source (Menéndez-Delmestre et al. 2009). The results of Takata et al. (2006) suggest bright [O III] emission
($F_{[\mathrm{OIII}]} = 6.0 \times 10^{-16}$ erg s^{-1} cm^{-2}) and a high [O III]/Hβ $\approx$10 ratio further indicating AGN activity. However in our observations [O III]$\lambda\lambda$4959, 5007 emission was undetected. By spatially integrating over the extent of a seeing disk and assuming an emission line

with a FWHM of 500 km s^{-1}, we infer a 3σ upper limit on the [O III] flux (luminosity) of $F_{[OIII]} < 4.6 \times 10^{-17}$ erg s^{-1} cm^{-2} ($L_{[OIII]} < 2.6 \times 10^{42}$ erg s^{-1}). This upper limit is considerably lower than the value quoted in Takata et al. (2006). This may arise due to the presence of a strong sky-line at the observed wavelength of the [O III]λ5007 emission line in this source, potentially resulting in an excess measurement of the flux quoted in Takata et al. (2006).

SMM J2217+0017

This source was identified as a sub-mm bright galaxy by Tamura et al. (2009). We did not detect [O III]$\lambda\lambda$4959, 5007 emission. This source was detected in Hα emission in the same data cube (Alaghband-Zadeh et al. 2012), therefore the non-detection is due to an [O III] flux that is below our detection threshold and not because of an incorrect redshift. Assuming an emission line of a FWHM of 350 km s^{-1} (to match the Hα observations; Alaghband-Zadeh et al. 2012) and integrating over the spatial extent of the Hα emission, we infer a 3σ upper limit on the [O III] flux (luminosity) of $F_{[OIII]} < 2.6 \times 10^{-17}$ erg s^{-1} cm^{-2} ($L_{[O\ III]} < 1.0 \times 10^{42}$ erg s^{-1}).

CHAPTER 4

Kiloparsec scale outflows are prevalent in luminous AGN: outflows and feedback in the context of the overall AGN population

Abstract

We present integral field unit (IFU) observations covering the [O III]$\lambda\lambda$4959, 5007 and Hβ emission lines of sixteen $z < 0.2$ type 2 active galactic nuclei (AGN). Our targets are selected from a well-constrained parent sample of $\approx 24,000$ AGN so that we can place our observations into the context of the overall AGN population. Our targets are radio-quiet with star formation rates ($\lesssim$[10–100] $M_{\odot}\,yr^{-1}$) that are consistent with normal star-forming galaxies. We decouple the kinematics of galaxy dynamics and mergers from outflows. We find high-velocity ionised gas (velocity widths $\approx$ 600–1500 $km\,s^{-1}$; maximum velocities $\leq 1700\,km\,s^{-1}$) with observed spatial extents of $\gtrsim$(6–16) kpc in all targets and observe signatures of spherical outflows and bi-polar superbubbles. We show that our targets are representative of $z < 0.2$, luminous (i.e., $L_{[O\ III]} > 10^{41.7}\,erg\,s^{-1}$) type 2 AGN and that ionised outflows are not only common but also in $\geq$70% (3σ confidence) of cases, they are extended over kiloparsec scales. Our study demonstrates that galaxy-wide energetic outflows are not confined to extreme star-forming galaxies or radio-luminous AGN; however, there may be a higher incidence of the most extreme outflow velocities in quasars hosted in ultra-luminous infrared galaxies. Both star formation and AGN activity appear to be energetically viable to drive the outflows and we find no definitive evidence that favours one process over the other. Although uncertain, we derive mass outflow rates (typically $\approx$10$\times$ the SFRs), kinetic energies ($\approx$ 0.5–10% of L_{AGN}) and momentum rates (typically $\gtrsim$ [10–20] $\times\, L_{AGN}/c$) consistent with theoretical models that predict that AGN-driven outflows play a significant role in shaping the evolution of galaxies.

4.1 Motivation

In Section 1.6 of this thesis we described how galaxy-wide AGN-driven outflows are predicted to be an integral part of the evolution of massive galaxies. Whilst IFU observations have shown that galaxy-wide outflows exist in AGN and have characterised their properties, the targets selected for observations previous to this work had been drawn from small and/or inhomogeneous parent samples (see Section 1.6.2). Importantly, it is not known how representative these observations are of the overall AGN population. In this chapter we make use of a parent sample of $\approx 24,000$ $z < 0.4$ AGN with optical spectra to select sources for IFU observations. Therefore, these IFU observations can be placed into the overall AGN population. A general introduction to this research is presented in Section 1.6, whilst in this chapter we only give a short introduction that is specific to the observations presented here. The subsequent sections of this chapter (Section 4.3 onwards) have been published, as written here, in Harrison et al. (2014).

4.2 Introduction

A diagnostic that is commonly used to identify outflowing ionised gas is broad and asymmetric [O III]λ5007 emission-line profiles (see Section 1.6.2). Spectroscopic surveys, such as that performed by the SDSS, mean that a systematic search can be performed to measure the prevalence of these outflow features as a function of host galaxy and AGN properties. Mullaney et al. (2013) used the SDSS spectroscopic database to study the one-dimensional kinematic properties of [O III]λ5007 by performing multi-component fitting to the optical emission-line profiles of $\approx 24,000$, $z < 0.4$ optically selected AGN. They showed that $\approx 17\%$ of the AGN have emission-line profiles that indicate that their ionised gas kinematics are *dominated* by outflows and that a considerably larger fraction are likely to host ionised outflows at lower levels. The fraction of AGN with ionised gas kinematics dominated by outflows increases to $\gtrsim 40\%$ for the more radio-luminous AGN (i.e., those with $L_{1.4\mathrm{GHz}} > 10^{23}\,\mathrm{W\,Hz^{-1}}$); by contrast, when taking into account intrinsic correlations, the ionised outflow fraction shows little dependence on [O III] luminosity or Eddington ratio (Mullaney et al. 2013). In agreement with smaller studies (e.g., Heckman et al. 1981; Whittle 1985, 1992; Gelderman & Whittle 1994; Nelson & Whittle 1996;

Nesvadba et al. 2011; Kim et al. 2013; see also Greene & Ho 2005), this result shows that ionised outflows are most common in AGN that have moderate-to-high radio luminosities. However, while insightful, the origin of the radio emission is often unknown, particularly at moderate radio luminosities (i.e., $L_{1.4\mathrm{GHz}} \approx 10^{23}$–$10^{24}\,\mathrm{W\,Hz^{-1}}$) where AGN cores, radio jets, shocks and high-levels of star formation could all contribute (e.g., Del Moro et al. 2013; Condon et al. 2013; Zakamska & Greene 2014). It is therefore vital to measure star-formation rates (SFRs) and to investigate the origin of the radio emission in the sources that host these outflows to fully interpret these results.

In this chapter we are interested in measuring the prevalence, properties, and the potential impact of galaxy-wide energetic outflows. We present Gemini (South) Multi-Object Spectrograph (GMOS; Allington-Smith et al. 2002) IFU observations of sixteen $0.08 < z < 0.2$ type 2 AGN drawn from the parent sample of ≈24,000 AGN from Mullaney et al. (2013). Using this parent sample we can place our IFU observations into the context of the overall AGN population. So that we can fully interpret our results we perform SED fitting and analyse the available radio data to measure SFRs, AGN luminosities and to search for evidence of radio jets in all of our targets. In Section 4.3, we give details of the IFU observations, data reduction and SED fitting. In Section 4.4 we provide details of our analyses of the ionised gas kinematics and in Section 4.5 we present our results. In Section 4.6 we discuss our results and their implication for understanding galaxy evolution and in Section 4.7 we give our conclusions. We provide background information and a discussion of the results on individual sources in Section 4.8. We have adopted $H_0 = 71\,\mathrm{km\,s^{-1}\,Mpc^{-1}}$, $\Omega_\mathrm{M} = 0.27$ and $\Omega_\Lambda = 0.73$ throughout; in this cosmology, $1''$ corresponds to ≈ 1.5–$3.3\,\mathrm{kpc}$ for the redshift range of our sample ($z = 0.08$–0.2).

4.3 Targets, observations and data reduction

4.3.1 Target selection

We are interested in studying the spatially resolved ionised gas kinematics in luminous AGN, with the aim of understanding the prevalence and properties of galaxy-wide ionised outflows. For this study, we selected sixteen $z < 0.2$ type 2 AGN from the parent catalogue of Mullaney et al. (2013) to observe with the Gemini-GMOS (South) IFU. We describe

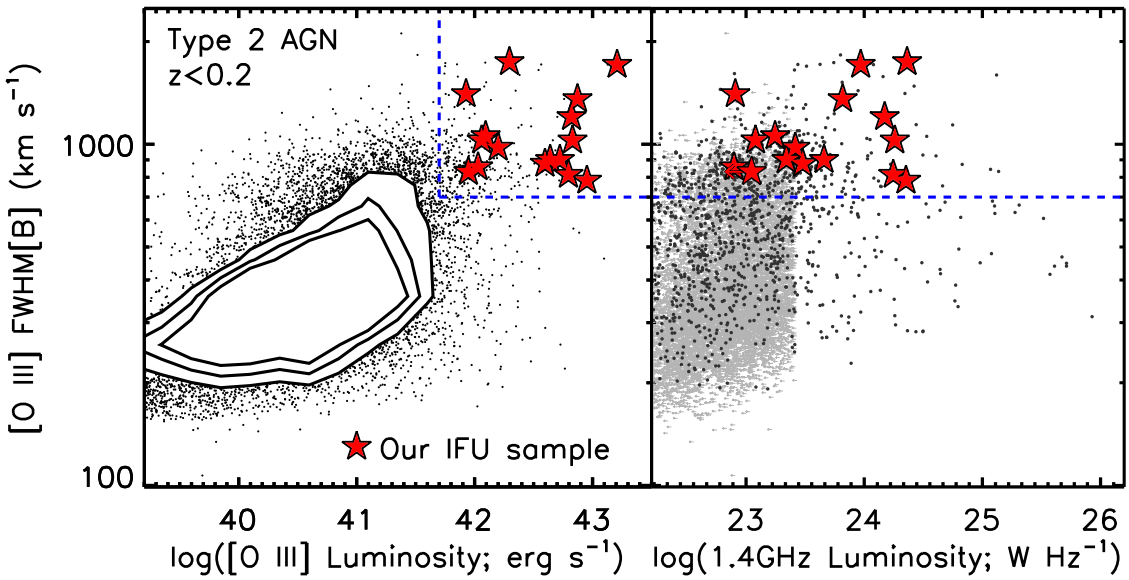

Figure 4.1: *Left:* The FWHM of the broadest, luminous (contributes at least 30% of the total flux; FWHM[B]) [O III] emission-line component versus total [O III] luminosity for our IFU targets (red stars) compared to the overall population of $z < 0.2$ type 2 AGN (black data points and contours; Mullaney et al. 2013). The dashed lines show the selection criteria used to select the luminous AGN ($L_{[\mathrm{O\ III}]} > 5 \times 10^{41}$ erg s^{-1}) with the spectral signatures of ionised outflows ([O III] FWHM[B] > 700 km s^{-1}). *Right:* FWHM[B] versus 1.4 GHz luminosity; the symbols are the same as in the left panel (with the addition of upper limits plotted in grey).

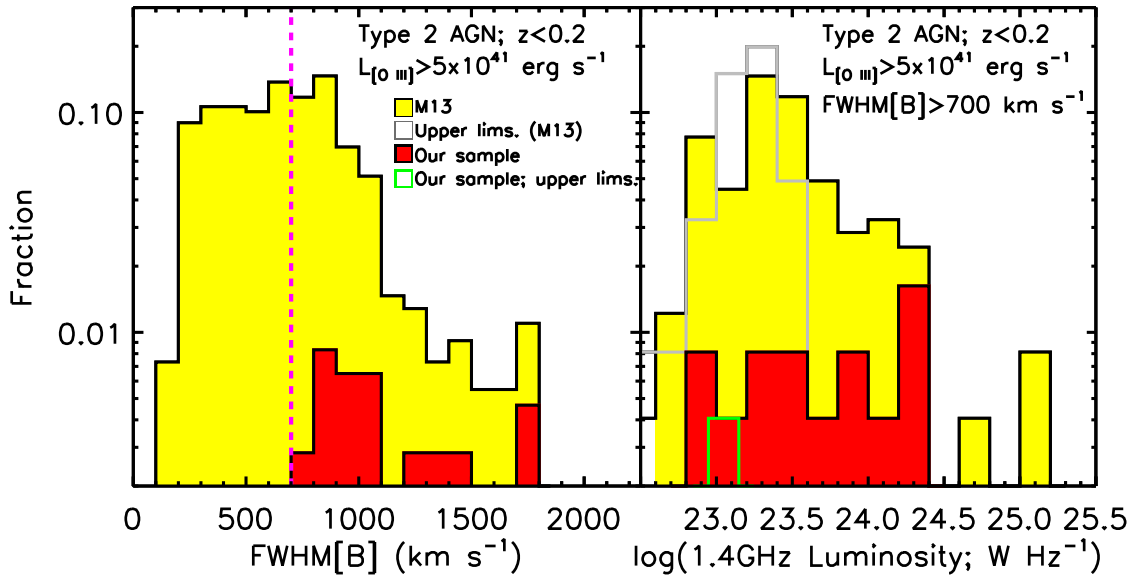

Figure 4.2: Histograms demonstrating how representative our IFU targets are of the overall luminous ($L_{[\mathrm{O\ III}]} > 5 \times 10^{41}\,\mathrm{erg\,s^{-1}}$) type 2 AGN population in the redshift range $z < 0.2$. *Left:* Histogram of the FWHM of the broadest, luminous [O III] component (FWHM[B]; see Fig. 4.1) from Mullaney et al. (2013; M13). The filled red histogram represents the sources selected for this work and yellow represents the parent sample. The vertical dashed line shows our selection criteria of FWHM[B] $> 700\,\mathrm{km\,s^{-1}}$. *Right:* Histogram of radio luminosity for the sources with FWHM[B] $> 700\,\mathrm{km\,s^{-1}}$ from the parent sample (yellow; Mullaney et al. 2013) and our IFU targets (red; Table 4.2). The grey and green empty histograms represent the sources with upper-limits from the parent sample and our IFU targets, respectively. Our targets are selected from the 45±3% of luminous type 2 AGN in this redshift range have luminous broad [O III] emission-line components and their radio luminosities are representative of the parent population (see Section 4.3.1).

TARGETS

Name (1)	RA (J2000) (2)	Dec (J2000) (3)	Run (4)	z_{sys} (5)	FWHM[B] (6)
J0945+1737	09:45:21.33	+17:37:53.2	10	0.1283	1027
J0958+1439	09:58:16.88	+14:39:23.7	10	0.1092	878
J1000+1242	10:00:13.14	+12:42:26.2	10	0.1480	815
J1010+1413	10:10:22.95	+14:13:00.9	10	0.1992	1711
J1010+0612	10:10:43.36	+06:12:01.4	10	0.0984	1743
J1100+0846	11:00:12.38	+08:46:16.3	10	0.1005	1203
J1125+1239	11:25:46.35	+12:39:22.6	12	0.1669	1028
J1130+1301	11:30:28.86	+13:01:19.6	12	0.1353	857
J1216+1417	12:16:22.73	+14:17:53.0	12	0.0818	1404
J1316+1753	13:16:42.90	+17:53:32.5	10	0.1505	1357
J1338+1503	13:38:06.53	+15:03:56.1	12	0.1857	901
J1339+1425	13:39:56.48	+14:25:29.6	12	0.1390	830
J1355+1300	13:55:45.66	+13:00:51.0	12	0.1519	1058
J1356+1026	13:56:46.10	+10:26:09.0	10	0.1238	783
J1430+1339	14:30:29.88	+13:39:12.0	10	0.0855	901
J1504+0151	15:04:20.90	+01:51:59.4	12	0.1827	978

Table 4.1: NOTES:
Details of the targets that we observed with the Gemini-GMOS IFU. (1) Object name; (2)–(3) optical RA and DEC positions from SDSS (DR7); (4) the Gemini-GMOS run when we observed this object (see Section 4.3.2); (5) systemic redshifts derived from this work (see Section 4.4.2); (6) FWHM (in $\mathrm{km\,s^{-1}}$) of the broadest, luminous (contributes at least 30% of the total flux) [O III]λ5007 emission-line component from Mullaney et al. (2013).

our selection criteria below (also illustrated in Figure 4.1) and we provide a list of the targets, along with their positions and redshifts, in Table 4.1.

Our parent catalogue (Mullaney et al. 2013) contains fits to the emission-line profiles of 24 264, $z < 0.4$, optical AGN (identified using a combination of "BPT" diagnostics, Baldwin et al. 1981, and emission-line widths) from the SDSS data release Data Release 7 (DR7; Abazajian et al. 2009). Mullaney et al. (2013) decompose the [O III]λ5007 emission-line profiles into two components ("narrow" and "broad") to identify emission-line profiles that are broad and asymmetric, indicative of outflow kinematics. A primary aim of this work is to establish if the broad and asymmetric emission-line features observed in one-dimensional spectra are spatially extended, and we therefore selected sources that have a luminous broad [O III]λ5007 emission-line component. Our definition of a luminous broad component is one that contributes at least 30% of the total flux and has FWHM $> 700\,\mathrm{km\,s^{-1}}$ (see Figure 4.1). Additionally, we only selected sources that are classified as type 2 AGN by Mullaney et al. (2013), i.e., the permitted and forbidden lines are of similar width, implying that we cannot directly see the broad-line region in these objects (e.g., Antonucci 1993). From these, we selected the sources that have total observed [O III] luminosities of $L_{[\mathrm{O\,III}]} > 5 \times 10^{41}\,\mathrm{erg\,s^{-1}}$ and have a redshift $z < 0.2$ to ensure sufficient emission-line flux for measuring the spatially resolved kinematics with reasonable exposure times for our IFU observations. Finally, we chose sixteen targets with celestial co-ordinates that are accessible with Gemini-South. Our final target list is given in Table 4.1 and we give notes in Section 4.8 on the relevant multi-wavelength observations of these targets that can be found in the literature. The majority of our targets have received little or no attention previously in the literature, with the exceptions of J0945+1737, J1316+1753 and J1356+1026 that have been studied in some detail (see Section 4.8).

It is important to address where our targets fit into the overall AGN population if we are to draw global conclusions from our observations. Firstly we note that our targets are all type 2 AGN, which are thought to constitute at least half of the overall AGN population (e.g., Lawrence & Elvis 2010), and that they have *observed* [O III] luminosities in the range $L_{[\mathrm{O\,III}]} = 10^{41.9}$–$10^{43.2}\,\mathrm{erg\,s^{-1}}$ (see Table 4.2) that fit the luminosity criteria for type 2 ("obscured") quasars (i.e., $L_{[\mathrm{O\,III}]} \gtrsim 10^{41.9}\,\mathrm{erg\,s^{-1}}$; Reyes et al. 2008). The

absorption corrected [O III] luminosities of our targets have the range $L_{[\mathrm{O\ III}]} = 10^{42.4}$–$10^{43.2}\,\mathrm{erg\,s^{-1}}$ (calculated using the Hα/Hβ emission-line flux ratios from Mullaney et al. 2013 and following Calzetti et al. 2000). Additionally, we emphasise that all of our targets are classified as "radio-quiet" in the $\nu L_{\nu}(1.4\,\mathrm{GHz})$-$L_{[\mathrm{O\ III}]}$ plane (Xu et al. 1999; Zakamska et al. 2004) which make up the majority of the luminous type 2 AGN population (i.e., ≈90% based on the sample in Zakamska et al. 2004). Furthermore, considering all galaxies at low redshift (i.e., $0.0 < z < 0.5$), the radio luminosities of our targets [i.e., $L_{1.4\mathrm{GHz}} = (< 0.8 - 25) \times 10^{23}\,\mathrm{W\,Hz^{-1}}$] are known to be common with a space density of $\approx 10^{-4}\,\mathrm{Mpc^{-3}}$ and $\approx 10^{-5}\,\mathrm{Mpc^{-3}}$ for sources with $L_{1.4\mathrm{GHz}} = 10^{23}\,\mathrm{W\,Hz^{-1}}$ and $L_{1.4\mathrm{GHz}} = 10^{24}\,\mathrm{W\,Hz^{-1}}$ respectively (Simpson et al. 2012).

The key advantage of selecting our sources from a large parent sample of AGN is that we can quantitatively define how representative our targets are. In Figure 4.2 we show histograms for the FWHM of the broad [O III] emission-line components for both the parent sample and our targets. Considering all of the type 2 AGN from Mullaney et al. (2013) with $z < 0.2$ and with an [O III] luminosity, $L_{[\mathrm{O\ III}]} > 5 \times 10^{41}\,\mathrm{erg\,s^{-1}}$ (i.e., to match our selection criteria), we find that 45±3% (246 out of 546 sources and assuming $\sqrt{N}$ errors) have a luminous [O III] component with FWHM[B] $> 700\,\mathrm{km\,s^{-1}}$ (Figure 4.2). This indicates that roughly half of luminous type 2 AGN have a luminous broad component to their [O III] emission-line profiles and demonstrates that our targets do not represent a rare sub-population. Additionally, this fraction can be considered a lower limit, as the fraction of sources that host weaker broad components will be considerably higher. In Figure 4.2 we also show histograms of the radio luminosities of our targets and the type 2 AGN in the parent sample that have luminous and broad [O III] emission-line components. Our targets cover a similar range in radio luminosities to those in the parent sample, further demonstrating that our targets are representative of the parent population.

4.3.2 Gemini-South GMOS observations and data reduction

The observations of our targets were performed using Gemini-South GMOS (Allington-Smith et al. 2002) in IFU mode. The GMOS IFU uses a lenslet array to slice the focal plane into several small components which are each coupled to a fibre. We made use of the one-slit mode with the B1200 grating to obtain the required wavelength coverage to

observe the [O III]λλ4959,4007 and Hβ emission-lines for all our targets. In this mode the IFU consists of 25×20 lenslets sampling a $5'' \times 3.''5$ field-of-view. The GMOS IFU also has a dedicated set of 250 lenslets to simultaneously observe the sky $\approx 1'$ away from the target field-of-view. We determined the instrumental dispersion for the observations of each source ($\Delta v \approx 50$–$60\,\mathrm{km\,s^{-1}}$, with uncertainties $\lesssim 5\,\mathrm{km\,s^{-1}}$) by measuring the widths of several sky lines close to the observed wavelengths of the emission lines. The emission-line profiles of our targets are typically non-Gaussian and the non-parametric line-widths we quote (see Section 4.4.1) are very large ($\gtrsim 500\,\mathrm{km\,s^{-1}}$); therefore, we do not correct for this instrumental broadening. This will result in the quoted line-width measurements being broadened by $\lesssim 2\%$.

The observations were undertaken during two observing programmes: GS-2010A-Q-8 (PI: Mullaney) taken between 2010 February 09 and 2010 March 19, and GS-2012A-Q-21 (PI: Harrison) taken between 2012 February 16 and 2012 June 26. For the observations in the 2012A run, that covered the fainter targets, the on-source exposures for each target consisted of 6×1500s, while for the 2010A run, that covered the brighter targets, the exposure times consisted of 4×1300s. Table 4.1 indicates during which run each target was observed. The observations were performed with V-band seeing of $\lesssim 0.8$ arcsec (typically ≈ 0.7 arcsec, from measurements of the acquisition images taken before each IFU observation).

We reduced the data using the standard Gemini IRAF GMOS pipeline to perform wavelength calibration and flat fielding and we used a dedicated set of IDL routines to perform sky subtraction, cosmic ray removal and cube construction. We did not resample the pixels and therefore the pixel scale of the final cubes is $0.''17 \times 0.''2$. To find spatial centroids for the individual data cubes, emission-line free continuum images from each exposure were produced that were then spatially aligned and co-added to create the final mosaics, using a median stack with a 3σ clipping threshold to remove the remaining cosmetic defects and cosmic rays. Flux calibration for each target was performed in two stages. Stage one involved reducing standard star observations in an identical manner to the targets and consequently obtaining the instrumental response using IRAF routines from the ONEDSPEC package. Stage two used the SDSS spectra to find the absolute flux calibration for each of the objects. This was achieved by fitting a low order polynomial to the emission-

line free SDSS spectrum and also an emission-line free spectrum extracted from our IFU data cubes over the same spatial region as covered by the SDSS fibres (i.e., $\approx 3''$ diameter). We verified that the equivalent widths of the emission lines were consistent between these two spectra and then used the ratio between these fits to apply the flux calibration to each of the data cubes. We estimate a conservative uncertainty of 15% on the absolute flux calibration using this process (see Abazajian et al. 2009 and Liu et al. 2013a)

4.3.3 Aligning the IFU data to SDSS images

As part of our analyses we compare the location of the kinematic features we observe in our IFU data, to the host galaxy morphologies based upon three-colour (g, r, i) SDSS images (Section 4.5.2). We aligned the SDSS three-colour images to our IFU data by matching the surface brightness peak in the g-band SDSS images to the surface brightness peak of images constructed from our IFU data cubes, collapsed around $\approx$5000 Å. We then rotated the SDSS images to match the orientation of our IFU data cubes. We note that we only use these images for qualitative descriptions of the galaxy morphology with respect to our IFU data and therefore we do not require a more accurate alignment process.

4.3.4 SFRs, AGN luminosities and the origin of the radio emission

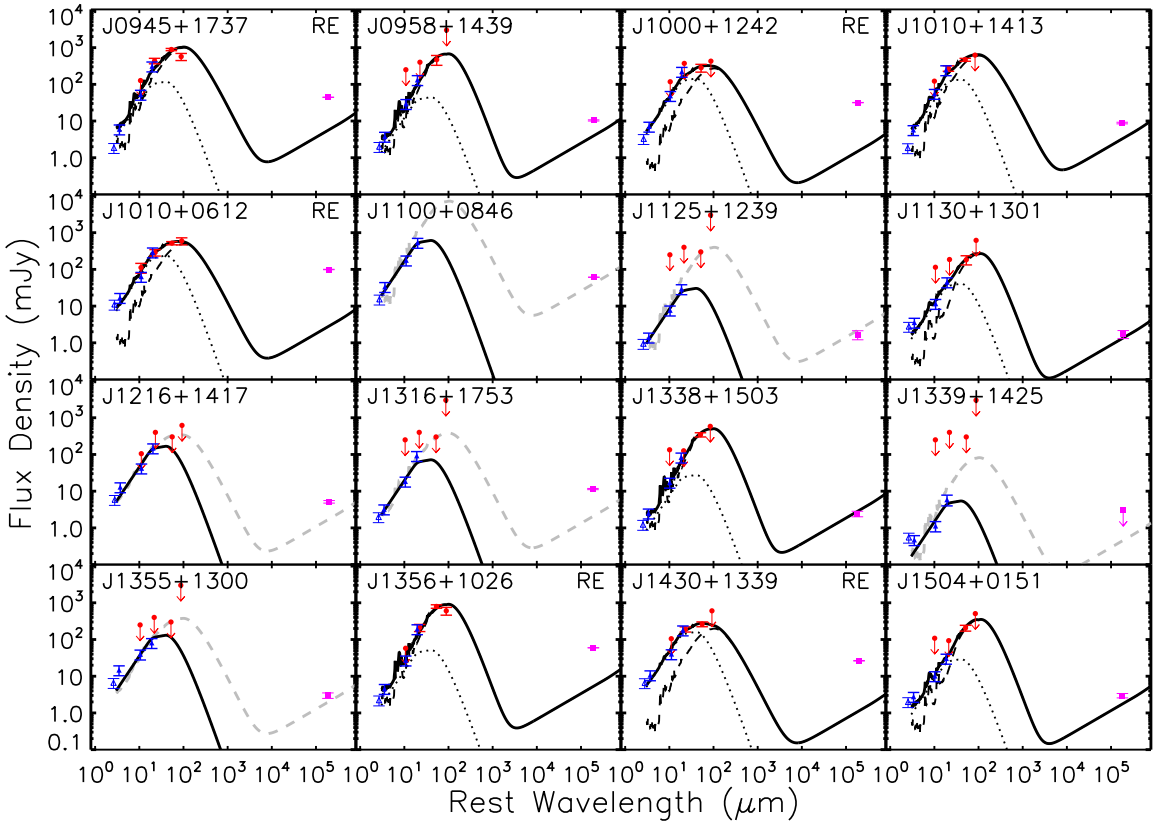

Figure 4.3: The infrared SEDs for each target in our sample. The flux densities used in the fitting procedure are shown as blue filled triangles (WISE data) and red filled circles (IRAS data; photometric data in Table 4.3). The first WISE band (at 3.4μm) falls outside of the wavelength range of our templates and is shown with an empty symbol. Also shown are the overall best-fit SEDs: the total SEDs are shown as solid curves, the AGN templates are shown as dotted curves and the starburst templates as dashed curves. The grey dashed curves show the upper-limits on the starburst templates for the sources that lack far-infrared data. Using these SED fits we obtain SFRs and AGN luminosities (see Section 4.3.4 and Table 4.2). We also plot the 1.4 GHz flux densities (square symbols) that are not included in the fitting but do illustrate that five of the sources have significant excess radio emission above that expected from star formation (indicated with "RE" in the top-right of their panels; see Section 4.3.4; Table 4.2).

TARGET PROPERTIES

Name	$\log[L_{[\mathrm{O\,III}]}]$	$\log[L_{\mathrm{H}\beta}]$	$S_{1.4}$	$\log[L_{1.4}]$	θ_{FIRST}	$\mathrm{PA}_{1.4}/R_{1.4}$	$\log[L_{\mathrm{IR,SF}}]$	SFR	$\log[L_{\mathrm{AGN}}]$	q_{IR}
	(erg s^{-1})	(erg s^{-1})	(mJy)	(W Hz^{-1})		°/″	(erg s^{-1})	($M_\odot$ yr^{-1})	(erg s^{-1})	
(1)	(2)	(3)	(4)	(5)	(6)	(7)	(8)	(9)	(10)	(11)
J0945+1737	42.83	41.80	44.5[4]	24.3	1.072[3]	112°/2.9	$45.5^{+0.1}_{-0.1}$	81^{+7}_{-25}	$45.5^{+0.2}_{-0.1}$	$1.8^{+0.1}_{-0.1}$
J0958+1439	42.60	41.49	10.4[4]	23.5	1.006[9]	-	$45.1^{+0.1}_{-0.1}$	36^{+12}_{-11}	$45.0^{+0.3}_{-0.3}$	$2.2^{+0.1}_{-0.1}$
J1000+1242	42.80	41.84	31.8[4]	24.2	1.111[4]	158°/3.3	$45.0^{+0.3}_{-0.2}$	29^{+18}_{-16}	$45.7^{+0.1}_{-0.1}$	$1.3^{+0.2}_{-0.2}$
J1010+1413	43.21	42.15	8.8[5]	24.0	1.044[13]	-	$45.7^{+0.2}_{-0.1}$	122^{+60}_{-32}	$46.0^{+0.2}_{-0.1}$	$2.3^{+0.2}_{-0.1}$
J1010+0612	42.30	41.48	99.3[1.3]	24.4	1.038[3]	-	$44.9^{+0.1}_{-0.1}$	23^{+4}_{-7}	$45.6^{+0.1}_{-0.1}$	$1.1^{+0.1}_{-0.1}$
J1100+0846	42.82	41.77	61.3[3]	24.2	1.0230[12]	-	<46.1	<365	$46.0^{+0.1}_{-0.1}$	<2.5
J1125+1239	42.06	40.94	1.7[5]	23.1	0.96[6]	-	<45.4	<66	$45.2^{+0.1}_{-0.2}$	<2.9
J1130+1301	42.03	40.88	1.7[4]	22.9	1.07[7]	122°/5.1†	$44.8^{+0.2}_{-0.2}$	18^{+7}_{-7}	$45.1^{+0.1}_{-0.1}$	$2.5^{+0.2}_{-0.2}$
J1216+1417	41.93	-	5.1[4]	22.9	1.07[2]	97°/2.7†	<44.6	<10	$45.3^{+0.1}_{-0.1}$	<2.1
J1316+1753	42.87	41.81	11.4[4]	23.8	1.04[1]	-	<45.5	<77	$45.4^{+0.1}_{-0.1}$	<2.2
J1338+1503	42.64	-	2.4[4]	23.3	1.06[5]	-	$45.5^{+0.1}_{-0.1}$	81^{+13}_{-13}	$45.2^{+0.3}_{-0.2}$	$2.7^{+0.2}_{-0.1}$
J1339+1425	41.95	40.84	<3.0	<23.2	-	-	<44.9	<23	$44.3^{+0.1}_{-0.1}$	-
J1355+1300	42.09	41.13	3.0[5]⋆	23.2	-	-	<45.4	<62	$45.7^{+0.1}_{-0.1}$	<2.7
J1356+1026	42.95	41.99	59.6[4]	24.4	1.014[2]	-	$45.4^{+0.1}_{-0.1}$	63^{+7}_{-17}	$45.1^{+0.3}_{-0.2}$	$1.6^{+0.1}_{-0.1}$
J1430+1339	42.72	41.88	26.4[4]	23.7	1.400[9]	77°/7.8	$44.4^{+0.2}_{-0.2}$	7^{+3}_{-3}	$45.3^{+0.1}_{-0.1}$	$1.3^{+0.2}_{-0.2}$
J1504+0151	42.20	-	3.0[4]	23.4	1.06[4]	-	$45.2^{+0.1}_{-0.1}$	44^{+10}_{-10}	$45.2^{+0.1}_{-0.2}$	$2.4^{+0.2}_{-0.1}$

Table 4.2: NOTES:
Details of our IFU targets that we observed with Gemini-GMOS. (1) Object name; (2)-(3) Total [O III]λ5007 and Hβ luminosities derived in this work, uncertainties are typically 15%; (4) 1.4 GHz flux densities obtained from the FIRST survey (Becker et al. 1995) and uncertainties that are defined as 3× the RMS noise of the radio map at the source position; (5) Rest-frame radio luminosities using a spectral index of $\alpha = 0.7$ and assuming $S_\nu \propto \nu^{-\alpha}$ (we note that a range of $\alpha = 0.2$–1.5 introduces an spread of $\lesssim \pm 0.1$ dex on the radio luminosity); (6) Radio morphology paramater, where sources with $\theta > 1.06$ are classified as extended in the 1.4 GHz FIRST data (see Section 4.3.4); (7) The deconvolved PA and major-axis radius from the FIRST survey for the radio-extended sources; (8)-(10) Infrared luminosties from star-formation, SFRs and bolometric AGN luminosities derived from our SED analyses (see Section 4.3.4); (11) The q_{IR} ("radio excess") parameter for each source, where sources with $q_{\mathrm{IR}} \leq 1.8$ are classified as "radio excess" (see Section 4.3.4).
⋆The 1.4 GHz flux density for SDSS 1355+1300 is taken from the NVSS survey (Condon et al. 1998).
†The uncertainty on θ is high and therefore these sources may not be truly extended in their FIRST images.

INFRARED PHOTOMETRIC DATA

Name	W1 (3.4μm)	W2 (4.6μm)	W3 (12μm)	W4 (22μm)	IRAS 12μm	IRAS 25μm	IRAS 60μm	IRAS 100μm
J0945+1737	1.9±0.6	6.0±1.8	53±16	310±90	<127	440±70	890±60	570±130
J0958+1439†	2.0±0.6	3.8±1.1	30±9	130±40	<250	<400	470±140	<3000
J1000+1242	3.3±1.0	7±2	49±15	220±70	<118	<372	280±70	<428
J1010+1413	1.8±0.6	5.7±1.7	56±17	250±70	<122	270±50	470±40	<625
J1010+0612	11±3	17±5	64±19	290±90	110±30	290±60	520±50	590±130
J1100+0846††	15±5	34±10	180±50	540±160	-	-	-	-
J1125+1239	1.0±0.3	1.4±0.4	8±2	29±9	<250	<400	<300	<3000
J1130+1301⋆	2.8±0.8	3.6±1.1	12±4	45±14	<114	<186	180±50	<619
J1216+1417	5.9±1.8	13±4	42±13	150±50	<105	<400	<300	<620
J1316+1753	2.0±0.6	3.2±1.0	19±6	90±30	<250	<400	<300	<3000
J1338+1503	1.2±0.4	2.5±0.8	17±5	80±30	<134	<126	340±50	<583
J1339+1425	0.5±0.2	0.5±0.1	1.1±0.4	6±2	<250	<400	<300	<3000
J1355+1300	7±2	15±4	40±13	80±20	<250	<400	<300	<3000
J1356+1026	2.2±0.7	4.6±1.4	27±8	190±60	<58	210±50	800±90	600±150
J1430+1339	7±2	11±3	40±12	180±50	<105	190±30	260±40	<605
J1504+0151	2.0±0.6	2.8±0.8	10±3	30±9	<108	<93	210±40	<508

Table 4.3: NOTES:
The mid-infrared–far-infrared photometric flux densities, uncertainties and upper limits for the targets in our sample (in units of mJy) which are used in our SED analysis (these photometric data are shown in Fig. 4.3). These were obtained from WISE and IRAS all-sky catalogues (Moshir et al. 1992; Wright et al. 2010; see Section 4.3.4 for details). The first WISE band (W1) falls outside of the wavelength range of our templates, therefore these flux densities are not included in the SED fitting procedure.
†The IRAS fluxes for J0958+1439 are from SCANPI (http://irsa.ipac.caltech.edu/applications/Scanpi); ††J1100+0846 was not covered by IRAS observations; ⋆J1130+1301 did not have an entry in the IRAS faint source catalogue; however, inspection of the images indicates that it is detected and therefore we obtained the fluxes from the IRAS reject catalogue.

To thoroughly interpret our results we investigate the properties of the AGN and host galaxies of our targets in more detail (i.e., we measure SFRs and AGN luminosities and explore the origin of the radio emission). To obtain the bolometric AGN luminosities and SFRs of our targets (see Table 4.2) we performed mid-infrared to far-infrared SED fitting to archival photometric data that is available for our targets (described below). Our procedure decomposes the emission from AGN activity and star-formation, so that we do not need to make any assumptions about the relative contribution from these two processes. At the end of this sub-section, we also briefly investigate the possible presence of radio AGN activity (i.e., radio cores or radio jets) in our targets by combining the results of our SED fitting with archival radio data.

For our SED fitting, we obtained mid-infrared to far-infrared photometric flux densities, uncertainties and upper limits (over 3μm–100μm; see Table 4.3) from (1) the Wide-field Infrared Survey Explorer all-sky survey (WISE; Wright et al. 2010) using the closest source to the SDSS position (all are $< 0.''6$) and (2) the Infrared Astronomical Satellite (IRAS; Neugebauer et al. 1984) faint source catalogue (Moshir et al. 1992) with a matching radius of $\leq 30''$[1]. We added in quadrature 30% of the measured flux densities to the quoted WISE uncertainties to account for calibration uncertainties in the WISE data (Wright et al. 2010) and the discrete nature of the SED templates used in our analysis (see below; also see Del Moro et al. 2013). For the sources that we were not able to obtain IRAS flux density measurements (see Table 4.3) we estimated conservative maximum upper limits of 0.25 mJy, 0.4 mJy, 0.3 mJy and 3 mJy for the 12μm, 25μm, 60μm, and 100μm bands respectively. One source (SDSS J1100+0846) falls into an area of the sky that was not observed by IRAS observations and we therefore cannot place photometric constraints on the IRAS bands for this source. The photometric data we used are shown in Figure 4.3.

To perform the SED fitting we followed the procedure described in Mullaney et al. (2011) that simultaneously fits an empirically derived AGN model (parametrised in an analytical form) and empirically derived host-galaxy templates to the infrared photometric data (Table 4.3). All of the sources in our sample are known to host an AGN (from optical

[1]We verified these matches by following the log likelihood method of matching IRAS to WISE counterparts outlined in Wang et al. (2014).

spectroscopy) and additionally all but one of the sources are classified as an infrared AGN based upon WISE colours (W2−W1 and W3−W2) by falling inside the "AGN-wedge" defined in Mateos et al. (2012).[2] We therefore simultaneously fit these data with the five star-forming galaxy templates ("SB1"–"SB5") and the mean AGN model, originally defined in Mullaney et al. (2011) and extended to cover the wavelength range 3–10^5 μm, by Del Moro et al. (2013).[3] To derive the AGN luminosities and SFRs (Table 4.2) we use the star-forming template plus AGN template combination that gives the lowest overall χ^2 value, rejecting all fits that lie above the photometric upper limits (given in Table 4.3; see Fig. 4.3). For the sources where we have no detections in the far-infrared bands (i.e., the IRAS bands), we are unable to measure reliable SFRs and we therefore calculate conservative upper limits by increasing the normalisation of the star-forming templates until either the photometric upper limits were reached or the solution was 3σ above one of the photometric data points.

We calculated the SFRs for each source (Table 4.2) by measuring the infrared luminosities of the star-formation components from the best-fitting SED solutions ($L_{\rm IR,SF}$; integrated over 8–1000μm) and using the relationship of Kennicutt (1998) (corrected to a Chabrier IMF by dividing by a factor of 1.7; Chabrier 2003). To determine the bolometric AGN luminosities for each source (Table 4.2), we first calculated the AGN continuum luminosity at 6μm from the best fitting SED solution and converted this to an AGN bolometric luminosity using a correction factor of $\times 8$ (Richards et al. 2006a; see Table 4.2). The conservative upper and lower bounds on both the SFRs and AGN luminosities are derived from summing in quadrature the range in solutions from the different star-formation templates (only those which did not exceed the upper limits) and the formal uncertainties

[2] SDSS J1339+1425 does not have WISE colours that place it inside the "AGN-wedge"; however, we still found that including an AGN template provided a better fit than any of the star-forming templates alone.

[3] We tested how much of an affect our limited range of templates has on our quoted results (Table 4.2) by: (1) re-fitting including an Arp 220 model SED and (2) allowing the second power-law slope of the AGN model to be a free parameter (i.e., α_2 in Mullaney et al. 2011). The first of these changes allows for a more extreme ULIRG-like SED that is not covered by our main SB templates. The second change allows for a very large range in intrinsic AGN SEDs, to account for the variations seen in AGN of different luminosities (see fig. 7 in Mullaney et al. 2011). When performing the SED fitting with these two additions we found that all the results were consistent within the errors of our quoted results (Table 4.2) with only two minor exceptions: (1) The SFR for J1430+1339 had an upper limit of < 2 $M_{\odot}\,yr^{-1}$ and (2) the AGN luminosity of J1504+0151 was $\log[L_{\rm AGN}] = 45.4^{+0.1}_{-0.3}\,{\rm erg\,s^{-1}}$. We therefore conclude our primary choice of templates are sufficient for this work.

from the best-fit solution. We emphasise that our method decomposes the emission due to an AGN and star formation, therefore removing the need to assume the relative contributions from these two processes. Furthermore, this procedure produces consistent SFRs and AGN luminosities with those derived from mid-infrared spectra where available (see Section 4.8 and Footnote 14; also see Del Moro et al. 2013).

The bolometric AGN luminosities for our targets span $L_{\rm AGN} = (0.2-10)\times10^{45}$ erg s^{-1} (with a median $L_{\rm AGN} = 2\times10^{45}$ erg s^{-1}) and therefore cover the classical "quasar" threshold of $L_{\rm AGN} = 10^{45}$ erg s^{-1}. We note that these mid-infrared derived AGN luminosities are a factor of $\approx$1–20 lower than those that would be predicted using the [O III] luminosity and the relationship of Heckman et al. (2004) (i.e., $L_{\rm AGN} = 3500L_{\rm [O\,III]}$). However, this is consistent with other studies of luminous ($L_{\rm [O\,III]} \gtrsim 10^{42}$ erg s^{-1}) type 2 AGN, at similar redshifts, that show that $L_{\rm [O\,III]}$ is not linearly correlated with the nuclear luminosity and can over predict the AGN luminosity by an order of magnitude or more (Schirmer et al. 2013; Hainline et al. 2013).

Of the sixteen sources in our sample, eight have far-infrared luminosities that classify them as luminous infrared galaxies (LIRGs; $L_{\rm IR,SF} = 10^{11}$–10^{12} L$_\odot$) and one as an ultra-luminous infrared galaxy (ULIRG: $L_{\rm IR,SF} > 10^{12}$ L$_\odot$). Of the remaining seven sources, six of them have upper-limits on their far-infrared luminosities which are less than or consistent with the luminosity of LIRGs (see Table 4.2).[4] These infrared luminosities correspond to SFRs of $\lesssim$[7–120]M$_\odot$ yr^{-1} and are typical for AGN of these luminosities at these redshifts (e.g., Zakamska et al. 2008; Mullaney et al. 2010; Rosario et al. 2012).

Finally, we investigate the origin of the radio emission from our targets. We plot the 1.4 GHz radio flux densities (given in Table 4.2) on the SEDs shown in Figure 4.3. We identify if there is radio emission significantly above that expected from their ongoing star-formation (e.g., Helou et al. 1985; Condon et al. 1995), that may indicate radio emission due to an AGN either in form of a radio core or radio jets (e.g., see Del Moro et al. 2013 and references there-in) or due to shocks (e.g., Zakamska & Greene 2014). To do this, we use the definition given by Ivison et al. (2010b) (see also Helou et al. 1985),

[4]The remaining source, SDSS J1100+0846, which is not covered by IRAS and therefore has poor FIR constraints, has an upper limit consistent with a ULIRG.

calculating the ratio between the far-infrared and radio emission ($q_{\rm IR}$) as

$$q_{IR} = \log\left[\frac{S_{\rm IR}/3.75\times10^{12}\,{\rm W m^{-2}}}{S_{1.4}/{\rm W\,m^{-2}\,Hz^{-1}}}\right] \quad (4.3.1)$$

where $S_{\rm IR}$ is the rest-frame far-infrared (8–1000 μm) flux and $S_{1.4}$ is the rest-frame 1.4 GHz flux density assuming, $S_\nu \propto \nu^{-\alpha}$, with a radio spectral index of $\alpha = 0.7$. We give the value of $q_{\rm IR}$ for each source in our sample in Table 4.2. The quoted uncertainties combine the uncertainties on $S_{1.4}$, $S_{\rm IR}$ and a range in the unknown radio spectral indices (we use $\alpha = 0.2$–1.5). Star-forming galaxies have $q_{\rm IR} \approx 2.4$ and we define "radio excess" sources as those with $q_{\rm IR} \leq 1.8$, i.e., $\gtrsim 2.5\sigma$ away from the peak seen in the star-forming galaxies (Ivison et al. 2010b; see also Del Moro et al. 2013 who use a similar definition). Using this definition we identify five of our targets as being radio excess and five sources that are classified as radio normal (see Table 4.2 and Figure 4.3); however, we cannot rule out low-level radio emission above that expected from star formation in these targets, as it can be difficult to identify using this method, especially in systems with high SFRs (e.g., Del Moro et al. 2013). The remaining six sources have upper limits on their $S_{\rm IR}$ values which results in upper limits on their $q_{\rm IR}$ values that are consistent with them being either radio normal or radio excess sources.

Based on FIRST and NVSS images, only one of our sources (J1430+1339) shows clear evidence for luminous extended radio structures on scales $>5''$ (see Table 4.2 and Section 4.8). Therefore, we follow the method of Kimball & Ivezić (2008) to search for evidence of extended radio structures (on ≈ 2–$5''$ scales) that compares the peak and integrated 1.4 GHz FIRST flux densities ($F_{\rm peak}$ and $F_{\rm int}$ respectively). They define the parameter $\theta = (F_{\rm int}/F_{\rm peak})^{0.5}$ and any source with $\theta > 1.06$ is classed as spatially resolved. We provide θ for all of our targets with FIRST detections in Table 4.2. For the five sources with $\theta > 1.06$, i.e., those that pass the criteria to be "resolved", we also provide the position angle and radius of the de-convolved major axis provided by FIRST. Of these five sources, two have very low 1.4 GHz flux densities and therefore the uncertainty on θ is high. The other three have stronger evidence for being spatially resolved and are also "radio excess" sources; therefore, they are the strongest candidates for having radio jets on ≈ 3–$8''$ scales (i.e., ≈ 7–12 kpc; Table 4.2), although shocks due to outflows are another

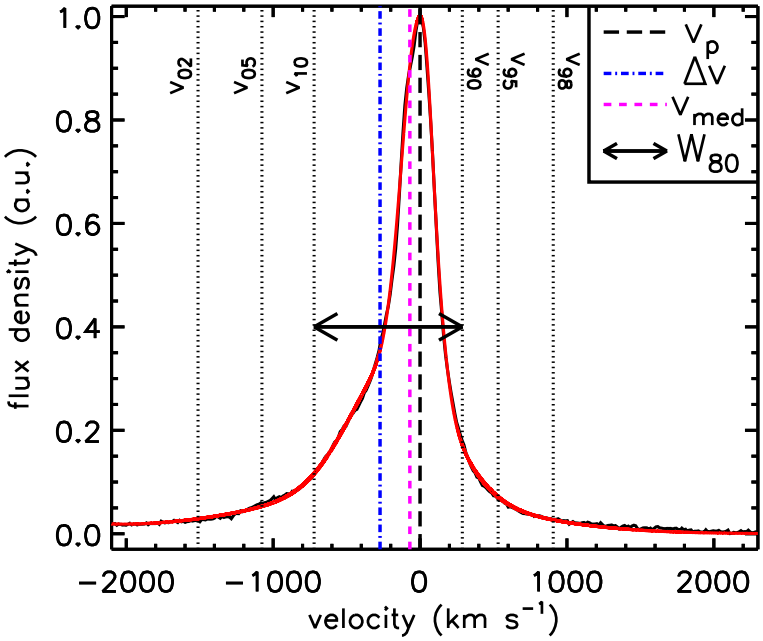

Figure 4.4: Illustration of the different non-parametric velocity definitions used in this work which are described in Section 4.4.1. We show an example [O III]λ5007 emission-line profile from our sample (black curve) and our fit to this profile (red curve). The vertical dotted lines show different percentiles to the flux contained in the overall emission-line profile (from left to right: 2nd; 5th; 10th; 90th; 95th and 98th). The long-dashed line shows the velocity of the peak flux density (v_p). The vertical short-dashed line shows the median velocity ($v_{\rm med}$) and the dot-dashed line shows the velocity offset of the underlying broad wings (Δv; see Section 4.4.1). The arrow indicates the line width that contains 80% of the flux (W_{80}).

possible explanation for this excess radio emission (Zakamska & Greene 2014). High-resolution radio imaging will be instrumental in determining the origin and morphology of the radio emission in the whole sample.

4.4 Velocity definitions and spatially resolved kinematics

4.4.1 Non-parametric velocity definitions

We are interested in the spatially-resolved kinematics of the [O III]λλ4959,5007 and Hβ emission lines for the sixteen type 2 AGN we observed with the Gemini-GMOS IFU. The combination of these emission-line species allows us to measure emission-line region sizes (Section 4.5.1), spatially resolve the ionised gas kinematics (Section 4.5.2) and calculate ionised gas masses (Section 4.5.3) for our targets. The emission-line profiles in

type 2 AGN are often found to be complex, consisting of multiple narrow and broad components (e.g., Veilleux 1991; Greene et al. 2011; Villar-Martín et al. 2011b), which is also the case for our sample (Fig. 4.5; Fig. 4.13–4.27). Due the complexity of the emission-line profiles we opted to use non-parametric definitions to characterise their widths and velocities within each pixel of the IFU data. We used an approach that: (1) is consistent for all of the targets in the sample; (2) allows us to de-couple galaxy dynamics, merger remnants and outflow features; and (3) provides results that are directly comparable to observations in the literature. The definitions that we have used throughout, for describing both the galaxy-integrated emission-line profiles and the spatially-resolved kinematics, are described below and are illustrated in Figure 4.4:

- The peak velocity (v_p) is the velocity of the peak flux density in the overall [O III]λ5007 emission-line profile. For our targets, this traces the brightest narrow emission-line component (i.e., those with FWHM $\lesssim 500\,\mathrm{km\,s^{-1}}$).

- The line width, W_{80}, is the velocity width of the line that contains 80% of the emission-line flux such that $W_{80} = v_{90} - v_{10}$, where v_{10} and v_{90} are the velocities at the 10th and 90th percentiles, respectively (Fig. 4.4). For a single Gaussian profile this is approximately the FWHM.

- To measure the velocity offset of the broad underlying wings we define the velocity offset, Δv, that is measured as $\Delta v = (v_{05} + v_{95})/2$, where v_{05} and v_{95} are the velocities at the 5th and 95th percentiles of the overall emission-line profiles respectively (Fig. 4.4). For a profile that is well characterised by a single narrow Gaussian component and a luminous broad Gaussian component, Δv is the velocity offset of the broad component. For a single Gaussian component $\Delta v = 0$.

- To enable us to compare to previous work, we also measured v_{02} and v_{98}, which are the 2nd and 98th percentiles of the flux contained in the overall emission-line profiles (as used in Rupke & Veilleux 2013)[5] and can be considered the "maximum" projected velocity of the gas.

[5] We note that Rupke & Veilleux (2013) fit a broad and narrow component to the emission lines and then define v_{98} for the broad component only. As a result their values are likely to be higher than our values that we defined from the *overall* emission-line profile so as not to make any assumptions on the kinematic structure of the emission lines (i.e., the number of distinct velocity components).

- Finally, we measured the median velocity ($v_{\rm med}$; Fig. 4.4) of the overall emission-line profile so that we can compare to the type 2 AGN observed in Liu et al. (2013b). We find that $v_{\rm med}$ is likely to be dominated by galaxy kinematics in many cases (i.e., galaxy rotation or mergers; see Section 4.5.2) and should be used with care if interpreting outflow kinematics.

We emphasise that these definitions are used to enable us to consistently compare all of the targets in our sample as well as compare to observations in the literature; however, for a few individual cases some care should be taken when interpreting these measurements due to the uniqueness and complexity of the emission-line profiles. For this reason we discuss the details of kinematics of individual sources in Section 4.8.

4.4.2 Emission-line profile fitting procedure

As several of the velocity definitions outlined above and illustrated in Fig. 4.4 are measured from the broad wings of the emission-line profiles they are subject to the influence of noise in the spectra, especially in the lower surface brightness regions of our IFU observations. To circumvent this issue, we characterise each emission-line profile using a combination of multiple Gaussian components. We note that we do not draw any physical meaning from the individual Gaussian components, they are only used to characterise the emission-line profiles. Below, we describe the emission-line profile fitting procedure that we use throughout for fitting the galaxy-integrated spectra and also the spectra used to produce the spatially resolved maps and velocity profiles described in Section 4.4.3.

Initially, we isolated the [O III]$\lambda\lambda$4959,5007 emission-line doublet from the underlying continuum by linearly interpolating each spectrum between line-free regions close to the emission lines, a commonly used method for type 2 AGN (e.g., Husemann et al. 2013; Liu et al. 2013b). The emission-line doublet was then fit with a minimising-χ^2 method, using the IDL routine MPFIT (Markwardt 2009) with Gaussian components. For every Gaussian component we simultaneously fit the [O III]λ5007 and [O III]λ4959 emission lines using the same line width, a fixed wavelength separation and the intensity ratio was fixed at [O III]λ4959/[O III]λ5007 = 0.33 (e.g., Dimitrijević et al. 2007). Initially we fit a single Gaussian component to the emission-line profile and consequently additional Gaussian components were added to the overall fit (up to a maximum of six components)

until the important values for our study (i.e., Δv, W_{80} and $v_{\rm p}$; see Fig. 4.4) became stable within $\leq$20%, i.e., the addition or removal of a Gaussian component does not change these values significantly. We only fitted more than one Gaussian component if the emission line was detected above a S/N threshold of $\approx$30, with this threshold being motivated by visually inspecting the fits and the reduced χ^2 values (see below). For spectra below this S/N threshold, W_{80} cannot be well characterised and we are also unable to define Δv. We included appropriate constraints to the line widths to avoid fitting excessively broad components to the continuum or narrow components to noise spikes (i.e., limited by the spectral resolution). We verified that our fitting procedure was effective across the whole field-of-view by visually inspecting the spectra and their best-fitting solutions extracted from 25 spatial regions for each object individually (Fig. 4.5; Fig. 4.13–4.27). An additional verification of the success of our fitting procedure was that, in all but one of the targets,[6] the median reduced χ^2 values of the fits to the individual pixels in the data cubes are between 1.0–1.8 with $\geq$60% of the pixels having reduced χ^2 values between 0.8–2.5.

Using the overall fits to the emission-line profiles, we measure the non-parametric velocity definitions defined in Section 4.4.1 (see Fig. 4.4). Random errors on these quantities were calculated by taking the 1σ spread of values calculated from a 1000 random spectra that were generated using the final models plus Gaussian random noise (based on the standard deviation of the continuum). To obtain the final quoted uncertainties, we added these random errors in quadrature with an estimated systematic error that we calculated from the range in the velocity values derived from adding or removing a Gaussian component to the final emission-line models. We note that these uncertainties are extremely small ($\lesssim$10%) in the high signal-to-noise ratio spectra and therefore the uncertainties will be dominated by the physical interpretation of these values (see Section 4.5).

To enable us to measure ionised gas masses (Section 4.5.3) we also measured the Hβ emission-line profiles and fluxes from our IFU data. To do this, we extract the Hβ emission-line profiles from the IFU data cubes in the same manner to that for [O III] and show them in Figure 4.5 and Figure 4.13–4.27. We find that the overall shapes of the Hβ emission-line profiles are in excellent agreement with the [O III] emission-line profiles

[6]The source with a higher median reduced χ^2=3.5 is SDSS J1356+1026 that we attribute to the highly complex emission-line profile and exceptionally low noise (Fig. 4.25).

for all but three of our sources (the exceptions are SDSS J1216+1417; SDSS J1338+1503; and SDSS 1504+0151). This indicates that for the majority of the sources, the Hβ emission lines are not significantly affected by stellar absorption features (which is true for many AGN with luminous emission lines; Soto & Martin 2010; Harrison et al. 2012a; Liu et al. 2013b) and this emission line traces the same kinematic components as the [O III] emission line (see also Rodríguez Zaurín et al. 2013). For these thirteen sources we measure the Hβ emission-line fluxes by fitting the [O III] emission-line models (described above) to the data at the observed wavelength of the Hβ emission lines, allowing only the overall normalisation to vary. The remaining three sources, which have different profiles for these two emission-line species, may have varying ionisation states for different kinematic components and/or have higher levels of Hβ stellar absorption features that is certainly plausible given the stellar continua and absorption features observed in their optical spectra (see Section 4.8). For this work, we wish to avoid using a variety of approaches for our targets; therefore, we choose to not use the Hβ emission lines in the analyses of these three sources.

Due to the lack of clearly defined stellar absorption lines in the spectra across our targets, we define the systemic redshift from the velocity of the peak flux density in the [O III]λ5007 emission line (see Fig. 4.5). This choice of systemic redshift effectively traces the mean velocity of the narrow components in the emission-line profiles, which are often attributed to galaxy kinematics (e.g., Greene & Ho 2005; Harrison et al. 2012a; Rupke & Veilleux 2013; also see Section 4.5.2); however, this might not always be the case and therefore places an uncertainty on our systemic redshift. For SDSS J0958+1439 and SDSS J1316+1753 where the overall emission line profiles lack a clear single peak (see Fig. 4.14 and Fig. 4.21) we take the flux weighted mean velocity of the narrow components (i.e., those with FWHM $< 500\,\mathrm{km\,s^{-1}}$) used in the fit to the galaxy-integrated spectrum (i.e., similar to the procedure used in Rodríguez Zaurín et al. 2013). Across the whole sample, the mean velocity offset between our systemic redshift and the SDSS redshift is $-18\,\mathrm{km\,s^{-1}}$ with a scatter of $54\,\mathrm{km\,s^{-1}}$. We note that any velocity *differences* that are measured (such as W_{80}) are unaffected by the choice in systemic redshift.

4.4.3 Velocity maps and velocity-distance profiles

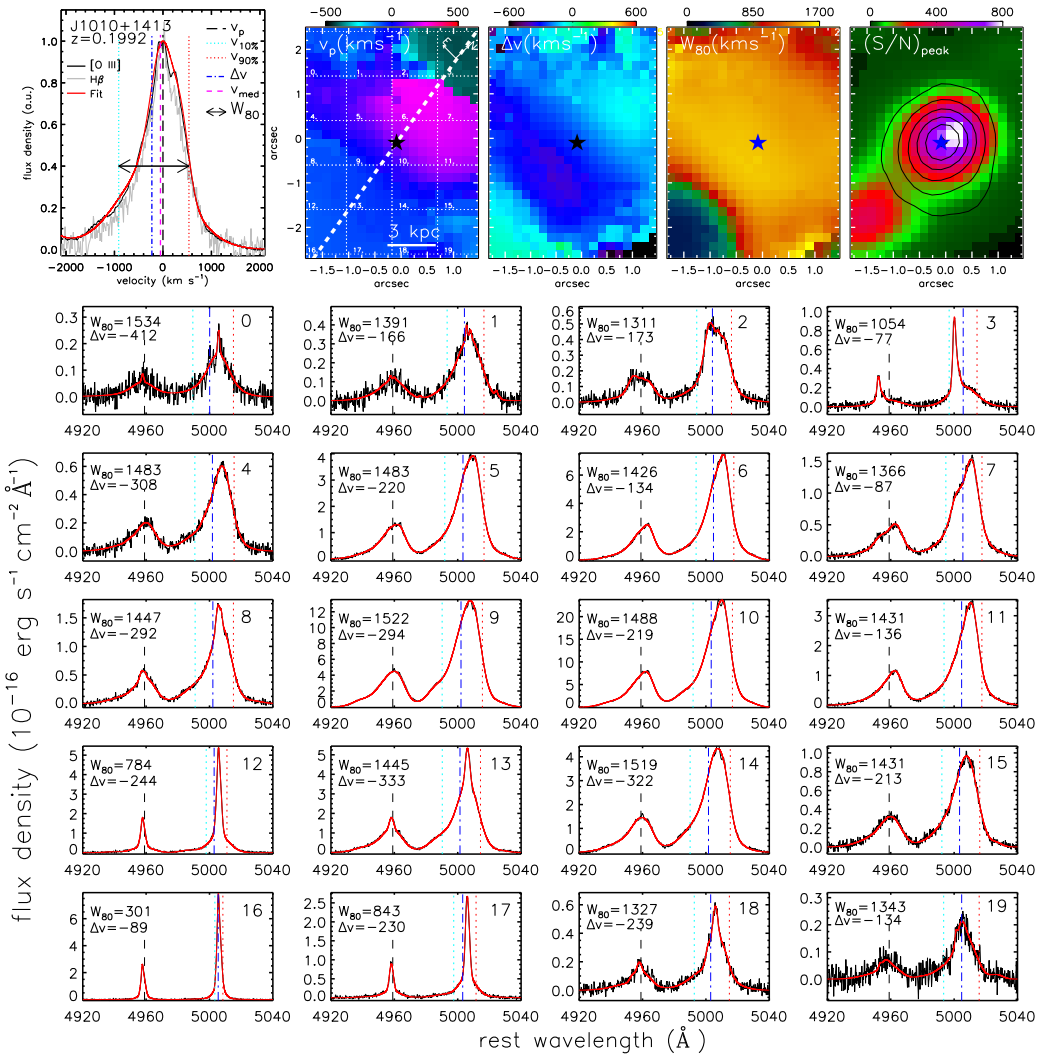

Figure 4.5: Our IFU data for an example object in our sample (SDSS J1010+1413). The equivalent plots for the rest of the sample can be found in Section 4.8. Upper panels from left to right: *Panel 1:* Galaxy-integrated [O III]λ5007 emission-line profile (black curve) extracted from the full field-of-view of the IFU. Zero velocity corresponds to the redshift given in Table 4.2 and the spectrum has been normalised to the peak flux density. The solid red curves indicate the best fit to the emission-line profile. The vertical dashed and dotted lines correspond to the non-parametric velocity definitions described in Figure 4.4 and Section 4.4.1. The Hβ emission-line profile is shown in grey; *Panel 2:* The velocity of the [O III] emission-line peak (v_p) at each pixel. The solid bars indicate 3 kpc in spatial extent and the dashed line indicates the kinematic "major axis" as defined in Section 4.4.3. The dotted lines and numbers indicate the spatial regions from which we extracted the spectra shown in the lower panels; *Panel 3:* The value of the velocity offset of the broad emission-line wings (Δv) at each pixel; *Panel 4:* The value of the emission-line width (W_{80}) at each pixel. *Panel 5:* Signal-to-noise ratio of the peak flux density of the [O III] emission-line profile at each pixel. The contours show the morphology of line-free continuum emission (collapsed around a ≈200 Å wavelength region centred on [O III]λ5007) indicated by lines of constant signal-to-noise ratio, starting at 15σ with increments of 10σ. The stars in each panel show the position of the peak of this continuum emission. *Lower panels:* Continuum-subtracted spectra extracted from the individual spatial regions indicated in Panel 2.

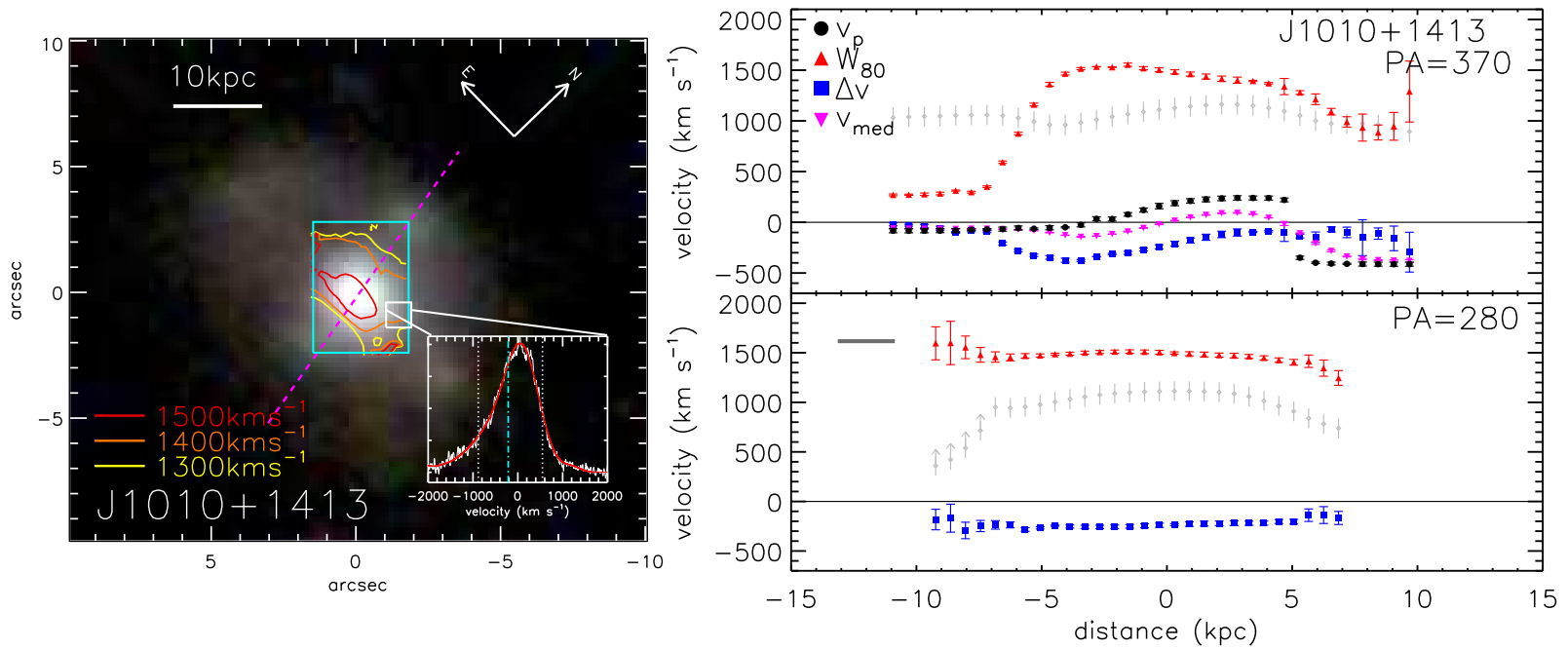

Figure 4.6: Our IFU data and SDSS image from an example object (J1010+1413) in our sample. The equivalent plots for the rest of the sample can be found in Section 4.8. *Left:* Three colour (*g*, *r*, *i*) SDSS image. The cyan box shows the field-of-view of our GMOS-IFU observations. The contours show values of W_{80} and highlights the spatial distribution where the [O III] emission-line profiles are broadest (see Fig. 4.5). The dashed line shows the kinematic "major axis" defined in Section 4.4.3. We also show an example [O III] emission-line profile extracted from the highlighted spatial region (white box; for curve and line definitions see Fig. 4.5). *Right upper:* [O III] velocity profiles (using the velocity definitions described in Section 4.4.1) along the kinematic "major axis" indicated in the left panel. Empty red triangles in Figures 4.13–4.27 are where the S/N of the spectra are low and the emission-line widths cannot be well characterised (see Section 4.4.2). The grey diamonds indicate the flux ratio: $1000 \times \log([\text{O III}]/\text{H}\beta)$. *Right lower:* Velocity profiles taken perpendicular to the kinematic "major axis" indicated in the left panel. The solid horizontal bar indicates the typical seeing of the observations (i.e., 0.″7). For this source very broad emission-line profiles ($W_{80} \gtrsim 800\,\mathrm{km\,s^{-1}}$) with a velocity offset of $\Delta v = -300\,\mathrm{km\,s^{-1}}$ are found over the full extent of the field-of-view ($\approx 16\,\mathrm{kpc}$). Extended broad emission is found in all of the objects in our sample but with a variety of morphologies.

We significantly detect [O III] emission to the edges of the IFU field-of-view in all sixteen sources (i.e., over $\geq$10–20 kpc; see discussion in Section 4.5.1). These extended emission-line regions enable us to trace the ionised gas kinematics over these scales. In Figure 4.5 we show example velocity maps of $v_{\rm p}$, W_{80} and Δv (for the target J1010+1413) that were created by measuring these quantities across the field-of-view following the procedure outlined in Section 4.4.2 (see Fig. 4.13–4.27 for these maps for the other targets). The spectra used to calculate these values are from averaging over 3×3 pixels (i.e., $\approx 0.''6$; comparable to the seeing of the observations) at the position of every pixel. At each position we measured the velocities from the fits to the [O III] emission-line profiles but only if it was detected in the spectra with a signal-to-noise ratio ≥ 7. In Figure 4.5 we also show the peak signal-to-noise ratio [$(S/N)_{\rm peak}$] map which is the ratio of the peak flux density of the fitted [O III] emission-line profile to the noise in the spectrum at each pixel position. These maps are discussed in Section 4.5.

To further aid our analyses we also produced velocity profiles along two axes through the IFU data cubes for each source (shown in Fig. 4.6 and Fig. 4.13–4.27). We firstly defined a "major axis" for each source based upon the velocity peak maps ($v_{\rm p}$; e.g., Fig. 4.5). The positional angle (PA) of the "major axis" for each source was chosen such that the velocity shear of the $v_{\rm p}$ map was the maximum. For a source where $v_{\rm p}$ traces galactic rotation this "major axis" corresponds to the kinematic major axis of the galaxy (for a discussion see Section 4.5.2). The second axis was taken perpendicular to the "major axis" (see e.g., Fig. 4.6). Using the PAs defined above we produced pseudo-long-slit spectra with a slit-width of five pixels ($\approx 0.8''$–$1''$). We obtained the spectra along each slit (from averaging over a length of 3 pixels) and calculated the velocity measurements outlined in Section 4.4.1. In these velocity profiles we also plot the ratio of the [O III] to Hβ emission line fluxes, plotting the 3σ lower-limit on this ratio when Hβ is not detected above 3σ.

4.5 Results

Using Gemini-GMOS IFU data we study the spatially resolved properties of the [O III]λλ4959,5007 and Hβ emission lines of sixteen luminous type 2 AGN (Table 4.2) chosen from our well constrained parent sample (described in Section 4.3.1; see Fig. 4.1

and Fig. 4.2). In Figure 4.5 and Figure 4.13–4.27 we show the spatially-integrated [O III] and Hβ emission-line profiles, the velocity maps and the peak [O III] signal-to-noise ratio maps for all of the sources in our sample. In Figure 4.6 and Figure 4.13–4.27 we show SDSS images and velocity-distance profiles, and in Table 4.4 we tabulate the values that we derive from the galaxy-integrated spectra, the emission-line images and the velocity maps. In the following sub-sections we present our results for the sample as a whole, firstly presenting the sizes and morphologies of the emission-line regions (Section 4.5.1) before presenting the spatially resolved kinematics (Section 4.5.2). We give notes on the results from our IFU data for the individual sources in Section 4.8.

4.5.1 Extended emission-line regions: sizes and morphologies

Although the ionised gas kinematics are the focus of this study, it is useful to make some initial comments on the emission-line region sizes and morphologies to compare to previous studies and to aid our later discussion. We detect [O III] emission over physical spatial extents of $\geq$10–20 kpc (i.e., in some cases the [O III] emission is extended beyond the IFU field-of-view). This is consistent with other studies that have shown that luminous AGN can have emission-line regions up to tens of kiloparsecs in size (e.g., Bennert et al. 2002; Humphrey et al. 2010; Greene et al. 2011; Schirmer et al. 2013; Harrison et al. 2012a; Husemann et al. 2013; Liu et al. 2013a; Hainline et al. 2013). In Figure 4.7 we show the peak [O III] signal-to-noise maps, for the whole sample, overlaid with contours showing the continuum-free [O III]λ5007 images (i.e., wavelength collapsed images around the emission line). We fit single ellipses to the [O III] emission-line images to calculate the semi-major axis ($R_{[\mathrm{O\ III}]}$; Table 4.4). The range of sizes we get from this method are $R_{[\mathrm{O\ III}]} = 1.5$–$4.3$ kpc, similar to, but generally higher than, the ULIRG-AGN composites observed in Rodríguez Zaurín et al. (2013). We note that if we subtract the typical seeing of the observations (see Table 4.4), in quadrature, from these size measurements they are reduced by ≈20% with a *worst-case* scenario of ≈50% if the seeing reached $0.''9$.[7] Based on a comparison to high-resolution imaging Rodríguez Zaurín et al. (2013) suggest that $R_{[\mathrm{O\ III}]}$ is an over-estimate of the emission-line region size for their sample; however, using

[7] The one source that has a $R_{[\mathrm{OIII}]}$ value smaller than $0.''9$ (i.e., our most pessimistic value of the seeing across the whole sample) was taken under good conditions of $\approx 0.''6$ and is therefore spatially resolved.

the kinematics of our IFU data we commonly find spatially resolved emission over much larger extents (see Section 4.5.2 and Table 4.4) and therefore find that $R_{[\mathrm{O\ III}]}$ is probably an underestimate of the size of the emission-line regions in our sources. Although we do not use identical methods, our observed sizes are comparable to, but towards the lower end of, those seen in the more luminous type 2 quasars in Liu et al. (2013a) as is expected by the [O III] size-luminosity relationship (e.g., Bennert et al. 2002; Hainline et al. 2013).

In agreement with previous studies of radio-quiet AGN (e.g., Husemann et al. 2013; Liu et al. 2013a, 2014) we find that the emission-line regions in our sample are predominantly round or moderately elliptical (Fig. 4.7). However, we find tentative evidence that radio excess sources (i.e., those with the strongest evidence of radio emission above that expected from star formation) have a higher incidence of extended and irregular morphologies. It has previously been shown that radio-loud quasars have a higher incidence of irregular morphologies than their radio-quiet counterparts (Liu et al. 2013a and references there-in). Although the radio data presented here are of insufficient spatial resolution to establish a direct (or lack there-of) connection, our results may imply that the presence of radio-AGN activity, even at modest luminosities, is connected to the morphologies of their emission-line regions (see also Husemann et al. 2013 and Section 4.8). Alternatively, the "radio excess" in these sources could be due to shocks that could also be responsible for the irregular emission line regions that we observe in Figure 4.7 (see Zakamska & Greene 2014). Multi-frequency high-resolution radio imaging is required to determine the origin and morphology of the radio emission in these objects.

4.5.2 Spatially-resolved ionised gas kinematics

Multiple kinematic components (i.e., multiple narrow and broad components) are seen in the galaxy-integrated emission-line profiles of the sources in our sample (Fig. 4.5; Fig. 4.13–4.27). There are several possible origins for these kinematic components such as merging nuclei, merger remnants or merger debris, halo gas, rotating gas discs and outflowing or inflowing gas. Indeed, previous spatially-resolved spectroscopy of type 2 AGN has shown that multiple kinematic processes are likely to contribute to the overall emission-line profiles of ionised gas (e.g., Holt et al. 2008; Fischer et al. 2011; Villar-Martín et al. 2011; Rupke & Veilleux 2013). By studying the spatially resolved veloc-

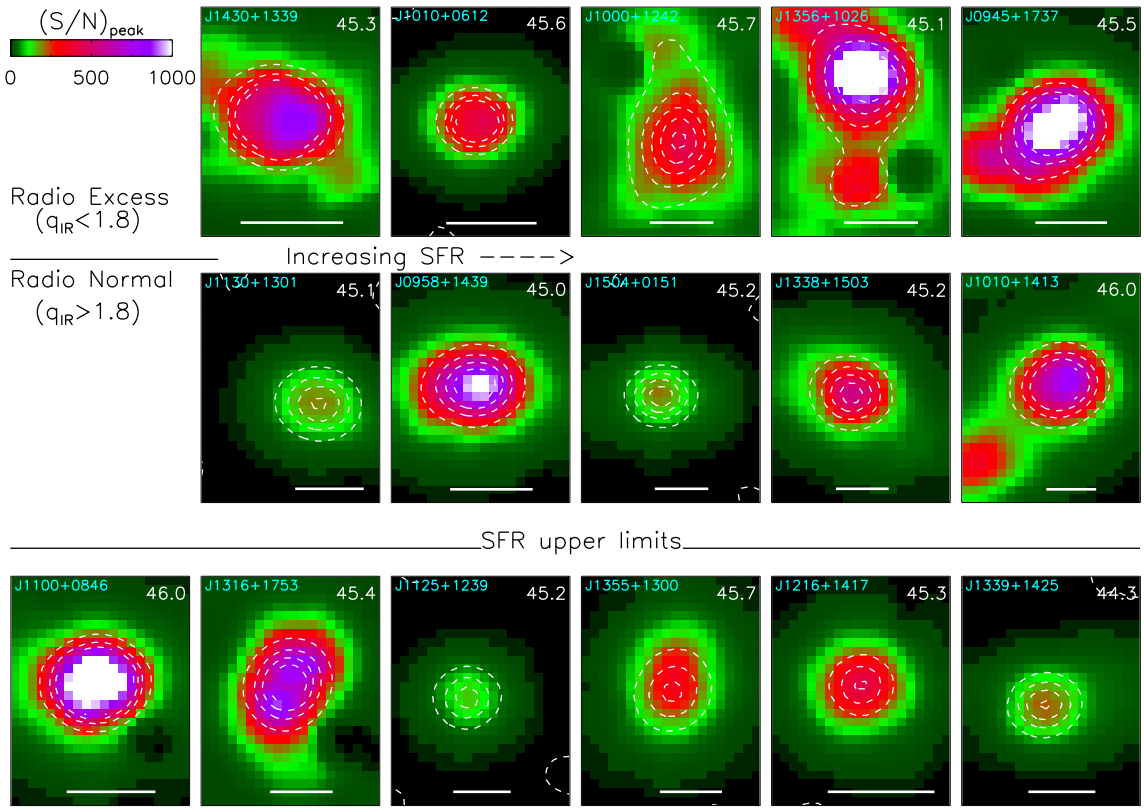

Figure 4.7: The [O III] peak signal-to-noise ratio maps (see Section 4.4.3) for all sixteen type 2 AGN in our sample. We have split the maps for the targets by radio excess (top row), radio normal (middle row) and those with only upper limits on their SFRs, for which we cannot determine their radio excess parameter (bottom row; see Table 4.2). The top two rows are arranged by SFR from the lowest (left) to the highest (right). The dashed contours show the morphology of the wavelength collapsed [O III]λ5007 images. The horizontal bars represent 3 kpc in extent. The numbers in the top-right of each map is the AGN luminosity for that source ($\log[L_{\rm AGN};{\rm erg\,s^{-1}}]$; Table 4.2). The [O III] images are predominantly round or moderately elliptical and there is tentative evidence that the radio excess sources show a higher incidence of irregular morphologies.

ity maps, velocity profiles and peak signal-to-noise maps from our IFU data (Fig. 4.5; Fig. 4.6; Fig. 4.13–4.27) we can distinguish between these scenarios and characterise individual kinematic components. Although the focus of our study is to identify and characterise galaxy-wide ionised outflows, in order to isolate the kinematics due to outflows we must also investigate these other kinematic features. In Section 4.5.2 we give a qualitative description of the observed kinematics due to galaxy rotation and merger features, including candidate dual AGN (summarised in Table 4.4), and in Section 4.5.2 we describe the outflow kinematics. The ionised gas kinematics for individual sources are described in Section 4.8. We note here that most of the analysis is described on the basis of inspecting our velocity maps and velocity-distance profiles; however, we checked that these maps are a reasonable representation of the data by inspecting the spectra extracted from several regions across the IFUs (these spectra are shown in Fig. 4.5 and Fig. 4.13–4.27).

Ionised gas kinematics: galaxy rotation, mergers and dual AGN

Rotating gas discs will produce regular velocity fields, with a gradient of blue to red and relatively narrow emission-line profiles (i.e., $W_{80} < 600\,\mathrm{km\,s^{-1}}$). As discussed in Section 4.4.1 the emission-line peak velocity ($v_{\rm p}$; see Fig. 4.4) predominantly traces the luminous narrow emission-line components in our data. We find regular v_p velocity fields and velocity profiles, indicative of tracing galaxy rotation (e.g., Courteau 1997), for seven of the sixteen objects in the sample. We give these a classification of "R" in Table 4.4 and give a justification for this, for individual sources, in Section 4.8. This interpretation of rotating discs is often supported by the kinematic "major axis" (defined in Section 4.4.3) being aligned with the morphological major axis in the disc-like galaxies revealed in the SDSS images and/or the optical continuum seen in our IFU data. Indeed, it has previously been observed that the narrow-components (or "cores"; i.e., with the broad-wings removed) of ionised emission-line profiles, can be good tracers of stellar dynamics (i.e., traces galactic rotation and/or stellar velocity dispersion) or molecular gas disks (e.g., Greene & Ho 2005; Barth et al. 2008; Barbosa et al. 2009; Rupke & Veilleux 2013; but see Zakamska & Greene 2014). Further confirmation that the v_p velocity fields are tracing rotation would require detailed kinematic analysis (e.g., Courteau 1997; Krajnović et al. 2006) that is beyond the scope of this paper. In a further five sources we see a veloc-

KINEMATIC MEASUREMENTS AND EMISSION-LINE REGION SIZES

Name	$\langle W_{80}\rangle$	$W_{80,\max}$	$\langle\Delta v\rangle$	$\lvert\Delta v_{\max}\rvert$	$\langle v_{02}\rangle$	$\Delta v_{\mathrm{med,max}}$	Gal. Kinematics	$R_{[\mathrm{O\ III}]}$	D_{600}
	($\mathrm{km\,s^{-1}}$)	($\mathrm{km\,s^{-1}}$)	($\mathrm{km\,s^{-1}}$)	($\mathrm{km\,s^{-1}}$)	($\mathrm{km\,s^{-1}}$)	($\mathrm{km\,s^{-1}}$)		(kpc)	(kpc)
(1)	(2)	(3)	(4)	(5)	(6)	(7)	(8)	(9)	(10)
J0945+1737	1009	1284	−273	284	−1511	138	I	2.7±1.6	≥12
J0958+1439	815	904	−46	107	−866	190	R	2.6±1.4	≥10
J1000+1242	795	873	−58	171	−761	311	R/I	4.3±1.8	14
J1010+1413	1449	1525	−229	350	−1523	299	R/I	3.9±2.3	≥16
J1010+0612	1280	1468	−95	216	−1267	138	R	1.6±1.3	≥6
J1100+0846	1066	1367	−30	148	−1192	55	R	1.9±1.3	≥10
J1125+1239	1285	1574	−265	424	−1547	73	F	2.9±2.0	≥9
J1130+1301	778	849	149	173	−616	140	R	2.8±1.7	8
J1216+1417	1228	1456	124	230	−1115	40	F	1.5±1.1	≥6
J1316+1753	1127	1169	−191	326	−1216	500	R/I	3.1±1.8	≥14
J1338+1503	890	1085	124	182	−813	145	R/I	3.5±2.2	≥13
J1339+1425	672	724	147	178	−505	84	R	2.5±1.7	6
J1355+1300	667	953	−184	277	−797	71	R	3.5±1.8	≥6
J1356+1026	900	964	−215	544	−1049	523	I	3.1±1.5	≥11
J1430+1339	822	1042	−152	268	−999	439	R/I	1.8±1.1	≥9
J1504+0151	1184	1181	−495	520	−1739	149	R	2.9±2.1	≥7

Table 4.4: NOTES:
Velocity values and sizes derived from the galaxy-integrated spectra and velocity maps shown in Figure 4.5 and Figures 4.13–4.27 (see Section 4.4.1 and Fig. 4.4 for velocity definitions). (1) Object name; (2) value of the [O III] emission-line width, W_{80}, derived from the galaxy-integrated spectra; (3) maximum value of W_{80} from the spatially resolved maps (with a 95% clipping threshold to remove spurious pixels); (4) velocity offset, Δv, derived from the galaxy-integrated spectrum; (5) absolute value of the maximum Δv in the spatially resolved maps (with 95% clipping); (6) the value of maximum [O III] velocity, v_{02}, derived from the integrated spectrum; (7) the maximum velocity shear of the median velocity, v_{med}, from the velocity maps (with 95% clipping); (8) qualitative description of the peak velocity maps: R=rotation-like velocity fields; R/I=red-blue velocity gradient but irregular velocity field; I= irregular velocity field; F=no velocity gradients (see Section 4.5.2); (9) observed semi-major axis of the [O III] emission-line region from fitting an ellipse with uncertainties that are the typical seeing (i.e., $0.''7$); (10) total projected extent of observed broad emission-line profiles (i.e., with $W_{80} > 600\,\mathrm{km\,s^{-1}}$) with conservative uncertainties of $2\times$ the seeing. Measurement uncertainties on the galaxy-integrated velocities are typically $< 10\%$ and therefore the dominant source of uncertainty is the physical interpretation of these values (see Section 4.5.2).

ity gradient from blue to red in the v_p velocity maps and profiles; however, the velocity fields are more irregular and therefore they may not be dominated by galaxy rotation but instead may trace kinematics due to other processes such as merging components or outflows (given a classification "R/I" in Table 4.4; see Section 4.8 for discussion of individual cases).

We next consider kinematics due to mergers. Mergers are known to create extended emission-line regions due to companion galaxies or merger debris and have previously been observed in spatially resolved spectroscopy of AGN (e.g., Villar-Martín et al. 2011a,b; Harrison et al. 2012a). Furthermore, they may be expected to be common in our sample as $\gtrsim$60% of type 2 AGN at moderate redshifts $z \approx 0.3$–0.4 show signs of morphological disturbance at some level in *HST* imaging (Villar-Martín et al. 2012).[8] The [O III] emission-line peak signal-to-noise ratio maps (Fig. 4.7) allows us to search for faint spatially-distinct emission-line regions which could indicate companion/merging galaxies, merger debris, tidal features or halo gas. Based on these maps, five sources show spatially distinct emission-line regions with distinct velocities to the rest of the host galaxy. One of these has clear signs of major-merger activity based on the SDSS image and our IFU data (J1356+1026; Fig. 4.25), three are likely to be distinct emission-line regions (i.e., merger debris or halo gas; J0945+1737; Fig. 4.13; J1010+1413; Fig. 4.5 and J1000+1242; Fig. 4.15) and one could have several interpretations (J1316+1753; Fig. 4.21; these objects are discussed in detail in Section 4.8).

Major mergers of galaxies naturally lead to the possibility of "dual" AGN; i.e., two nuclei which are gravitationally bound and are both actively accreting material. Systematic spectroscopic searches for AGN with luminous double peaked [O III] emission-line profiles has become a popular method to identify candidate dual AGN (e.g., Wang et al. 2009; Smith et al. 2010; Liu et al. 2010; Ge et al. 2012; Comerford et al. 2013). However, these double peaks could also be due to other processes such as rotating gas disks, merging components or outflows, all illuminated by a single AGN (e.g., Fu et al. 2011, 2012; see Comerford et al. 2012 for a discussion). Two of our sources show luminous dou-

[8] We note that Villar-Martín et al. 2012 refer to low-level morphological disturbances of several types based on the classifications of Ramos Almeida et al. 2011. The number of *major mergers* observed in AGN is much lower (e.g., Cisternas et al. 2011).

ble peaks (J1316+1753 and J1356+1026) in their galaxy-integrated [O III] emission-line profiles. Based on our data, the strongest case for a dual AGN is J1356+1026 (see also Greene et al. 2012), where we observe two distinct emission-line and continuum regions (see Section 4.8 for further discussion of these two sources).

Ionised gas kinematics: galaxy-wide outflows

In the IFU data of all sixteen targets we find broad [O III]$\lambda\lambda$4959,5007 emission-line profiles across the field-of-view (i.e., $W_{80,\mathrm{max}} \approx 720$–$1600\,\mathrm{km\,s^{-1}}$; Table 4.4) with a range of maximum projected velocity offsets ($|\Delta v_{\mathrm{max}}| = 110$–$540\,\mathrm{km\,s^{-1}}$; Table 4.4). Such broad (i.e., $W_{80} \gtrsim 600\,\mathrm{km\,s^{-1}}$) and asymmetric [O III] emission-line profiles, are difficult to explain with mergers or galaxy rotation, even for the most massive galaxies, and are attributed to high-velocity outflowing gas (e.g. Heckman et al. 1981; Veilleux et al. 1995; Greene & Ho 2005; Barth et al. 2008; Nesvadba et al. 2008; Greene et al. 2011; Westmoquette et al. 2012; Harrison et al. 2012a; Liu et al. 2013b; Rupke & Veilleux 2013). As with all of these studies we favour outflow over inflow due to the exceptionally high velocities and line-widths that we observe. In the previous sub-section we isolated kinematic components due to other features (e.g., mergers and galaxy rotation) and we find that these have little effect on the observed kinematic structure of the line-width, W_{80} and also in most cases that of the velocity offset, Δv (the exceptions are J1356+1026 and J1316+1753 for which Δv is affected, see Section 4.8 for details); i.e., these maps are dominated by outflow kinematics. We therefore use these maps to describe the outflow kinematic structures and morphologies. We note that Liu et al. (2013b) use the velocity structure of the median velocity (v_{med}; Fig 4.4), in which they predominantly see a blue to red velocity gradient, as part of their outflow analysis of their IFU data of $z = 0.3$–0.6 radio-quiet luminous type 2 AGN. We observe a very similar range in maximum line-widths and v_{med} maximum velocity gradients (i.e., $\Delta v_{\mathrm{med,max}} \approx 55$–$520\,\mathrm{km\,s^{-1}}$; Table 4.4) to the objects in Liu et al. (2013b). However, by spatially resolving v_{med} we find that this quantity is predominantly dominated by the kinematics of the v_p velocity field (Fig. 4.6; Fig. 4.13–4.27) and consequently v_{med} can often be dominated by kinematics due to galaxy rotation and mergers (see Section 4.5.2). Therefore, we favour Δv over v_{med} to describe the projected outflow velocity offset for the rest of our analysis.

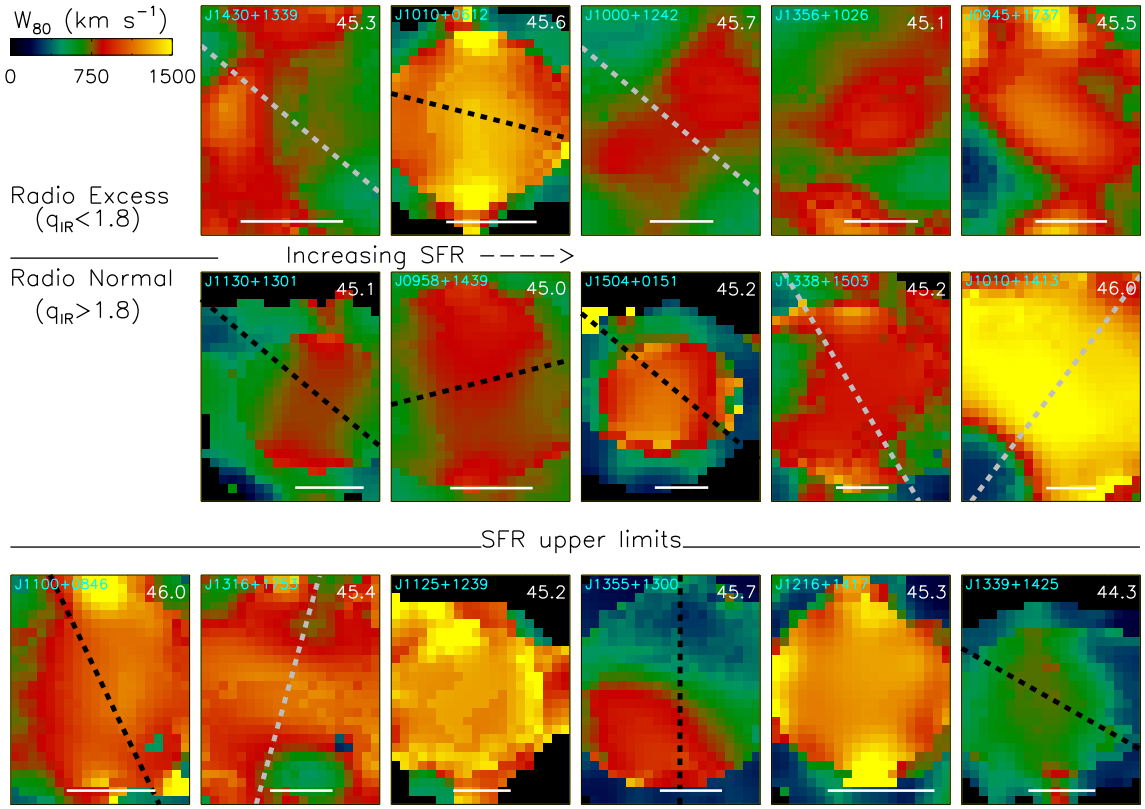

Figure 4.8: Maps of W_{80} for all sixteen type 2 AGN in our sample that illustrate the spatial extent and morphology of the outflows (Section 4.5.2). The maps are ordered in an identical manner to Fig. 4.7. The dashed lines correspond to the "major axes" based on the kinematics of the narrow emission-line components (Section 4.4.3). Black dashed lines are those with blue to red velocity gradients indicative of rotation (i.e., "R" in Table 4.4) and grey are those with irregular blue to red velocity gradients (i.e., "R/I" in Table 4.4). Sources without a clear blue to red velocity gradient do not have these "major axes" shown. The solid horizontal bars represent 3 kpc in extent and the number in the top-right of each map is $\log[L_{\rm AGN}; {\rm erg\,s^{-1}}]$ for that source. We observe a wide variety in the morphology of the kinematically disturbed ionised gas and there is no obvious connection between outflow morphology and SFR, radio excess or AGN luminosity.

For an outflow consisting of ionised clouds (observable in [O III] emission) embedded in a bulk outflow (e.g., Heckman et al. 1990; Crenshaw & Kraemer 2000) the projected velocity offsets will be sensitive to inclination effects while the emission-line widths (i.e., W_{80}) are more likely to reflect typical bulk motions and be less sensitive to inclination (also see discussion in Harrison et al. 2012a). We therefore concentrate on the W_{80} maps to investigate the sizes and morphologies of the outflows (Fig. 4.8), comparing them with the Δv maps when appropriate (discussed in Section 4.8 for individual objects). The *observed* outflow velocities and morphologies will also depend on other factors. For example, an outflow with the far side obscured by dust can explain the excess of blue wings in [O III] emission-line profiles (e.g., Heckman et al. 1981; Vrtilek 1985; Veilleux 1991), while outflowing redshifted components can be explained if the outflow is highly inclined and/or is extended beyond the likely obscuring material (e.g., Barth et al. 2008; Crenshaw et al. 2010; Greene et al. 2012; Rupke & Veilleux 2013). We observe both red and blue velocity offsets in our sample (Table 4.4). A range of structures of outflows have been observed in galaxies both with and without powerful AGN, including spherically-symmetric outflows and bi-polar superbubbles (e.g., Veilleux et al. 1994; Greene et al. 2012; Liu et al. 2013b; Rupke & Veilleux 2013). Detailed modelling of the outflow kinematics of individual objects is beyond the scope of this paper; however, we briefly describe the morphology and kinematics of the outflows that we observe in our sample below (we describe individual objects in more detail in Section 4.8).

We define the quantity D_{600} (values in Table 4.4) which is the maximum projected spatial extent of the broad [O III] emission-line profiles (with $W_{80} > 600\,\mathrm{km\,s^{-1}}$; i.e., where the kinematics are likely to be dominated by outflows) based upon the velocity profiles (Fig. 4.6 and Fig. 4.13–4.27). The outflow features are located over large extents in all sources ($D_{600} \gtrsim$ [6–16] kpc; Table 4.4) with the spatial extents being mostly lower limits due to the limited field-of-view of our observations. We note that in most cases the broad [O III] emission is clearly spatially extended, due to the morphological or kinematic structure that we observe (see below) and in all cases it is extended beyond the seeing; however, a conservative uncertainty on these D_{600} measurements would be $\approx 2\times$ seeing (see Table 4.4). Although our sample was initially selected to have luminous and broad [O III] emission-line components (see Section 4.3.1), these results demonstrate that when

these components are seen in the one-dimensional spectra of luminous type 2 AGN (as is the case for at least 45±3% of objects; see Section 4.3.1 and Fig. 4.2), they are always found over galaxy-wide scales. To assess how confident we can be of the fraction of extended ionised outflows within our selection criteria we ran Monte Carlo simulations. To do this, we took 246 mock galaxies (i.e., the number from the parent catalogue that met our selection criteria; Section 4.3.1), assigned them as either "extended" or "not-extended" (in various ratios) and randomly drew 16 objects from this sample 10^4 times. We found that, at most, 30% of the sources can be "not-extended" in the parent population for the probability of selecting 16 "extended" sources by random chance to be $\leq$0.3% (i.e., the 3σ confidence level). In other words, when broad and luminous emission-line components are observed in one-dimensional spectra (i.e., when $\gtrsim$30% of the ionised gas appears to be outflowing; Section 4.3.1) of luminous ($L_{[\mathrm{O\ III}]} > 5 \times 10^{41}\,\mathrm{erg\,s^{-1}}$) $z < 0.2$ type 2 AGN, we can be confident, with 3σ significance, that in *at least* 70% of instances these features are extended on kiloparsec scales or greater.

In Figure 4.8 we show the W_{80} maps for the whole sample to illustrate the morphology of the outflows. From this figure we can see a large diversity in the morphology. Several of the sources show a preferential axis, which is orientated away from the galaxy "major axis" (albeit not always perpendicular); however, in some cases we require a stronger constraint on the major axis of the host galaxies to confirm the relative orientations. This is consistent with the collimated winds emerging along the minor axis seen in star-forming galaxies (e.g., Heckman et al. 1990; Rupke & Veilleux 2013). The most impressive outflows that we observe are those which have the kinematic features of ≈10–15 kpc scale super-bubbles; i.e., high-velocity bi-polar emission-line regions each side of the nucleus. Combining our IFU data with archival imaging and spectroscopic data (see Section 4.8) we identify three super-bubble candidates (one was previously known: J1356+1026; Greene et al. 2012 and, as far as we are aware, two are new: J1000+1242 and J1430+1339; see Section 4.8). In two cases (J1356+1026 and J1430+1339) we only observe the base of these bubbles and therefore require IFU observations with a larger field-of-view to fully characterise the kinematics of the outflow structure. In the third case (J1000+1242) we see a clear blue and red sided outflow. Similar outflows have been seen in galaxies both with and without luminous AGN (e.g., Veilleux et al. 1994; Greene

et al. 2012; Rupke & Veilleux 2013).

In four of our targets the morphologies of the outflows are circular (Fig. 4.8) with reasonably constant W_{80} and Δv values seen across the extent of the emission-line regions. This kinematic structure is seen in the majority of the more luminous type 2 AGN in Liu et al. (2013b) who argue that these structures are characteristic of spherically symmetric, or wide-angle bi-conal outflows, and a power-law [O III] surface-brightness profile (see Liu et al. 2014 for similar observations of type 1 AGN). We note that circular morphologies could (at least partially) be an artefact of the fitting routine since in areas of low surface brightness only single Gaussian components are fit and we are not able to fully characterise the emission-line profile (see Section 4.4.2); however, this is not likely to be the full explanation for the observed morphologies (see Section 4.8; also see Fig. 5 of Liu et al. 2013b). Finally, in one source (J1355+1300) we observe a spatially distinct high-velocity region, offset from the nucleus, that has a few possible interpretations including a small-scale outflowing bubble (see Section 4.8 for a discussion).

4.5.3 Outflow properties: estimates of mass, energy and momentum

The mass, energy and momentum being carried by galaxy-wide outflows are important quantities to constrain in order to understand the role that outflows play in galaxy formation (discussed in Section 4.6.2) and to also help determine the physical mechanisms that are driving them (discussed in Section 4.6.1). Outflows are likely to be entraining gas in multiple phases (i.e., ionised, molecular and neutral) and multiple gas phase observations are required to fully characterise the outflow properties (e.g., Shih & Rupke 2010; Mahony et al. 2013; Rupke & Veilleux 2013). However, the warm ionised gas, which we observe in our observations, provides initial information on the outflows in this sample and could represent a large fraction of the overall mass and energy of the total outflows, as has been shown for some AGN (e.g., Rupke & Veilleux 2013). The kinematic structures of the outflows across our sample are diverse and complex (see Section 4.5.2) which makes accurate characterisation of the outflows challenging without doing detailed kinematic modelling of individual systems. However, as is often invoked throughout the literature, we can apply some simple outflow models to the whole sample to provide first order constraints on the mass, energy and momentum involved in the outflows and to

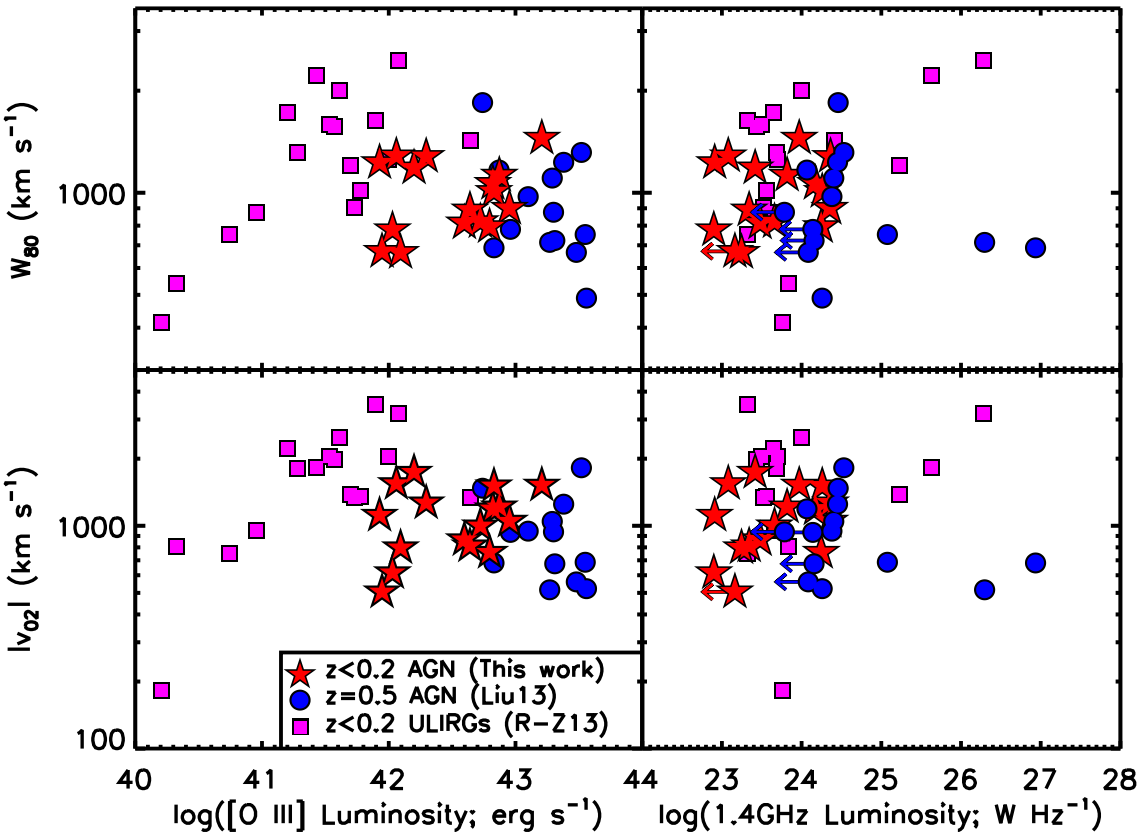

Figure 4.9: Line-width (W_{80}) and maximum velocity (v_{02}) versus [O III] luminosity and 1.4 GHz radio luminosity for our targets (red stars; see Table 4.2 and Table 4.4). Also shown are $z \approx 0.3$–0.6 type 2 quasars (blue circles; Liu et al. 2013b) and $z < 0.2$ ULIRG–AGN (magenta squares; Rodríguez Zaurín et al. 2013). High velocity and disturbed ionised gas is found in AGN over four orders of magnitude in both [O III] and radio luminosity; however, no clear trends are observed between these quantities from these samples.

enable a direct comparison to other studies. As most of the calculations outlined below require measurements of the Hβ luminosity we do not include the three sources where we did not make this measurement (see Section 4.4.2).

An important quantity for measuring ionised gas masses, and hence mass outflow rates, is the electron density (n_e). This quantity is often measured from the emission-line ratio [S II]λ6716/λ6731 which is sensitive to electron density (e.g., Osterbrock & Ferland 2006). The [S II] doublet is not covered in our IFU observations; however, using single-component Gaussian fitting to the SDSS spectra we find that the emission-line ratios for our sources are in the range [S II]λ6716/λ6731 = 0.8–1.2, corresponding to a range in $n_e \approx 200$–$1000\,\mathrm{cm}^{-3}$ with a median of $n_e = 500\,\mathrm{cm}^{-3}$ (Osterbrock & Ferland 2006; assuming $T_e = 10^4$ K). This range of n_e is in agreement with that previously found for type 2 AGN (e.g., Greene et al. 2011). We note that these are average electron densities within the SDSS fibre and the values for the *outflowing* kinematic components are unknown and have the potential to be outside of the electron density range that the [S II]λλ6716,6731 doublet is sensitive to (i.e., $n_e \gtrsim 10^{4-5}\,\mathrm{cm}^{-3}$; Osterbrock & Ferland 2006; see discussion in Holt et al. 2011 and Rodríguez Zaurín et al. 2013), providing a source of uncertainty in the mass and energy outflow rates in *all* studies that use this method. However, we note that Greene et al. (2011) provide convincing arguments that the emission-line regions in their $z < 0.5$ radio-quiet type 2 AGN are likely to be clumpy and that standard mass estimates (such as those we derive below) are likely to be under-estimated.

The observed ionised gas mass (i.e., the gas which is emitting in Hβ) can be estimated assuming purely photoionised gas with "Case B" recombination (with an intrinsic line ratio of Hα/Hβ = 2.9) and an electron temperature of $T = 10^4$ K, following Nesvadba et al. (2011) and Osterbrock & Ferland (2006), using the relation:[9]

$$\frac{M_{\mathrm{gas}}}{2.82\times10^{9}\mathrm{M}_{\odot}} = \left(\frac{L_{\mathrm{H}\beta}}{10^{43}\,\mathrm{erg\,s}^{-1}}\right)\left(\frac{n_e}{100\,\mathrm{cm}^{-3}}\right)^{-1} \tag{4.5.2}$$

[9]To be consistent with Liu et al. (2013b), Equation (2) is given in the exact form that is provided in Nesvadba et al. (2011). However, we note that if you follow section 4.2 in Osterbrock & Ferland (2006) with the appropriate value for the recombination coefficient of Hβ for the conditions described (i.e., $\alpha_{\mathrm{H}\beta}^{\mathrm{eff}} = 3.03\times10^{-14}$ cm^3 s^{-1}) the normalisation constant in Equation 4.5.2 is 6.78×10^8 M$_\odot$. This factor of four difference to the quoted normalisation constant has no significant bearing on our order of magnitude estimates of the gas mass.

This relationship between the observed line-emitting gas mass, n_e and $L_{\mathrm{H}\beta}$ (or an equivalent using $L_{\mathrm{H}\alpha}$) is commonly adopted in studies of outflows (e.g., Holt et al. 2006; Genzel et al. 2011; Rodríguez Zaurín et al. 2013; Liu et al. 2013b; Schnorr-Müller et al. 2014) with normalisation factors that vary within a factor of a few, depending on the exact assumptions. Using our extinction un-corrected $L_{\mathrm{H}\beta}$ values (Table 4.2), we obtain total observed ionised gas masses of $M_{\mathrm{gas}} = (2\text{–}40) \times 10^7$ M$_\odot$, assuming the commonly adopted $n_e = 100\,\mathrm{cm}^{-3}$ (e.g., Liu et al. 2013b), or $M_{\mathrm{gas}} = (0.4\text{–}8) \times 10^7$ M$_\odot$ assuming our median value of $n_e = 500\,\mathrm{cm}^{-3}$. We note that the ionised gas phase will make up only a fraction of the *total* gas content. For example, taking a typical SFR for our targets (40 M$_\odot$ yr^{-1}) and assuming a star forming region of ≈ 1 kpc would imply molecular gas masses of $\approx 10^{10}$ M$_\odot$ (Genzel et al. 2011)

The simplest method that we can use to estimate the total kinetic energy in the outflows is the following,

$$E_{\mathrm{kin}} = \frac{1}{2} M_{\mathrm{gas}} v_{\mathrm{gas}}^2, \tag{4.5.3}$$

Following Liu et al. (2013b) we assume $n_e = 100\,\mathrm{cm}^{-3}$ and that all of the observed ionised gas is involved in the outflow[10] with a bulk-outflow velocity $v_{\mathrm{gas}} = W_{80}/1.3$ (suitable for the spherically symmetric or wide-angle bi-cone outflow models outlined Liu et al. 2013b; see also Harrison et al. 2012a for different arguments on using line-widths to estimate the bulk velocities). Across the sample this leads to total kinetic energies of $E_{\mathrm{kin}} = (0.5\text{–}50) \times 10^{56}$ erg. Assuming the typical maximum radial extent of the outflows is 6 kpc (see Table 4.4) and a continuous outflow, this implies outflow lifetimes of $t_{\mathrm{out}} \approx 6\,\mathrm{kpc}/v_{\mathrm{gas}} = (5\text{–}11)$ Myrs and consequently outflow kinetic energy rates of $\dot{E}_{\mathrm{kin}} = (0.1\text{–}30) \times 10^{42}\,\mathrm{erg\,s}^{-1}$.

An alternative approach is to assume a spherical volume of outflowing ionised gas (following e.g., Rodríguez Zaurín et al. 2013; see also Holt et al. 2006), which gives mass

[10] As discussed in Section 4.5.2 not all of the ionised gas appears to be involved in an outflow. The broad kinematic components (FWHM$>$700 km s^{-1}) in the [O III] and Hβ emission lines typically contribute 30–80% of the total flux (based on Mullaney et al. 2013) which may give an estimate of the fraction of gas involved in the outflows. However, the emission-line ratios of up to Hα/H$\beta = 8$ (from Mullaney et al. 2013) implying that the intrinsic $L_{\mathrm{H}\beta}$ values (and hence total calculated masses) may be up to a factor of 10 times higher than the observed values (following Calzetti et al. 2000). Therefore, these two effects will cancel each other out to some level and this assumption is sufficient for our order-of-magnitude estimates

outflow rates of

$$\dot{M}_{\rm out,M1} = \frac{3M_{\rm gas}v_{\rm out}}{r} \tag{4.5.4}$$

and outflow kinetic energy rates of

$$\dot{E}_{\rm out,M1} = \frac{\dot{M}}{2}\left(v_{\rm out}^2 + 3\sigma^2\right) \tag{4.5.5}$$

where σ is the velocity dispersion and $v_{\rm out}$ is the outflow velocity. To match Rodríguez Zaurín et al. (2013) as closely as possible[11] we take the outflow velocity to be $v_{\rm out} = \Delta v$, the velocity dispersion to be $\sigma = W_{80}/2.355$, the outflow radius to be $r = R_{[\rm O\ III]}$ (Table 4.4) and again use $n_e = 100\,{\rm cm}^{-3}$. Using this approach (we will call "Method 1") we obtain $\dot{M}_{\rm out,M1} = 3$–$70\ {\rm M}_\odot\,{\rm yr}^{-1}$ and $\dot{E}_{\rm out,M1} = (0.3\text{–}30)\times10^{42}\,{\rm erg\,s}^{-1}$. This range in outflow kinetic energy rate is in excellent agreement with the range of values using the previous method, which we will now ignore, and the two methods agree within a factor ≤ 3 for all sources. Both of these methods provide lower limits, as we are only observing the line-emitting gas and hence the total mass involved in the outflow could be much higher (see also e.g., Greene et al. 2011; Liu et al. 2013b).

We also consider the mass and energy injection rates assuming an energy conserving bubble in a uniform medium (e.g., Heckman et al. 1990; Veilleux et al. 2005; Nesvadba et al. 2006 and references there-in), which gives the relation:

$$\dot{E}_{\rm out,M2} \approx 1.5\times10^{46} r_{10}^2 v_{1000}^3 n_{0.5}\,{\rm erg\,s}^{-1}, \tag{4.5.6}$$

where r_{10} is taken to be half the extent of the observed broad [O III] emission (in units of 10 kpc; we assume $r_{10} = 0.6$ for all sources; Table 4.4), v_{1000} are the velocity offsets in units of $1000\,{\rm km\,s}^{-1}$ (we assume $v_{1000} = W_{80}/1300$; Table 4.4) and $n_{0.5} \approx 1$, is the ambient density (ahead of the expanding bubble in units of $0.5\,{\rm cm}^{-3}$). Using this method (we will call "Method 2") we obtain values of $\dot{E}_{\rm out,M2} \approx (0.7\text{–}7)\times10^{45}\,{\rm erg\,s}^{-1}$. The mass outflow rates are then given by $\dot{M}_{\rm out,M2} = 2\dot{E}_{\rm out,M2}/v_c^2 \approx (9\text{–}20)\times10^3\ {\rm M}_\odot\,{\rm yr}^{-1}$.

We consider "Method 1" and "Method 2" to be lower and upper bounds of the mass

[11] We note that Rodríguez Zaurín et al. (2013) use a different definition of $v_{\rm out}$ to Δv; however, the two methods agree within a factor of $\approx$(1–3) with a median of 1.1. Likewise, their definition for σ agrees with $\sigma = W_{80}/2.355$ within a factor of $\approx$(1–2) and median of 1.2.

outflow rates and kinetic energy rates (see also discussion in Greene et al. 2012) and the fiducial values we will use throughout are the mean (in log space) of these two values which are $\dot{E}_{\rm out} = (0.15\text{–}45) \times 10^{44}\,{\rm erg\,s^{-1}}$ and $\dot{M}_{\rm out} = 170\text{–}1200\,{\rm M_{\odot}\,yr^{-1}}$. Comparing these values to those found using the approach followed in Liu et al. (2013a,b) provides confirmation that using these fiducial values are reasonable. They argue that the NLR in luminous type 2 AGN can be well described by relatively dense clouds embedded in a hot, low-density, volume-filling wind. A spatial profile with a constant [O III]/Hβ emission-line ratio followed by a sharp decline in this value indicates the break where the clouds become optically thin to ionising radiation (see full description in Liu et al. 2013b). In four of our sources (these are J0958+1439; J1100+0846; J1316+1753; J1339+1425; see Section 4.8) we see the same sharp decline in the [O III]/Hβ ratio (in most of the other sources this transition may happen beyond our field-of-view). For these four sources, the kinetic energies and mass outflow rates using their method (see Section 4.8) are all within a factor of ≈1–3 of the fiducial values we chose to adopt here.[12]

Finally, in preparation for our discussion in Section 4.6.1, we estimate the mean and upper and lower bounds of outflow momentum rates by taking the mass outflow rates calculated above and assuming $\dot{P}_{\rm out} = \dot{M}_{\rm out} v_{\rm gas}$.

4.6 Discussion

We have presented our IFU data for a sample of sixteen luminous type 2 AGN which traces the ionised gas kinematics (via [O III] and Hβ emission lines) over kiloparsec scales. We have decoupled the kinematics of outflows from other kinematic components, such as galaxy dynamics and mergers, and shows that energetic, galaxy-wide ionised outflows are ubiquitous in our sample. Our sample is selected from a well constrained parent sample so that we can place our observations into the context of the overall AGN population. In this section we use our observations, combined with previous observations from the literature, to discuss the likely driving mechanisms of the outflows (Section 4.6.1) and the role that these outflows may play in galaxy evolution (Section 4.6.2).

[12] Although here we use a different method to Liu et al. 2013b we verified our results using a similar method to these authors using IRAF ELLIPSE.

4.6.1 What drives the outflows?

The dominant processes that drive galaxy-wide outflows in massive galaxies and the efficiency to which they are able to couple to the gas are currently sources of uncertainty in galaxy formation models. Several possible mechanisms have been suggested to drive galaxy-wide outflows, for example: the mechanical input from stellar winds and supernovae (e.g., Leitherer et al. 1999; Heckman et al. 1990); direct radiation pressure from the luminosity of an AGN or star formation (e.g., Murray et al. 2005); the interaction of radio jets (launched by the AGN) with a clumpy and multiphase ISM (e.g., Sutherland & Bicknell 2007; Wagner et al. 2012); and AGN winds, initially launched at the accretion disk, that propagate through the galaxy and sweep up the ISM (e.g., King et al. 2011; Faucher-Giguère & Quataert 2012). In this subsection we will investigate which of these processes could be responsible for driving the outflows observed in our targets.

Morphology and structure

A possible method to distinguish between an AGN-driven and star-formation driven outflow could be the morphology and structure of the outflow. Galactic-scale star-formation driven outflows are known to propagate along low density regions, perpendicular to galaxy discs (e.g., Heckman et al. 1987; Ohyama et al. 2002; Veilleux et al. 2005). In contrast, outflows driven by an AGN on *small scales* have no relation between the orientation of the outflow and the disk in the host galaxy (e.g., Fischer et al. 2013). However, if AGN-driven outflows propagate to galaxy-wide scales they may also be forced to propagate away from the galaxy disk along a path of least resistance (e.g., Faucher-Giguère & Quataert 2012; Gabor & Bournaud 2014) which could make galactic-scale outflows driven from a nuclear star forming region or an AGN indistinguishable (see also Hopkins & Elvis 2010; Heckman et al. 2011 and Diamond-Stanic et al. 2012 for other reasons why it could be difficult to distinguish between AGN and star formation driven outflows). In some observations compact radio jets ($\lesssim$ few kiloparsec in size) are inferred to play a role, where the combination of high resolution radio data and spatially resolved spectroscopy has shown that high velocity gas (in multiple phases) is spatially co-incident with radio emission (Baldwin et al. 1980; Whittle et al. 1988; Capetti et al. 1999; Whittle & Wilson 2004; Morganti et al. 2005, 2013; Emonts et al. 2005; Leipski & Bennert 2006; Barbosa et al.

2009; Fu & Stockton 2009; Storchi-Bergmann et al. 2010; Shih et al. 2013). However, even when radio jets *are* present it appears that they may not always be fully responsible for the observed outflows and other processes are also required (e.g., Villar-Martín et al. 1999; Rupke & Veilleux 2011; Riffel et al. 2014).

The morphologies of the outflows in our targets are illustrated in Figure 4.8. In our sample we observe no obvious relationship between the morphology of the observed outflows and the SFRs, AGN luminosities or radio excess parameters of the host galaxies; i.e., irrespective of the host galaxy or AGN properties we see a range in outflow morphology including those which are escaping away from the galaxy discs. This is in broad agreement with Rupke & Veilleux (2013) who find no structural difference between the outflows in the ULIRGs with and without luminous AGN. Interestingly, all of superbubble candidates are radio excess sources (see Section 4.5.2 and Section 4.8). However, deeper and higher-resolution radio data are required to search for small and low luminosity radio jets, which we cannot identify in the FIRST data, and to ultimately determine the origin of the radio emission (see Section 4.3.4).

Outflow velocities compared to AGN and galaxy properties

Another possible method to determine the driving mechanism of outflows is to search for trends between outflow properties and properties of the host galaxy or AGN. Positive correlations have been claimed to exist between outflow properties, albeit using different observations, for each of SFR (e.g., Rupke et al. 2005b; Martin 2005; Bradshaw et al. 2013), AGN luminosity (e.g., Cicone et al. 2014) and radio luminosity (e.g., Nesvadba et al. 2011). Of course these analyses are complicated by the fact that AGN luminosity, SFR and radio luminosity are closely related (e.g., Tadhunter et al. 1998; Ivison et al. 2010b; Mullaney et al. 2012b; Chen et al. 2013) and that small duty cycles may mean that an AGN-driven outflow may be observed when the AGN itself is no longer observable (e.g., King et al. 2011; Gabor & Bournaud 2014).

In Fig. 4.9 we show that the line widths (W_{80}) and maximum velocities (v_{02}) of our sample are comparable to those found in more luminous type 2 AGN (Liu et al. 2013b)

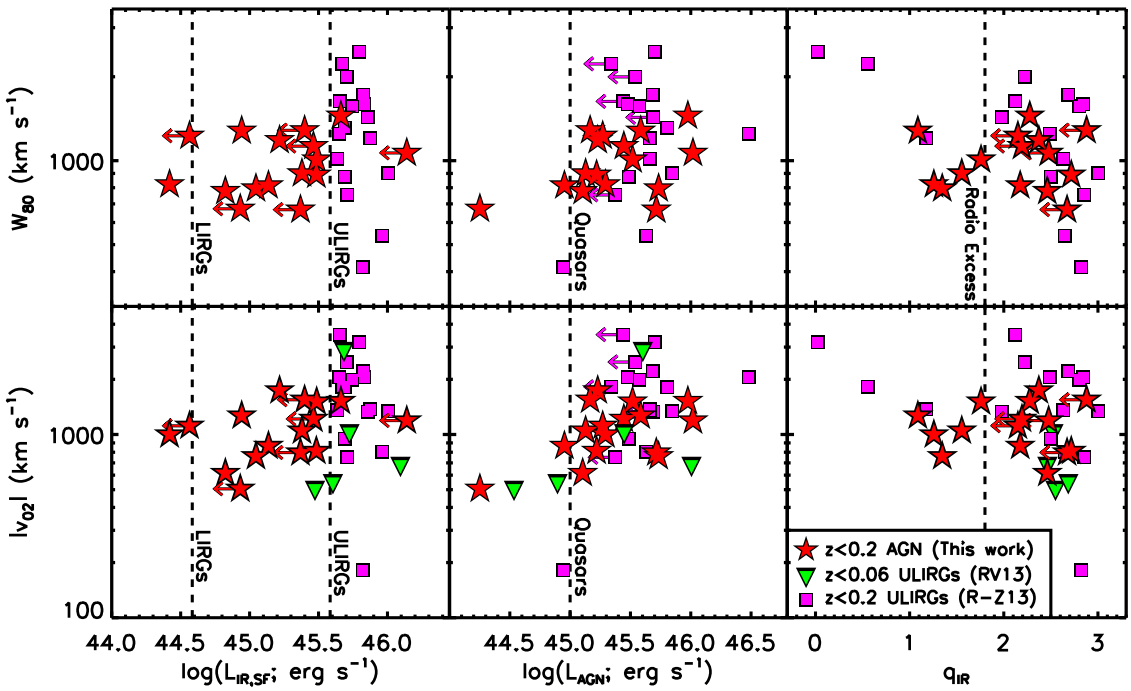

Figure 4.10: Line-width (W_{80}) and maximum velocity (v_{02}) versus infrared luminosity from star formation, AGN luminosity and q_{IR} for our targets (red stars; see Table 4.2 and Table 4.4). Also shown are $z < 0.2$ ULIRG–AGN composite galaxies (magenta squares; Rodríguez Zaurín et al. 2013) and $z < 0.06$ ULIRGs (green triangles; Rupke & Veilleux 2013). There is tentative evidence that most extreme velocities and line-widths are preferentially found in systems with high star-formation rates (i.e., ULIRGs) that host the most luminous AGN (i.e., 'quasars'). There is no such effect seen when comparing systems where there is excess radio emission AGN; however, low-level excess radio emission is difficult to identify using this method especially in high SFR systems (see Section 4.3.4).

and ULIRG-AGN composite galaxies (Rodríguez Zaurín et al. 2013).[13] We observe no clear trends between v_{02} or W_{80} and $L_{[\mathrm{O\ III}]}$, despite four orders of magnitude in [O III] luminosity. Additionally, although limited in dynamic range, we do not see any obvious correlation in W_{80} or v_{02} with radio luminosity (Fig. 4.9). These conclusions are consistent with Mullaney et al. (2013) who demonstrate that the broadest emission lines are prevalent for AGN with radio luminosities of $L_{1.4\mathrm{GHz}} \gtrsim 10^{23}\,\mathrm{W\,Hz^{-1}}$ (i.e., the range that is covered in Fig. 4.9), but found no clear trends with [O III] luminosity when taking radio-luminosity matched samples of AGN. We note that Figure 4.1 is not radio-luminosity matched so gives an apparent positive trend between [O III] luminosity and line width; see Mullaney et al. (2013) for details.

In Figure 4.10 we compare the galaxy-integrated line-widths (W_{80}) and maximum velocities (v_{02}) to the infrared luminosities from star formation ($L_{\mathrm{IR,SF}}$; a proxy for SFR), bolometric AGN luminosities (L_{AGN}) and the radio excess parameter (q_{IR}) derived in Section 4.3.4. We also compare to the ULIRG-AGN composite galaxies from Rodríguez Zaurín et al. (2013)[14] and the $z < 0.06$ ULIRGs from Rupke & Veilleux (2013) (who make these velocity measurements from various ionised emission-line species). In Figure 4.10, the only possible trend we observe is between the maximum velocity (v_{02}) and AGN luminosity, although we are limited in measurements below $L_{\mathrm{AGN}} = 10^{45}\,\mathrm{erg\,s^{-1}}$. Based on these samples, although high-velocity outflow features are observed across the samples, the most extreme velocities (i.e., $v_{02} \gtrsim 2000\,\mathrm{km\,s^{-1}}$) and line-widths (i.e., $W_{80} \gtrsim 1500\,\mathrm{km\,s^{-1}}$) appear to be predominantly found in the quasar-ULIRG composite galaxies (Fig. 4.10). This is in broad agreement with other studies of the outflows in ULIRGs and quasars, in multiple different gas phases, that find the most extreme outflows in the quasar-ULIRG composites (e.g., Harrison et al. 2012a; Westmoquette et al. 2012;

[13] Although Rodríguez Zaurín et al. (2013) do not quote the values of W_{80} and v_{02} directly, we reconstructed the emission-line profiles (from the Gaussian components given in their paper) and then measured these values directly.

[14] We fit the SEDs to the IRAS and WISE data for these sources in a consistent manner to that described in Section 4.3.4; however, we only accept AGN components if the AGN template contributes $\geq$50% of the flux at 19μm due to the difficulty in reliably identifying low-luminosity AGN in ULIRGs using this method (see Del Moro et al. 2013). Eight of these ULIRGs also have AGN luminosities derived from Spitzer infrared spectra in Veilleux et al. (2009) that we use in favour of our AGN luminosities. We found that the AGN luminosities and IR luminosities are well matched (within a factor of $\lesssim$2) between our method and that in Veilleux et al. (2009).

Veilleux et al. 2013; Cicone et al. 2014; Hill & Zakamska 2014). Further evidence that the incidence of extreme ionised outflows in quasar-ULIRG composite galaxies is high, compared to the overall population, is that 16/17 of the objects in Rodríguez Zaurín et al. (2013) have extreme ionised gas kinematics (i.e., significant broad [O III] emission-line components) which is much larger than we find for the overall optical AGN population (see Section 4.3.1), and considerably higher than expected given their moderate [O III] luminosities (i.e., $L_{[\mathrm{O\ III}]} \lesssim 10^{42}\,\mathrm{erg\,s^{-1}}$; Fig. 4.1). Furthermore, the flux-weighted average line-widths ($\mathrm{FWHM_{avg}} \gtrsim 800\,\mathrm{km\,s^{-1}}$) of these quasar-ULIRG composites are representative of the top $\approx$ 2–3% most extreme objects in Mullaney et al. (2013). This result is not sufficient to establish which process is driving the observed outflows, but instead may demonstrate that the most extreme outflows are most prevalent during an active star formation and AGN phase as is predicted by some evolutionary models (e.g., Sanders et al. 1988; Hopkins et al. 2008).

Finally, we note that Mullaney et al. (2013) show that the fraction of sources with their ionised gas dominated by outflows, was considerably higher for sources with moderate-to-high radio luminosities ($L_{1.4\,\mathrm{GHz}} \gtrsim 10^{23}\,\mathrm{W\,Hz^{-1}}$). Based on the analysis of the radio emission in our sources and the comparison samples (Section 4.3.4; Figure 4.10), star formation could contribute considerably to the radio emission at these luminosities. Additionally, as noted by Zakamska & Greene (2014), radio emission could be produced by shocks due to outflows that were driven by e.g., quasar winds. Further analysis of the parent population is required to establish the physical process that is driving the trend between radio luminosity and ionised outflows.

Coupling efficiencies and momentum fluxes

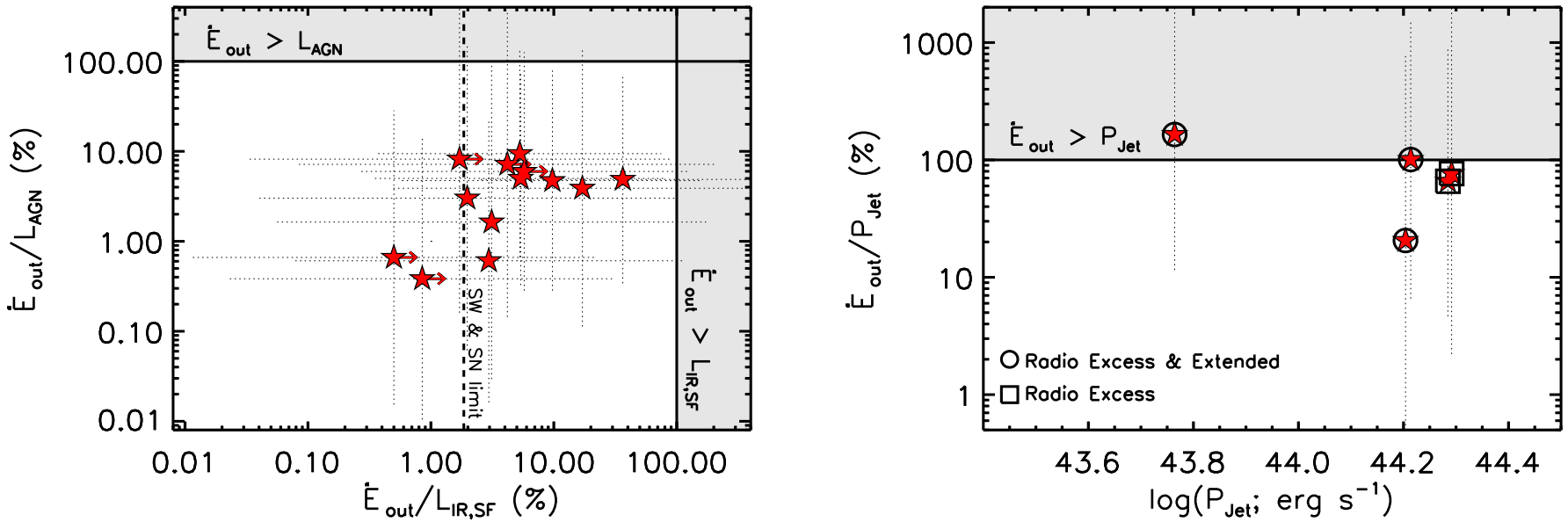

Figure 4.11: *Left panel:* The ratio of our estimated outflow kinetic energy rates ($\dot{E}_{\rm out}$; Section 4.5.3) to the AGN luminosity (ordinate) and to the star-formation luminosity (abscissa) for the thirteen sources in our sample for which we estimated $\dot{E}_{\rm out}$. The dotted lines illustrate the ratios from using our upper and lower bounds on the $\dot{E}_{\rm out}$ values (Section 4.5.3). The shaded regions indicate where >100% coupling efficiency is required between the input energy and the gas to power the outflows. The dashed vertical line is the estimated maximum mechanical input expected from supernovae and stellar winds (see Section 4.6.1). *Right panel:* Similar to the left panel, but showing the ratio of $\dot{E}_{\rm out}$ to the estimated jet power, as a function of jet power, for the five sources with the strongest evidence of hosting radio jets (see Section 4.3.4). Based on our simplifying assumptions a similar outflow coupling efficiency is required for AGN (i.e., $\approx$ 0.5–10%) and star formation (i.e., $\gtrsim$ 0.5–40%); however, stellar winds and supernovae are less likely to be fully responsible for the observed outflows. Radio jets would require uncomfortably high coupling efficiencies to power the outflows in some cases (although see Section 4.6.1).

A popular method to investigate the likely drivers of galactic-scale outflows is to compare the energy and momentum available from each potential driver (i.e., supernovae and stellar winds, radiation pressure [from AGN or star formation], AGN winds, or radio jets) to the kinetic energy and momentum in the outflows. Although we are limited by a large uncertainty in the outflow kinetic energies (see Section 4.5.3), we have measured SFRs and AGN luminosities and have identified the sources that are most likely to host radio jets (see Section 4.3.4 and Table 4.2). In Figure 4.11 we compare the ratio of our outflow kinetic energy rates ($\dot{E}_{\rm out}$) with (1) the bolometric AGN luminosities; (2) the infrared star-formation luminosities[15] and (3) the mechanical radio jet power (estimated using the 1.4 GHz luminosity and the relationship in Cavagnolo et al. 2010). In Figure 4.12 we compare the momentum rates of the outflows ($\dot{P}_{\rm out}$) with the momentum flux output radiatively by (1) star formation (i.e., $L_{\rm IR,SF}/c$) and (2) the AGN (i.e., $L_{\rm AGN}/c$). Using these results we now explore the plausibility of different potential driving mechanisms and compare to theoretical predictions.

Figure 4.11 shows that a similar outflow coupling efficiency is required to both of the radiative output of the AGN (i.e., $\approx$0.5–10%) and that of star formation (i.e., $\gtrsim$0.5–40%), indicating that either of these processes could power the outflows if they are able to couple their energy to the gas. One way for star formation to drive an outflow is from stellar winds and supernovae. An estimate of the maximum energy injection from stellar winds and supernovae, which is used throughout the literature, is $\approx 7\times10^{41}({\rm SFR/M_\odot\,yr^{-1}})\,{\rm erg\,s^{-1}}$ (applicable for stellar ages $\gtrsim$40 Myrs and following Leitherer et al. 1999; Veilleux et al. 2005).[16] This corresponds to a maximum $\dot{E}_{\rm out}/L_{\rm IR,SF}\approx 2\%$ (following Kennicutt 1998 but correcting to a Chabrier IMF) that we indicate Figure 4.11. Based on these assumptions, stellar winds and supernovae are unlikely to be fully responsible for the observed outflows. If we instead consider a momentum driven wind with momentum deposition from the radiation pressure of stars, we expect $\dot{P}_{\rm out}=\tau L_{\rm SF,IR}/c$ (following Murray et al. 2005) that, based on our calculations, would require unrealistically high optical depths (i.e., $\tau\gg1$; see Figure 4.12). Further investigation of the possibility that star formation

[15] We note that for infrared luminous galaxies (i.e., $L_{\rm IR}\geq10^{11}{\rm L_\odot}$), the infrared luminosity makes up the bulk of the bolometric luminosity; e.g., Sanders & Mirabel 1996; Veilleux et al. 2005.

[16] If we were to follow instead Dalla Vecchia & Schaye 2008 to estimate this energy input, the values would be a factor of $\approx$2 lower.

drives the outflows could be achieved using high resolution optical-continuum imaging to measure the SFR surface densities in our targets (e.g., Murray et al. 2011; Heckman et al. 2011; Diamond-Stanic et al. 2012; Förster Schreiber et al. 2013).

The estimated coupling efficiencies between the bolometric AGN luminosity and the outflows (i.e., $\approx$ 0.5–10%) are consistent with those predicted by various models (e.g., Di Matteo et al. 2005; Hopkins & Elvis 2010; Zubovas & King 2012; Debuhr et al. 2012). However, we note that these coupling efficiencies do not tell us *how* the AGN couples to the gas. It is thought that direct radiation pressure from an AGN is unlikely to drive momentum-driven galaxy-wide outflows (e.g., King et al. 2011; Debuhr et al. 2012) and this is supported by the high outflow momentum rates we observe (Figure 4.12). However, it has been predicted that for high-accretion rate AGN, an accretion-disc wind could sweep up material and become a galaxy-wide energy-driven outflow (e.g., King et al. 2011; Faucher-Giguère & Quataert 2012; Debuhr et al. 2012; Zubovas & King 2012). These models predict momentum rates of $\dot{P}_{\rm out} \approx 10$–$40 L_{\rm AGN}/c$ on $\approx$1–10 kpc scales, that is in good agreement with our observations (Figure 4.12) as well as multi-gas-phase outflow observations of other AGN (e.g., Cicone et al. 2014; Zubovas & King 2012 and references there-in). An AGN could also couple to the gas in their host galaxies though the interaction of a radio jet with the ISM. In Figure 4.11 we show that the coupling efficiencies between the radio jet power and the outflows is estimated to be $\approx$20–160% (calculated for the sources with the strongest evidence for radio AGN activity only; see Section 4.3.4). These basic calculations may rule out radio jets being solely responsible for all of the outflows observed (Fig. 4.11; but see Section 4.8 for a discussion on the radio jets in individual objects); however these numbers are uncertain and reasonably high coupling efficiencies are predicted for outflows driven by jet-ISM interactions (e.g., Wagner et al. 2012 predict $\approx$ 10–40%).

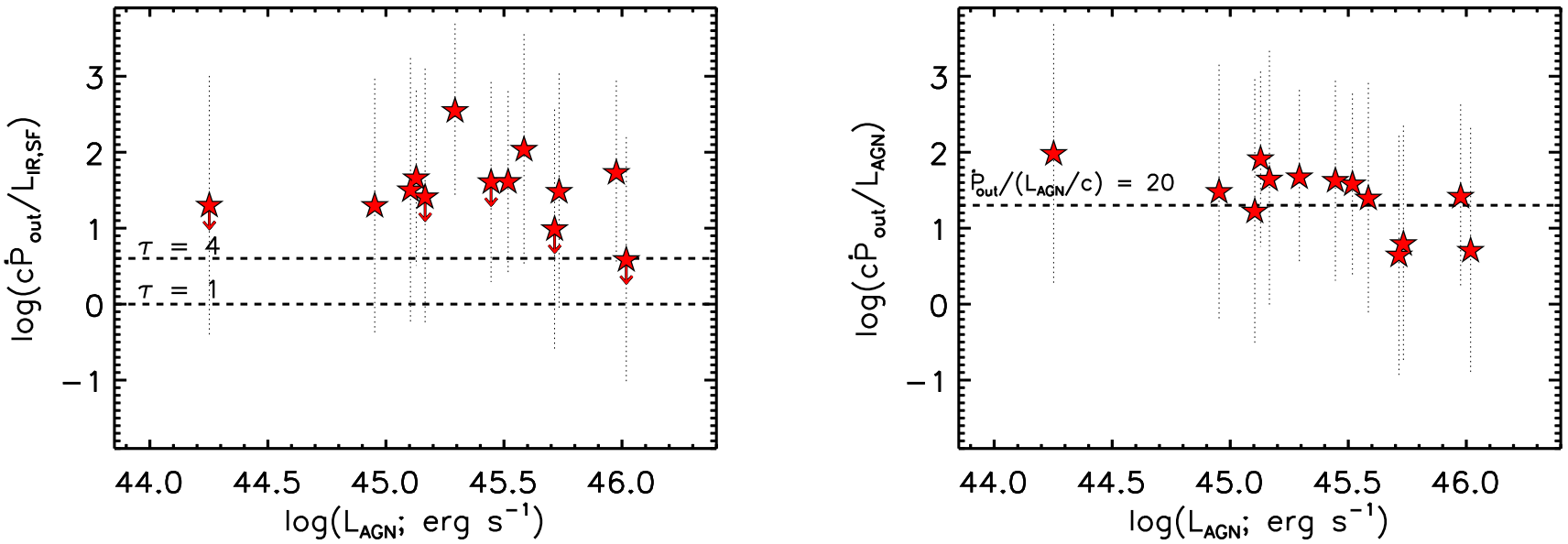

Figure 4.12: *Left Panel:* Momentum rates of the outflows ($\dot{P}_{\rm out}$) normalised to the star formation luminosity ($L_{\rm IR,SF}/c$) versus AGN luminosity. The dashed lines represent the required optical depths if the outflows are driven by radiation pressure from star formation (see Section 4.6.1). *Right Panel:* Momentum rate of the outflows normalised to the AGN luminosities ($L_{\rm AGN}/c$) versus AGN luminosity. In both panels the vertical dotted lines represent the upper and lower bounds in $\dot{P}_{\rm out}$ (see Section 4.5.3). Based on our assumptions, the outflows are unlikely to be purely radiatively driven but are broadly consistent with theoretical predictions of galactic-scale energy-driven outflows that are launched by an AGN accretion-disc wind (i.e., $\dot{P}_{\rm out} \gtrsim 10$–$40 L_{\rm AGN}/c$; e.g., Zubovas & King 2012; Faucher-Giguère & Quataert 2012; Debuhr et al. 2012).

In summary, based on our analyses we find no definitive evidence that the outflows we observe are universally driven by the AGN (either launched by accretion-disk winds or radio jets) or by star formation. However, using the arguments that we have presented we find that supernovae, stellar winds, radio jets or radiation pressure are unlikely to be solely responsible for all of the outflows that we observe. Although uncertain, we have shown that the outflows we observe have properties that are broadly consistent with predictions of energy-conserving outflows that are initially driven by accretion-disc winds. It is certainly viable that multiple processes contribute to driving the observed outflows as has been seen in local systems, where star-formation winds, nuclear winds (potentially AGN-driven) and radio jets all are playing a role (e.g., Cecil et al. 2001; Storchi-Bergmann et al. 2010; Rupke & Veilleux 2011; also see discussion on our individual targets in Section 4.8). As has been highlighted throughout this section, multi-phase (i.e., ionised, atomic and molecular) observations of the outflows, combined with high resolution multi-wavelength imaging will provide the required information to determine the relative role of these different outflow driving mechanisms in our targets.

4.6.2 What role do these outflows play in galaxy evolution?

Galaxy-wide outflows are required in galaxy formation models, driven by both star formation and AGN activity, to reproduce the observable properties of galaxies and the intergalactic medium (e.g., Silk & Rees 1998; Di Matteo et al. 2005; Hopkins et al. 2008; Dalla Vecchia & Schaye 2008 Booth & Schaye 2010; Debuhr et al. 2012; Hopkins et al. 2013a). In these models some fraction of the gas escapes from the potential of the host galaxy, regulating future star formation and black hole growth and enriching the larger-scale environment with metals. In this section we will assess what impact the outflows that we observed may have on the evolution of their host galaxies.

If we consider the estimated mass outflow rates (derived in Section 4.5.3) we find that they are $\approx$6–20 times greater than the SFRs of our targets (with one exception at 100 times [J1430+1339] and excluding upper limits). These "mass loading" values are typically higher than those observed in star-forming galaxies but similar to those seen in luminous AGN, derived from a variety of observations of outflows in different gas phases (e.g., Martin 1999; Heckman et al. 2000; Newman et al. 2012; Cicone et al. 2014). We

do not know the multi-phase outflowing gas properties of our targets; however, these observations imply that the star forming material may be rapidly depleted, as has also been suggested from molecular gas observations of a few nearby ULIRG-AGN composite galaxies (Cicone et al. 2014).

We can assess if the outflows will be able to escape the potential of their host galaxies. The escape velocities of typical type 2 AGN within the luminosity range of our sample are $\approx$ 500–1000 km s^{-1} (assuming an isothermal sphere of mass out to 100 kpc; Greene et al. 2011). These escape velocities correspond to circular velocities of $\approx$ 200–400 km s^{-1}, which are likely to be representative of the intrinsic values for our galaxies, based on those in which we identify rotation (see Section 4.5.2). If we assume the intrinsic bulk velocities of the outflows are $v_{\rm out} = W_{80}/1.3$ (see Section 4.5.3) then we have a range of outflow velocities $v_{\rm out}$ = 510–1100 km s^{-1} (with a median of 780 km s^{-1}) which are comparable to the escape velocities. The maximum projected velocities are even higher (up to $v_{02} \approx -1700$ km s^{-1}; Table 4.4). If we instead consider a $\approx 10^{11}$ M$_\odot$ galaxy inside a $\approx 10^{13}$ M$_\odot$ dark matter halo with Navarro-Frenk-White (Navarro et al. 1996) density profile, the gas is unlikely to escape unless it is travelling at $\gtrsim$1000 km s^{-1} (see the calculation in section 5.2 of Harrison et al. 2012a). Indeed, some models have shown that even massive outflows may stall in the galaxy halo, re-collapse and cool at later times (along with new fuel supplies), resulting in re-ignition of star formation and black hole growth (e.g., Lagos et al. 2008; McCarthy et al. 2011; Gabor et al. 2011; Rosas-Guevara et al. 2013; Hopkins et al. 2013b; see also Gabor & Bournaud 2014).

In summary, while it is not possible to constrain the ultimate fate of outflowing gas from observations, we have observed outflows with extremely high velocities and the estimated outflow kinetic energy rates (i.e., $\approx$ 0.5–10% of $L_{\rm AGN}$) and momentum rates ($\gtrsim$ 10–20 $\times L_{\rm AGN}/c$) are in broad agreement with the requirements of models that invoke AGN-driven outflows to regulate star formation and black hole growth in luminous AGN (e.g., Di Matteo et al. 2005; Hopkins & Elvis 2010; Debuhr et al. 2012). Even if the outflows do not escape the galaxy halos, they may be the required pre-cursor to the postulated "maintenance mode" of feedback that appears to be necessary to control the level of cooling in massive halos at later times (e.g., Churazov et al. 2005; McCarthy et al. 2011; Gabor et al. 2011; Bower et al. 2012).

4.7 Conclusions

We have presented optical IFU observations covering the [O III]λλ4959,5007 and Hβ emission lines of sixteen $z = 0.08$–0.2 type 2 AGN. Our targets were selected from a parent sample of $\approx 24,000$ AGN (Mullaney et al. 2013) and we demonstrated that they are representative of the 45±3% of luminous ($L_{[\mathrm{O\ III}]} \geq 5 \times 10^{41}$ erg s^{-1}) $z < 0.2$ type 2 AGN that have a significant fraction ($\gtrsim$30%) of their ionised gas outflowing (Section 4.3.1). The fraction of AGN with ionised outflows at lower levels will be much higher. We use infrared SED decomposition on our targets to derive SFRs ($\lesssim$ [10–100]M$_{\odot}$ yr^{-1}) and AGN luminosities ($L_{\mathrm{AGN}} = 10^{44.3}$–$10^{46.0}$ erg s^{-1}) for our targets. We also show that the radio emission in our targets (luminosity range: $L_{1.4\mathrm{GHz}} \leq 10^{24.4}$ W Hz^{-1}) is due to a combination of star formation and other processes, with five targets showing a "radio excess" above that expected from star formation and at least three of these showing spatially resolved radio emission (on scales $R_{1.4} \gtrsim 7$ kpc) that could be due to radio jets or shocks (Section 4.3.4). In summary, our targets are taken from a well constrained parent sample and are not extreme star-forming galaxies or radio loud AGN that have been the focus of many similar studies.

The main results are:

- We find extended [O III] emission-line regions over the full-field-of-view of our IFU observations (i.e., total extents of ≥10–20 kpc). In most of the sources these emission-line regions are circular or moderately elliptical; however, we observe some irregular morphologies, particularly in the radio excess sources (see Section 4.5.1).

- By tracing narrow [O III] emission-line components across the field-of-view, we identify a range of kinematic features associated with galaxy dynamics including galaxy rotation, merger debris and double nuclei. We isolate these kinematic components from any kinematics due to outflows (see Section 4.5.2).

- We find high-velocity and disturbed ionised gas (velocity widths of $W_{80} \approx 600$–1500 km s^{-1}) extended over $\gtrsim$ (6–16) kpc in all of our targets. With our knowledge of the parent sample we conclude that, ≥70% (3σ confidence level) of the outflow

features observed in the [O III] emission-line profiles of $z < 0.2$ luminous type 2 AGN are extended on kiloparsec scales (see Section 4.5.2).

- The bulk outflow velocities across the sample are $v_{\rm out} \approx 510$–$1100\,{\rm km\,s^{-1}}$, which are comparable to the galaxy escape velocities. The maximum projected gas velocities reach up to $v_{02} \approx 1700\,{\rm km\,s^{-1}}$ (see Section 4.5.2). These velocities indicate that ionised gas is currently being unbound from their host galaxies but it is not clear if it will permanently escape their host galaxy halos (see Section 4.6.2).

- We observe a range of kinematic structure in the outflows including signatures of spherical outflows and bi-polar superbubbles. In several cases the outflows are preferentially oriented away from the plane of the host galaxy. We observe no obvious relationships between the outflow kinematic structures and the AGN luminosities, SFRs or the presence or absence of radio AGN activity (see Section 4.5.2 and Section 4.6.1). However, we do find that all of our three superbubble candidates are radio excess sources.

- Based on our analyses we find that both star formation and AGN activity may contribute to driving the outflows that we observe, with no definitive evidence that favours one over the other in the sample as a whole; however, we discuss individual objects in more detail (see Section 4.6.1). By combining our observations with those from the literature, we show that kiloparsec-scale ionised outflows are not confined to the most luminous AGN, extreme star-forming galaxies or radio-loud AGN; however, we find that the most extreme ionised gas velocities (with maximum velocities: $v_{02} \gtrsim 2000\,{\rm km\,s^{-1}}$ and line-widths $W_{80} \gtrsim 1500\,{\rm km\,s^{-1}}$) are preferentially found in quasar-ULIRG composite galaxies (see Section 4.6.1).

- Although based on simplifying assumptions, we estimate kinetic energy outflow rates ($\dot{E}_{\rm out} \approx (0.15$–$45) \times 10^{44}\,{\rm erg\,s^{-1}}$) and mass outflow rates (typical $\approx 10\times$ the SFRs) that imply that considerable mass and energy are being carried in the observed outflows (see Section 4.5.3).

- It is not possible to provide *direct* evidence of the long-term impact of individual outflows; however, although uncertain, we find that the mass outflow rates, the

outflow kinetic energy rates (≈ 0.5–10% of $L_{\rm AGN}$) and the outflow momentum rates (typically $\gtrsim$10–20$\times L_{\rm AGN}/c$) are in broad agreement with theoretical predictions of AGN-driven outflows that are postulated to play a significant role in shaping the evolution of galaxies (see Section 4.6.2).

In this paper we have investigated the prevalence, properties and potential impact of galaxy-wide ionised outflows. By selecting targets for detailed observations from our well constrained parent sample we have been able to place our observations into the context of the overall AGN population. We have established that galaxy-wide ionised outflows are prevalent in AGN. Our investigation was based upon tracing the ionised gas since it is currently the only suitable gas phase for performing large statistical studies of outflows; however, it is imperative that we now obtain multi gas-phase observations of outflows from representative samples of objects, such as our targets, to fully characterise the properties and impact of galaxy-wide outflows in the global population.

4.8 Notes on individual sources

In this section we provide some notes on individual sources by highlighting relevant previous multi-wavelength observations from the literature and describing some of the key features in our IFU observations. The majority of these sources have received little or no attention previously in the literature, with the exceptions of J0945+1737, J1316+1753 and J1356+1026 that have been studied in some detail. The IFU data for all of our sources are displayed in this section (Fig. 4.13–4.27), except for J1010+1413 that can be found in Figure 4.5 and Figure 4.6 as it is used as an example in the main text.

J0945+1737

In agreement with our classifications (see Table 4.2) the source J0945+1737 has previously been identified as a LIRG with a type 2 AGN nucleus (Kim et al. 1995; Veilleux et al. 1995) and as a type 2 ("obscured") quasar by Reyes et al. (2008). It has been shown to have a single nucleus based upon *HST* observations (Cui et al. 2001). The infrared luminosity that we measure (Table 4.2) is consistent with previous measurements (Cui et al. 2001) and our AGN luminosity measurement is consistent with that derived from *Spitzer*

infrared spectroscopy (Sargsyan et al. 2008). This source has evidence for a galaxy-scale radio jet due to its radio excess, above that expected from star formation, and the extended radio emission observed in FIRST ($R_{1.4} \approx 6.6$ kpc; see Section 4.3.4 and Table 4.2).

Our IFU data for this source are shown in Figure 4.13. The [O III] peak velocity (v_p) field is irregular (Fig. 4.13) and therefore, based on these data alone, we do not attribute the v_p velocity field to galaxy rotation; however, we do note that the continuum image from our IFU data is elongated roughly in alignment with our kinematic "major axis". The high-velocity broad underlying wings in the [O III] emission-line profile are located over the full field-of-view ($\approx 8 \times 11$ kpc) but dominate in the central regions (with $W_{80} \approx 1100\,\mathrm{km\,s^{-1}}$ and $\Delta v \approx -260\,\mathrm{km\,s^{-1}}$), preferentially located along a N–S axis (i.e., with a PA ≈ 0). This is not parallel to the radio axis based on the FIRST data (PA $\approx 110^\circ$) that may disfavour a connection between a radio jet and the outflow; however, high resolution radio data are required to accurately measure the morphology and origin of the radio emission.

J0958+1439

The IFU data for J0958+1439 are shown in Figure 4.14. The data reveal that the "flat-top" emission-line profile seen in the galaxy-integrated spectrum is primarily due to the sum of two luminous narrow kinematic components separated in velocity by $\approx 400\,\mathrm{km\,s^{-1}}$, with the red component dominating in the south and the blue in the north. At the limit of our resolution ($\approx$1.4 kpc) we do not see two separate continuum or emission-line regions. Additionally, the similarity of the Hβ and [O III] emission-line profiles indicate similar [O III]/Hβ flux ratios for each kinematic component (also seen in the velocity profile; Fig. 4.14) suggesting that the two kinematic components are illuminated by a single AGN. The kinematic "major axis" we identify from the peak-velocity (v_p) map is oriented parallel to the morphological major axis observed in the SDSS image and our continuum data (Fig. 4.14). Overall, we favour the interpretation that the v_p velocity map is tracing galaxy rotation, although we cannot rule out a late stage merger without higher spatial resolution imaging or spectroscopic data.

In addition to the narrow [O III] emission-line components there are underlying broad wings in the emission-line profile over the full field-of-view ($\approx 7 \times 10$ kpc; Fig. 4.14).

These broad emission-line profiles (with $W_{80} \approx 850\,\mathrm{km\,s^{-1}}$ and $\Delta v \approx -50\,\mathrm{km\,s^{-1}}$) are more dominant perpendicular to the kinematic "major axis". This potentially indicates that the outflow is escaping away from a galactic disk. The emission-line flux ratio $\log([\mathrm{O\ III}]/\mathrm{H}\beta) \approx 1.1$ remains constant over the central $\approx 6\,\mathrm{kpc}$ and then abruptly declines, in a similar manner to that seen in the type 2 quasars of Liu et al. (2013a) (see Section 4.5.3). Therefore, to measure the outflow kinetic energy following Liu et al. (2013b) we adopt a value of $R_{\mathrm{br}} = 3\,\mathrm{kpc}$ and measure a Hβ surface brightness of $\Sigma_{\mathrm{H}\beta} = 1.4 \times 10^{-15}\,\mathrm{erg\,s^{-1}\,arcsec^{-2}}$ in an annulus at this radius (corrected for cosmological dimming). Using this method we obtain an outflow kinetic energy of $\dot{E} \approx 2.8 \times 10^{43}\,\mathrm{erg\,s^{-1}}$, which is in excellent agreement with the value that we derive in Section 4.5.3 of $\dot{E}_{\mathrm{out}} \approx 2.7 \times 10^{43}\,\mathrm{erg\,s^{-1}}$.

J1000+1242

Reyes et al. (2008) previously identified J1000+1242 as a type 2 ("obscured") quasar. This source has excess radio emission (above that expected from star formation; Table 4.2) that is marginally resolved based on the FIRST data ($R_{1.4} \approx 8.4\,\mathrm{kpc}$ with a PA $\approx 160^{\circ}$; see Section 4.3.4 and Table 4.2). Although fairly irregular, our IFU data reveal a velocity gradient from blue to red in the peak of the [O III] emission-line profile ($\Delta v_p \approx 200\,\mathrm{km\,s^{-1}}$) at a PA of $\approx 240^{\circ}$ (Fig. 4.15). The peak signal-to-noise ratio map, combined with the velocity maps reveal a distinct luminous emission-line region $\approx 3.5\,\mathrm{kpc}$ north-east of the nucleus that has a reasonably narrow emission-line profile ($W_{80} \lesssim 600\,\mathrm{km\,s^{-1}}$). This feature may be merger debris, halo gas or an outflow remnant (see Section 4.5.2).

Roughly perpendicular to the v_p velocity gradient (with a PA ≈ 160–170°) we observe regions with broad underlying wings (with $W_{80} \approx 850\,\mathrm{km\,s^{-1}}$) in the [O III] emission-line profile. From the spectra in boxes 12, 17 and 18 in Figure 4.15 it can be seen that this broad emission is built up from multiple narrow components. This emission shows a velocity shift from blue (with $\Delta v \approx -100\,\mathrm{km\,s^{-1}}$) to red (with $\Delta v \approx 100\,\mathrm{km\,s^{-1}}$) over ≈ 10–$15\,\mathrm{kpc}$. We also see an irregular morphology of the emission-line region. All of the above indicates that we are observing an outflowing bi-polar superbubble, with a strikingly similar kinematic structure to previously identified superbubbles (i.e., J1356+1026 from Greene et al. 2012; J0319-0019 from Liu et al. 2013b; and Mrk 273 from Rupke &

Veilleux 2013). The PA of the superbubbles we observe in J1000+1242 is parallel to the axis of the extended radio emission and found over a similar spatial extent, potentially demonstrating a direct connection between a radio jet and the outflow, although shock-induced radio emission is another possibility. The SDSS image of this source (Fig. 4.15) is extended beyond the field-of-view of our observations and therefore IFU observations over larger regions are required to trace the full kinematic structure of this target.

J1010+1413

We show our IFU data for J1010+1413 in Figure 4.5 and Figure 4.6. This source has the broadest [O III] emission-line width of the entire sample ($W_{80} = 1450\,\mathrm{km\,s^{-1}}$) and is kinematically complex. In the central regions we observe a smooth gradient from red to blue in the [O III] peak velocity (v_p; Fig. 4.6), although the overall velocity field is irregular (Fig. 4.5). There are luminous narrow [O III] emission-line components located to the north and south of the nucleus, separated by $\approx$16 kpc in projected distance and $\approx 350\,\mathrm{km\,s^{-1}}$ in projected velocity, that appear to be associated with emission-line regions that are apparent in the SDSS image (Fig. 4.6). These features may be merger debris, halo gas or outflow remnants (see Section 4.5.2). The extremely broad emission-line profiles, with velocity offsets reaching up to $\Delta v \approx -350\,\mathrm{km\,s^{-1}}$, is located out to the very edge of the field-of-view (i.e., over $\gtrsim 16$ kpc).

J1010+0612

Reyes et al. (2008) previously identified J1010+0612 as a type 2 ("obscured") quasar. This source has a clear radio excess above that expected from star formation alone (Table 4.2). Based on the FIRST data we do not spatially resolve any radio emission on scales $\gtrsim 2''$ (see Section 4.3.4 and Table 4.2).

We show our IFU data for this object in Figure 4.16. We identify a regular blue to red velocity field, indicative of galactic rotation, in the [O III] peak velocity (with $\Delta v_p \approx 300\,\mathrm{km\,s^{-1}}$). Broad underlying wings lead to emission-line widths of $W_{80} \approx 1100-1300\,\mathrm{km\,s^{-1}}$ and velocity offsets of $\Delta v \approx -100\,\mathrm{km\,s^{-1}}$ and are located over the full extent of the field-of-view ($\approx 6 \times 9$ kpc) with a roughly circular morphology.

J1100+0846

Reyes et al. (2008) previously identified J1100+0846 as a type 2 ("obscured") quasar and we show our IFU data for this object in Figure 4.17. Although the peak velocity (v_p) map shows some irregular features we see a smooth velocity gradient ($\Delta v_p \approx 100\,\mathrm{km\,s^{-1}}$) along a PA $\approx 250^\circ$. Additionally, this kinematic "major axis" is parallel to the morphological major axis seen in the SDSS image (with hints of the same axis in our continuum image), providing evidence that kinematics due to galaxy rotation are being observed. Broad wings (leading to $W_{80} \approx 700$–$1100\,\mathrm{km\,s^{-1}}$) are observed in the emission-line profiles over the full field-of-view ($\approx 9 \times 6\,\mathrm{kpc}$). The uncertainties on the velocity offset of the broad emission (i.e., Δv) are large; however, the velocity seems to be highest in the southern regions with velocities between $\Delta v \approx -100\,\mathrm{km\,s^{-1}}$ and $-80\,\mathrm{km\,s^{-1}}$. These blue-shifted velocities could indicate the near-side of an outflow that is moving away from the almost face on galaxy disc. In the velocity profile (Fig. 4.17), we observe that the emission-line flux ratio of $\log([\mathrm{O\,III}]/\mathrm{H}\beta) \approx 1.0$–$1.1$ is constant over the central regions then declines at a break radius of $R_{\mathrm{br}} = 2.5\,\mathrm{kpc}$ (see Section 4.5.3). We therefore measure a Hβ surface brightness of $\Sigma_{\mathrm{H}\beta} = 1.7 \times 10^{-15}\,\mathrm{erg\,s^{-1}\,arcsec^{-2}}$ in an annulus at this break radius (corrected for cosmological dimming) and calculate the outflow kinetic energy following Liu et al. (2013b). The kinetic outflow energy we obtain using this method, i.e., $\dot{E} \approx 6.3 \times 10^{43}\,\mathrm{erg\,s^{-1}}$, is in excellent agreement with the value that we calculate in Section 4.5.3, i.e., $\dot{E}_{\mathrm{out}} \approx 6.9 \times 10^{43}\,\mathrm{erg\,s^{-1}}$.

J1125+1239

We show our IFU observations for J1125+1239 in Figure 4.18. We observe an emission-line region that is extended right to the edges of the field-of-view (over $\gtrsim 13\,\mathrm{kpc}$). We do not observe any velocity gradients in the peak of the [O III] emission-line profile (i.e., v_p; Fig. 4.18). There is faint, high velocity ($\Delta v \approx -250$ to $-300\,\mathrm{km\,s^{-1}}$) and extremely broad [O III] emission ($W \approx 1200$–$1500\,\mathrm{km\,s^{-1}}$), out to the very edges of the field-of-view. Due to the low surface brightness the morphology of the broad emission is uncertain; however, the SDSS image shows faint extended emission beyond the IFU field-of-view, parallel to the axis where we predominantly observe this broad emission (i.e., PA $\approx 250^\circ$; Fig. 4.18).

J1130+1301

We show our IFU observations for J1130+1301 in Figure 4.19. The peak velocity map (v_p) is indicative of galactic rotation showing a smooth velocity gradient from red to blue with $\Delta v_p \approx 300\,\mathrm{km\,s^{-1}}$. This interpretation is strengthened by the kinematic major axis being aligned with the morphological major axis observed in the SDSS image and the continuum observed in our data. The broad emission-line wings (with $W_{80} > 600\,\mathrm{km\,s^{-1}}$) are found perpendicular to the galaxy major axis over ≈ 8 kpc. Although both blue and red wings are observed in the emission-line profile the red wing is more luminous resulting in an overall velocity offset that is positive (i.e., $\Delta v \approx 150\,\mathrm{km\,s^{-1}}$).

J1216+1417

Spectroscopy of J1216+1417 has previously identified Wolf-Rayet star spectral features in this source and consequently shows that a recent star formation episode has occurred (i.e., $\approx$ 2–5 Myrs; Brinchmann et al. 2008). Furthermore, a subtle 4000Å break and stellar absorption features are seen in the SDSS spectrum and may explain why the Hβ emission-line profile is different to that seen in [O III] (Fig. 4.20). We show our IFU data in Figure 4.20. We see little velocity structure in the v_p velocity map. The [O III] emission line profile is irregular, with both a blue wing (out to $v \approx 1000\,\mathrm{km\,s^{-1}}$) and a large red wing out to $v \approx 2000\,\mathrm{km\,s^{-1}}$. This is seen in both lines of the [O III]λλ4959,5007 emission-line doublet indicating that it is a true [O III] feature associated with this source. Further kinematic analysis, beyond the scope of this work, is required to fully identify the origin of these high-velocity wings. The blue and red wings observed in the [O III] emission line are predominantly found in a circular region across the central $\gtrsim 6$ kpc; however, the low surface brightness of the emission in the outer regions puts some uncertainty on the spatial extent and morphology.

J1316+1753

The target J1316+1753 has a double peaked [O III] emission-line profile, with components separated by $\approx$400–500 $\mathrm{km\,s^{-1}}$ (Fig. 4.21). As a result of this, this source has previously been identified as a dual AGN candidate (Xu & Komossa 2009; also see Sec-

tion 4.5.2). In the peak signal-to-noise ratio map we observe two spatial regions separated by $\approx$ 2–3 kpc and orientated with a PA $\approx 130^{\circ}$ associated with these kinematics components; however, at the resolution of our observations ($\approx$ 2 kpc) we do not observe two continuum peaks (Fig. 4.21). The similarity of the emission-line ratios in both systems, and the lack of a double continuum source, suggests that these kinematic components may be illuminated by a single ionising source. Also, the kinematic components have similar fluxes and the velocities are independent of projected distance from the centre; therefore, the double-peaked profile may by the result of gas kinematics, jet interactions and/or AGN-driven outflows (Fig. 4.21; also see Xu & Komossa 2009; Smith et al. 2010; Barrows et al. 2013). The lack of evidence for extended luminous radio emission on $\gtrsim 2''$ scales from the FIRST data (Table 4.2) could argue against a jet interaction (as seen in other sources e.g., Rosario et al. 2010); however, deep and high-resolution radio data would be required to confirm this. Additionally the axis of the two components is aligned with the morphological major axis seen in the SDSS image and the continuum emission seen in our data (Fig. 4.21). Overall, all of these observations favour the scenarios of a rotating gas disk or two merging components (separated by $\lesssim$ 2 kpc) illuminated by a single AGN to explain the double peaked [O III] emission-line profile in this source (also see Smith et al. 2012 and Comerford et al. 2012). Combining these IFU data with deep high-spatial resolution optical, X-ray and radio images would provide the data required to robustly distinguish between all of the possible scenarios.

In addition to the narrow components our IFU data for J1316+1753 (Fig. 4.21) reveal a very broad [O III] emission-line profile ($W_{80} \approx 1100$–$1200\,\mathrm{km\,s^{-1}}$), preferentially located perpendicular to the kinematic "major axis" defined from the v_p map. This [O III] emission has a velocity offset of $\Delta v \approx -200\,\mathrm{km\,s^{-1}}$ and is extended right to the edge of the field-of-view (i.e., over $\gtrsim$ 14 kpc). In the velocity profile, we observe an emission-line flux ratio of $\log([\mathrm{O\ III}]/\mathrm{H}\beta) \approx 1.0$–$1.1$ over the central regions, that declines at a break radius of $R_{\mathrm{br}} = 5$ kpc (see Section 4.5.3). Therefore we measure a Hβ surface brightness of $\Sigma_{\mathrm{H}\beta} = 6.2 \times 10^{-16}\,\mathrm{erg\,s^{-1}\,arcsec^{-2}}$ in an annulus at this break radius (corrected for cosmological dimming) and measure the outflow kinetic energy following Liu et al. (2013b). Following this method we obtain an outflow kinetic energy of $\dot{E} \approx 5.4 \times 10^{43}\,\mathrm{erg\,s^{-1}}$ that is within a factor of 3 of the value we calculated in Sec-

tion 4.5.3, i.e., $\dot{E}_{\rm out} \approx 1.7 \times 10^{44}\,{\rm erg\,s^{-1}}$.

J1338+1503

We show our IFU data for J1338+1503 in Figure 4.22. We note that hints of stellar continua are seen in the SDSS spectrum and contamination from stellar absorption may cause the difference in the Hβ and [O III] emission-line profiles (Fig. 4.22). The peak velocity map (v_p) for J1338+1503 is irregular; however, we do see a general shift from blue to red. This source has a predominantly red wing, in addition to a weaker blue wing leading to an overall velocity offset of $\Delta v \approx 120\,{\rm km\,s^{-1}}$ across the central few kiloparsecs. The broad emission ($W_{80} \approx 900\,{\rm km\,s^{-1}}$) is preferentially found perpendicular to the velocity gradient (i.e., the kinematic "major axis") that we observe in v_p (Fig. 4.22).

J1339+1425

The source J1339+1425 is the least luminous AGN in our sample (in both $L_{\rm AGN}$ and $L_{[\rm O\ III]}$) and is the only source not detected at 1.4 GHz by FIRST or NVSS (Table 4.2). We show our IFU data for this source in Figure 4.23 where we observed [O III] emission right to the edge of the field-of-view of our observations (i.e., over $\gtrsim$12 kpc). This emission-line region is dominated by narrow kinematic components (i.e., with $W_{80} < 600\,{\rm km\,s^{-1}}$) that trace out a small velocity gradient ($\Delta v_p \approx 100\,{\rm km\,s^{-1}}$) from blue to red. We find that the kinematic major axis is broadly consistent with the continuum morphological axis observed in our data and the SDSS image (Fig. 4.23). We therefore appear to be tracing galactic rotation in the v_p map.

Across the central $\approx$6 kpc we observe a blue- and red-wing in the [O III] emission-line profile, with an overall velocity offset of $\Delta v \approx 150\,{\rm km\,s^{-1}}$, that is preferentially located at $\approx 50^\circ$–70° away from this kinematic "major axis". In the velocity profile, we observe that the emission-line flux ratio $\log([\rm O\ III]/{\rm H}\beta) \approx 1.1$ is constant over the central regions and then declines at a break radius of $R_{\rm br} = 2$ kpc (see Section 4.5.3). We therefore measure a Hβ surface brightness of $\Sigma_{\rm H\beta} = 7.5 \times 10^{-16}\,{\rm erg\,s^{-1}\,arcsec^{-2}}$ in an annulus at this break radius (corrected for cosmological dimming) and calculate the outflow kinetic energy following Liu et al. (2013b). Using this method we obtain an outflow kinetic energy of $\dot{E} \approx 5.5 \times 10^{42}\,{\rm erg\,s^{-1}}$ that is within a factor of ≈ 3 of the value we calculated in

Section 4.5.3, i.e., $\dot{E}_{\rm out} \approx 1.5 \times 10^{43}\,{\rm erg\,s^{-1}}$.

J1355+1300

We show our IFU data for J1355+1300 in Figure 4.24. The majority of the emission-line region is dominated by narrow [O III] emission-line profiles ($W_{80} \approx 300$–$400\,{\rm km\,s^{-1}}$) and we observe a small velocity gradient (with $\Delta v_p \approx 100\,{\rm km\,s^{-1}}$) from blue-to-red in a north-south direction in the peak velocity map (v_p) indicative of galactic rotation. Located $\approx 3\,{\rm kpc}$ to the south-east of the nucleus there is a distinct kinematic component with a velocity between $\approx -500\,{\rm km\,s^{-1}}$ and $-600\,{\rm km\,s^{-1}}$ which has a high-velocity blue-wing in the emission-line profile (see grids of spectra in Fig. 4.24). The similarity of the galaxy-integrated [O III] and Hβ emission-line ratios for this kinematic component (see Fig. 4.24) could imply that the ionising source is the same as that for the rest of the emission-line region and is therefore likely to be illuminated by the central source. At the depth of our observations, we observe no spatially distinct continuum source or emission-line region coincident with this kinematic component (Fig. 4.24). The exact origin of this high-velocity feature is difficult to determine with these observations alone; however, the highly-disturbed nature and lack of associated continuum strongly suggests an outflow. This feature is similar to that seen in J1430+1339 and therefore could indicate a smaller-scale outflowing bubble and/or could be due to a jet-ISM interaction at this position (as is seen in other sources, e.g., Emonts et al. 2005). Due to the faintness of the radio emission, and the lack of IRAS detections we are unable to constrain the radio excess parameter for this source (see Section 4.3.4 and Table 4.2); therefore, deep and high-resolution radio imaging is required to determine if radio jets are present and if they are aligned with this high-velocity feature.

J1356+1026

As a well known type 2 ("obscured") quasar (Reyes et al. 2008) this source has already received a lot of attention in the literature. Two merging galactic nuclei with a projected separation of $\approx 2.5\,{\rm kpc}$ are seen in the optical and near-infrared (Shen et al. 2011; Fu et al. 2011; Greene et al. 2012). In agreement with this, our IFU data reveal two continuum sources and, moderately offset from this, corresponding emission-line regions with

distinct velocities (Fig. 4.25). We note that Fu et al. (2012) did not confidently associate an emission-line region with the southern nucleus in their IFU data, although our data are unambiguous (Fig. 4.7 and Fig. 4.25). Combined with the observation that these kinematic components have slightly different [O III]/Hβ emission-line flux ratios implies two distinct type 2 quasars (Fig. 4.25; also see Greene et al. 2012). This source has a clear radio excess above that expected from star formation alone (see Section 4.3.4 and Table 4.2). However, there is no evidence for *extended* radio emission at the few mJy level on scales of $\gtrsim 2''$ based on the FIRST data (Section 4.3.4; Table 4.2).

Using longslit observations, Greene et al. (2012) revealed [O III] emission extended over 10s of kiloparsecs, reaching beyond the field-of-view of our IFU observations. In particular they reveal a "bubble" of [O III] emission with a spatial extent of 12 kpc to the south and high-velocity "clumps" to the north. The "bubble" and "clumps" reach a projected velocity of $\approx 250\,\mathrm{km\,s^{-1}}$. Greene et al. (2012) postulate a quasi-spherical outflow that extends from the south to the north, where the outflow is forced into this bi-polar shape due to high density regions of gas and dust in the central galaxies (e.g., Faucher-Giguère & Quataert 2012). Our IFU observations (Fig. 4.25) cover the base of these features. It is worth noting that, despite our lack of spatial coverage and different approaches, our outflow energy injection rate estimate ($\dot{E}_{\mathrm{out}} \approx 1.3 \times 10^{44}\,\mathrm{erg\,s^{-1}}$; Section 4.5.3) is consistent with the fiducial range $= 10^{44}$–$10^{45}\,\mathrm{erg\,s^{-1}}$ quoted in Greene et al. (2012). Based on our SED fitting (Section 4.3.4) the bolometric luminosity of the AGN in this source is $\approx 1 \times 10^{45}\,\mathrm{erg\,s^{-1}}$ while the infrared-luminosity from star formation is $\approx 2 \times 10^{45}\,\mathrm{erg\,s^{-1}}$ (SFR $\approx 60\,\mathrm{M_{\odot}\,yr^{-1}}$; Table 4.2). Therefore, in contrast to the conclusions of Greene et al. (2012), we find there is a comparable amount of energy available from the AGN and star formation to power the outflow. The observed radio emission in FIRST is on much smaller scales than the ≈ 10 kpc outflowing bubble, that may argue against a jet-driven outflow; however, deep and high-resolution radio imaging is required to determine the origin and morphology of the radio emission in this source.

J1430+1339

Reyes et al. (2008) previously identified J1430+1339 as a type 2 ("obscured") quasar. Additionally, this source was identified by Galaxy Zoo (Keel et al. 2012) as having an

extended emission-line region, due to the arc shaped "purple haze" to the north east of the SDSS image (Fig. 4.26). This galaxy has consequently received the nickname the "Teacup". Follow-up *HST* imaging[17] has revealed that this is actually a 5–10 kpc emission-line "loop" accompanied by a smaller emission-line "arc" on the opposite side of the nucleus, potentially analogous to the bi-polar outflow observed in J1356+1026 (Fig. 4.25; Greene et al. 2012). The exact origin of these emission-line regions are unknown; however, our IFU data (Fig. 4.26) cover the base of the north-east loop and reveal it has a velocity of $\approx -900\,\mathrm{km\,s^{-1}}$ from the systemic with a high velocity tail out to $\approx -1400\,\mathrm{km\,s^{-1}}$. The [O III] peak signal-to-noise map shows faint extended features similar to those seen in outflowing superbubbles (e.g., Liu et al. 2013b). Additionally these features look remarkably similar to the bi-conal shells of ionised gas seen in the high-redshift radio galaxy MRC 0406–244 that appear to be due to gas that has been expelled from the host galaxy by radio jets and/or star formation (Hatch et al. 2013; see also Nesvadba et al. 2008). Indeed, the PA of these high velocity ionised gas features in J1430+1339 are roughly aligned with, and found over a similar scale to, the extended radio emission seen in the FIRST data (see Section 4.3 and Table 4.2). High-resolution radio imaging of this source will play a crucial role in determining the true origin of the radio emission (e.g., radio jets or shocks). IFU observations covering the full extent of the emission-line region will reveal the full velocity structure in these regions. The peak velocity (v_p) map shows a large velocity gradient from blue to red ($\Delta v_p \approx 600\,\mathrm{km\,s^{-1}}$) along an axis with PA $\approx 30^\circ$ (Fig. 4.26).

J1504+0151

Reyes et al. (2008) previously identified this source as being a type 2 ("obscured") quasar. We note that there are stellar continuum and absorption features visible in the SDSS spectrum of this source and therefore contamination from stellar absorption may result in the different Hβ and [O III] emission line profiles (Fig. 4.27). This source is one of the faintest in our sample; however, we still observe an [O III] emission-line region out to the edges of the field-of-view (i.e., over $\gtrsim 13$ kpc; Fig. 4.27). The peak velocity map (v_p)

[17] http://blog.galaxyzoo.org/2012/06/14/hubble-spies-the-teacup-and-i-spy-hubble

shows a smooth velocity gradient from blue to red (with $\Delta v_p \approx 150\,\mathrm{km\,s^{-1}}$) indicative of galaxy rotation with a PA $\approx 140^\circ$. Due to the faint emission lines, it is difficult to establish the true extent and morphology of the broad, high-velocity emission (which has $W_{80} \approx 1000\,\mathrm{km\,s^{-1}}$ and a velocity offset between $\Delta v \approx -300$ and $-500\,\mathrm{km\,s^{-1}}$); however, it appears to dominate in the central few kiloparsecs (Fig. 4.27).

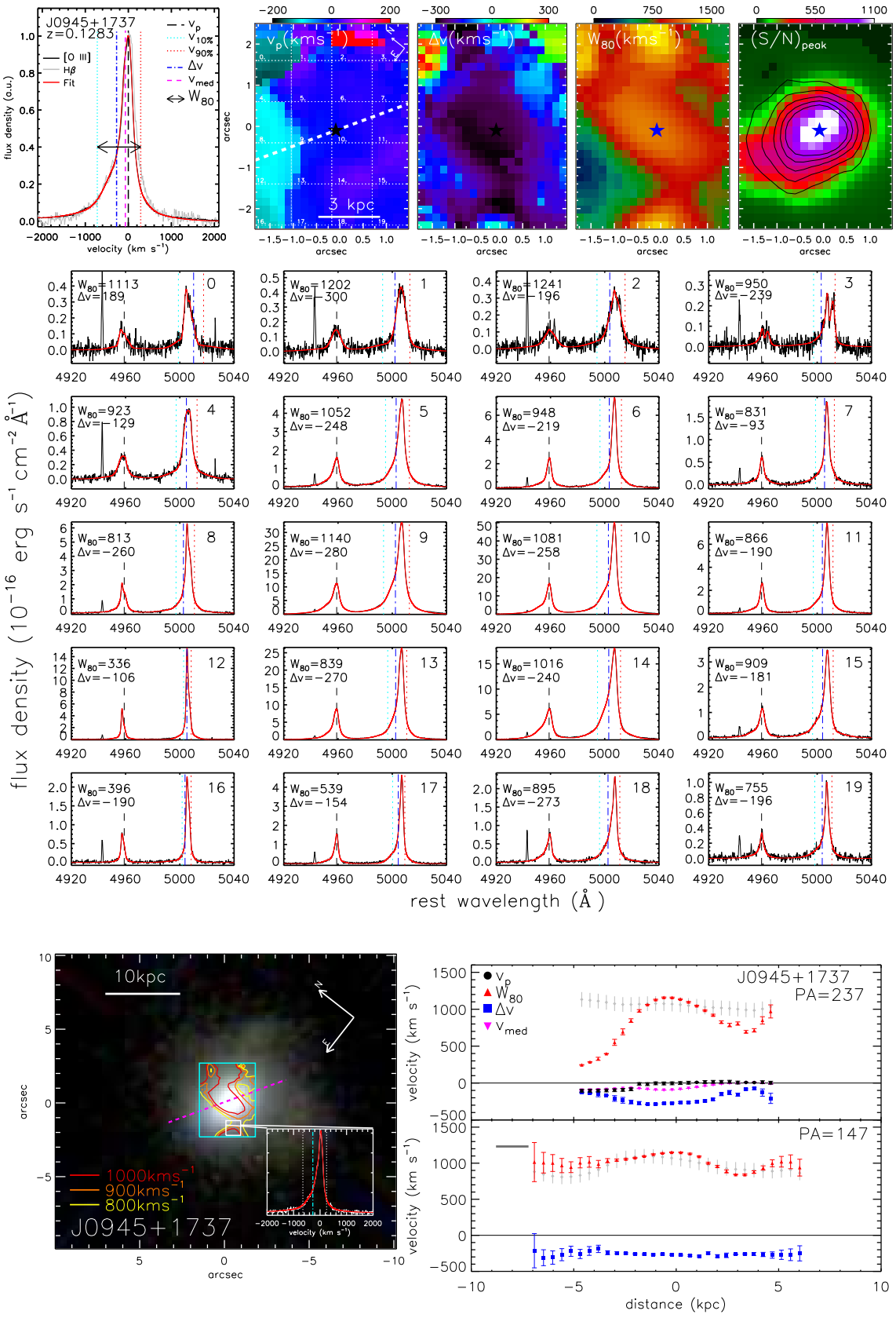

Figure 4.13: Same as Figure 4.5 and Figure 4.6 but for SDSS J0945+1737

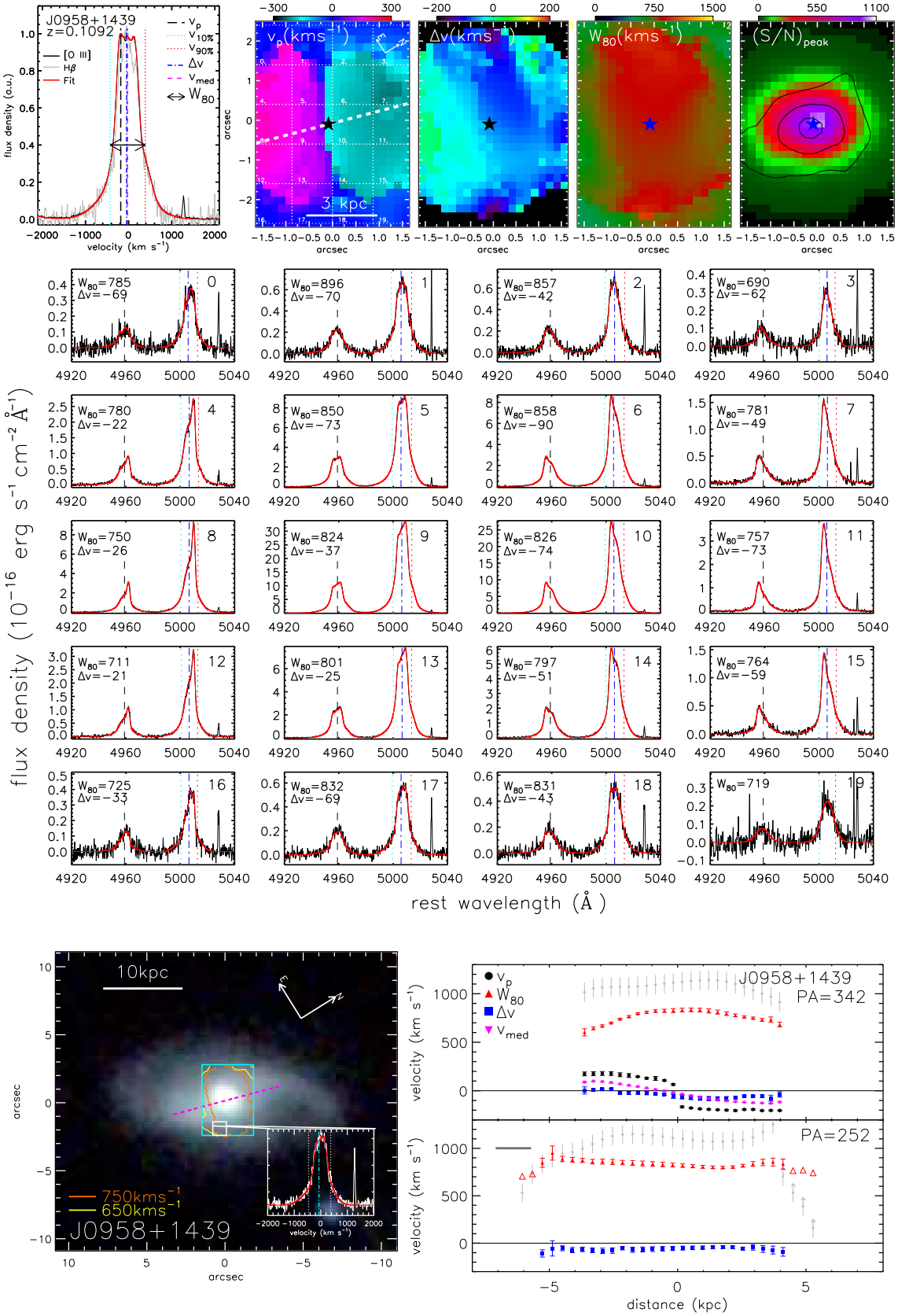

Figure 4.14: Same as Figure 4.5 and Figure 4.6 but for SDSS J0958+1439

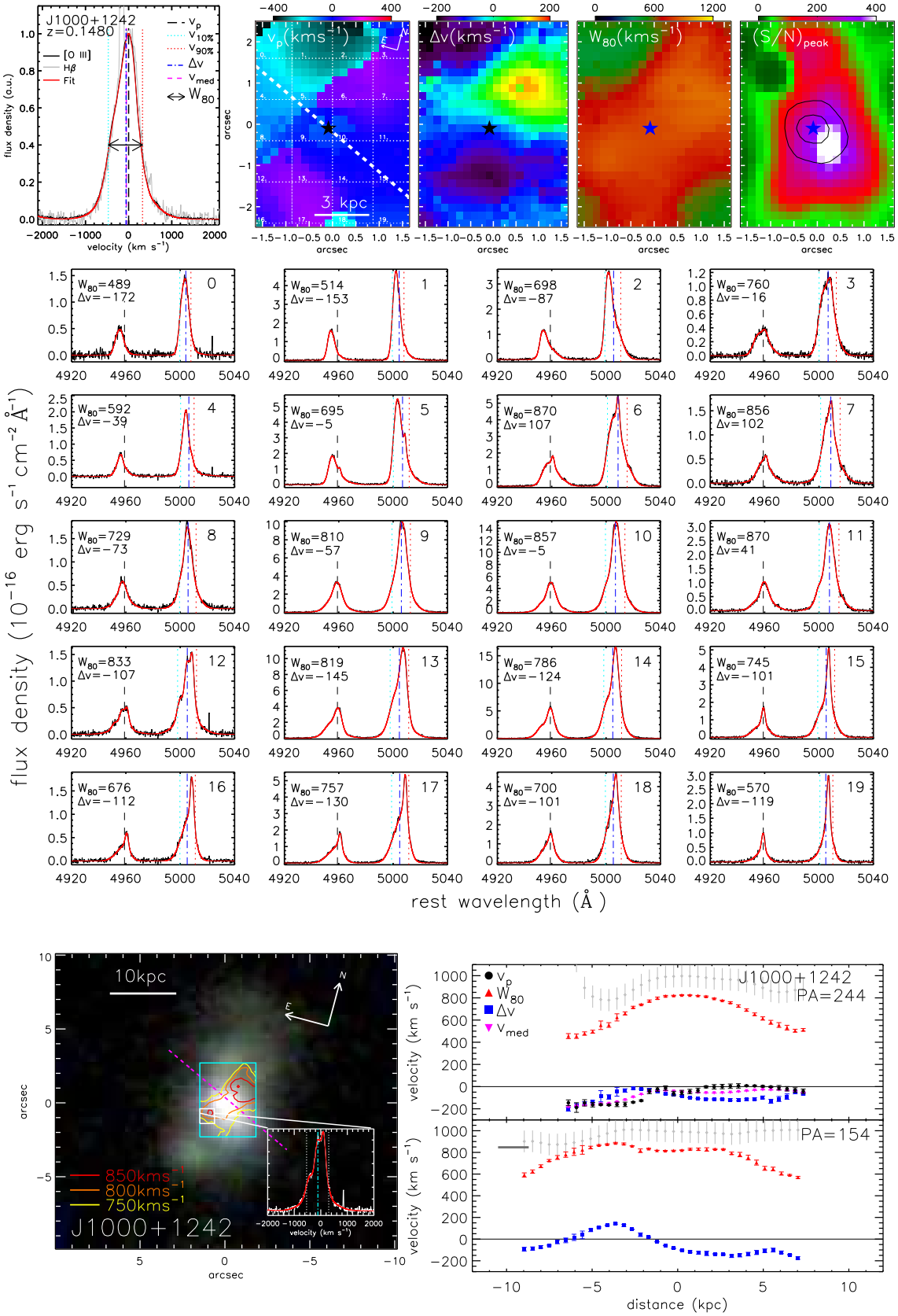

Figure 4.15: Same as Figure 4.5 and Figure 4.6 but for SDSS J1000+1242

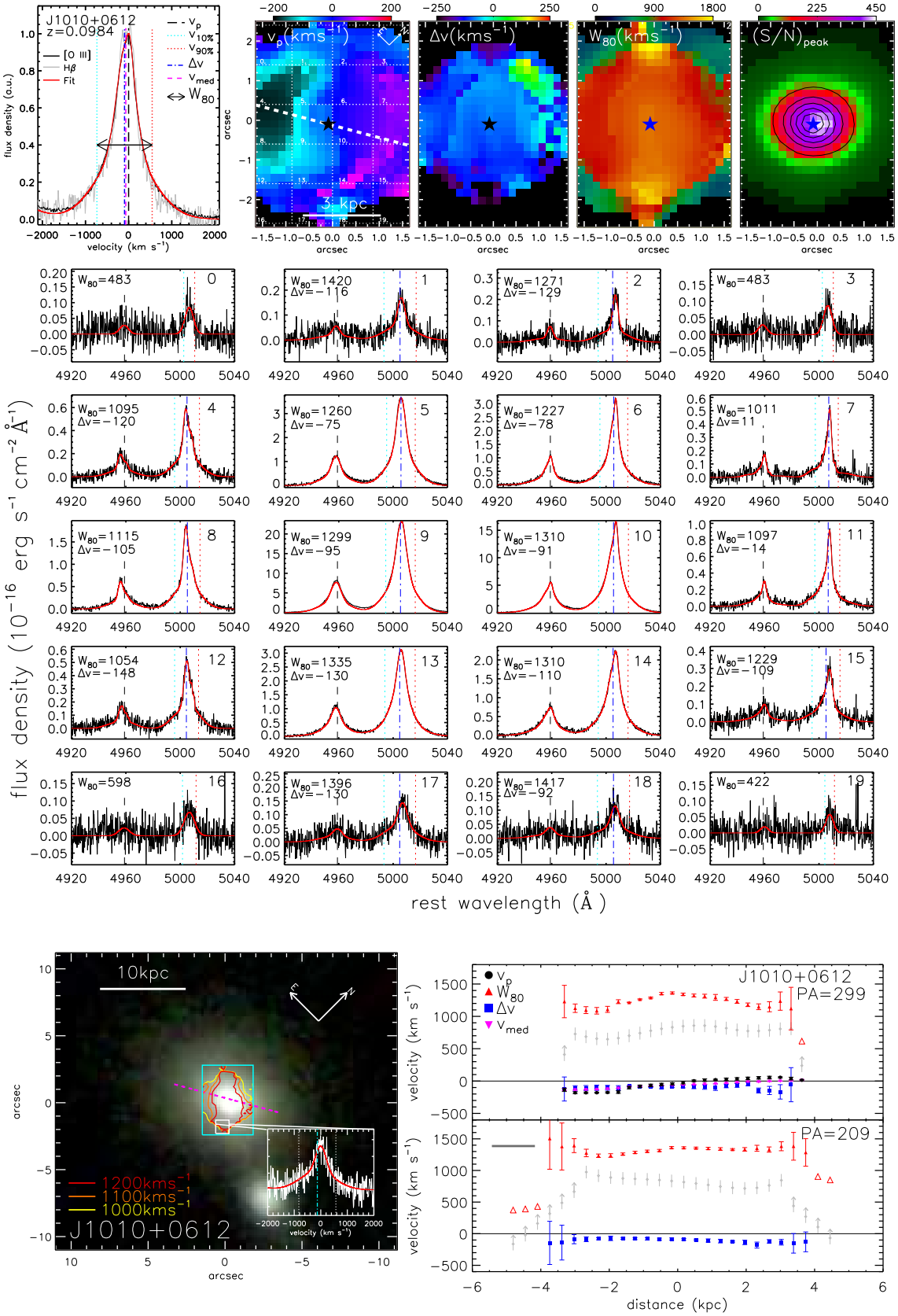

Figure 4.16: Same as Figure 4.5 and Figure 4.6 but for SDSS J1010+0612

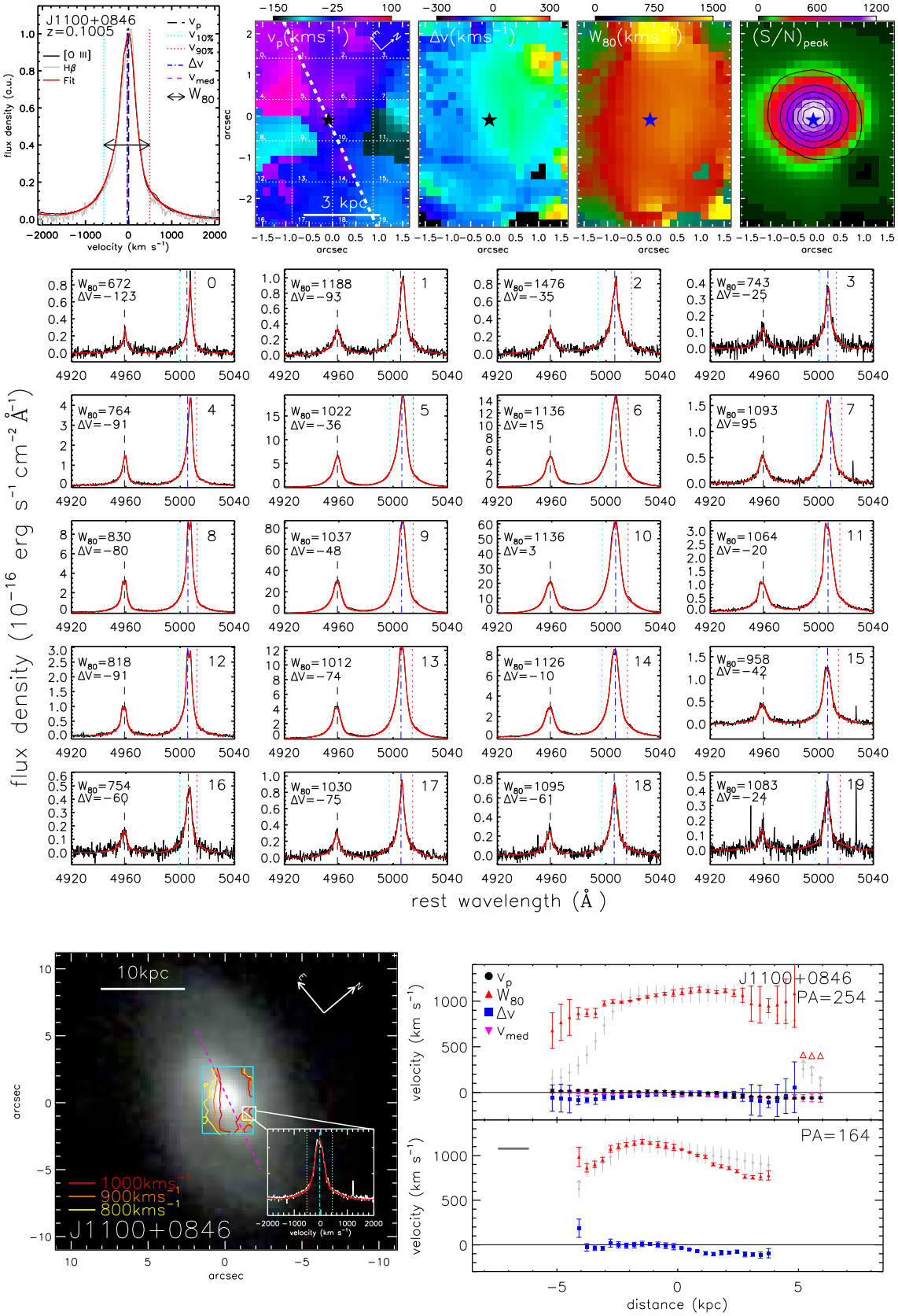

Figure 4.17: Same as Figure 4.5 and Figure 4.6 but for SDSS J1100+0846

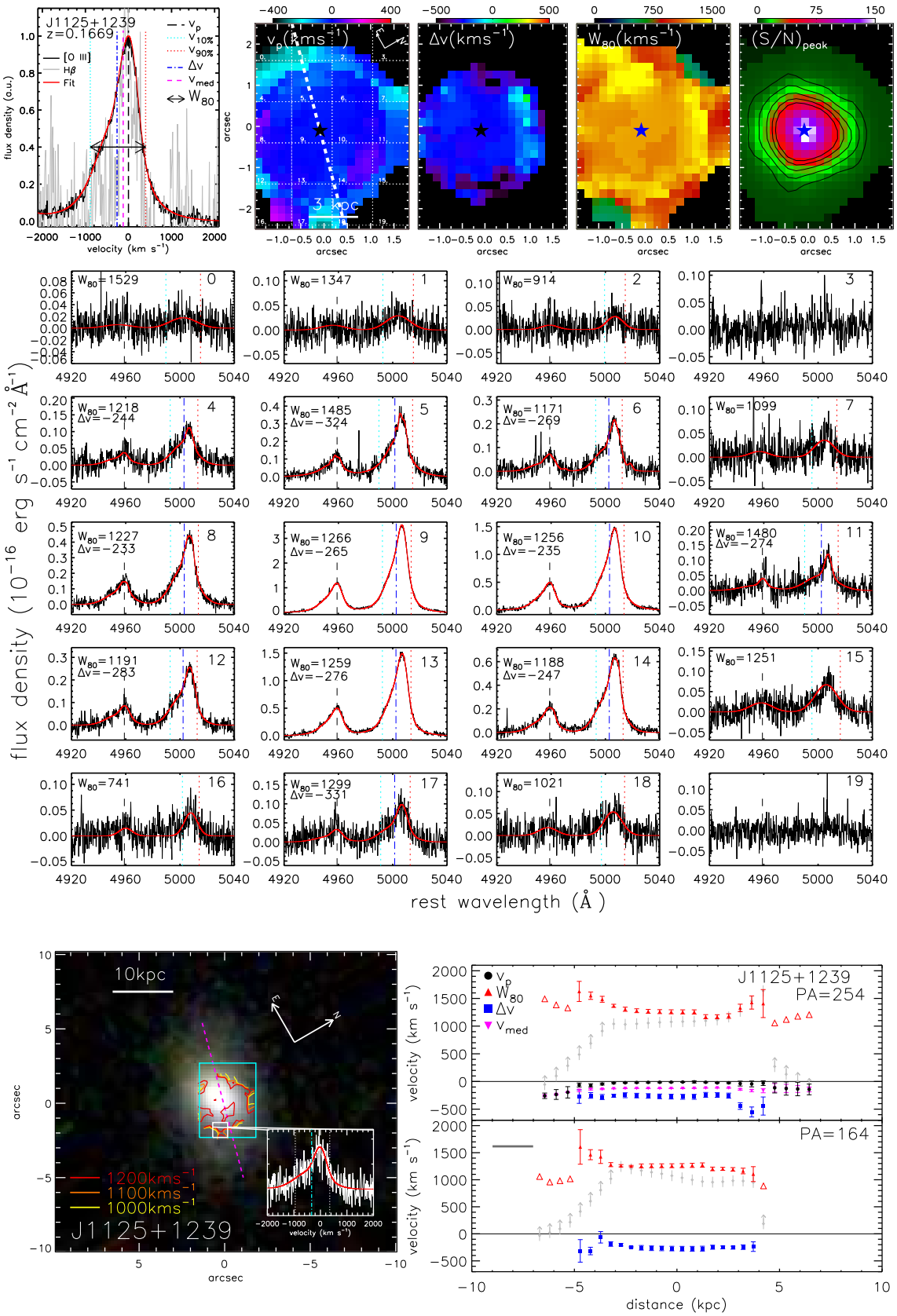

Figure 4.18: Same as Figure 4.5 and Figure 4.6 but for SDSS J1125+1239

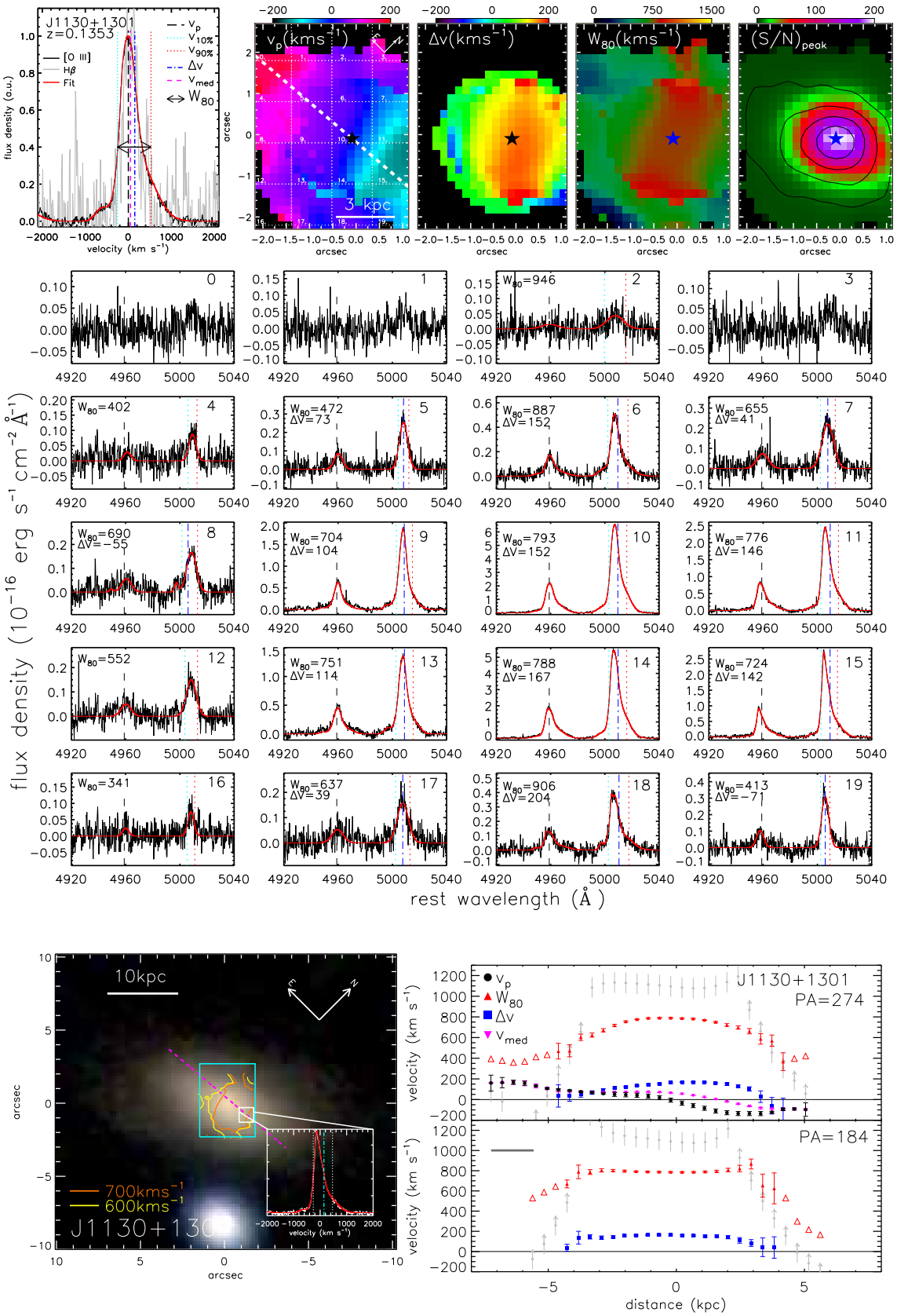

Figure 4.19: Same as Figure 4.5 and Figure 4.6 but for SDSS J1130+1301

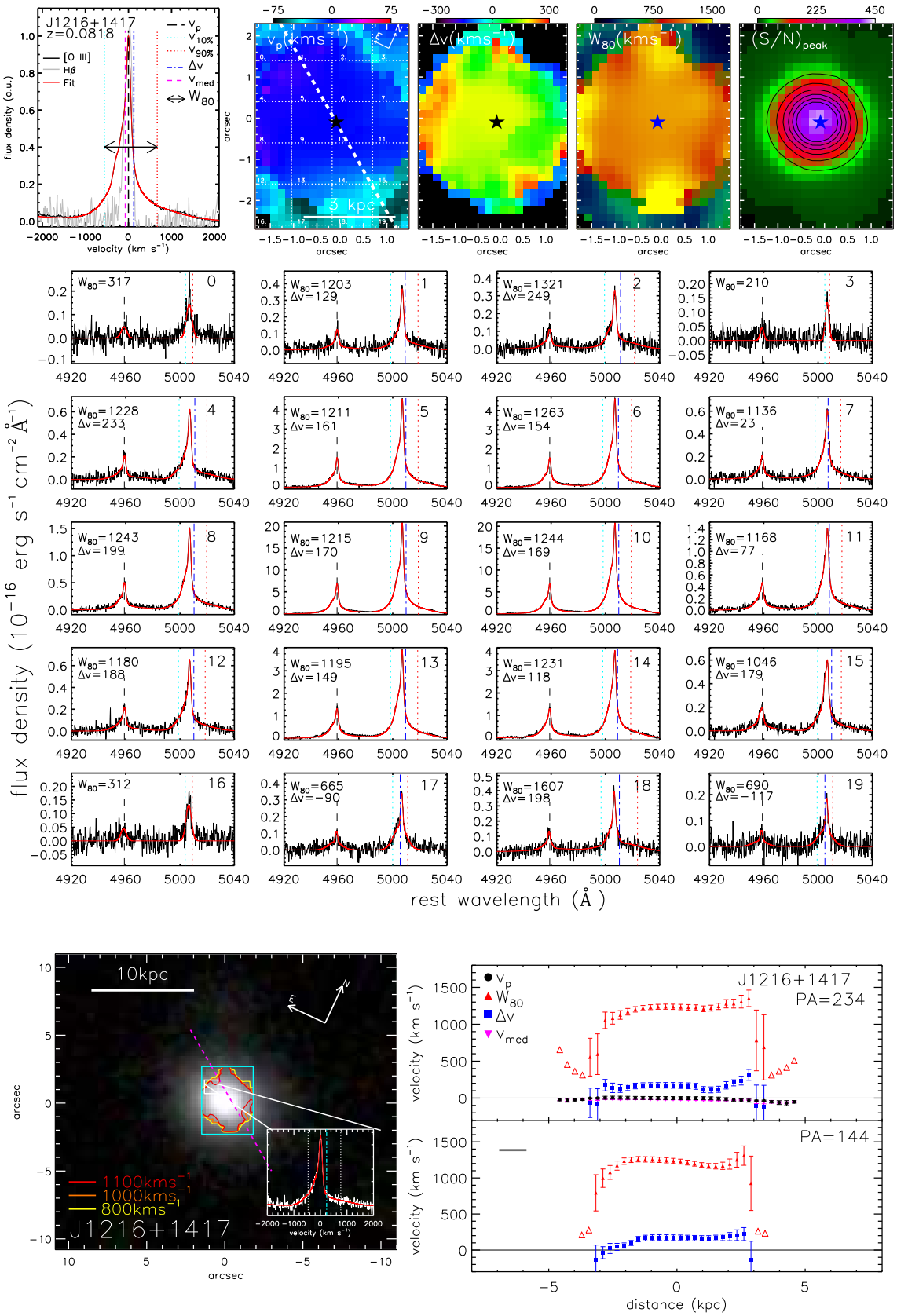

Figure 4.20: Same as Figure 4.5 and Figure 4.6 but for SDSS J1216+1417

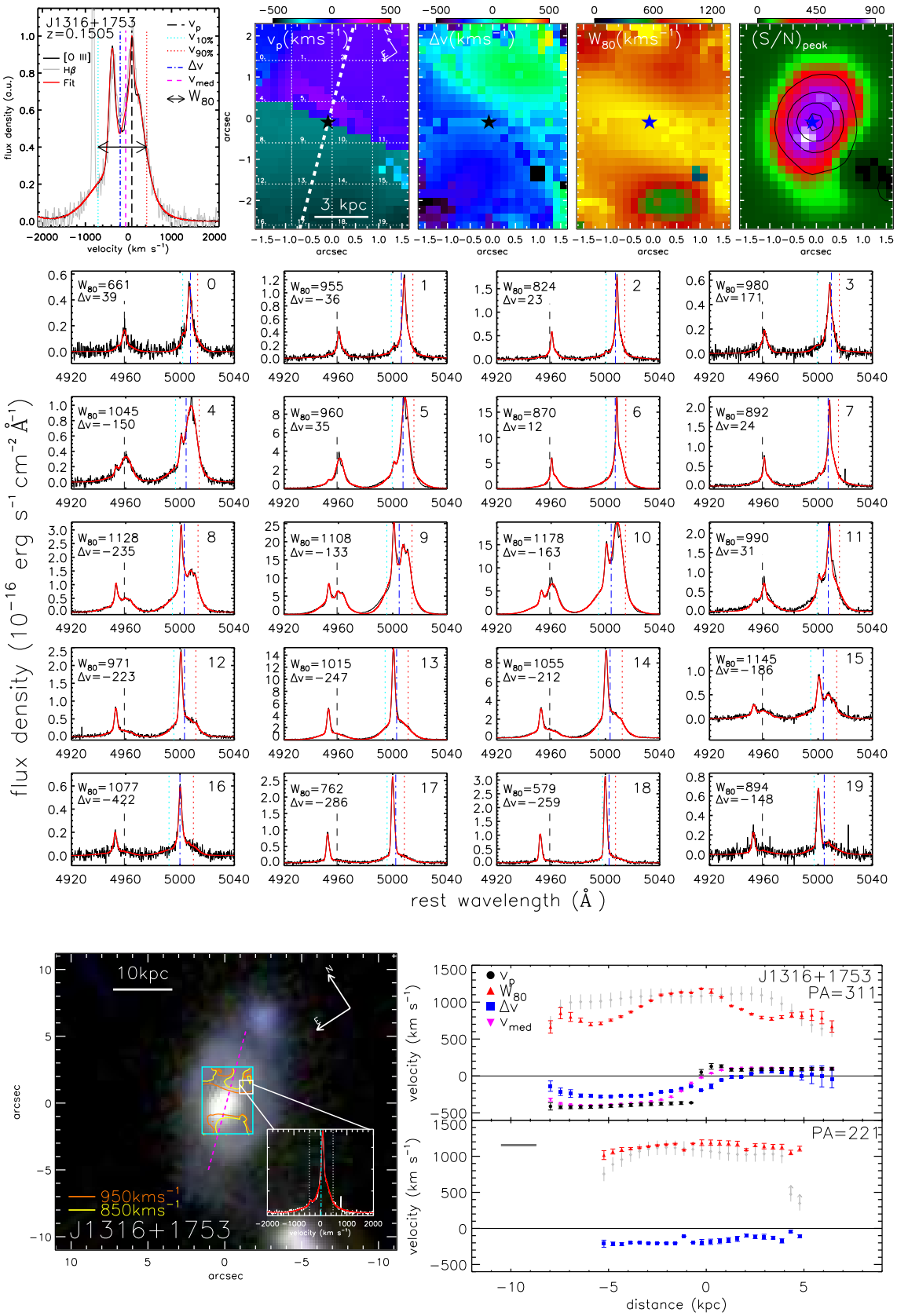

Figure 4.21: Same as Figure 4.5 and Figure 4.6 but for SDSS J1316+1753

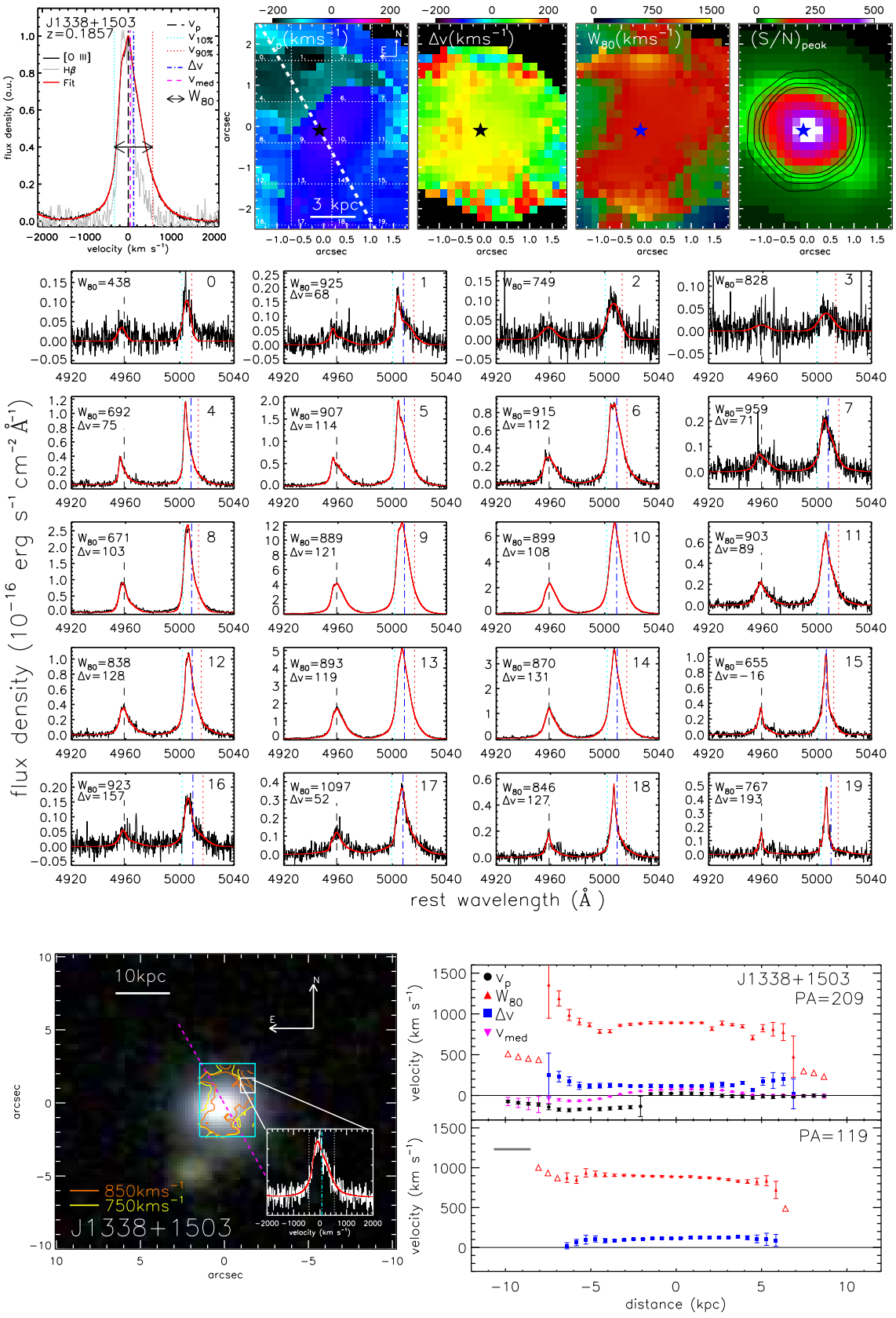

Figure 4.22: Same as Figure 4.5 and Figure 4.6 but for SDSS J1338+1503

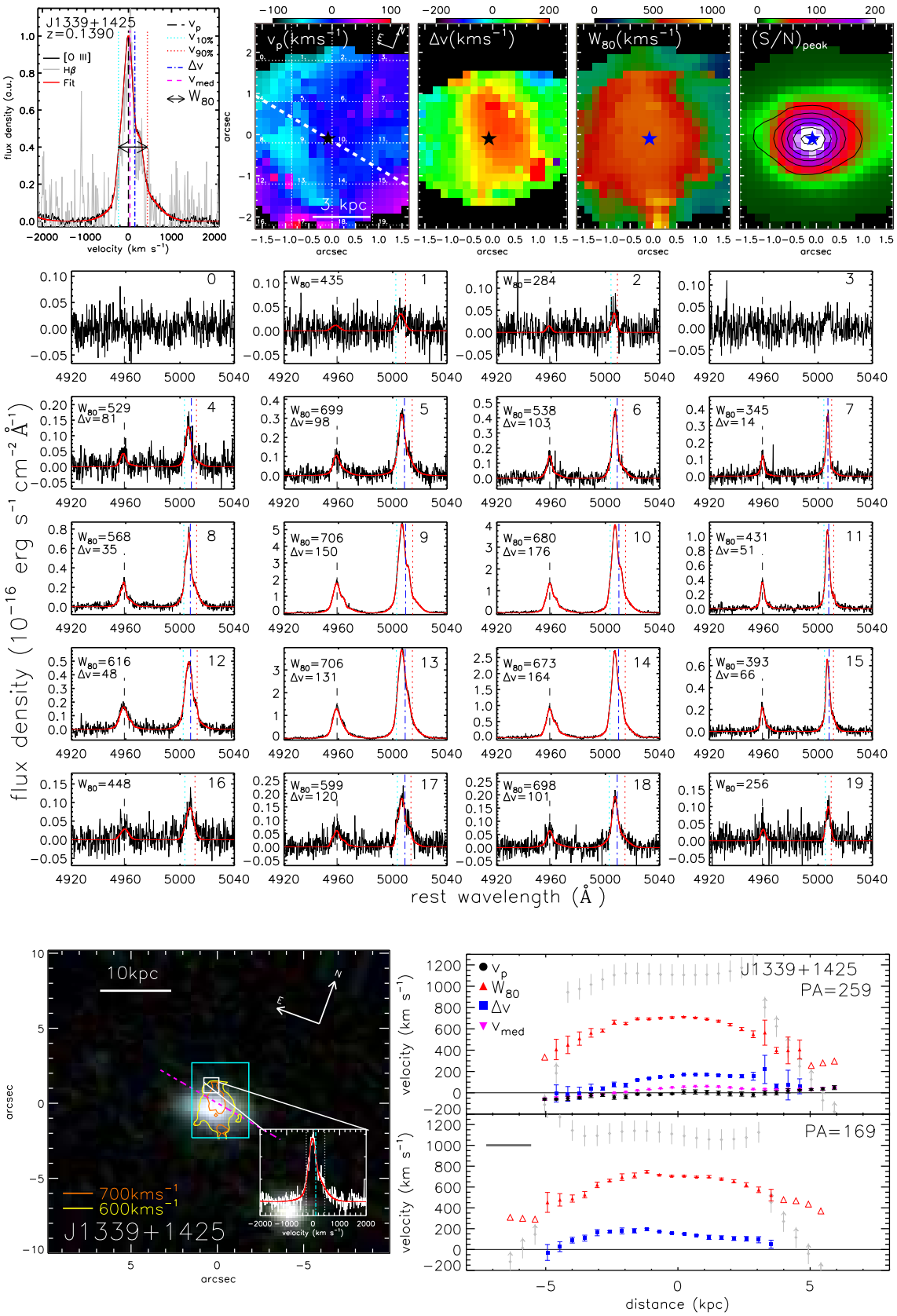

Figure 4.23: Same as Figure 4.5 and Figure 4.6 but for SDSS J1339+1425

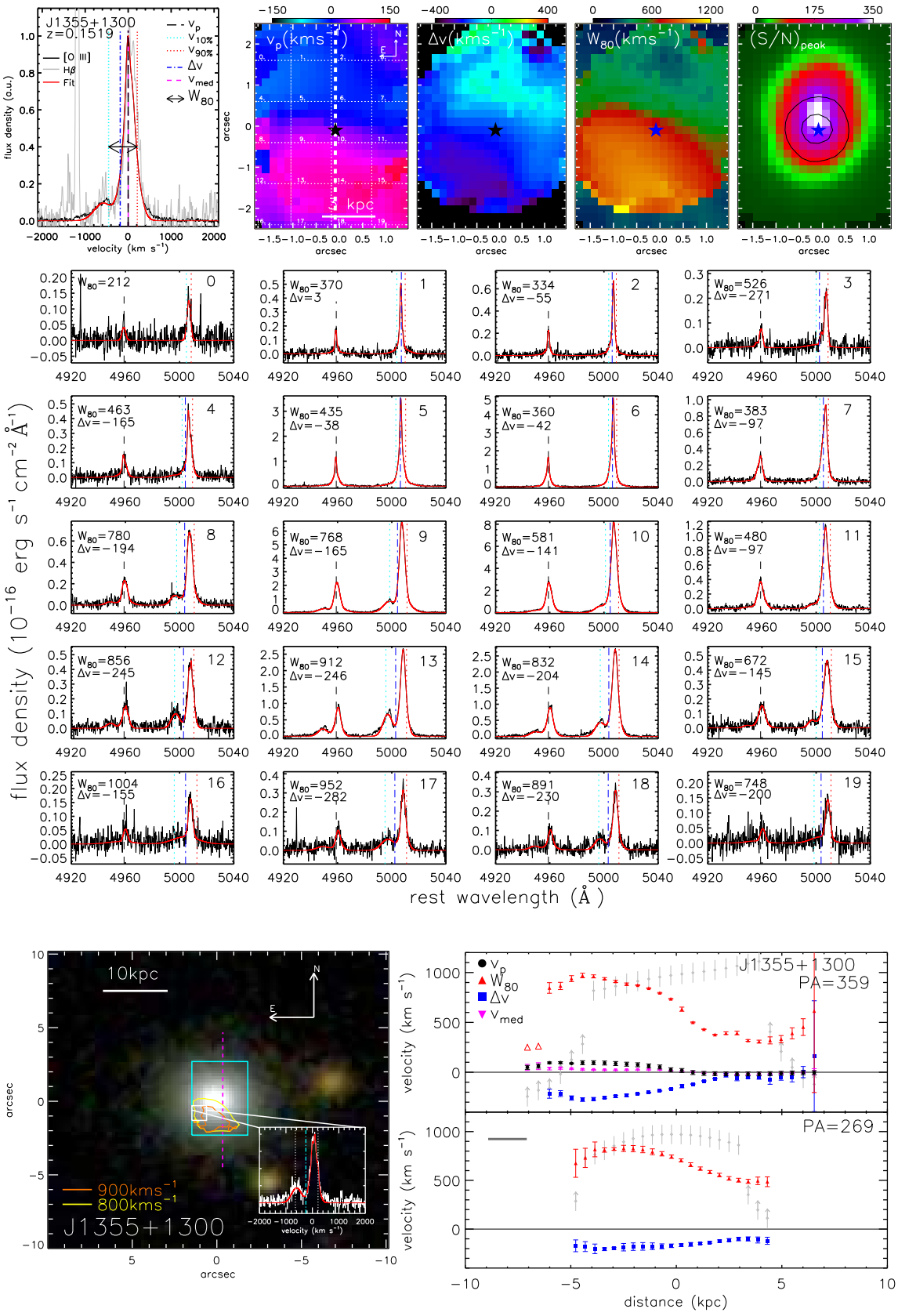

Figure 4.24: Same as Figure 4.5 and Figure 4.6 but for SDSS J1355+1300

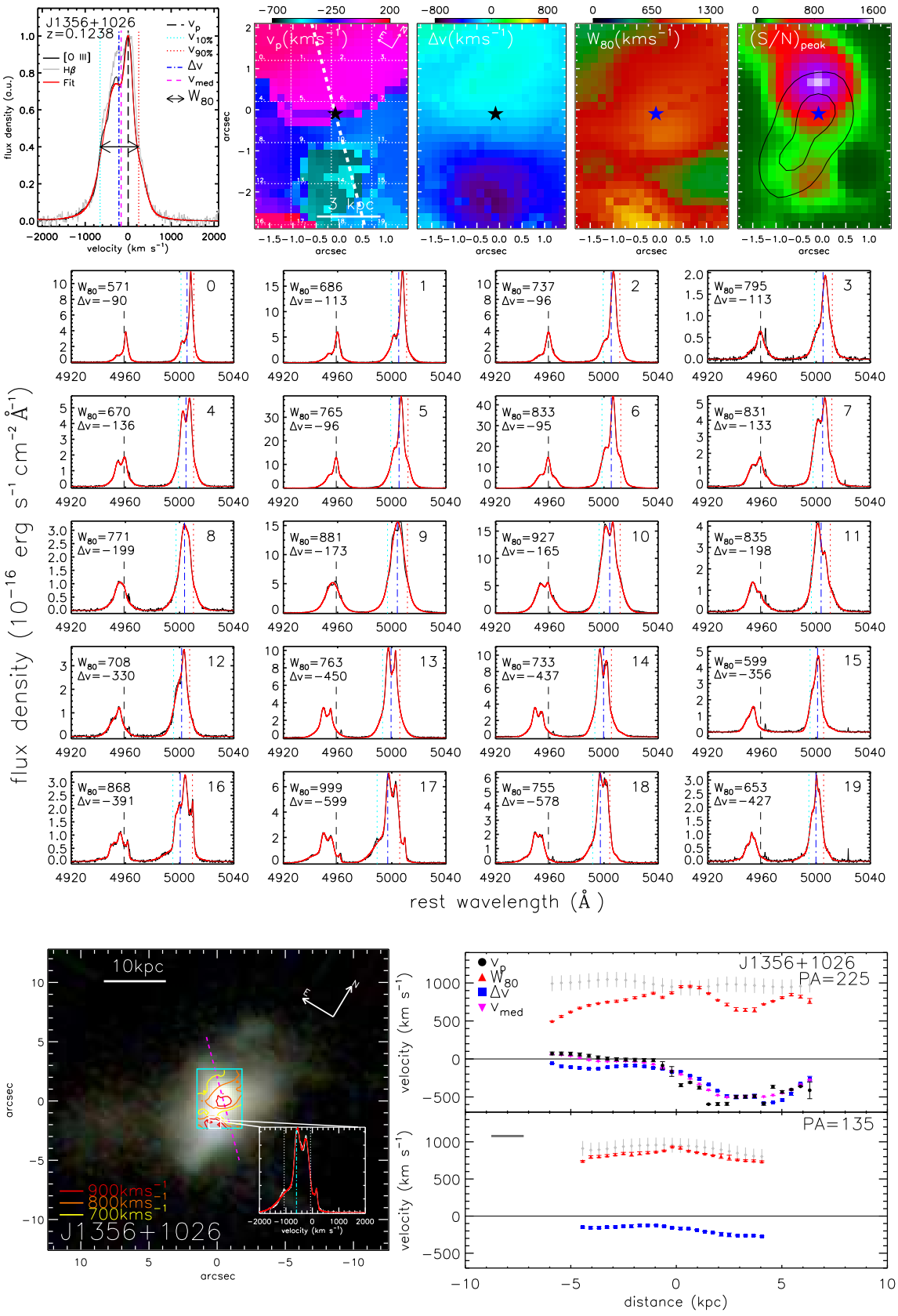

Figure 4.25: Same as Figure 4.5 and Figure 4.6 but for SDSS J1356+1026

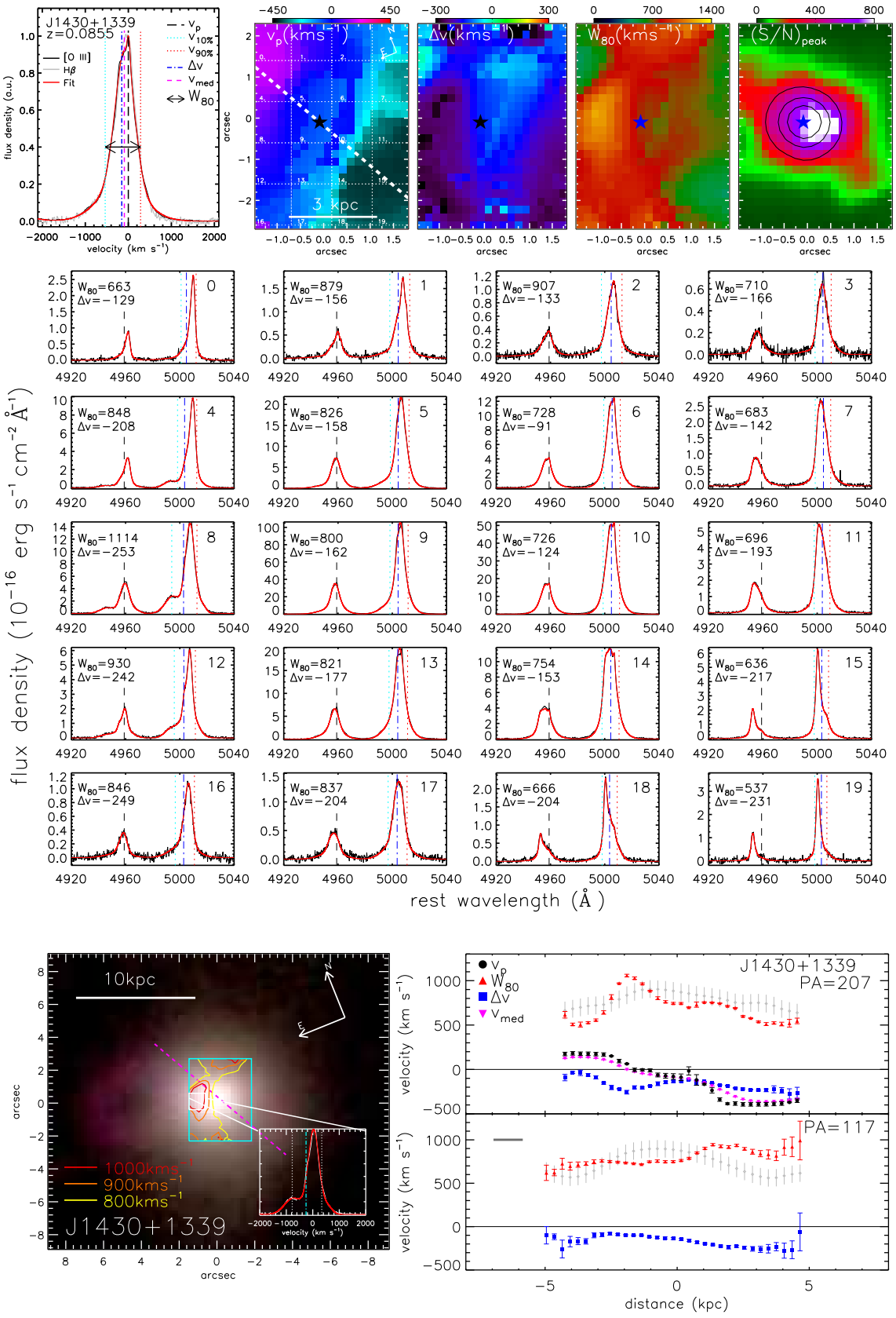

Figure 4.26: Same as Figure 4.5 and Figure 4.6 but for SDSS J1430+1339

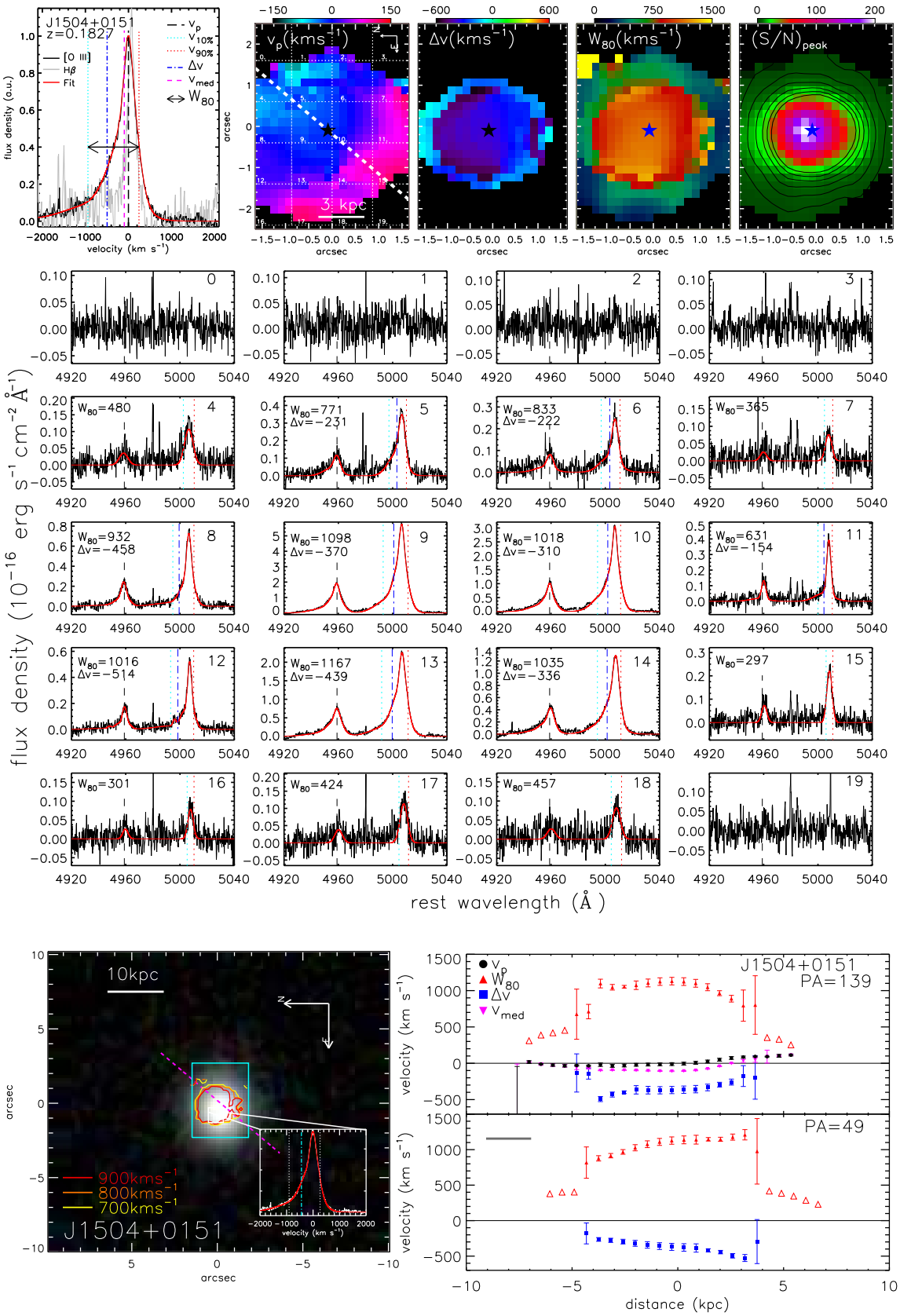

Figure 4.27: Same as Figure 4.5 and Figure 4.6 but for SDSS J1504+0151.

CHAPTER 5

No submillimetre signature of star formation suppression among X-ray luminous AGN

Abstract

Many theoretical models require powerful active galactic nuclei (AGN) to suppress star formation in distant galaxies and reproduce the observed properties of today's massive galaxies. A recent study based on *Herschel*-SPIRE submillimetre observations claimed to provide direct support for this picture, reporting a significant decrease in the mean star-formation rates (SFRs) of the most luminous AGN ($L_{\rm X} > 10^{44}$ erg s^{-1}) at $z \approx 1$–3 in the *Chandra* Deep Field-North (CDF-N). In this chapter we extend these results using *Herschel*-SPIRE 250μm data in the COSMOS and CDF-S fields to achieve an order of magnitude improvement in the number of sources at $L_{\rm X} > 10^{44}$ erg s^{-1}. On the basis of our analysis, we find no strong evidence for suppressed star formation in $L_{\rm X} > 10^{44}$ erg s^{-1} AGN at $z \approx 1$–3. The mean SFRs of the AGN are constant over the broad X-ray luminosity range of $L_{\rm X} \approx 10^{43}$–$10^{45}$ erg s^{-1} (with mean SFRs consistent with typical star-forming galaxies at $z \approx 2$; $\langle {\rm SFRs} \rangle \approx 100$–$200\,{\rm M}_{\odot}\,{\rm yr}^{-1}$). We suggest that the previous CDF-N results were likely due to low number statistics. We discuss our results in the context of current theoretical models.

5.1 Motivation

In Section 1.6 of this thesis we described how many theoretical models predict that the most luminous AGN drive outflows and suppress star formation in their host galaxies. In the previous chapters of this thesis we have searched for and characterised galaxy-

wide outflows in AGN. In this chapter we ask if there is evidence that luminous AGN have suppressed star formation rates (SFRs). Several papers, previous to the work presented here, had investigated the SFRs of moderate luminosity X-ray detected AGN (i.e., $L_{2-8\,\mathrm{keV}} \approx 10^{42-44}\,\mathrm{erg\,s^{-1}}$) and found the general agreement that the average SFRs are consistent with non-AGN host galaxies (see Section 1.6.3 and below). However, there are significant differences in the results presented on the SFRs of the most luminous AGN (i.e., $L_{2-8\,\mathrm{keV}} \gtrsim 10^{44}\,\mathrm{erg\,s^{-1}}$). The motivation of the work presented in this chapter was to investigate the reasons for these discrepancies and provide a clearer picture on the SFRs of luminous AGN. A general introduction is provided in Section 1.6, whilst in this chapter we only give a short introduction that is focused on the work presented here. The subsequent sections of this chapter (Section 5.3 onwards) have been published, as written here, in Harrison et al. (2012b).

5.2 Introduction

A large suite of studies have investigated the relationship between AGN activity and star formation out to high redshifts ($z \approx 3$), using deep X-ray and infrared data to constrain the AGN activity and star formation rates (SFRs), respectively (Mullaney et al. 2010; Hatziminaoglou et al. 2010; Lutz et al. 2010; Shao et al. 2010; Mainieri et al. 2011; Mullaney et al. 2012a; Santini et al. 2012; Rosario et al. 2012; Page et al. 2012; Rovilos et al. 2012). These studies have shown that the mean SFRs of moderate-luminosity AGN ($L_{\mathrm{X}} \approx 10^{42}$–$10^{44}\,\mathrm{erg\,s^{-1}}$) out to $z \approx 3$ are comparable to those of star-forming galaxies with similar redshifts (e.g., Noeske et al. 2007; Elbaz et al. 2007; Daddi et al. 2007a; Pannella et al. 2009). However, while these studies find broadly similar results for the average SFRs of moderate-luminosity AGN, the picture for luminous AGN ($L_{\mathrm{X}} > 10^{44}\,\mathrm{erg\,s^{-1}}$) is less clear, with the majority of these studies arguing that the mean SFR either rises or remains flat towards the highest luminosities (e.g., Lutz et al. 2010; Shao et al. 2010; Rosario et al. 2012; Rovilos et al. 2012).

Recently, Page et al. (2012) used *Chandra* X-ray and *Herschel*-SPIRE submillimetre data in the *Chandra* Deep Field-North (CDF-N) to report that the mean SFRs of luminous AGN ($L_{\mathrm{X}} > 10^{44}\,\mathrm{erg\,s^{-1}}$) at $z \approx 1$–3 are significantly lower than those of moderate-

luminosity AGN. The implications of this study are potentially very significant as they imply a direct, empirical connection between luminous AGN activity and the suppression of star formation. However, these results are in disagreement with other studies, many of which also used *Herschel* data in similarly deep fields (e.g., Lutz et al. 2010; Shao et al. 2010; Rosario et al. 2012; Rovilos et al. 2012).

The aim of this chapter is to extend the Page et al. (2012) study using *Herschel*-SPIRE 250μm data in the wider-area COSMOS field, improving the source statistics for $L_{\rm X} > 10^{44}$ erg s^{-1} AGN by an order of magnitude. Indeed, a clear limitation of the Page et al. (2012) study was the small number of sources in the $L_{\rm X} > 10^{44}$ erg s^{-1} bins ($\approx$ 7–14 objects). We note that our study only explores the mean SFRs using stacking analysis and does not explore the individual detection rates (i.e., figure 1 of Page et al. 2012); however, significant differences in the detection fractions should lead to differences in the mean SFRs. We also repeat our analysis using *Herschel*-SPIRE 250μm data in the CDF-N and *Chandra* Deep Field South (CDF-S) fields to explore the effect of using smaller fields. In our analysis we use $H_0 = 71\,{\rm km\,s^{-1}}$, $\Omega_{\rm M} = 0.27$, $\Omega_\Lambda = 0.73$ and assume a Salpeter initial mass function (IMF).

5.3 Catalogues and data

5.3.1 X-ray data

Our samples of AGN are X-ray selected and cover a broad range of luminosities ($L_{\rm X} = 10^{42} - 10^{45}$ erg s^{-1}) over the redshift range $z = 1$–3 (see Figure 5.1). We use the CDF-N (Alexander et al. 2003a), CDF-S (Xue et al. 2011) and COSMOS (Elvis et al. 2009) AGN samples to obtain statistically meaningful numbers of AGN in key $L_{\rm X}$ ranges. Redshifts for the CDF-N and CDF-S samples were taken from Bauer et al. in prep. and Xue et al. (2011), respectively. Redshifts for the COSMOS sample were taken from Civano et al. (2012). Unless otherwise stated, we include both photometric and spectroscopic redshifts, which comprise $\approx 53\%$ and $\approx 47\%$ of the combined samples respectively; however, we note that our conclusions do not change if we only consider spectroscopic redshifts. Following Page et al. (2012) we derive the rest-frame observed (i.e., not absorption-corrected) 2–8 keV luminosity ($L_{\rm X}$) of AGN in each field using $L_{\rm X} = 4\pi D^2 F_{\rm X} (1+z)^{(\Gamma-2)}$,

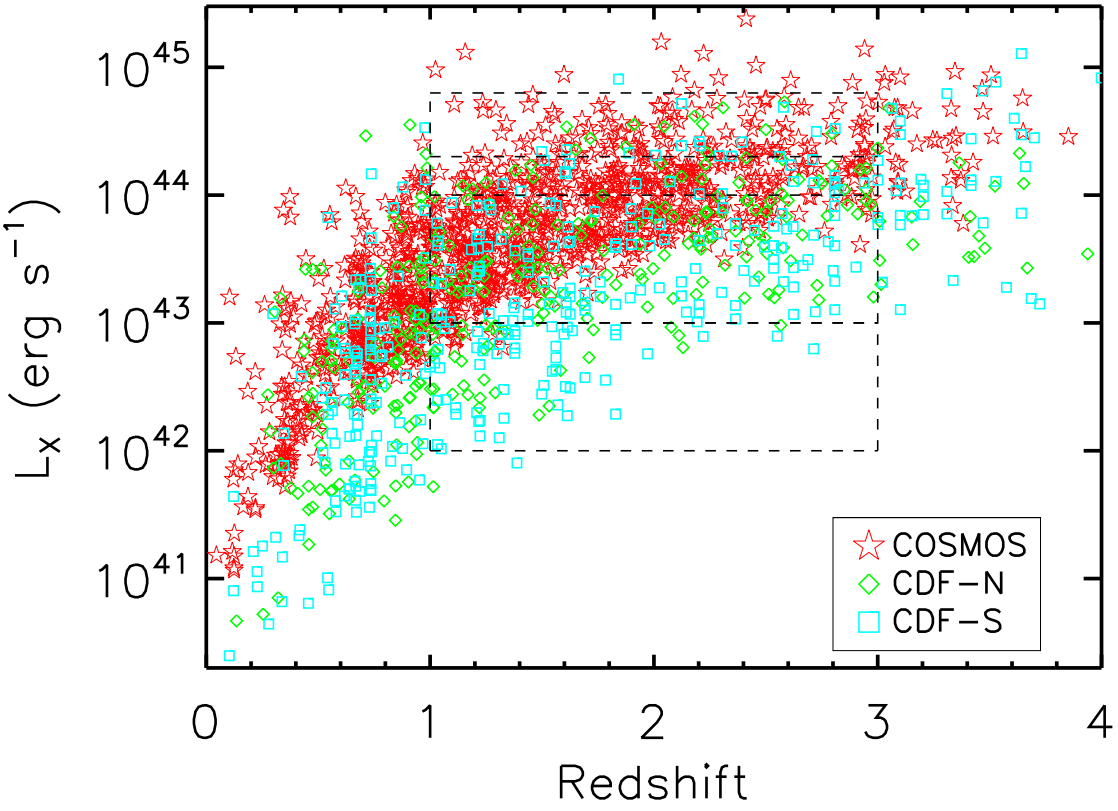

Figure 5.1: Rest-frame 2–8 keV luminosities (not-absorption corrected) of the X-ray AGN detected in the three deep fields (see §5.3 for details) versus redshift. The areas of parameter space used in our stacking procedures (see Figure 5.3) are illustrated with the dashed lines. Caution should be taken when interpreting the lowest X-ray luminosity bin ($L_{\rm X} = 10^{42}$–10^{43} erg s^{-1}) as it is incomplete at $z \gtrsim 2$

where $F_{\rm X}$ is the observed X-ray flux[1] (2–8 keV), D is the luminosity distance, z is the redshift and Γ is the spectral index used for k-corrections (we assume $\Gamma = 1.9$).

In Figure 5.1 we show $L_{\rm X}$ versus redshift for the X-ray AGN in each of these fields. These three samples are highly complimentary: the ultra-deep CDF-N and CDF-S samples provide large numbers of moderate luminosity AGN at $z = 1$–3 (i.e., $L_{\rm X} = 10^{42} - 10^{44}$ erg s^{-1}) while the shallower, wider-area COSMOS survey populates the high-luminosity ($L_{\rm X} > 10^{44}$ erg s^{-1}) portion of the parameter space largely missed by these small area surveys.

[1] We note Elvis et al. (2009) report 2–10 keV fluxes, which we convert to 2–8 keV fluxes by assuming $\Gamma = 1.9$ (i.e., a factor of $\approx$0.85 correction).

$L_{\rm X}$ range (1)	$N_{\rm AGN}$ (2)	$\langle z \rangle$ (3)	$\langle L_{\rm X} \rangle$ (4)	$\langle S_{250} \rangle$ (5)	$\langle {\rm SFR} \rangle$ (6)
CDF-N (HerMES; Figure 5.2)*					
$43.00-43.33$	8	1.8	43.2	$5.4^{+3.0}_{-3.0}$	108^{+61}_{-60}
$43.33-43.66$	20	1.7	43.5	$9.4^{+2.3}_{-2.4}$	176^{+105}_{-54}
$43.66-44.00$	11	1.9	43.8	$10.9^{+3.7}_{-3.6}$	297^{+100}_{-134}
$44.00-44.33$	12	2.0	44.2	$4.8^{+2.5}_{-2.4}$	115^{+56}_{-55}
$44.33-44.80$	7	2.1	44.6	<4.4	<127
CDF-N (GOODS-*H*; Figure 5.3)					
$42.00-43.00$	35	1.3	42.8	$3.5^{+1.1}_{-1.1}$	46^{+14}_{-14}
$43.00-44.00$	114	1.9	43.6	$6.8^{+1.0}_{-0.9}$	151^{+22}_{-21}
$44.00-44.80$	37	2.2	44.3	$2.2^{+0.9}_{-0.9}$	69^{+25}_{-26}
CDF-S (Figure 5.3)					
$42.00-43.00$	53	1.4	42.7	$4.3^{+1.0}_{-1.1}$	63^{+16}_{-16}
$43.00-44.00$	114	1.9	43.5	$5.3^{+1.0}_{-1.0}$	117^{+22}_{-21}
$44.00-44.80$	35	2.2	44.3	$7.2^{+1.4}_{-1.4}$	276^{+59}_{-92}
COSMOS (Figure 5.3)					
$44.00-44.30$	173	2.0	44.1	$6.0^{+0.9}_{-0.9}$	145^{+22}_{-22}
$44.30-44.80$	111	2.1	44.5	$6.3^{+1.1}_{-1.1}$	175^{+50}_{-31}

Table 5.1: (1) X-ray luminosity (2–8 keV) range of each bin ($\log[{\rm erg\,s^{-1}}]$); (2) Number of X-ray AGN in each bin; (3) Mean redshift; (4) Mean $L_{\rm X}$ ($\log[{\rm erg\,s^{-1}}]$); (5) Mean 250μm flux and uncertainties (mJy); (6) Mean star formation rate ($M_\odot\,{\rm yr^{-1}}$). The quoted uncertainties are derived from our bootstrap method (see §5.4). *To be consistent with Page et al. (2012) we use the same $L_{\rm X}$ bins and only include AGN with spectroscopic redshifts when stacking the HerMES data for the CDF-N field (see §5.5).

5.3.2 IR Data

The mean SFRs for our AGN samples are derived from 250μm observations taken by the SPIRE instrument on board *Herschel* which are relatively unaffected by contamination from the AGN (e.g., Hatziminaoglou et al. 2010) or obscuration due to dust. Our results are primarily based on the observations of the CDF-N, CDF-S and COSMOS fields undertaken as part of the HerMES campaign (described in Oliver et al. 2012). We downloaded the individual level-2 data products from each scan of each field (totalling ~ 14 hours, ~ 20 hours and ~ 50 hours in CDF-N, CDF-S and COSMOS, respectively) from the *Herschel* ESA archive and then aligned and coadded the images. The coadded images were then aligned onto a common world co-ordinate system. We also checked for consistency between our own coadds and those produced using the standard HIPE v9.0 pipeline.

We also make use of 250μm SPIRE observations of the CDF-N field that were undertaken as part of the GOODS-*Herschel* program (GOODS-*H*; P.I.: D. Elbaz) that cover the whole of the CDF-N (totalling 44 hours when combined with the HerMES observations). The observations and steps used to produce the science images are described in Elbaz et al. (2011). We note that our results derived from the GOODS-*H* CDF-N observations are consistent with those derived from the HerMES observations of the same field.

5.4 Measuring average star formation rates

To determine the mean SFRs of AGN as a function of $L_{\rm X}$ we split our samples into a number of $L_{\rm X}$ bins (see Table 5.1). The majority of the X-ray AGN are not individually detected by *Herschel*-SPIRE (e.g., Hatziminaoglou et al. 2010; Page et al. 2012) and therefore, we rely on stacking analysis to obtain the mean 250μm fluxes of our AGN samples in each bin. We stack at the optical positions of all X-ray AGN in our samples, whether they are individually 250μm-detected or not (following Page et al. 2012). The point-spread function (PSF) of the SPIRE 250μm science images is normalised to 1 and in units of mJy beam^{-1}, such that the mean 250μm flux was taken to be the central pixel value of each stacked image.

To determine if the measured fluxes from our stacked images are significantly above the background we employed a Monte-Carlo approach, which quantifies the level of back-

ground and confusion noise (i.e., flux contribution to our stacked images from nearby, unassociated sources). Firstly, along with each "true" stacked image we also made 10,000 "random" stacks, stacking the same number of random positions around the field as in our true stacks. The mean flux of the random stacks was subtracted from that of the true stack, effectively removing any systematic contribution from the background or confusion. Secondly, we compare our measured "corrected" fluxes of our true stacks to the distribution of fluxes from our random stacks. We consider a stacked signal to be significant if the flux is greater than the flux of 95% of the random trials. Following this criterion, all but one of our stacked images have flux measurements that are significant (see §5.5 for details). We note that this method of randomly choosing positions to estimate the background does not take into account any clustering between X-ray AGN and IR-sources (this was also not considered in Page et al. 2012). While this will not affect the SFR-$L_{\rm X}$ trends, the mean background subtracted from each stacked image may be slightly under-estimated, resulting in the absolute mean SFRs quoted being slightly over-estimated. However, we note that our results are consistent with studies that are less affected by confusion noise (e.g., Mullaney et al. 2012a; Rosario et al. 2012), giving confidence in our procedures.

We used the spectral energy distribution (SED) library of Chary & Elbaz (2001) to convert mean 250μm fluxes from our stacked images to mean integrated 8–1000 μm infrared luminosities ($L_{\rm IR}$), selecting a redshifted Chary & Elbaz (2001) SED on the basis of the monochromatic luminosity probed by the 250μm waveband. These mean $L_{\rm IR}$ values were converted to mean SFRs using Kennicutt (1998). In the redshift range $z = 1$–3 investigated here, the observed 250μm fluxes correspond to the peak of the SEDs in the rest frame. As such the L_{250} to $L_{\rm IR}$correction factors do not vary much as a function of SED shape when compared to using shorter wavelengths (see Figure 3 in Elbaz et al. 2010). Indeed, when we compared *all* of the Chary & Elbaz (2001) SEDs, redshifted to $z = 2$, the conversion factors were consistent within $\approx$20%; we also repeated our analysis using the main-sequence SED from Elbaz et al. (2011) for all of the bins and found no significant difference. While the choice of SED adds a small additional uncertainty in the measured SFRs (such that quoted absolute SFRs should be used with care), all of the observed trends, and hence the main conclusions of this chapter, remain unaffected. We also show in §5.5 that we reproduce the results of Page et al. (2012).

Upper and lower limits on the mean SFRs for each of our L_X bins were calculated using a bootstrapping technique, therefore taking into account the distribution of SFRs in each stack. We randomly subsample (with replacement) the AGN in each of our bins, restack and recalculate the mean SFR. We did this 10,000 times for each bin to produce a distribution of mean SFRs. The quoted upper and lower limits on the mean SFRs correspond to the 16th and 84th percentiles (i.e., incorporating 68%, or $\approx \pm 1\sigma$) of this distribution (Table 5.1).

5.5 Results and discussion

We first stacked sub-samples of X-ray AGN in the CDF-N. In an attempt to reproduce the results of Page et al. (2012) we split the sample into the same luminosity bins used in their study (Table 5.1) and only included AGN with spectroscopic redshifts; see Figure 5.2. We find excellent agreement between our mean SFRs and those of Page et al. (2012) (i.e., data points are consistent within their uncertainties), demonstrating the compatibility of the procedures used to derive these results.[2] In agreement with Page et al. (2012), we do not obtain a significant flux measurement from the stacked 250μm image of our highest L_X bin ($\log[L_X/\mathrm{erg\,s^{-1}}] = 44.33$–$44.80$). However, unlike Page et al. (2012), we find our upper limit is consistent with the mean SFRs of the lowest L_X bins.

The non-detection at FIR wavelengths of the AGN in our highest L_X bin in the CDF-N field, combined with the small numbers of AGN in this bin (7 sources), clearly demonstrates the need for larger numbers of sources at high X-ray luminosities. To achieve this, we performed the same stacking procedures using the COSMOS survey. The inclusion of the COSMOS AGN means that the number of sources in our highest L_X bins are now greater by an order of magnitude (Figure 5.1 and Table 5.1). As such, we can now place tighter constraints on the mean SFRs of high-luminosity AGN. On the basis of our stacking analysis in the COSMOS field, we find that the mean SFRs of AGN with $L_X > 10^{44}$ erg s^{-1} are consistent with those of $L_X = 10^{43}$–10^{44} erg s^{-1} AGN ($\approx$100–200 $\mathrm{M_\odot\,yr^{-1}}$; see Figure 5.3 and Table 5.1). This implies that the mean SFR of $z = 1$–3

[2] We note that Page et al. (2012) used a different technique to that adopted by us here; they derive average SFRs by fitting a modified black body to the SPIRE fluxes of each source.

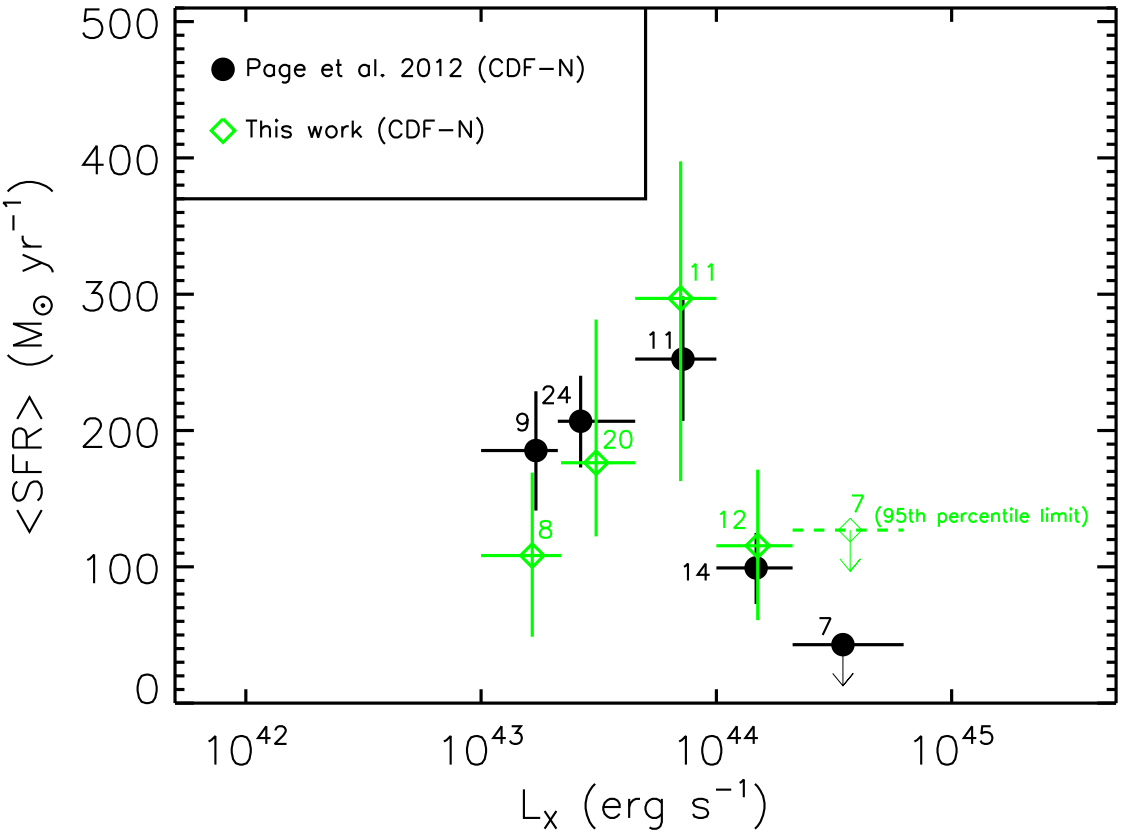

Figure 5.2: Mean star formation rate (SFR) vs. X-ray luminosity for AGN in the CDF-N field compared to Page et al. (2012); see §5.4 for details. We find excellent agreement between our mean SFRs and those of Page et al. (2012) across all L_X bins; we indicate the number of sources in each bin (the differences in the number of objects between our study and Page et al. (2012) are due to differences in the redshift catalogues). We note that for Page et al. (2012) the values were extracted directly from their figures as tabulated values were unavailable. As with Page et al. (2012), we do not measure a significant flux in the highest L_X bin for which we also include the 95th percentile limit (see §5.4). This limit is broadly consistent with the mean SFRs for our lower L_X bins.

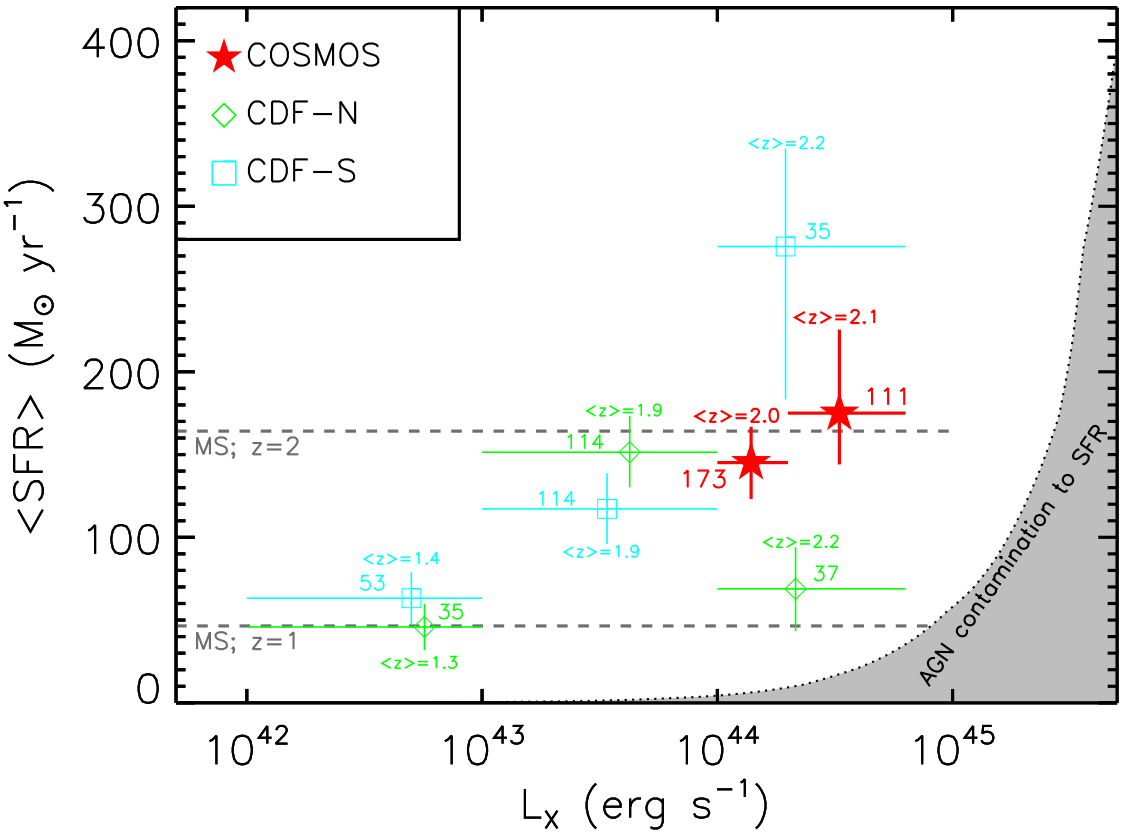

Figure 5.3: Mean SFR vs. L_X for AGN in the three fields (see §5.4 for details). We indicate the number of, and the average redshift of, the AGN in each bin (Table 5.1). The dotted curve indicates the contamination to the measured SFR from AGN activity (i.e., the amount that the SFRs will be boosted by due to contamination of the 250μm flux [rest-frame 83μm at $z = 2$] by AGN activity) and is calculated using the L_X-L_{MIR} relation of Gandhi et al. (2009) and the intrinsic AGN SED of Mullaney et al. (2011). The dashed lines show the average SFR expected (derived from Elbaz et al. 2011) for a galaxy with a stellar mass of 9×10^{10} $M_\odot$ (i.e., about the mean stellar mass of X-ray detected AGN hosts; e.g., Xue et al. 2010; Mullaney et al. 2012a) at $z = 1.0$ and $z = 2.0$. We find that the mean SFR distribution at $L_X > 10^{42}$ erg s^{-1} is roughly equal to that expected from typical star-forming galaxies at the average redshifts of our bins (our $L_X < 10^{43}$ erg s^{-1} bins have lower mean redshifts and hence lower mean SFRs; e.g., Mullaney et al. 2012a). We show that there are variations in the measured mean SFRs between the small CDF-N and CDF-S fields and argue that this, combined with low number statistics drive the Page et al. (2012) results shown in Figure 5.2.

AGN is independent of X-ray luminosity (although increases with increasing redshifts), in broad agreement with Rosario et al. (2012) and indicates that the flat SFR distribution at $L_{\rm X} < 10^{44}$ erg s^{-1} (e.g., Lutz et al. 2010; Shao et al. 2010; Mullaney et al. 2012a; Rosario et al. 2012) continues out to at least $L_{\rm X} \approx 10^{44.8}$ erg s^{-1}.[3]

The results derived from our stacking of AGN in the COSMOS field may suggest that poor source statistics and potentially field–to–field variations (i.e., cosmic variance) are at least partially responsible for the disagreement between the results from COSMOS and CDF-N at high X-ray luminosities. To further investigate this we also stacked the SPIRE data in the CDF-S field, which is of a similar size as the CDF-N and contains approximately the same number of high $L_{\rm X}$ AGN (Figure 5.1). We also restack the CDF-N AGN using the deeper 250μm observations taken as part of the GOODS-*H* program since this is of comparable depth to the HerMES CDF-S observations. As shown in Figure 5.3, we find broad agreement between the mean SFRs of moderate luminosity AGN (i.e., $L_{\rm X} < 10^{44}$ erg s^{-1}) in both fields: the mean SFRs with X-ray luminosity over the range $L_{\rm X} \approx 10^{42}$–$10^{44}$ erg s^{-1} are consistent with those expected from typical star-forming galaxies with the average redshifts and typical stellar masses observed for the AGN host galaxies. The increasing specific SFRs with redshift (e.g., Elbaz et al. 2011) is likely to drive the apparent increase in the mean SFRs between $L_{\rm X} \approx 10^{42}$–$10^{43}$ erg s^{-1} and $L_{\rm X} \approx 10^{43}$–$10^{44}$ erg s^{-1} (i.e., they have different mean redshifts).

In contrast to the lower X-ray luminosity systems, the mean SFRs of AGN between CDF-N and CDF-S appears to diverge at the highest X-ray luminosities (i.e., $L_X > 10^{44}$ erg s^{-1}). We note that the higher mean SFR observed for high $L_{\rm X}$ AGN in the CDF-S is broadly consistent with the results found by Lutz et al. (2010) and Rovilos et al. (2012) in the same field. Despite these field–to–field variations the mean SFRs in the CDF-S and CDF-N fields are consistent with that found in the COSMOS field (within $\approx 1\sigma$ and $\approx 3\sigma$ respectively).

We now consider if our main result indicates that luminous AGN activity does not suppress star formation in the host galaxies. Any *observed* change in the mean SFRs due

[3] We note that this approach is different to averaging over *all* $L_{\rm X}$ and $L_{\rm IR}$ over *all* star-forming galaxies (whether X-ray detected or not) where a clear relationship between $L_{\rm X}$ and SFR is found (see Mullaney et al. 2012b).

to luminous AGN activity will depend on the relative timescales of the process of shutting down star formation and of the luminous AGN activity itself. For example, if the time between the onset of luminous AGN activity and the shut down of star formation is longer than the AGN lifetime (which may in itself be highly variable; e.g., Novak et al. 2011) then it would be challenging to observe significantly reduced mean SFRs, simply on the basis of an X-ray luminosity threshold. A major uncertainty in providing a detailed assessment of possible connections between luminous AGN and the suppression of star formation is due to the relative lifetimes of these processes. Modelling suggests that episodes of the most luminous AGN activity last $<$80 Myrs (Hopkins et al. 2005a; Novak et al. 2011) while studies based on black hole mass functions and AGN luminosity functions imply that luminous AGN activity could last in excess of $\approx 10^8$ years (e.g. Marconi et al. 2004; Kelly et al. 2010; Cao 2010). Observations of AGN-driven $\approx$1000 km s^{-1} outflows, found over kilo-parsec scales in $z \approx$ 1–3 ultra-luminous infrared galaxies (ULIRGs; Harrison et al. 2012a) indicate that star-formation episodes could be rapidly shut down; indeed, detailed studies of local ULIRGs with AGN-driven molecular outflows indicate that their gas reservoirs could be completely removed in $\approx$ 1–40 Myrs (e.g., Feruglio et al. 2010; Sturm et al. 2011). Therefore, while to first order our results may appear to suggest that luminous AGN do not suppress star formation, it is also possible that the timescales for luminous AGN activity and the suppression of star-formation are comparable, meaning that any signatures of suppression would be very challenging to detect with the current data. Clearer signatures of suppressed star formation may be more apparent when considering subsets of the AGN population which may represent specific evolutionary stages (e.g., Page et al. 2004; Stevens et al. 2005).

To summarise, we find no evidence for the significantly reduced mean SFRs among high luminosity AGN, and the mean SFRs measured are consistent with that expected from typical star-forming galaxies at the average redshifts and typical stellar masses of our bins. We have suggested that, depending on the timescales involved, it could be challenging to see the signature of suppressed star formation simply on the basis of an X-ray luminosity threshold.

CHAPTER 6

Conclusions and future work

This thesis has presented observational experiments to address theoretical predictions on the influence of AGN on the evolution of galaxies. This chapter summarises the main results from the work presented in this thesis and the main outstanding issues that are still to be addressed. On-going and future projects are also described, along with some of their preliminary results.

6.1 Summary of the presented work

This thesis has placed observational constraints on the influence of AGN on the evolution of galaxies by studying bolometrically luminous AGN (i.e., $L_{\rm AGN} \gtrsim 10^{43}\,{\rm erg\,s^{-1}}$). Luminous AGN are predicted to be capable of driving galaxy-wide outflows that can influence the evolution of their host galaxies by suppressing or enhancing star formation and driving gas out into the larger scale environment (see Section 1.6). In this thesis the prevalence and properties of galaxy-wide outflows have been explored as well as searching for observational evidence that luminous AGN are suppressing star formation in their host galaxies. The main results are summarised below.

6.1.1 The identification and characterisation of galaxy-wide outflows in ULIRGs hosting AGN activity

Chapter 3 presented IFU observations of eight high-redshift ($z = 1.4$–3.4) ULIRGs that host AGN activity to search for and to characterise galaxy-wide ionised outflows. High-redshift ULIRGs are galaxies that are believed to be progenitors of today's massive elliptical galaxies. The sources were selected from a sample of known ULIRG/AGN com-

posite galaxies that show broad and luminous emission-lines in their one-dimensional spectra. In the four systems with the highest quality data the signatures of large-scale energetic outflows were identified: extremely broad [O III] emission lines (FWHM $\approx$ 700–1400 km s^{-1}) across $\approx$4–15 kpc, with high velocity offsets from the systemic redshifts (up to $\approx$850 km s^{-1}). It was estimated that these outflows are depositing energy into their host galaxies at considerable rates ($\dot{E} \approx 10^{43}$–10^{45} erg s^{-1}). Based on the measured maximum velocities ($v_{\rm max} \approx$ 400-1400 km s^{-1}) the outflows observed are likely to unbind some fraction of the gas from their host galaxies, but are unlikely to completely remove gas from the galaxy halos. The galaxies observed here are two to three orders of magnitude more common than the extreme high-redshift radio galaxies that are often associated with powerful large-scale outflows at high redshift. Fundamentally, these outflows may represent a crucial phase in the evolution of massive galaxies.

6.1.2 Galaxy-wide outflows in the context of the overall AGN population

Chapter 4 presented IFU observations of sixteen $z < 0.2$ type 2 AGN to search for and to characterise galaxy-wide ionised outflows. An important advantage of this work, over previous work, is that the targets were selected from a well constrained parent sample of $\approx 24,000$ AGN, which means that the observations can be placed into the context of the overall AGN population. The sixteen sources were selected to be luminous ($L_{[\rm O\ III]} > 5 \times 10^{41}$ erg s^{-1}) and have a broad [O III] emission-line component, based on the fitting to their one-dimensional spectra by Mullaney et al. (2013). A "broad component" was defined as a component with FWHM>700 km s^{-1} and that contributes at least 30% of the total emission-line flux. Using the parent sample, it was shown that 45$\pm$3% of the AGN in this luminosity and redshift range have broad components. High-velocity ionised gas (velocity widths $\approx$ 600–1500 km s^{-1} and maximum velocities $\leq$ 1700 km s^{-1}) with observed spatial extents of $\gtrsim$6–16 kpc was found in all of the IFU targets. It was shown that the targets are representative of $z < 0.2$, luminous (i.e., $L_{[\rm O\ III]} > 10^{41.7}$ erg s^{-1}) type 2 AGN and that ionised outflows are not only common but also that they are extended over kiloparsec scales in $\geq$70% (3σ confidence) of cases. The morphologies of the

emission-line regions and outflows were explored. Overall, the results show that galaxy-wide ionised outflows are an extremely common feature in galaxies that host luminous AGN. By applying some simple outflow models we estimate that the mass outflow rates are high (typically $\approx$10$\times$ the SFRs), indicating that these outflows have the potential to deplete the gas supply for future star formation in their host galaxies. Furthermore, the calculated estimates imply outflow kinetic energies ($\approx$ 0.5–10% of $L_{\rm AGN}$) and momentum rates (typically $\gtrsim$ [10–20] $\times L_{\rm AGN}/c$) consistent with theoretical models that predict that AGN-driven outflows play a significant role in shaping the evolution of galaxies.

6.1.3 Searching for observational evidence that luminous AGN suppress star formation

Chapter 5 presented results from stacking 250μm *Herschel* photometric data at the positions of $\approx$ 700 $z = 1$–3 X-ray detected AGN. The average 250 μm luminosities were used, derived from the stacks, as a proxy for the SFRs of the AGN host galaxies to investigate the average SFRs as a function of X-ray luminosity. Earlier published work had provided contradictory results on the SFRs of the most luminous AGN (i.e., $L_{2-8\,\rm keV} \gtrsim 10^{44}\,\rm erg\,s^{-1}$). In particular a result presented in *Nature* claimed evidence for the suppression of star formation by luminous AGN, in apparent contradiction with most earlier work. In this work the contradictory results were reconciled by showing that they are likely to be a result of small number statistics and field-to-field variations. Overall, it was found that the mean SFRs of AGN are constant over a broad X-ray luminosity range of $L_{2-8\,\rm keV} \approx 10^{43}$–$10^{45}$ erg s^{-1}, with mean SFRs that are consistent with typical star-forming galaxies at $z \approx 2$ (i.e., $\langle \rm SFRs \rangle \approx 100$–$200\,\rm M_{\odot}\,yr^{-1}$). Therefore, on the basis of this analysis, no strong evidence for suppressed star formation in luminous AGN at $z \approx 1$–3 was found. The implications of these results were discussed and it was suggested that due to the different timescales of luminous AGN activity and star formation episodes, it could be challenging to see the signature of suppressed star formation simply on the basis of an X-ray luminosity threshold.

6.2 Overall summary and outstanding issues

The work in this thesis has demonstrated that energetic galaxy-wide ionised outflows are a common feature of luminous AGN (Chapter 3 and Chapter 4). Firstly, they have been shown to exist in high-redshift ULIRGs that host AGN, which are galaxies thought to represent a key phase in the evolution of galaxies. By using a large sample of low redshift AGN it was also demonstrated that galaxy-wide ionised outflows are prevalent in luminous AGN. Importantly, all of the targets studied in this thesis were chosen to be more representative of the overall luminous AGN population compared to the objects studied in the majority of previous work. The estimated outflow properties (i.e., energetics and mass outflows rates) imply that the outflows could have a significant influence on the evolution of their host galaxies; however, measuring the properties of the outflows using tracers of other gas phases, in addition to the warm ionised gas traced here, will tighten these constraints (discussed in the next section). If the observed outflows are AGN driven, they provide a mechanism for an AGN to directly impact upon the evolution of their host galaxies, inline with some predictions from models of galaxy evolution. Whilst these results provide tentative evidence that the most powerful outflows are located in AGN host-galaxies (Chapter 3) and that AGN seem to be more energetically viable at driving the outflows compared to star formation (Chapter 3 and Chapter 4) these results do not yet conclusively determine which process drives the outflows. In apparent *contradiction* with some theoretical predictions, no evidence was found to indicate that luminous AGN have suppressed SFRs compared to the overall star-forming galaxy population (Chapter 5). It is clear that there is a requirement to have strong observational constraints on which mechanisms drive galaxy-wide outflows in luminous AGN and what long-term impact these outflows have on the evolution of galaxies. In the following section I outline some ongoing and future projects that are designed to address these issues.

6.3 Ongoing and Future Work

The work in this thesis has resulted in a number of follow-up projects to address the key outstanding questions. In this section, the ongoing and future projects are outlined, followed by some final remarks on the status of the research that is covered in this thesis.

6.3.1 What physical processes drive the outflows in AGN?

A key question to answer is what physical process (or processes) drive the galaxy-wide outflows that have been observed in the host galaxies of the luminous AGN studied in this thesis (i.e., Chapter 3 and Chapter 4) and those studied in other work. Possibilities include stellar or supernovae winds, radio jets and AGN accretion-disc winds. Indirect methods were used in this thesis to make a first attempt to answer this question (e.g., by estimating the energetics in the outflows compared to the energetic output of the AGN, star formation and possible radio jets); however, more direct methods would be preferable. A couple of my ongoing projects designed to move towards answering this question are described below.

Radio jets and star formation have been proposed as plausible driving mechanisms for high-velocity outflows. High spatial resolution radio data provides the opportunity to test these ideas. I have been awarded time on the radio interferometers JVLA (Project ID: VLA/13B-127; PI: Harrison) and e-MERLIN (Project ID: CY1022; PI: Harrison) to observe the objects identified as having galaxy-wide outflows in Chapter 4 of this thesis. These radio observations will be used to search for emission associated with radio jets and star formation and their spatial distribution will be compared to the structures of the outflows that were have observed. Both of the observing programmes are still open; however, data from both observatories have recently been taken. Figure 6.1 shows preliminary JVLA data for the type 2 AGN J1430+1339, that was studied in Chapter 4, along with *HST* data and the IFU data for this source. This source shows a dramatic bi-polar radio structure that is aligned with the emission-line gas. Although speculative at this stage, this could be a radio-quiet analogue of the powerful radio-galaxies which exhibit radio jets interacting with gas on scales of tens of kiloparsec (e.g., Villar-Martín et al. 1999; Tadhunter et al. 2000; Solórzano-Iñarrea & Tadhunter 2003; Nesvadba et al. 2006, 2008). Furthermore, we could be observing outflowing bubbles of gas expanding out into the larger-scale environment, as has been observed in local clusters, groups and massive elliptical galaxies (see review by McNamara & Nulsen 2012). This could provide some of the most direct evidence for how a luminous AGN (i.e., $L_{\rm AGN} = 10^{45.3}\,{\rm erg\,s^{-1}}$), with a *moderate* radio luminosity (i.e., $L_{1.4{\rm GHz}} = 10^{23.7}\,{\rm W\,Hz^{-1}}$) interacts with its host galaxy and larger scale environment over $\approx$10–20 kpc scales. Detailed analyses on the full set of

radio data, combined with the IFU observations will reveal the origin of the radio emission in this object and the rest of the sample.

Several theoretical models predict that AGN-driven winds, initially launched close to the accretion disk, propagate into the host galaxy and become galaxy-wide outflows (e.g., King 2003; Faucher-Giguère & Quataert 2012). Although both sub-parsec scale outflows and galaxy-wide outflows have been observed in AGN, there is currently no strong observational evidence that indicates that the outflows identified on these two spatial scales are directly related. In a first attempt to address this, I was awarded time on the IFU instruments Gemini-North/GMOS (Prog. ID: GN-2012B-Q-246; PI: Harrison) and ESO/VIMOS: (Prog. ID: 090.B-0060[A]; PI: Harrison) to observe five $z \approx 0.5$ broad absorption-line quasars (BALQSOs). BALQSOs exhibit broad and high-velocity ($v \approx 0.01$–$0.1c$; e.g., Weymann et al. 1991) absorption-line features in their spectra that are associated with accretion-disk winds on sub-parsec scales. The IFU data will be used to search for and to characterise galaxy-wide ionised outflows following the analyses outlined in Chapter 3 and Chapter 4. I will compare the properties of any observed galaxy-wide outflows to the properties of the high-velocity small-scale outflows that can be characterised using the broad absorption lines.

6.3.2 What are the multi gas-phase properties of galaxy-wide outflows?

The observations of the outflows in this thesis have studied the warm ($T \approx 10^4$ K) ionised gas that can be traced by rest-frame optical emission lines (e.g., [O III]λ5007 and Hβ). As demonstrated in Chapter 4, one clear advantage of tracing outflows in this gas phase, over other gas phases, is that large statistical spectroscopic surveys, such as the SDSS, can be exploited to understand the overall population. However, galaxy-wide outflows are likely to consist of multiple gas phases (i.e., warm ionised, hot ionised, atomic and molecular). Observations of all gas phases are required to build up a full picture of the total mass and energy involved in these outflows. In turn this then helps address the overall impact that these outflows will have on their host galaxies.

I was awarded time on the IRAM-30m telescope to observe the CO(1–0) emission

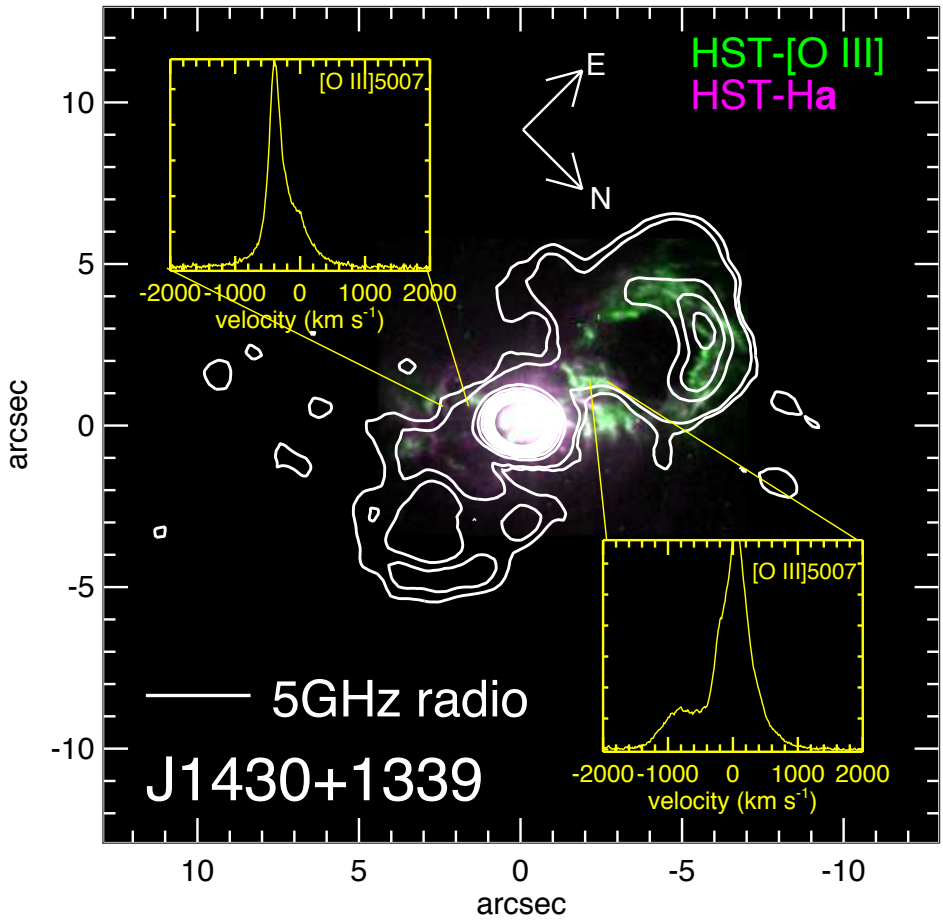

Figure 6.1: Composite HST narrow-band image of J1430+1339 with the [O III] emission shown in green and the Hα emission shown in purple. The contours show the surface brightness of the 5 GHz radio continuum from the new JVLA observations. Also shown are two [O III] emission-line profiles extracted from the IFU data that is presented in Chapter 3 of this thesis. The spectra are extracted from $\approx 1''$ spatial regions and show high velocity features on each side of the nucleus.

lines for six of the objects studied in Chapter 4 (Prog. ID: 083-13; PI: Harrison). The CO(1–0) emission-line can be used as a tracer of the molecular gas. This programme was designed to trace the total molecular gas mass in the objects and to constrain the level of outflowing molecular gas. A direct comparison could then be made to the properties of the outflowing ionised gas. Unfortunately the observing run was scheduled for a week that had appalling weather conditions, such that most (≈90%) of the data were unusable and the rest were of low quality. Figure 6.2 shows the small fraction of usable data from the project that resulted in a detection of two of the objects observed. There is tentative evidence that the molecular gas could reach velocities comparable to that observed in the ionised gas (see Fig. 6.2). Interferometers such as IRAM/PdBI and ALMA provide other opportunities to observe the CO emission lines in these or other sources, with the added benefit of providing spatial information. I will continue to apply for time to search for and characterise molecular outflows.

X-ray observations provide the possibility of tracing the properties of the hot (i.e., $T \gtrsim 10^6$ K) ionised gas. This gas phase may make up a large component of any observed outflows. Furthermore, X-ray observations, in combination with radio observations, have been used to show that radio jets are preventing the cooling of hot gas in the halos of AGN (discussed in Section 1.6; review in McNamara & Nulsen 2012). In the most recent call for proposals, we applied for *Chandra* observations of J1430+1339 (the source shown in Figure 6.1; PI: Del Moro) to: (1) measure the level of obscuration and the intrinsic power of the central AGN; (2) attempt to detect hot X-ray emitting gas associated with the outflows we observed (in Chapter 4); (3) establish if there is X-ray emission associated with the radio lobes so that we can further characterise their properties. This will serve as a preliminary experiment with the long-term goal of obtaining X-ray observations of the full sample of objects that is presented in Chapter 4.

6.3.3 What is the prevalence of ionised outflows in galaxies across cosmic time?

In Chapter 4 of this thesis a parent sample of $\approx 24,000$ AGN was used, for which we have previously studied the prevalence of ionised outflows from 1-dimensional SDSS spectra

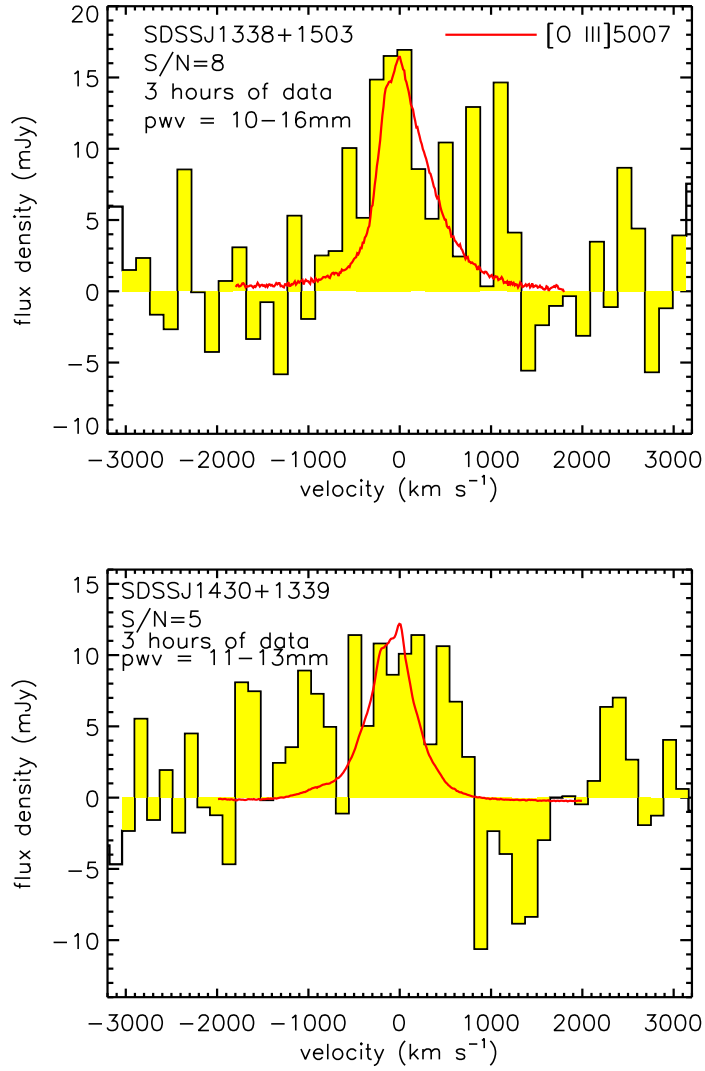

Figure 6.2: Data from the IRAM-30m programme to observe the CO(1–0) emission-line profiles of the type 2 AGN studied in Chapter 4 of this thesis. Only a small fraction ($\approx$ 10%) of the data was usuable and no data was taken under the requested conditions due to poor weather during the observing run. The CO(1–0) emission lines for two of the targets are shown (yellow-filled histograms) with the [O III]λ5007 emission lines overlaid (red curves). There is tentative evidence that, in at least SDSS J1338+1503, there is molecular gas [traced by the CO(1–0) emission-line profile] with velocities comparable to that seen in the ionised gas (traced by the [O III]λ5007 emission-line profile).

(Mullaney et al. 2013). This parent sample enabled the IFU observations to be placed into the context of the overall AGN population. Two obvious follow-up questions to ask are: (1) how representative are the observations of the overall *galaxy* population and (2) are outflows more (or less) prevalent in galaxies that host an AGN? As an initial test of these questions, I took the ≈240,000 $z < 0.4$ extragalactic sources from the SDSS DR7 spectroscopic catalogue that met the original selection criteria of Mullaney et al. (2013) (i.e., the sources that are detected in [O III], Hα, Hβ and [N II]). Using the standard BPT diagram (Fig. 1.3), in combination with the Hα emission-line widths I classified the objects as type 1 AGN, type 2 AGN, composites or H II galaxies (see Kewley et al. 2006 and Section 1.3.3 for details of these classification methods). [O III] luminosity matched samples were then constructed (see caption in Fig. 6.3) and the spectra were stacked around the [O III]λ5007 emission line. These stacks are shown in Figure 6.3 and the pre-liminary conclusion is that the non-AGN host galaxies (i.e., the H II galaxies) do not show strong features of ionised outflows when compared to the AGN (i.e., on average they do not show the broad high-velocity wings in the emission-line profiles that are observed in the AGN). This may mean that AGN are required to drive the most powerful ionised outflows. Following Mullaney et al. (2013) we now intend to perform detailed emission-line profile decomposition on the full galaxy parent sample. We will use this parent sample to assess how common outflows features are across the galaxy population and to perform similar follow-up experiments to that performed in Chapter 4. The provisional programme name is GALPAKA (Galaxy and AGN Line Profile And Kinematic Analysis; see Fig. 6.4).

The project outlined above is to study the prevalence of ionised outflows in low redshift galaxies (i.e., $z < 0.4$). Whilst this provides the benefit of pre-existing spectroscopic surveys and any follow-up observations will have high signal-to-noise and spatial resolution, this does not cover the peak epoch of galaxy and BH growth where AGN-driven outflows and rapid modes of AGN feedback are predicted to be most prevalent (i.e., $z \approx 0.5$–3; discussed in Section 1.6). Although galaxy-wide outflows were observed in $z \approx 1$–3 AGN in Chapter 3, there was not have a good handle on how representative these observations are of the overall high-redshift galaxy and AGN population. This is primarily due to the absence of systematic spectroscopic surveys of high-redshift galaxies (i.e., $z \gtrsim 0.5$). However, I am addressing this by using the newly commissioned KMOS

instrument on ESO/VLT (see Fig. 6.4). This instrument provides the opportunity to observe with 24 NIR IFUs simultaneously inside a 7 arc minute field-of-view. I am involved in the Durham guaranteed time project (PI: Sharples) to measure the ionised gas kinematics of ≈1000 distant galaxies and AGN. Galaxy-wide ionised outflows will be searched for and characterised (i.e., by measuring spatial extents and energetics) following similar methods to those used in this thesis. I will investigate the prevalence and properties of outflows as a function of AGN luminosity, mass and star formation rate and compare to the outflows observed in the low redshift galaxies (see Fig. 6.4).

6.3.4 What impact do outflows have on galaxy evolution?

A key prediction of some theoretical models is that AGN inject energy or momentum into the gas in their host galaxies which results in either a suppression or enhancement of the star formation rate in their host galaxies (discussed in Section 1.6). In Chapter 5 of this thesis it was found that the average SFRs of AGN host galaxies are not appreciably different from the overall star forming galaxy population, even at high AGN luminosities (i.e., $L_{2-8\,\mathrm{keV}} \gtrsim 10^{44}\,\mathrm{erg\,s^{-1}}$). However, a mean SFR only provides limited information as it does not tell you everything about the underlying SFR distribution. A more detailed approach, and a direct test for theoretical models, would be to measure the individual SFRs for a complete sample of AGN. This would result in SFR distributions that can be compared to non-AGN host galaxies and to model predictions. We have begun to investigate this by performing SED fitting (following the method developed for Chapter 4) to the extensive photometric data available for X-ray selected AGN in the deepest extragalactic fields (Stanley, Harrison et al. in prep). However, a significant challenge is that even the deepest *Herschel* observations only detect galaxies with the highest SFRs (i.e., typically above the "main sequence" described in Section 1.5.2), making it difficult to obtain good SFR measurements for the whole sample. Therefore, we have also applied for ALMA observations to obtain continuum measurements of the *Herschel* undetected AGN. One recently completed programme (2012.1.00869.S; PI: Mullaney) of 30 $z > 1.5$ X-ray detected AGN already provides data that enables SFR measurements ≈3 times deeper than can be achieved using the *Herschel* data alone. We have now had accepted ALMA observations of a further 86 X-ray AGN (PI: Alexander) that, when combined with the

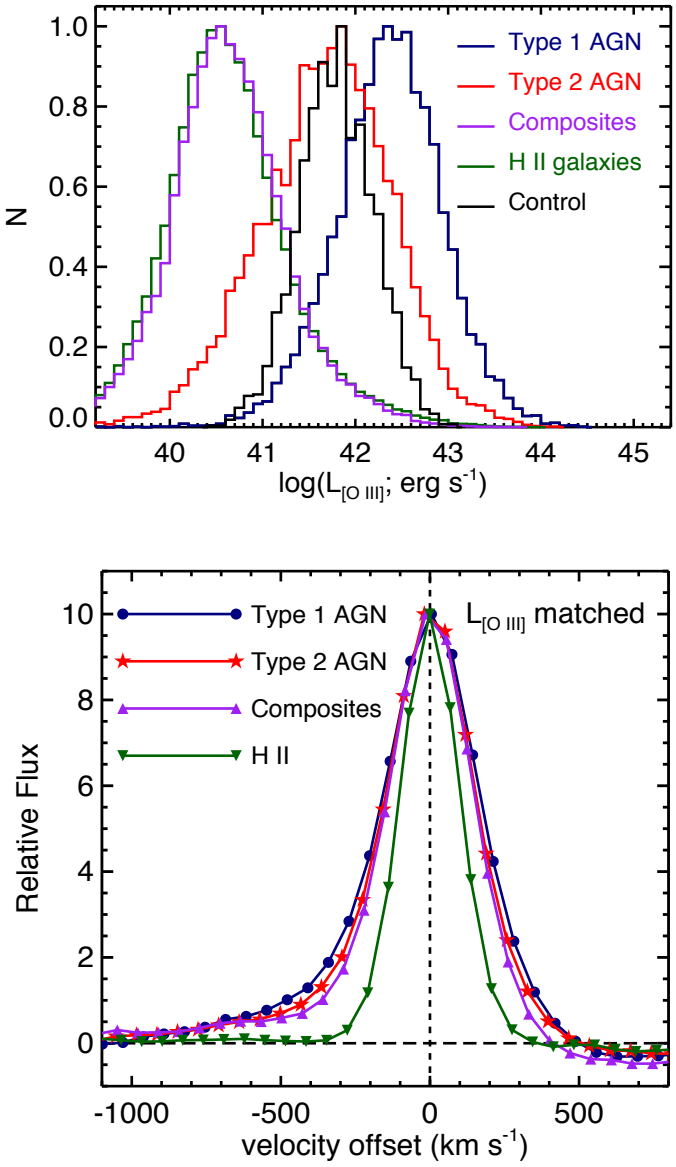

Figure 6.3: *Upper:* Normalised [O III] luminosity distributions for the $z < 0.4$ emission-line galaxies investigated here that have been grouped using the classifications: type 1 AGN; type 2 AGN; composites; H II galaxies. Also shown is a "control" distribution that I used to create [O III] luminosity matched samples from each group. I randomly selected 2500 sources from each group such that they have the same luminosity distribution as the "control" distribution. *Lower:* Stacks of the spectra in the luminosity-matched random samples from each group around the [O III]λ5007 emission line. These initial results suggest that, on average, the H II galaxies do not show a luminous high-velocity prominent wing, which could indicate that they do not contain as prominent ionised outflows compared to the galaxies that host AGN.

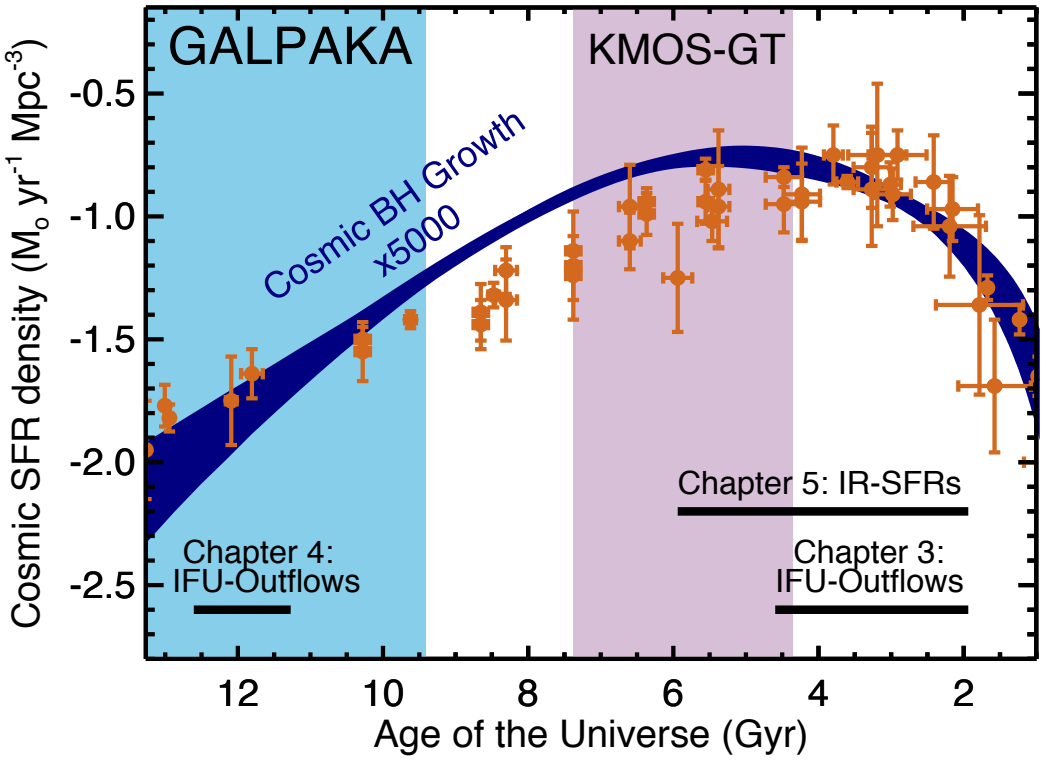

Figure 6.4: Volume-averaged star formation rate (SFR) density (circles; Madau & Dickinson 2014) and black-hole (BH) growth (blue shaded region; Aird et al. 2010) versus age of the Universe. The labelled solid lines show the epochs covered by the observations described in this thesis. The shaded regions show the epochs covered by the major parent samples that will be used for future programmes. GALPAKA provides a sample of nearby galaxies that can be studied in exquisite detail, whilst the KMOS guaranteed time (GT) programme covers the epoch where AGN activity and star formation were occurring at much higher levels.

previous ALMA and *Herschel* data, will give us a complete sample of 132 $z > 1.5$ AGN (with $L_X > 10^{43}\,\mathrm{erg\,s^{-1}}$) where we can measure individual SFRs down to "quiescent" levels (i.e., significantly below the "main sequence" of star formation.

Another challenge of extragalactic astronomy is to constrain the long-term impact of galaxy-wide outflows on the evolution of their host galaxies. Whilst observations have shown that galaxy-wide outflows are *potentially* expelling significant fractions of gas (as shown in Chapter 3 and Chapter 4), due to the timescales involved ($\gtrsim$10 Myrs) it is not possible to *directly* determine the ultimate fate of this gas or the overall impact that these outflows have on individual galaxies. To address this fundamental limitation, I will use the 3-dimensional velocity fields of the galaxies produced by the cosmological hydrodynamical simulation EAGLE (i.e., "mock" IFU observations; see Fig. 6.5) that has been devloped in Durham and Leiden, to perform similar analyses to those used on the real IFU data. I will then compare these directly to the observations from the previous and ongoing observing programmes (see Fig. 6.4). Towards this goal I have also performed IFU observations with VLT/VIMOS (Project ID: 092.B-0062(A); PI: Harrison) of the targets in Chapter 4 that have outflows that appear to be extended beyond the Gemini/GMOS field of view (i.e., on greater than $5'' \times 3.''5$ scales). The VLT/VIMOS observations have a much larger field-of-view (i.e., $13'' \times 13''$) than Gemini/GMOS which means that I will have characterised the *full* kinematic structure of the outflows *for the whole sample* presented in Chapter 4 and I can then compare these data to the simulated outflows from EAGLE (see Fig. 6.5). By compiling the data from all of the observing programmes with the results from EAGLE, it will be possible to compare the gas kinematics of 100s of galaxies and AGN from simulations to observations that are well matched in resolution (i.e., $\approx$0.5–3 kpc; see Fig. 6.5). Principally, I will assess whether the outflows that play a significant role in the evolution of the simulated galaxies have properties that match the observations.

6.4 Final remarks

Over the last twenty-five years AGN have moved to the forefront of extragalactic astronomy research, largely due to theoretical predictions that state that AGN play a funda-

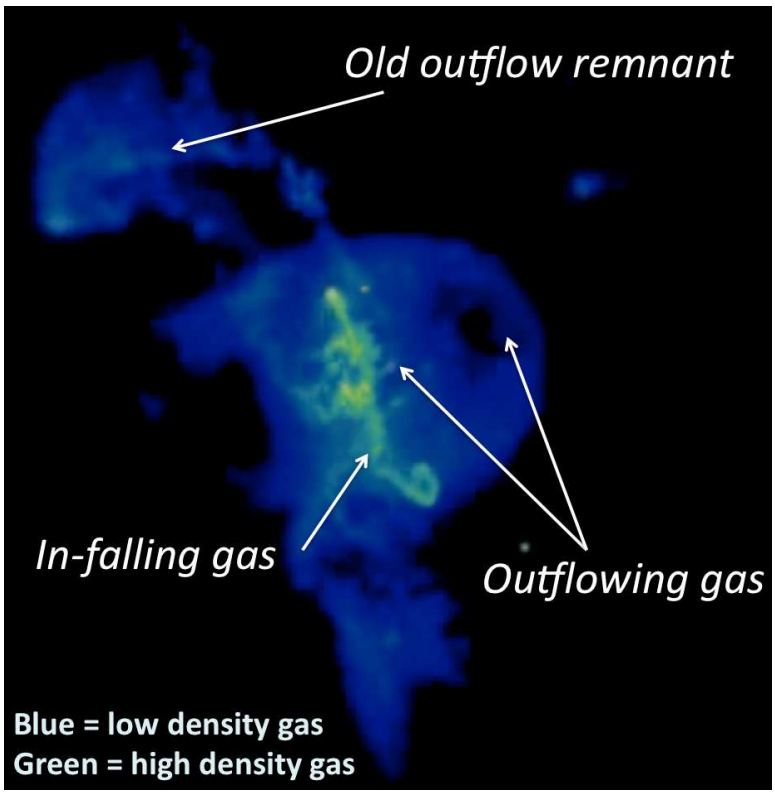

Figure 6.5: A snap-shot of a 600 kpc box around a galaxy undergoing an energetic outflow from a preliminary EAGLE run. The image is courtesy of R. Bower and the Virgo Consortium.

mental role in the evolution of massive galaxies. AGN are thought to inject energy and momentum into the gas in their host galaxies and the larger scale environment, although the details of how this occurs is still under debate. The observational data certainly suggests that some of the theoretical predictions are broadly correct. For example, at low redshift in low accretion-rate AGN, radio jets appear to be preventing the cooling of hot gas. Additionally, as demonstrated in this thesis, energetic galaxy-wide outflows can be found in the host galaxies of luminous AGN across a wide range of redshifts, in broad agreement with theoretical predictions. However, the physical drivers of these outflows and long-term impact that they have is still to be fully understood. Fundamentally, we lack a consensus view on whether luminous AGN are a universal requirement to create the properties of the galaxies and the IGM that we see around us today. As outlined in this chapter we have already embarked on an extensive programme making use of new facilities such as ALMA, JVLA, e-MERLIN and KMOS to address many of the outstanding issues. Initial results show promising signs of what is to come. Furthermore, with revolutionary multi-wavelength observational facilities such as Astro-H, LSST, JWST, SKA and SPICA in the process of being developed we will soon have access to a considerable amount of even higher quality observational data covering X-ray to radio wavelengths. A careful utilisation of these data and comparison to cutting-edge theoretical models, should provide further detailed insight into *the influence of active galactic nuclei on the evolution of galaxies*.

Bibliography

Abazajian, K. N., Adelman-McCarthy, J. K., Agüeros, M. A., et al. 2009, ApJS, 182, 543

Aird, J., Nandra, K., Laird, E. S., et al. 2010, MNRAS, 401, 2531

Akiyama, M. 2005, ApJ, 629, 72

Alaghband-Zadeh, S., Chapman, S. C., Swinbank, A. M., et al. 2012, MNRAS, 424, 2232

Alatalo, K., Blitz, L., Young, L. M., et al. 2011, ApJ, 735, 88

Alexander, D. M., Bauer, F. E., Chapman, S. C., et al. 2005, ApJ, 632, 736

Alexander, D. M., & Hickox, R. C. 2012, New A Rev., 56, 93

Alexander, D. M., Swinbank, A. M., Smail, I., McDermid, R., & Nesvadba, N. P. H. 2010, MNRAS, 402, 2211

Alexander, D. M., Bauer, F. E., Brandt, W. N., et al. 2003a, AJ, 126, 539

—. 2003b, AJ, 125, 383

Alexander, D. M., Chary, R.-R., Pope, A., et al. 2008a, ApJ, 687, 835

Alexander, D. M., Brandt, W. N., Smail, I., et al. 2008b, AJ, 135, 1968

Allington-Smith, J., & Content, R. 1998, PASP, 110, 1216

Allington-Smith, J., Murray, G., Content, R., et al. 2002, PASP, 114, 892

Alonso-Herrero, A., Pereira-Santaella, M., Rieke, G. H., & Rigopoulou, D. 2012, ApJ, 744, 2

Antonucci, R. 1993, ARA&A, 31, 473

Assef, R. J., Stern, D., Kochanek, C. S., et al. 2013, ApJ, 772, 26

Baade, W., & Minkowski, R. 1954, ApJ, 119, 215

Baldwin, J. A., Carswell, R. F., Wampler, E. J., et al. 1980, ApJ, 236, 388

Baldwin, J. A., Phillips, M. M., & Terlevich, R. 1981, PASP, 93, 5

Barbosa, F. K. B., Storchi-Bergmann, T., Cid Fernandes, R., Winge, C., & Schmitt, H. 2009, MNRAS, 396, 2

Barrows, R. S., Sandberg Lacy, C. H., Kennefick, J., et al. 2013, ApJ, 769, 95

Barth, A. J., Greene, J. E., & Ho, L. C. 2008, AJ, 136, 1179

Becker, R. H., White, R. L., & Helfand, D. J. 1995, ApJ, 450, 559

Bennert, N., Falcke, H., Schulz, H., Wilson, A. S., & Wills, B. J. 2002, ApJ, 574, L105

Bennert, V. N., Auger, M. W., Treu, T., Woo, J.-H., & Malkan, M. A. 2011, ApJ, 742, 107

Benson, A. J., Bower, R. G., Frenk, C. S., et al. 2003, ApJ, 599, 38

Best, P. N., & Heckman, T. M. 2012, MNRAS, 421, 1569

Best, P. N., Kaiser, C. R., Heckman, T. M., & Kauffmann, G. 2006, MNRAS, 368, L67

Best, P. N., Kauffmann, G., Heckman, T. M., et al. 2005, MNRAS, 362, 25

Bianchi, S., Maiolino, R., & Risaliti, G. 2012, Advances in Astronomy, 2012

Binney, J., & Tremaine, S. 1987, Galactic dynamics, Princeton series in astrophysics (Princeton University Press)

Bîrzan, L., McNamara, B. R., Nulsen, P. E. J., Carilli, C. L., & Wise, M. W. 2008, ApJ, 686, 859

Bîrzan, L., Rafferty, D. A., McNamara, B. R., Wise, M. W., & Nulsen, P. E. J. 2004, ApJ, 607, 800

Blustin, A. J., Branduardi-Raymont, G., Behar, E., et al. 2003, A&A, 403, 481

Bock, D. C.-J., Large, M. I., & Sadler, E. M. 1999, AJ, 117, 1578

Boehringer, H., Voges, W., Fabian, A. C., Edge, A. C., & Neumann, D. M. 1993, MNRAS, 264, L25

Booth, C. M., & Schaye, J. 2010, MNRAS, 405, L1

Borgani, S., Fabjan, D., Tornatore, L., et al. 2008, Space Sci. Rev., 134, 379

Boroson, T. 2005, AJ, 130, 381

Boroson, T. A., & Green, R. F. 1992, ApJS, 80, 109

Boroson, T. A., Persson, S. E., & Oke, J. B. 1985, ApJ, 293, 120

Bower, R. G., Benson, A. J., & Crain, R. A. 2012, MNRAS, 422, 2816

Bower, R. G., Benson, A. J., Malbon, R., et al. 2006, MNRAS, 370, 645

Bower, R. G., McCarthy, I. G., & Benson, A. J. 2008, MNRAS, 390, 1399

Boyle, B. J., Fong, R., Shanks, T., & Peterson, B. A. 1990, MNRAS, 243, 1

Boyle, B. J., Shanks, T., Croom, S. M., et al. 2000, MNRAS, 317, 1014

Bradshaw, E. J., Almaini, O., Hartley, W. G., et al. 2013, MNRAS, 433, 194

Brandt, W. N., Alexander, D. M., Hornschemeier, A. E., et al. 2001, AJ, 122, 2810

Brinchmann, J., Kunth, D., & Durret, F. 2008, A&A, 485, 657

Burbridge, G. R. 1963, Radiotekhnika, 168

Calzetti, D., Armus, L., Bohlin, R. C., et al. 2000, ApJ, 533, 682

Cano-Díaz, M., Maiolino, R., Marconi, A., et al. 2012, A&A, 537, L8

Cao, X. 2010, ApJ, 725, 388

Capetti, A., Axon, D. J., Macchetto, F. D., Marconi, A., & Winge, C. 1999, Mem. Soc. Astron. Italiana, 70, 41

Cardamone, C. N., Urry, C. M., Damen, M., et al. 2008, ApJ, 680, 130

Cardamone, C. N., van Dokkum, P. G., Urry, C. M., et al. 2010, ApJS, 189, 270

Carilli, C. L., Perley, R. A., & Harris, D. E. 1994, MNRAS, 270, 173

Castor, J., McCray, R., & Weaver, R. 1975, ApJ, 200, L107

Cattaneo, A., & Bernardi, M. 2003, MNRAS, 344, 45

Cattaneo, A., Faber, S. M., Binney, J., et al. 2009, Nature, 460, 213

Cavagnolo, K. W., McNamara, B. R., Nulsen, P. E. J., et al. 2010, ApJ, 720, 1066

Cecil, G., Bland-Hawthorn, J., Veilleux, S., & Filippenko, A. V. 2001, ApJ, 555, 338

Chabrier, G. 2003, PASP, 115, 763

Chapman, S. C., Blain, A. W., Smail, I., & Ivison, R. J. 2005, ApJ, 622, 772

Chapman, S. C., Smail, I., Blain, A. W., & Ivison, R. J. 2004, ApJ, 614, 671

Chary, R., & Elbaz, D. 2001, ApJ, 556, 562

Chen, C.-T. J., Hickox, R. C., Alberts, S., et al. 2013, ApJ, 773, 3

Churazov, E., Sazonov, S., Sunyaev, R., et al. 2005, MNRAS, 363, L91

Churazov, E., Sunyaev, R., Forman, W., & Böhringer, H. 2002, MNRAS, 332, 729

Cicone, C., Maiolino, R., Sturm, E., et al. 2014, A&A, 562, A21

Ciotti, L., Ostriker, J. P., & Proga, D. 2010, ApJ, 717, 708

Cisternas, M., Jahnke, K., Inskip, K. J., et al. 2011, ApJ, 726, 57

Civano, F., Elvis, M., Brusa, M., et al. 2012, ApJS, 201, 30

Clements, D. L., Vaccari, M., Babbedge, T., et al. 2008, MNRAS, 387, 247

Colina, L., Arribas, S., & Borne, K. D. 1999, ApJ, 527, L13

Colina, L., Arribas, S., & Monreal-Ibero, A. 2005, ApJ, 621, 725

Colless, M., Dalton, G., Maddox, S., et al. 2001, MNRAS, 328, 1039

Comerford, J. M., Gerke, B. F., Stern, D., et al. 2012, ApJ, 753, 42

Comerford, J. M., Schluns, K., Greene, J. E., & Cool, R. J. 2013, ApJ, 777, 64

Condon, J. J., Anderson, E., & Broderick, J. J. 1995, AJ, 109, 2318

Condon, J. J., Cotton, W. D., Greisen, E. W., et al. 1998, AJ, 115, 1693

Condon, J. J., Kellermann, K. I., Kimball, A. E., Ivezić, Ž., & Perley, R. A. 2013, ApJ, 768, 37

Coppin, K., Chapin, E. L., Mortier, A. M. J., et al. 2006, MNRAS, 372, 1621

Coppin, K. E. K., Swinbank, A. M., Neri, R., et al. 2008, MNRAS, 389, 45

Courteau, S. 1997, AJ, 114, 2402

Cowie, L. L., Barger, A. J., & Kneib, J.-P. 2002, AJ, 123, 2197

Cox, T. J., Dutta, S. N., Di Matteo, T., et al. 2006, ApJ, 650, 791

Crenshaw, D. M., & Kraemer, S. B. 2000, ApJ, 532, L101

Crenshaw, D. M., Kraemer, S. B., & George, I. M. 2003, ARA&A, 41, 117

Crenshaw, D. M., Schmitt, H. R., Kraemer, S. B., Mushotzky, R. F., & Dunn, J. P. 2010, ApJ, 708, 419

Croton, D. J., Springel, V., White, S. D. M., et al. 2006, MNRAS, 365, 11

Cui, J., Xia, X.-Y., Deng, Z.-G., Mao, S., & Zou, Z.-L. 2001, AJ, 122, 63

Daddi, E., Dickinson, M., Morrison, G., et al. 2007a, ApJ, 670, 156

Daddi, E., Alexander, D. M., Dickinson, M., et al. 2007b, ApJ, 670, 173

Dalla Vecchia, C., & Schaye, J. 2008, MNRAS, 387, 1431

Danielson, A. L. R., Lehmer, B. D., Alexander, D. M., et al. 2012, MNRAS, 422, 494

Davies, R. I. 2007, MNRAS, 375, 1099

Debuhr, J., Quataert, E., & Ma, C.-P. 2012, MNRAS, 420, 2221

Del Moro, A., Alexander, D. M., Mullaney, J. R., et al. 2013, A&A, 549, A59

Di Matteo, T., Springel, V., & Hernquist, L. 2005, Nature, 433, 604

Diamond-Stanic, A. M., Moustakas, J., Tremonti, C. A., et al. 2012, ApJ, 755, L26

Dicken, D., Tadhunter, C., Axon, D., et al. 2009, ApJ, 694, 268

—. 2010, ApJ, 722, 1333

Dicken, D., Tadhunter, C., Morganti, R., et al. 2008, ApJ, 678, 712

Dimitrijević, M. S., Popović, L. Č., Kovačević, J., Dačić, M., & Ilić, D. 2007, MNRAS, 374, 1181

Done, C., Davis, S. W., Jin, C., Blaes, O., & Ward, M. 2012, MNRAS, 420, 1848

Donley, J. L., Rieke, G. H., Pérez-González, P. G., & Barro, G. 2008, ApJ, 687, 111

Donley, J. L., Rieke, G. H., Rigby, J. R., & Pérez-González, P. G. 2005, ApJ, 634, 169

Donley, J. L., Koekemoer, A. M., Brusa, M., et al. 2012, ApJ, 748, 142

Dressler, A. 1989, in IAU Symposium, Vol. 134, Active Galactic Nuclei, ed. D. E. Osterbrock & J. S. Miller, 217

Dressler, A., & Richstone, D. O. 1988, ApJ, 324, 701

Dunn, R. J. H., & Fabian, A. C. 2008, MNRAS, 385, 757

Eisenhauer, F., Abuter, R., Bickert, K., et al. 2003, in Society of Photo-Optical Instrumentation Engineers (SPIE) Conference Series, Vol. 4841, Instrument Design and Performance for Optical/Infrared Ground-based Telescopes, ed. M. Iye & A. F. M. Moorwood, 1548–1561

Elbaz, D., Daddi, E., Le Borgne, D., et al. 2007, A&A, 468, 33

Elbaz, D., Hwang, H. S., Magnelli, B., et al. 2010, A&A, 518, L29

Elbaz, D., Dickinson, M., Hwang, H. S., et al. 2011, A&A, 533, A119

Elvis, M. 2012, Journal of Physics Conference Series, 372, 012032

Elvis, M., Maccacaro, T., Wilson, A. S., et al. 1978, MNRAS, 183, 129

Elvis, M., Wilkes, B. J., McDowell, J. C., et al. 1994, ApJS, 95, 1

Elvis, M., Civano, F., Vignali, C., et al. 2009, ApJS, 184, 158

Emonts, B. H. C., Morganti, R., Tadhunter, C. N., et al. 2005, MNRAS, 362, 931

Engel, H., Tacconi, L. J., Davies, R. I., et al. 2010, ApJ, 724, 233

Fabian, A. C. 1999, MNRAS, 308, L39

—. 2012, ARA&A, 50, 455

Fabjan, D., Borgani, S., Tornatore, L., et al. 2010, MNRAS, 401, 1670

Fath, E. A. 1909, Lick Observatory Bulletin, 5, 71

Faucher-Giguère, C.-A., & Quataert, E. 2012, MNRAS, 425, 605

Feldman, F. R., Weedman, D. W., Balzano, V. A., & Ramsey, L. W. 1982, ApJ, 256, 427

Ferrarese, L., & Merritt, D. 2000, ApJ, 539, L9

Feruglio, C., Maiolino, R., Piconcelli, E., et al. 2010, A&A, 518, L155

Fischer, T. C., Crenshaw, D. M., Kraemer, S. B., & Schmitt, H. R. 2013, ApJS, 209, 1

Fischer, T. C., Crenshaw, D. M., Kraemer, S. B., et al. 2011, ApJ, 727, 71

Förster Schreiber, N. M., Genzel, R., Newman, S. F., et al. 2013, arXiv:1311.2596

Fu, H., Myers, A. D., Djorgovski, S. G., & Yan, L. 2011, ApJ, 733, 103

Fu, H., & Stockton, A. 2009, ApJ, 690, 953

Fu, H., Yan, L., Myers, A. D., et al. 2012, ApJ, 745, 67

Gabor, J. M., & Bournaud, F. 2014, arXiv:1402.4482

Gabor, J. M., Davé, R., Oppenheimer, B. D., & Finlator, K. 2011, MNRAS, 417, 2676

Gandhi, P., Horst, H., Smette, A., et al. 2009, A&A, 502, 457

Ganguly, R., & Brotherton, M. S. 2008, ApJ, 672, 102

Gaspari, M., Melioli, C., Brighenti, F., & D'Ercole, A. 2011, MNRAS, 411, 349

Ge, J.-Q., Hu, C., Wang, J.-M., Bai, J.-M., & Zhang, S. 2012, ApJS, 201, 31

Gebhardt, K., Bender, R., Bower, G., et al. 2000, ApJ, 539, L13

Gelderman, R., & Whittle, M. 1994, ApJS, 91, 491

Genzel, R., Newman, S., Jones, T., et al. 2011, ApJ, 733, 101

George, I. M., & Fabian, A. C. 1991, MNRAS, 249, 352

Gerssen, J., Wilman, D. J., Christensen, L., Bower, R. G., & Wild, V. 2009, MNRAS, 393, L45

Giacconi, R., Zirm, A., Wang, J., et al. 2002, ApJS, 139, 369

Gibson, R. R., Jiang, L., Brandt, W. N., et al. 2009, ApJ, 692, 758

Gofford, J., Reeves, J. N., Turner, T. J., et al. 2011, MNRAS, 414, 3307

Goulding, A. D., & Alexander, D. M. 2009, MNRAS, 398, 1165

Goulding, A. D., Forman, W. R., Hickox, R. C., et al. 2014, ApJ, 783, 40

Granato, G. L., De Zotti, G., Silva, L., Bressan, A., & Danese, L. 2004, ApJ, 600, 580

Greene, J. E., & Ho, L. C. 2005, ApJ, 627, 721

Greene, J. E., Ho, L. C., & Barth, A. J. 2008, ApJ, 688, 159

Greene, J. E., Zakamska, N. L., Ho, L. C., & Barth, A. J. 2011, ApJ, 732, 9

Greene, J. E., Zakamska, N. L., & Smith, P. S. 2012, ApJ, 746, 86

Greene, J. E., Peng, C. Y., Kim, M., et al. 2010, ApJ, 721, 26

Greenstein, J. L., M. T. A. 1963, Nature, 197, 1041

Gültekin, K., Richstone, D. O., Gebhardt, K., et al. 2009, ApJ, 698, 198

Hainline, K. N., Hickox, R., Greene, J. E., Myers, A. D., & Zakamska, N. L. 2013, ApJ, 774, 145

Hainline, L. J., Blain, A. W., Smail, I., et al. 2011, ApJ, 740, 96

—. 2009, ApJ, 699, 1610

Hardcastle, M. J., Evans, D. A., & Croston, J. H. 2007, MNRAS, 376, 1849

Häring, N., & Rix, H.-W. 2004, ApJ, 604, L89

Harms, R. J., Ford, H. C., Tsvetanov, Z. I., et al. 1994, ApJ, 435, L35

Harrison, C. M., Alexander, D. M., Mullaney, J. R., & Swinbank, A. M. 2014, MNRAS, 441, 3306

Harrison, C. M., Alexander, D. M., Swinbank, A. M., et al. 2012a, MNRAS, 426, 1073

Harrison, C. M., Alexander, D. M., Mullaney, J. R., et al. 2012b, ApJ, 760, L15

Hatch, N. A., Röttgering, H. J. A., Miley, G. K., et al. 2013, MNRAS, 436, 2244

Hatziminaoglou, E., Omont, A., Stevens, J. A., et al. 2010, A&A, 518, L33

Heavens, A., Panter, B., Jimenez, R., & Dunlop, J. 2004, Nature, 428, 625

Heckman, T., & Best, P. 2014, arXiv:1403.4620

Heckman, T. M., Armus, L., & Miley, G. K. 1987, AJ, 93, 276

—. 1990, ApJS, 74, 833

Heckman, T. M., Kauffmann, G., Brinchmann, J., et al. 2004, ApJ, 613, 109

Heckman, T. M., Lehnert, M. D., Strickland, D. K., & Armus, L. 2000, ApJS, 129, 493

Heckman, T. M., Miley, G. K., & Green, R. F. 1984, ApJ, 281, 525

Heckman, T. M., Miley, G. K., van Breugel, W. J. M., & Butcher, H. R. 1981, ApJ, 247, 403

Heckman, T. M., Borthakur, S., Overzier, R., et al. 2011, ApJ, 730, 5

Helou, G., Soifer, B. T., & Rowan-Robinson, M. 1985, ApJ, 298, L7

Herschel, W. 1786, Royal Society of London Philosophical Transactions Series I, 76, 457

Hewett, P. C., Foltz, C. B., & Chaffee, F. H. 1993, ApJ, 406, L43

Hickox, R. C., Jones, C., Forman, W. R., et al. 2007, ApJ, 671, 1365

—. 2009, ApJ, 696, 891

Hickox, R. C., Myers, A. D., Brodwin, M., et al. 2011, ApJ, 731, 117

Hickox, R. C., Wardlow, J. L., Smail, I., et al. 2012, MNRAS, 421, 284

Hill, M. D., & Shanks, T. 2011, MNRAS, 410, 762

Hill, M. J., & Zakamska, N. L. 2014, MNRAS, 439, 2701

Hlavacek-Larrondo, J., Allen, S. W., Taylor, G. B., et al. 2013, ApJ, 777, 163

Ho, L. C. 2002, ApJ, 564, 120

—. 2008, ARA&A, 46, 475

Ho, L. C., Filippenko, A. V., & Sargent, W. L. W. 1997a, ApJS, 112, 315

—. 1997b, ApJ, 487, 568

Hobbs, A., Nayakshin, S., Power, C., & King, A. 2011, MNRAS, 413, 2633

Holt, J., Tadhunter, C., Morganti, R., et al. 2006, MNRAS, 370, 1633

Holt, J., Tadhunter, C. N., & Morganti, R. 2008, MNRAS, 387, 639

Holt, J., Tadhunter, C. N., Morganti, R., & Emonts, B. H. C. 2011, MNRAS, 410, 1527

Hönig, S. F., Beckert, T., Ohnaka, K., & Weigelt, G. 2006, A&A, 452, 459

Hopkins, P. F., Cox, T. J., Hernquist, L., et al. 2013a, MNRAS, 430, 1901

Hopkins, P. F., & Elvis, M. 2010, MNRAS, 401, 7

Hopkins, P. F., Hernquist, L., Cox, T. J., et al. 2005a, ApJ, 630, 716

—. 2006, ApJS, 163, 1

Hopkins, P. F., Hernquist, L., Cox, T. J., & Kereš, D. 2008, ApJS, 175, 356

Hopkins, P. F., Hernquist, L., Martini, P., et al. 2005b, ApJ, 625, L71

Hopkins, P. F., Kereš, D., Murray, N., et al. 2013b, MNRAS, 433, 78

Hopkins, P. F., Richards, G. T., & Hernquist, L. 2007, ApJ, 654, 731

Hubble, E. 1929, Proceedings of the National Academy of Science, 15, 168

Hubble, E. P. 1925, Popular Astronomy, 33, 252

—. 1926, ApJ, 64, 321

Huggins, W., & Miller, W. A. 1864, Royal Society of London Philosophical Transactions Series I, 154, 437

Humphrey, A., Villar-Martín, M., Sánchez, S. F., et al. 2010, MNRAS, 408, L1

Husemann, B., Wisotzki, L., Sánchez, S. F., & Jahnke, K. 2013, A&A, 549, A43

Ibar, E., Ivison, R. J., Best, P. N., et al. 2010, MNRAS, 401, L53

Ishibashi, W., & Fabian, A. C. 2012, MNRAS, 427, 2998

Ivison, R. J., Papadopoulos, P. P., Smail, I., et al. 2011, MNRAS, 412, 1913

Ivison, R. J., Smail, I., Papadopoulos, P. P., et al. 2010a, MNRAS, 404, 198

Ivison, R. J., Greve, T. R., Smail, I., et al. 2002, MNRAS, 337, 1

Ivison, R. J., Greve, T. R., Dunlop, J. S., et al. 2007, MNRAS, 380, 199

Ivison, R. J., Magnelli, B., Ibar, E., et al. 2010b, A&A, 518, L31

Jahnke, K., & Macciò, A. V. 2011, ApJ, 734, 92

Jarrett, T. H., Cohen, M., Masci, F., et al. 2011, ApJ, 735, 112

Juneau, S., Dickinson, M., Alexander, D. M., & Salim, S. 2011, ApJ, 736, 104

Kauffmann, G., Heckman, T. M., & Best, P. N. 2008, MNRAS, 384, 953

Kauffmann, G., Heckman, T. M., Tremonti, C., et al. 2003, MNRAS, 346, 1055

Keel, W. C., Chojnowski, S. D., Bennert, V. N., et al. 2012, MNRAS, 420, 878

Kellermann, K. I., Sramek, R., Schmidt, M., Shaffer, D. B., & Green, R. 1989, AJ, 98, 1195

Kelly, B. C., Vestergaard, M., Fan, X., et al. 2010, ApJ, 719, 1315

Kennicutt, Jr., R. C. 1998, ARA&A, 36, 189

Kerr, R. P. 1963, Phys. Rev. Lett., 11, 237

Kewley, L. J., Dopita, M. A., Leitherer, C., et al. 2013, ApJ, 774, 100

Kewley, L. J., Dopita, M. A., Sutherland, R. S., Heisler, C. A., & Trevena, J. 2001, ApJ, 556, 121

Kewley, L. J., Groves, B., Kauffmann, G., & Heckman, T. 2006, MNRAS, 372, 961

Khachikian, E. E., & Weedman, D. W. 1971, Astrofizika, 7, 389

Kim, D.-C., Sanders, D. B., Veilleux, S., Mazzarella, J. M., & Soifer, B. T. 1995, ApJS, 98, 129

Kim, M., Ho, L. C., Lonsdale, C. J., et al. 2013, ApJ, 768, L9

Kimball, A. E., & Ivezić, Ž. 2008, AJ, 136, 684

Kimura, M., Maihara, T., Iwamuro, F., et al. 2010, PASJ, 62, 1135

King, A. 2003, ApJ, 596, L27

—. 2005, ApJ, 635, L121

King, A. R., Zubovas, K., & Power, C. 2011, MNRAS, 415, L6

Kirkpatrick, A., Pope, A., Charmandaris, V., et al. 2013, ApJ, 763, 123

Komossa, S., Xu, D., Zhou, H., Storchi-Bergmann, T., & Binette, L. 2008, ApJ, 680, 926

Koratkar, A., & Blaes, O. 1999, PASP, 111, 1

Kormendy, J. 1993, in The Nearest Active Galaxies, ed. J. Beckman, L. Colina, & H. Netzer, 197–218

Kormendy, J., Bender, R., & Cornell, M. E. 2011, Nature, 469, 374

Kormendy, J., & Ho, L. C. 2013, ARA&A, 51, 511

Kormendy, J., & Richstone, D. 1995, ARA&A, 33, 581

Kovács, A., Chapman, S. C., Dowell, C. D., et al. 2006, ApJ, 650, 592

Krajnović, D., Cappellari, M., de Zeeuw, P. T., & Copin, Y. 2006, MNRAS, 366, 787

Lacy, M., Storrie-Lombardi, L. J., Sajina, A., et al. 2004, ApJS, 154, 166

Lagos, C. D. P., Cora, S. A., & Padilla, N. D. 2008, MNRAS, 388, 587

Laing, R. A., Riley, J. M., & Longair, M. S. 1983, MNRAS, 204, 151

Lansbury, G. B., Alexander, D. M., Del Moro, A., et al. 2014, ArXiv e-prints

Laor, A., & Behar, E. 2008, MNRAS, 390, 847

Lauer, T. R., Tremaine, S., Richstone, D., & Faber, S. M. 2007, ApJ, 670, 249

Lawrence, A., & Elvis, M. 2010, ApJ, 714, 561

Le Tiran, L., Lehnert, M. D., van Driel, W., Nesvadba, N. P. H., & Di Matteo, P. 2011, A&A, 534, L4

Ledlow, M. J., Smail, I., Owen, F. N., et al. 2002, ApJ, 577, L79

Lehmer, B. D., Alexander, D. M., Bauer, F. E., et al. 2010, ApJ, 724, 559

Lehnert, M. D., & Heckman, T. M. 1996, ApJ, 462, 651

Lehnert, M. D., Nesvadba, N. P. H., Le Tiran, L., et al. 2009, ApJ, 699, 1660

Leipski, C., & Bennert, N. 2006, A&A, 448, 165

Leitherer, C., Schaerer, D., Goldader, J. D., et al. 1999, ApJS, 123, 3

Lilly, S. J., Eales, S. A., Gear, W. K. P., et al. 1999, ApJ, 518, 641

Lipari, S., Sanchez, S. F., Bergmann, M., et al. 2009, MNRAS, 392, 1295

Lípari, S., Bergmann, M., Sanchez, S. F., et al. 2009, MNRAS, 398, 658

Liu, G., Zakamska, N. L., & Greene, J. E. 2014, arXiv:1401.0536

Liu, G., Zakamska, N. L., Greene, J. E., Nesvadba, N. P. H., & Liu, X. 2013a, MNRAS, 430, 2327

—. 2013b, MNRAS, 436, 2576

Liu, X., Shen, Y., Strauss, M. A., & Greene, J. E. 2010, ApJ, 708, 427

Luo, B., Bauer, F. E., Brandt, W. N., et al. 2008, ApJS, 179, 19

Lusso, E., Comastri, A., Vignali, C., et al. 2010, A&A, 512, A34

Lutz, D. 2014, arXiv:1403.3334

Lutz, D., Maiolino, R., Spoon, H. W. W., & Moorwood, A. F. M. 2004, A&A, 418, 465

Lutz, D., Mainieri, V., Rafferty, D., et al. 2010, ApJ, 712, 1287

Lynden-Bell, D. 1969, Nature, 223, 690

Madau, P., & Dickinson, M. 2014, arXiv:1403.0007

Madau, P., Ferguson, H. C., Dickinson, M. E., et al. 1996, MNRAS, 283, 1388

Magorrian, J., Tremaine, S., Richstone, D., et al. 1998, AJ, 115, 2285

Mahony, E. K., Morganti, R., Emonts, B. H. C., Oosterloo, T. A., & Tadhunter, C. 2013, MNRAS, 435, L58

Mainieri, V., Bongiorno, A., Merloni, A., et al. 2011, A&A, 535, A80

Maiolino, R., Gallerani, S., Neri, R., et al. 2012, MNRAS, 425, L66

Marconi, A., & Hunt, L. K. 2003, ApJ, 589, L21

Marconi, A., Risaliti, G., Gilli, R., et al. 2004, MNRAS, 351, 169

Markwardt, C. B. 2009, in Astronomical Society of the Pacific Conference Series, Vol. 411, Astronomical Data Analysis Software and Systems XVIII, ed. D. A. Bohlender, D. Durand, & P. Dowler, 251

Martin, C. L. 1999, ApJ, 513, 156

—. 2005, ApJ, 621, 227

Mateos, S., Alonso-Herrero, A., Carrera, F. J., et al. 2012, MNRAS, 426, 3271

Matsuoka, Y. 2012, ApJ, 750, 54

Matthews, T. A., & Sandage, A. R. 1963, ApJ, 138, 30

McCarthy, I. G., Schaye, J., Bower, R. G., et al. 2011, MNRAS, 412, 1965

McCarthy, I. G., Schaye, J., Ponman, T. J., et al. 2010, MNRAS, 406, 822

McCarthy, P. J., Baum, S. A., & Spinrad, H. 1996, ApJS, 106, 281

McClintock, J. E., & Remillard, R. A. 2006, Black hole binaries, ed. W. H. G. Lewin & M. van der Klis, 157–213

McGregor, P. J., Hart, J., Conroy, P. G., et al. 2003, in Society of Photo-Optical Instrumentation Engineers (SPIE) Conference Series, Vol. 4841, Instrument Design and Performance for Optical/Infrared Ground-based Telescopes, ed. M. Iye & A. F. M. Moorwood, 1581–1591

McLean, I. S., Steidel, C. C., Epps, H., et al. 2010, in Society of Photo-Optical Instrumentation Engineers (SPIE) Conference Series, Vol. 7735, Society of Photo-Optical Instrumentation Engineers (SPIE) Conference Series

McLeod, B., Fabricant, D., Nystrom, G., et al. 2012, PASP, 124, 1318

McLure, R. J., Jarvis, M. J., Targett, T. A., Dunlop, J. S., & Best, P. N. 2006, MNRAS, 368, 1395

McNamara, B. R., & Nulsen, P. E. J. 2012, New Journal of Physics, 14, 055023

McNamara, B. R., Wise, M., Nulsen, P. E. J., et al. 2000, ApJ, 534, L135

Menéndez-Delmestre, K., Blain, A. W., Swinbank, M., et al. 2013, ApJ, 767, 151

Menéndez-Delmestre, K., Blain, A. W., Smail, I., et al. 2009, ApJ, 699, 667

Merloni, A., & Heinz, S. 2007, MNRAS, 381, 589

Merloni, A., Bongiorno, A., Bolzonella, M., et al. 2010, ApJ, 708, 137

Messier, C. 1781, Catalogue des Nébuleuses & des amas d'Étoiles (Catalog of Nebulae and Star Clusters), Tech. rep.

Miller, N. A., Fomalont, E. B., Kellermann, K. I., et al. 2008, ApJS, 179, 114

Miyoshi, M., Moran, J., Herrnstein, J., et al. 1995, Nature, 373, 127

Morganti, R., Frieswijk, W., Oonk, R. J. B., Oosterloo, T., & Tadhunter, C. 2013, A&A, 552, L4

Morganti, R., Oosterloo, T. A., Tadhunter, C. N., van Moorsel, G., & Emonts, B. 2005, A&A, 439, 521

Morrison, G. E., Owen, F. N., Dickinson, M., Ivison, R. J., & Ibar, E. 2010, ApJS, 188, 178

Moshir, M., Kopman, G., & Conrow, T. A. O. 1992, IRAS Faint Source Survey, Explanatory supplement version 2

Mullaney, J. R., Alexander, D. M., Fine, S., et al. 2013, MNRAS, 433, 622

Mullaney, J. R., Alexander, D. M., Goulding, A. D., & Hickox, R. C. 2011, MNRAS, 414, 1082

Mullaney, J. R., Alexander, D. M., Huynh, M., Goulding, A. D., & Frayer, D. 2010, MNRAS, 401, 995

Mullaney, J. R., Pannella, M., Daddi, E., et al. 2012a, MNRAS, 419, 95

Mullaney, J. R., Daddi, E., Béthermin, M., et al. 2012b, ApJ, 753, L30

Murray, N., Ménard, B., & Thompson, T. A. 2011, ApJ, 735, 66

Murray, N., Quataert, E., & Thompson, T. A. 2005, ApJ, 618, 569

Mushotzky, R. F., Cowie, L. L., Barger, A. J., & Arnaud, K. A. 2000, Nature, 404, 459

Navarro, J. F., Frenk, C. S., & White, S. D. M. 1996, ApJ, 462, 563

Nayakshin, S., & Zubovas, K. 2012, MNRAS, 427, 372

Nelson, C. H., & Whittle, M. 1996, ApJ, 465, 96

Nenkova, M., Sirocky, M. M., Ivezić, Ž., & Elitzur, M. 2008, ApJ, 685, 147

Nesvadba, N. P. H., Lehnert, M. D., De Breuck, C., Gilbert, A., & van Breugel, W. 2007a, A&A, 475, 145

Nesvadba, N. P. H., Lehnert, M. D., De Breuck, C., Gilbert, A. M., & van Breugel, W. 2008, A&A, 491, 407

Nesvadba, N. P. H., Lehnert, M. D., Eisenhauer, F., et al. 2006, ApJ, 650, 693

Nesvadba, N. P. H., Polletta, M., Lehnert, M. D., et al. 2011, MNRAS, 415, 2359

Nesvadba, N. P. H., Lehnert, M. D., Genzel, R., et al. 2007b, ApJ, 657, 725

Neugebauer, G., Habing, H. J., van Duinen, R., et al. 1984, ApJ, 278, L1

Newman, S. F., Genzel, R., Förster-Schreiber, N. M., et al. 2012, ApJ, 761, 43

Noeske, K. G., Weiner, B. J., Faber, S. M., et al. 2007, ApJ, 660, L43

Novak, G. S., Ostriker, J. P., & Ciotti, L. 2011, ApJ, 737, 26

Ohyama, Y., Taniguchi, Y., Iye, M., et al. 2002, PASJ, 54, 891

Oliver, S. J., Bock, J., Altieri, B., et al. 2012, MNRAS, 424, 1614

Osterbrock, D. E. 1989, Astrophysics of gaseous nebulae and active galactic nuclei, ed. Osterbrock, D. E.

Osterbrock, D. E., & Ferland, G. J. 2006, Astrophysics of gaseous nebulae and active galactic nuclei

O'Sullivan, E., Forbes, D. A., & Ponman, T. J. 2001, MNRAS, 328, 461

Page, M. J., Carrera, F. J., Stevens, J. A., Ebrero, J., & Blustin, A. J. 2011, MNRAS, 416, 2792

Page, M. J., Stevens, J. A., Ivison, R. J., & Carrera, F. J. 2004, ApJ, 611, L85

Page, M. J., Symeonidis, M., Vieira, J. D., et al. 2012, Nature, 485, 213

Pannella, M., Carilli, C. L., Daddi, E., et al. 2009, ApJ, 698, L116

Pâris, I., Petitjean, P., Aubourg, É., et al. 2012, A&A, 548, A66

Peng, C. Y. 2007, ApJ, 671, 1098

Pérez-González, P. G., Rieke, G. H., Villar, V., et al. 2008, ApJ, 675, 234

Persic, M., & Rephaeli, Y. 2007, A&A, 463, 481

Peterson, B. M., Ferrarese, L., Gilbert, K. M., et al. 2004, ApJ, 613, 682

Peterson, J. R., Kahn, S. M., Paerels, F. B. S., et al. 2003, ApJ, 590, 207

Pier, E. A., & Krolik, J. H. 1992, ApJ, 401, 99

Polletta, M., Courvoisier, T. J.-L., Hooper, E. J., & Wilkes, B. J. 2000, A&A, 362, 75

Puchwein, E., Sijacki, D., & Springel, V. 2008, ApJ, 687, L53

Quilis, V., Bower, R. G., & Balogh, M. L. 2001, MNRAS, 328, 1091

Rafferty, D. A., Brandt, W. N., Alexander, D. M., et al. 2011, ApJ, 742, 3

Ramos Almeida, C., Tadhunter, C. N., Inskip, K. J., et al. 2011, MNRAS, 410, 1550

Rees, M. J. 1984, ARA&A, 22, 471

Reeves, J. N., O'Brien, P. T., & Ward, M. J. 2003, ApJ, 593, L65

Rengelink, R. B., Tang, Y., de Bruyn, A. G., et al. 1997, A&AS, 124, 259

Reyes, R., Zakamska, N. L., Strauss, M. A., et al. 2008, AJ, 136, 2373

Richards, G. T., Fan, X., Schneider, D. P., et al. 2001, AJ, 121, 2308

Richards, G. T., Lacy, M., Storrie-Lombardi, L. J., et al. 2006a, ApJS, 166, 470

Richards, G. T., Strauss, M. A., Fan, X., et al. 2006b, AJ, 131, 2766

Riechers, D. A., Hodge, J., Walter, F., Carilli, C. L., & Bertoldi, F. 2011, ApJ, 739, L31

Riffel, R. A., Storchi-Bergmann, T., & Riffel, R. 2014, ApJ, 780, L24

Rizza, E., Loken, C., Bliton, M., et al. 2000, AJ, 119, 21

Rodighiero, G., Cimatti, A., Gruppioni, C., et al. 2010, A&A, 518, L25

Rodighiero, G., Daddi, E., Baronchelli, I., et al. 2011, ApJ, 739, L40

Rodríguez Zaurín, J., Tadhunter, C. N., Rose, M., & Holt, J. 2013, MNRAS, 432, 138

Rosario, D. J., Shields, G. A., Taylor, G. B., Salviander, S., & Smith, K. L. 2010, ApJ, 716, 131

Rosario, D. J., Santini, P., Lutz, D., et al. 2012, A&A, 545, A45

—. 2013, ApJ, 771, 63

Rosas-Guevara, Y. M., Bower, R. G., Schaye, J., et al. 2013, arXiv:1312.0598

Rosse, T. E. O. 1850, Royal Society of London Philosophical Transactions Series I, 140, 499

Rovilos, E., Comastri, A., Gilli, R., et al. 2012, A&A, 546, A58

Rowan-Robinson, M. 1995, MNRAS, 272, 737

Roy, A. L., & Norris, R. P. 1997, MNRAS, 289, 824

Rupke, D. S., Veilleux, S., & Sanders, D. B. 2005a, ApJS, 160, 87

—. 2005b, ApJS, 160, 115

Rupke, D. S. N., & Veilleux, S. 2011, ApJ, 729, L27+

—. 2013, ApJ, 768, 75

Salpeter, E. E. 1964, ApJ, 140, 796

Sanders, D. B., & Mirabel, I. F. 1996, ARA&A, 34, 749

Sanders, D. B., Soifer, B. T., Elias, J. H., Neugebauer, G., & Matthews, K. 1988, ApJ, 328, L35

Santini, P., Rosario, D. J., Shao, L., et al. 2012, A&A, 540, A109

Sargent, W. L. W., Young, P. J., Lynds, C. R., et al. 1978, ApJ, 221, 731

Sargsyan, L., Mickaelian, A., Weedman, D., & Houck, J. 2008, ApJ, 683, 114

Saslaw, W. C. 1974, in IAU Symposium, Vol. 58, The Formation and Dynamics of Galaxies, ed. J. R. Shakeshaft, 305

Schartmann, M., Meisenheimer, K., Camenzind, M., et al. 2008, A&A, 482, 67

Schartmann, M., Meisenheimer, K., Klahr, H., et al. 2009, MNRAS, 393, 759

Scheiner, J. 1899, ApJ, 9, 149

Schirmer, M., Diaz, R., Holhjem, K., Levenson, N. A., & Winge, C. 2013, ApJ, 763, 60

Schmidt, M. 1963, Nature, 197, 1040

Schmidt, M., & Green, R. F. 1983, ApJ, 269, 352

Schneider, D. P., Hall, P. B., Richards, G. T., et al. 2005, AJ, 130, 367

Schnorr-Müller, A., Storchi-Bergmann, T., Nagar, N. M., et al. 2014, MNRAS, 437, 1708

Scott, S. E., Fox, M. J., Dunlop, J. S., et al. 2002, MNRAS, 331, 817

Seyfert, C. K. 1943, ApJ, 97, 28

Shakura, N. I., & Sunyaev, R. A. 1973, A&A, 24, 337

Shankar, F., Weinberg, D. H., & Miralda-Escudé, J. 2009, ApJ, 690, 20

Shao, L., Lutz, D., Nordon, R., et al. 2010, A&A, 518, L26

Sharples, R., Bender, R., Agudo Berbel, A., et al. 2013, The Messenger, 151, 21

Shen, Y., Liu, X., Greene, J. E., & Strauss, M. A. 2011, ApJ, 735, 48

Shen, Y., Strauss, M. A., Ross, N. P., et al. 2009, ApJ, 697, 1656

Shih, H.-Y., & Rupke, D. S. N. 2010, ApJ, 724, 1430

Shih, H.-Y., Stockton, A., & Kewley, L. 2013, ApJ, 772, 138

Silk, J. 2013, ApJ, 772, 112

Silk, J., & Rees, M. J. 1998, A&A, 331, L1

Silva, L., Granato, G. L., Bressan, A., & Danese, L. 1998, ApJ, 509, 103

Silverman, J. D., Green, P. J., Barkhouse, W. A., et al. 2008, ApJ, 679, 118

Silverman, J. D., Kovač, K., Knobel, C., et al. 2009, ApJ, 695, 171

Simpson, C., Westoby, P., Arumugam, V., et al. 2013a, MNRAS, 433, 2647

Simpson, C., Martínez-Sansigre, A., Rawlings, S., et al. 2006, MNRAS, 372, 741

Simpson, C., Rawlings, S., Ivison, R., et al. 2012, MNRAS, 421, 3060

Simpson, J., Swinbank, M., Smail, I., et al. 2013b, ArXiv e-prints

Slipher, V. M. 1915, Popular Astronomy, 23, 21

—. 1917a, Proceedings of the American Philosophical Society, 56, 403

—. 1917b, Lowell Observatory Bulletin, 3, 59

Smail, I., Chapman, S. C., Blain, A. W., & Ivison, R. J. 2004, ApJ, 616, 71

Smail, I., Chapman, S. C., Ivison, R. J., et al. 2003, MNRAS, 342, 1185

Smith, H. E., Lonsdale, C. J., & Lonsdale, C. J. 1998, ApJ, 492, 137

Smith, K. L., Shields, G. A., Bonning, E. W., et al. 2010, ApJ, 716, 866

Smith, K. L., Shields, G. A., Salviander, S., Stevens, A. C., & Rosario, D. J. 2012, ApJ, 752, 63

Smolčić, V. 2009, ApJ, 699, L43

Smolčić, V., Finoguenov, A., Zamorani, G., et al. 2011, MNRAS, 416, L31

Smolčić, V., Zamorani, G., Schinnerer, E., et al. 2009, ApJ, 696, 24

Solórzano-Iñarrea, C., & Tadhunter, C. N. 2003, MNRAS, 340, 705

Soltan, A. 1982, MNRAS, 200, 115

Somerville, R. S., Hopkins, P. F., Cox, T. J., Robertson, B. E., & Hernquist, L. 2008, MNRAS, 391, 481

Soto, K. T., & Martin, C. L. 2010, ApJ, 716, 332

Spergel, D. N., Verde, L., Peiris, H. V., et al. 2003, ApJS, 148, 175

Springel, V., Di Matteo, T., & Hernquist, L. 2005, MNRAS, 361, 776

Steffen, A. T., Strateva, I., Brandt, W. N., et al. 2006, AJ, 131, 2826

Stern, D., Eisenhardt, P., Gorjian, V., et al. 2005, ApJ, 631, 163

Stern, D., Assef, R. J., Benford, D. J., et al. 2012, ApJ, 753, 30

Stevens, J. A., Page, M. J., Ivison, R. J., et al. 2005, MNRAS, 360, 610

Stockton, A. 1976, ApJ, 205, L113

Stockton, A., & MacKenty, J. W. 1987, ApJ, 316, 584

Storchi-Bergmann, T., Lopes, R. D. S., McGregor, P. J., et al. 2010, MNRAS, 402, 819

Sturm, E., González-Alfonso, E., Veilleux, S., et al. 2011, ApJ, 733, L16

Sutherland, R. S., & Bicknell, G. V. 2007, ApJS, 173, 37

Swinbank, A. M., Chapman, S. C., Smail, I., et al. 2006, MNRAS, 371, 465

Swinbank, A. M., Smail, I., Chapman, S. C., et al. 2004, ApJ, 617, 64

Swinbank, A. M., Smail, I., Bower, R. G., et al. 2005, MNRAS, 359, 401

Swinbank, A. M., Webb, T. M., Richard, J., et al. 2009, MNRAS, 400, 1121

Tacconi, L. J., Genzel, R., Smail, I., et al. 2008, ApJ, 680, 246

Tadhunter, C. 2008, New A Rev., 52, 227

Tadhunter, C., & Tsvetanov, Z. 1989, Nature, 341, 422

Tadhunter, C., Wills, K., Morganti, R., Oosterloo, T., & Dickson, R. 2001, MNRAS, 327, 227

Tadhunter, C., Dicken, D., Holt, J., et al. 2007, ApJ, 661, L13

Tadhunter, C. N., Morganti, R., Robinson, A., et al. 1998, MNRAS, 298, 1035

Tadhunter, C. N., Villar-Martin, M., Morganti, R., Bland-Hawthorn, J., & Axon, D. 2000, MNRAS, 314, 849

Takata, T., Sekiguchi, K., Smail, I., et al. 2006, ApJ, 651, 713

Tamura, Y., Kohno, K., Nakanishi, K., et al. 2009, Nature, 459, 61

Tasse, C., Best, P. N., Röttgering, H., & Le Borgne, D. 2008, A&A, 490, 893

Thorne, K. S. 1974, ApJ, 191, 507

Tombesi, F., Cappi, M., Reeves, J. N., & Braito, V. 2012, MNRAS, 422, L1

Tombesi, F., Cappi, M., Reeves, J. N., et al. 2010, A&A, 521, A57

Tonry, J. L. 1984, ApJ, 283, L27

Tozzi, P., Gilli, R., Mainieri, V., et al. 2006, A&A, 451, 457

Treister, E., & Urry, C. M. 2012, Advances in Astronomy, 2012

Treister, E., Urry, C. M., Chatzichristou, E., et al. 2004, ApJ, 616, 123

Tremaine, S., Gebhardt, K., Bender, R., et al. 2002, ApJ, 574, 740

Trump, J. R., Hall, P. B., Reichard, T. A., et al. 2006, ApJS, 165, 1

Trump, J. R., Impey, C. D., Elvis, M., et al. 2009, ApJ, 696, 1195

Ueda, Y., Akiyama, M., Ohta, K., & Miyaji, T. 2003, ApJ, 598, 886

Urry, C. M., & Padovani, P. 1995, PASP, 107, 803

Valiante, E., Lutz, D., Sturm, E., et al. 2007, ApJ, 660, 1060

van de Voort, F., Schaye, J., Booth, C. M., & Dalla Vecchia, C. 2011, MNRAS, 415, 2782

Vasudevan, R. V., & Fabian, A. C. 2009, MNRAS, 392, 1124

Veilleux, S. 1991, ApJS, 75, 383

Veilleux, S., Cecil, G., & Bland-Hawthorn, J. 2005, ARA&A, 43, 769

Veilleux, S., Cecil, G., Bland-Hawthorn, J., et al. 1994, ApJ, 433, 48

Veilleux, S., Kim, D.-C., & Sanders, D. B. 1999, ApJ, 522, 113

Veilleux, S., Kim, D.-C., Sanders, D. B., Mazzarella, J. M., & Soifer, B. T. 1995, ApJS, 98, 171

Veilleux, S., & Osterbrock, D. E. 1987, ApJS, 63, 295

Veilleux, S., Rupke, D. S. N., Kim, D.-C., et al. 2009, ApJS, 182, 628

Veilleux, S., Meléndez, M., Sturm, E., et al. 2013, ApJ, 776, 27

Veron, M. P. 1981, A&A, 100, 12

Villar-Martín, M., Cabrera Lavers, A., Bessiere, P., et al. 2012, MNRAS, 423, 80

Villar-Martín, M., Fosbury, R. A. E., Binette, L., Tadhunter, C. N., & Rocca-Volmerange, B. 1999, A&A, 351, 47

Villar-Martín, M., Humphrey, A., Delgado, R. G., Colina, L., & Arribas, S. 2011a, MNRAS, 418, 2032

Villar-Martín, M., Tadhunter, C., Humphrey, A., et al. 2011b, MNRAS, 416, 262

Vrtilek, J. M. 1985, ApJ, 294, 121

Wada, K., & Norman, C. A. 2002, ApJ, 566, L21

Wagner, A. Y., Bicknell, G. V., & Umemura, M. 2012, ApJ, 757, 136

Walker, M. F. 1968, ApJ, 151, 71

Wall, J. V., & Peacock, J. A. 1985, MNRAS, 216, 173

Wampler, E. J., Burbidge, E. M., Baldwin, J. A., & Robinson, L. B. 1975, ApJ, 198, L49

Wang, J., Mao, Y. F., & Wei, J. Y. 2011, ApJ, 741, 50

Wang, J.-M., Chen, Y.-M., Hu, C., et al. 2009, ApJ, 705, L76

Wang, L., Rowan-Robinson, M., Norberg, P., Heinis, S., & Han, J. 2014, arXiv:1402.4991

Wang, S. X., Brandt, W. N., Luo, B., et al. 2013, ApJ, 778, 179

Wardlow, J. L., Smail, I., Coppin, K. E. K., et al. 2011, MNRAS, 415, 1479

Weaver, R., McCray, R., Castor, J., Shapiro, P., & Moore, R. 1977, ApJ, 218, 377

Webb, T. M., Eales, S. A., Lilly, S. J., et al. 2003, ApJ, 587, 41

Weedman, D. W. 1970, ApJ, 159, 405

—. 1976, QJRAS, 17, 227

—. 1977, ARA&A, 15, 69

Weedman, D. W., Hao, L., Higdon, S. J. U., et al. 2005, ApJ, 633, 706

Westmoquette, M. S., Clements, D. L., Bendo, G. J., & Khan, S. A. 2012, MNRAS, 424, 416

Weymann, R. J., Morris, S. L., Foltz, C. B., & Hewett, P. C. 1991, ApJ, 373, 23

Whittle, M. 1985, MNRAS, 213, 1

—. 1992, ApJ, 387, 109

Whittle, M., Pedlar, A., Meurs, E. J. A., et al. 1988, ApJ, 326, 125

Whittle, M., & Wilson, A. S. 2004, AJ, 127, 606

Wiersma, R. P. C., Schaye, J., Theuns, T., Dalla Vecchia, C., & Tornatore, L. 2009, MNRAS, 399, 574

Willott, C. J., Rawlings, S., Archibald, E. N., & Dunlop, J. S. 2002, MNRAS, 331, 435

Willott, C. J., Rawlings, S., Blundell, K. M., & Lacy, M. 1998, MNRAS, 300, 625

Wilson, A. S., & Heckman, T. M. 1985, in Astrophysics of Active Galaxies and Quasi-Stellar Objects, ed. J. S. Miller, 39–109

Wright, E. L., Eisenhardt, P. R. M., Mainzer, A. K., et al. 2010, AJ, 140, 1868

Xu, C., Livio, M., & Baum, S. 1999, AJ, 118, 1169

Xu, D., & Komossa, S. 2009, ApJ, 705, L20

Xue, Y. Q., Brandt, W. N., Luo, B., et al. 2010, ApJ, 720, 368

Xue, Y. Q., Luo, B., Brandt, W. N., et al. 2011, ApJS, 195, 10

Yee, H. K. C., & Green, R. F. 1987, ApJ, 319, 28

York, D. G., Adelman, J., Anderson, Jr., J. E., et al. 2000, AJ, 120, 1579

Yuan, F., & Narayan, R. 2014, arXiv:1401.0586

Zakamska, N. L., Gómez, L., Strauss, M. A., & Krolik, J. H. 2008, AJ, 136, 1607

Zakamska, N. L., & Greene, J. E. 2014, arXiv:1402.6736

Zakamska, N. L., Strauss, M. A., Heckman, T. M., Ivezić, Ž., & Krolik, J. H. 2004, AJ, 128, 1002

Zeldovich, Y. B., & Novikov, I. D. 1964, Dokl. Acad. Nauk. SSSR, 158, 811

Zhang, K., Dong, X.-B., Wang, T.-G., & Gaskell, C. M. 2011, ApJ, 737, 71

Zheng, X. Z., Xia, X. Y., Mao, S., Wu, H., & Deng, Z. G. 2002, AJ, 124, 18

Zubovas, K., & King, A. 2012, ApJ, 745, L34

—. 2014, arXiv:1401.0392

Appendix A

AGN emission lines: some relevant information and applications

This thesis makes extensive use of rest-frame optical emission lines to trace the ionised gas in AGN. Two types of emission lines are referred to throughout this thesis, *permitted lines* and *forbidden lines*. Permitted lines are those that have transition probabilities, such that the typical decay times by photon emission are very short ($\approx 10^{-8}$ s), and these lines can be produced in both high-density and low-density environments. In contrast, forbidden lines are transitions from meta-stable states and in high density environments these states are most likely to be collisionally de-excited (by another particle) before they are de-excited by photon emission. In short, there isn't sufficient time for a photon to be produced before the excited state is collisionally de-excited. In this appendix brief details of the production mechanisms of the main emission lines used in this thesis are provided. Details of how these lines are used to identify AGN and how they are used to derive physical properties of ionised outflows are also given.

A.1 Forbidden emission lines

The main forbidden emission-line used throughout this thesis is the doublet [O III]λ4959,5007. The O III species is twice-ionised oxygen (i.e., two electrons are removed and the clearer notation that is used in chemistry is O^{2+}). The creation of O III by photoionization requires photons with $h\nu \geq 35.1$ eV and therefore it is preferentially found around sources of a hard (high energy) continuum. O III has 6 electrons, with two electrons in the 1s sub-shell, two electrons in the 2s sub-shell and two electrons in the 2p sub-shell (see Fig. A.1). The 2p sub-shell is partially filled (i.e., it only contains two of

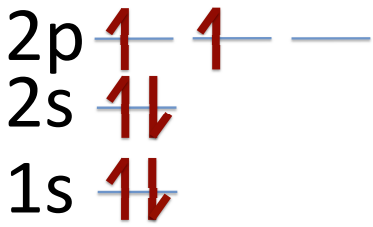

Figure A.1: The electron orbitals for the six electrons in an O III ion. The electrons are represented as half arrows and the arrow direction corresponds to the electron spin. The blue horizontal lines represent the orbitals. The outer 2p sub-shell is only partially filled. These two electrons can be moved into higher-energy configurations of orbitals and spin by collisional excitation. When the ion de-excites back to a lower energy configuration, [O III] emission lines are produced. Fig. A.2 shows an energy level diagram for O III.

the six possible electrons). It is the two electrons moving between different configurations *within* the 2p sub-shell (i.e., moving between orbitals and changing spin) that is responsible for the production of the [O III] emission lines. These two electrons determine the possible electron quantum states of the O III ion. These different quantum states can be notated with the term-symbol:

$$^{2S+1}L_J \tag{1.1.1}$$

Where S is the spin quantum number, J is the total angular momentum quantum number and L is the orbital quantum number. L has standard labels for each value, the first of which are: "S" (for $L = 0$); "P" (for $L = 1$) and "D" (for $L = 2$). The values of L and S are determined by the sum of the corresponding individual quantum numbers of the two outer electrons (that are set by the orbitals that they are located in and their spins). In this ion the 2p sub-shell is less than half-filled (see Fig. A.1) which means that we can define $J = |L - S|$. Each combination of L and S results in a different energy level and, in the case where $(2S + 1) > 1$, these levels are split further for each of the individual J values. An energy-level diagram for [O III] is shown in Figure A.2. The electrons can be collisionally excited to higher energy levels and then the [O III] emission lines are emitted when the ion de-excites to a lower energy level. In low density environments (where collisional de-excitations are negligible), the relative number of [O III]λ5007 photons and [O III]λ4959 photons is set by the ratio of the probabilities associated with the transitions that produce them (i.e., $= 2.9$; Osterbrock & Ferland 2006) and the result is the familiar

[O III]λ4959,5007 emission-line doublet with a flux ratio of 2.9 between the two components. In high density environments (i.e., electron densities $n_e \gtrsim 7 \times 10^5\,\mathrm{cm}^{-3}$; Osterbrock & Ferland 2006), the $^1D_2$ excited state shown in Figure A.2 is de-excited by collisions before it can be de-excited by photon production. This is why the [O III]λ4959,5007 emission-line doublet is not produced in the high-density ($n_e \gtrsim 10^8\,\mathrm{cm}^{-3}$) BLRs of AGN.

The N II ion (used for emission-line diagnostics, see Section A.3) has two electrons in the outer 2p sub-shell and consequently this ion has the same set of electron configurations as O III (see Figure A.2), although the energy level of each configuration is different. The other forbidden emission lines used in this thesis are the two lines that make up the [S II]λλ6716,6731 doublet. In the low density limit ($n_e \approx 1\,\mathrm{cm}^{-3}$), every collisional excitation is followed by the emission of a photon, while in the high density limit ($n_e \gtrsim 10^5\,\mathrm{cm}^{-3}$) collisional de-excitations dominate. Between the two density regimes, the relative intensity of the [S II]λλ6716,6731 emission lines is a function of the electron density (and also temperature); therefore, for a fixed temperature the emission-line ratio [S II]λ6716/[S II]λ6731 can be used as a tracer of electron density (Osterbrock & Ferland 2006). We use [S II]λλ6716,6731 as a measure of n_e in Chapter 3 and Chapter 4.

A.2 Permitted emission lines

The two permitted emission lines that are used in this thesis are Hα ($\lambda = 6563$Å) and Hβ ($\lambda = 4861$Å). These lines are part of the Balmer emission-line series that are produced when the single electron in a hydrogen atom transitions from a higher principle energy level to the second principle energy level (i.e., $n = 3$–∞ to $n = 2$). Hα and Hβ are produced due to the transitions from $n = 3$ and $n = 4$ respectively. In the context of emission-line regions in AGN (and other "nebulae"; Osterbrock & Ferland 2006), these lines are referred to as recombination lines. In the emission-line regions of AGN (where there are plenty of photons with $h\nu \geq 13.6$eV), electrons are constantly being removed and re-combined with hydrogen nuclei. During re-combination, an electron is captured into an excited state and the electron consequently cascades down the energy levels. The photons

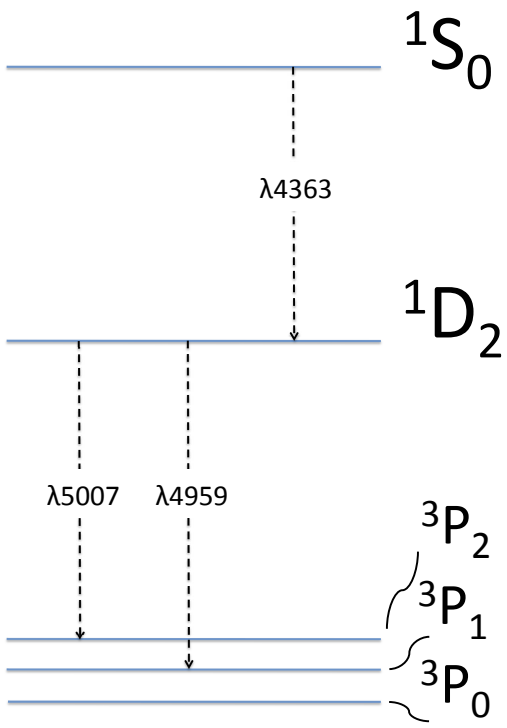

Figure A.2: Energy-level diagram for the lowest terms of [O III] for the $2p^2$ configuration (Fig. A.1). For clarity, the splitting of the ^3P term has been exaggerated. Strong optical emission lines are shown by the dotted lines.

emitted during this process are the "recombination lines" .[1]

A.3 BPT diagram

The relative ratios of different emission lines can be used to identify the continuum ionising source (as discussed in Section 1.3.3). AGN have a high level of photoelectric heating, and also an ability to liberate high ionisation potential electrons, due to their hard radiation field (i.e., they produce significant emission with short wavelengths; Fig. 1.2). The increased gas temperature means that collisionally excited forbidden lines become stronger (e.g., [O III] and [N II]; see Section A.1). The ratio of these forbidden lines to recombination lines (Section A.2) is consequently higher in the presense of an AGN compared to emission-line regions that do not host an AGN. This means that several different emission-line ratio diagnostics, applied to the spectra of galaxies, can be used to identify AGN activity. The most popular of these is the Baldwin-Phillips-Terlevich diagram (BPT diagram; Baldwin et al. 1981; also see Veilleux & Osterbrock 1987) which uses the ratios [N II]λ6583/Hα and [O III]λ5007/Hβ (Fig. 1.3). The close wavelengths of the pairs of lines in these ratios means that differential dust reddening is minimal. The boundaries to isolate AGN on the BPT diagram have been created both from modelling (of the ionization conditions and using stellar population synthesis; e.g., Kewley et al. 2001) and from empirical methods (e.g., Ho et al. 1997a; Kauffmann et al. 2003).

A.4 Gas masses, mass outflow rates and energy injection rates

Recombination lines are useful to give an estimate of the ionised gas mass in the emission-line region of an AGN, under certain assumptions. In Chapter 4 we use the Hβ line to estimate the ionised gas mass and, therefore, we give a brief explanation of how this can be achieved here. Firstly, under the assumption of pure hydrogen that is fully ionised, we

[1] In AGN NLRs Hα also has a small contribution from collisional excitation to the $n = 3$ level. This is why the intrinsic Balmer decrement is approximately Hα/Hβ = 3.1 and is in excess of the recombination-only value of 2.85 (Osterbrock & Ferland 2006).

can estimate an ionised gas mass (M) with,

$$M = n_e m_p V \varepsilon, \tag{1.4.2}$$

where n_e is the electron density, m_p is the mass of the proton, V is the total volume, and ε is the filling factor. Here the filling factor is the fraction of the total volume that contributes to the mass (i.e. if the volume is made up of "clumps" rather than being a uniform distribution). Under "Case B" conditions (e.g., Osterbrock & Ferland 2006), the gas is assumed to be optically thick to ionising photons and recombinations are only considered to the excited states. All recombinations to the ground state result in photons that are immediately absorbed by a nearby atom and the total number of ionising photons is in balance with the re-combinations to excited levels. Under these assumptions, the relative intensities of different recombination lines can be calculated and each recombination line has a resultant, temperature dependent, "effective recombination coefficient" ($\alpha^{\rm eff}$; e.g., Osterbrock & Ferland 2006). Assuming uniform temperature the luminosity of the Hβ recombination line can then be expressed as

$$L_{\rm H\beta} = n_e n_p \alpha^{\rm eff}_{\rm H\beta} h\nu_{H\beta} V \varepsilon \tag{1.4.3}$$

Combining Equation 1.4.2 with Equation 1.4.3 results in an estimate of the (Hβ emitting) ionised hydrogen gas mass of,

$$M = \frac{L_{\rm H\beta} m_p}{n_e \alpha^{eff}_{H\beta} h\nu_{H\beta}}, \tag{1.4.4}$$

that can be expressed in the convenient form,

$$\frac{M}{6.78\times10^8\,{\rm M}_\odot} = \left(\frac{L_{\rm H\beta}}{10^{43}\,{\rm erg\,s^{-1}}}\right)\left(\frac{n_e}{100\,{\rm cm^{-3}}}\right)^{-1}, \tag{1.4.5}$$

which uses the assumption that $\alpha^{\rm eff}_{\rm H\beta} = 3.03\times10^{-14}\,{\rm cm^3\,s^{-1}}$ (applicable for Case B conditions and $T = 10^4$ K; Osterbrock & Ferland 2006).

In Chapter 4 we assume a spherical outflow to estimate values of the rate of kinetic energy in the outflows ($\dot{E}$) and the mass outflow rates ($\dot{M}$). The derivation of the equations used in this chapter are given here. For a spherical outflow of fully ionised hydrogen the

mass outflow rate is

$$\dot{M} = n_e m_p v_{\rm out} A \varepsilon \tag{1.4.6}$$

where $v_{\rm out}$ is the outflow velocity and A is the surface area. Substituting in Equation 1.4.2 and the values of A and V for a sphere, results in a mass outflow rate of

$$\dot{M} = \frac{3 M v_{\rm out}}{r} \tag{1.4.7}$$

We can then combine the bulk outflow kinetic energy rate with the turbulent kinetic energy rate to get a total kinetic energy rate of

$$\dot{E} = \frac{\dot{M}}{2}\left(v_{\rm out}^2 + 3\sigma^2\right), \tag{1.4.8}$$

where σ is the velocity dispersion.

In Chapter 3 and Chapter 4 we model the outflow as an energy conserving bubble, expanding into a uniform medium. This model was applied to make a direct comparison to previous work that used the same model (e.g., Nesvadba et al. 2008; Greene et al. 2012). The details of the derivation are too long to be provided here, but can be found in Castor et al. (1975); see Weaver et al. (1977) and Veilleux et al. (2005) for more detail. In summary, a wind that provides a constant supply of energy, forms a hot shocked cavity that sweeps up a bubble (or shell) of shocked interstellar medium. This bubble is then driven into the ambient interstellar medium. If radiative losses of the overall outflow are negligible the expanding bubble is energy conserving. Here we provide the derivation of Equation 3.6.1 (used in Chapter 3 and Chapter 4), starting with Equation (51) of Weaver et al. (1977) that describes the evolution of the radius, $r(t)$, of such an energy-conserving expanding bubble. This equation can be written in the form,

$$r(t) = 1.07 n_0^{-1/5} \dot{E}_{44}^{1/5} t_6^{3/5} \,{\rm kpc}, \tag{1.4.9}$$

where t_6 is the age of the bubble in Myr, n_0 is the ambient density ahead of the expanding bubble in units of cm^{-3} and $\dot{E}_{44}$ is the energy injection rate of the wind in units of 10^{44} erg s^{-1} (here we are assuming that none of the energy injected by the wind is radiated away; see e.g., Veilleux et al. 2005). Differentiating this equation results in the following

expression for the velocity of the expanding shell,

$$v(t) = 640\dot{E}_{44}^{1/5} n_0^{-1/5} t_6^{-2/5} \,\mathrm{km\,s^{-1}} \tag{1.4.10}$$

Substituting Equation 1.4.9 into Equation 1.4.10 we can then write the shell velocity as

$$v(t) = 670\dot{E}_{44}^{1/3} n_0^{-1/3} r_{\mathrm{kpc}}^{-2/3} \,\mathrm{km\,s^{-1}} \tag{1.4.11}$$

Finally, rearranging Equation 1.4.11 results in an expression for the energy injection rate of the expanding bubble of,

$$\dot{E} \approx 3 \times 10^{46} r_{10\,\mathrm{kpc}}^2 v_{1000\,\mathrm{km\,s^{-1}}}^3 n_0 \,\mathrm{erg\,s^{-1}}, \tag{1.4.12}$$

The true energy injection rate will need to be multiplied by the covering factor of the bubble ($\Omega/4\pi$; see Greene et al. 2012), although we have neglected this factor in this work (see Section 4.5.3).

Appendix B

Assumed cosmology

This thesis covers observations of extragalactic objects across a wide range of redshifts. A cosmological model, with a set of parameters, has been assumed throughout to convert the measured quantities of flux, redshift and angular size into luminosities and physical sizes. This appendix provides an extremely brief outline of: (1) the assumed cosmological model; (2) the values of the cosmological parameters adopted; (3) how the derived quantities are determined using this cosmological model and set of parameters.

B.1 The model

We assume an expanding, homogeneous and isotropic universe where the scale factor $a(t)$ is used to describe the rate at which the Universe is expanding. The space-time separation between two events can be described by

$$ds^2 = c^2dt^2 - a(t)^2\left(\frac{dr^2}{1-k(r/R)^2} + r^2d\Omega^2\right),\ d\Omega^2 = d\theta^2 + \sin^2\theta d\phi^2 \qquad (2.1.1)$$

where (t, r, θ, ϕ) are the co-moving co-ordinates, $k = \pm 1, 0$ and c is the speed of light. If we assume photons (that have $ds = 0$) are moving radially (i.e., $d\Omega = 0$), it can be shown that light is effectively redshifted by the expansion of the Universe. For a photon emitted with wavelength λ_e at time t_e the observed wavelength λ_o at time t_o is related to the scale factor as,

$$\frac{\lambda_o}{\lambda_e} = \frac{a(t_o)}{a(t_e)} \equiv (1+z) \qquad (2.1.2)$$

where z is defined as the cosmological redshift. Cosmological redshifts for extragalactic objects are quoted throughout this thesis. These redshifts have been predominantly

been derived using the observed wavelengths (λ_o) of emission lines and following Equation 2.1.2.

The evolution of the scale factor can be described by Friedmann's Equations which follow,

$$\left(\frac{\dot{a}}{a}\right)^2 = H^2 = \frac{8\pi G}{3}\rho - \frac{kc^2}{a^2} + \frac{\Lambda c^2}{3} \tag{2.1.3}$$

$$\frac{\ddot{a}}{a} = \dot{H} + H^2 = -\frac{4\pi G}{3}\left(\rho + \frac{3p}{c^2}\right) + \frac{\Lambda c^2}{3} \tag{2.1.4}$$

where ρ is the density of the Universe, k is related to the curvature, p is the pressure, G is the gravitational constant, c is the speed of light and Λ is the cosmological constant. The value of ρ can be split into matter density $\rho_m \propto a^{-3}$ and photon density $\rho_r \propto a^{-4}$. If non-zero and positive, the last terms (i.e., those involving Λ) imply a "negative pressure" or "dark energy". It is convenient to define $H_0^2 = 8\pi G\rho_c/3$, where ρ_c is called the "critical density" (which assumes $k = \Lambda = 0$ in Equation 2.1.3) and to paramaterise Equation 2.1.3 as

$$H^2 = \left(\frac{\dot{a}}{a}\right)^2 = H_0^2\left(\frac{\Omega_m}{a^3} + \frac{\Omega_r}{a^4} + \frac{\Omega_k}{a^2} + \Omega_\Lambda\right) = H_0^2 E(a)^2 \tag{2.1.5}$$

where $\Omega_m = \rho_m/\rho_c$, $\Omega_r = \rho_r/\rho_c$, $\Omega_k = -c^2k/H_0^2$ and $\Omega_\Lambda = \Lambda c^2/3H_0^2$. These constants (or density parameters) tells us how much matter, radiation, curvature and the cosmological constant contribute to the total density at the current epoch. Their values, along with the value of H_0, are important for deriving quantities associated with extragalactic objects that depend on the value of the scale factor (e.g., their luminosities, ages, physical sizes; see next section). These values are determined experimentally by combining observations of the cosmic microwave background, Type 1a supernovae and the matter power spectrum. In this thesis we assume that $H_0 = 71\,\mathrm{km\,s^{-1}\,Mpc^{-1}}$, $\Omega_\mathrm{M} = 0.27$, $\Omega_\Lambda = 0.73$, $k = 0$ and that Ω_r is negligible (following Spergel et al. 2003).

B.2 Cosmic time and distances

The two main measurements that are dependent on the assumed cosmology in this thesis are:

- The (proper) *physical diameters* that are derived from measured angular sizes on

the sky and redshifts.

- The *luminosities* that are derived from measured fluxes and redshifts.

Brief details of how these quantities are related to the assumed cosmology are provided here.

At the time an object emits light, the proper distance to an object is $a_e r_e$, where r_e is the co-moving distance and is defined as (follows from Equation 2.1.1),

$$r_e = \int_0^{r_e} \frac{dr}{\sqrt{1-kr^2}} \tag{2.2.6}$$

Consequently, the physical diameter l is related to the angular size θ by

$$a_e r_e = l/\theta \tag{2.2.7}$$

We define the *angular diameter distance* (d_A) of an observed object with known l and measured θ as

$$d_A \equiv l/\theta \tag{2.2.8}$$

where it now follows that $d_A = r_e a_e$ and this distance can be derived for an assumed cosmology and measured redshift (see Section B.1). The values of physical sizes of the outflows in this thesis are derived following Equation 2.2.8.

The observed flux (F_o) is the amount of photon energy (E_o) passing through a unit area per unit time interval (Δt_o) and can be expressed as

$$F_o = \frac{E_o}{\Delta t_o} \frac{1}{4\pi(a_o r_o)^2} \tag{2.2.9}$$

$$= \frac{E_e}{(1+z)^2 \Delta t_e} \frac{1}{4\pi(1+z)^2(a_e r_e)^2} \tag{2.2.10}$$

$$= \frac{L}{4\pi(1+z)^4(a_e r_e)^2} \tag{2.2.11}$$

where emitted quantities and observed quantities have been related following Section B.1. The *luminosity distance* (d_L) is defined as

$$F_o = \frac{L}{4\pi d_L^2} \tag{2.2.12}$$

where L is the luminosity of the emitting object. It can now be seen that

$$d_L = (1+z)^2 a_e r_e = (1+z)^2 d_A \tag{2.2.13}$$

Luminosities quoted in this thesis are derived from the measured fluxes and redshifts, following Equation 2.2.12.

Finally, following Equation 2.1.5, the age of the Universe at a certain redshift, $t_A(z)$, can be determined by,

$$H_0 t_A(z) = \int_0^{t_A} H_0 \, dt = \int_0^a \frac{da}{aE(a)} = \int_z^\infty \frac{dz}{(1+z)E(z)} \tag{2.2.14}$$

Appendix C

Acronyms

2dFGRS	Two-degree-Field Galaxy Redshift Survey
2QZ	The 2dF QSO Redshift Survey
ACS	Advanced Camera for Surveys
AGN	Active Galactic Nuclei
ALMA	Atacama Large Millimeter/submillimeter Array
BALQSO	Broad Absorption Line Quasi-Stellar Object
BH	Black Hole
BLR	Broad Line Region
BPT	Baldwin-Phillips-Terlevich
C-COSMOS	Chandra COSMOS
CDF-N	Chandra Deep Field-North
CDF-S	Chandra Deep Field-South
COSMOS	COSMOlogical evolution Survey
DR7	Data Release 7
EAGLE	Evolution of GaLaxies and their Environment
E-CFDS	Extended-Chandra Deep Field South
e-MERLIN	Enhanced Multi-Element Radio Linked Interferometer Network
ESA	European Space Agency
ESO	European Southern Observatory
FIR	Far Infrared
FIRST	Faint Images of the Radio Sky
FMOS	Fibre Multi-Object Spectrograph
FWHM	Full Width at Half Maximum
GALPAKA	Galaxy and AGN Line Profile And Kinematic Analysis
GMOS	Gemini Multi-Object Spectrograph
GOODS	Great Observatories Origins Deep Survey
GOODS-N	GOODS-North
GOODS-S	GOODS-South
GRASIL	GRAphite and SILicate
GT	Guaranteed Time
HerMES	Herschel Multi-tiered Extragalactic Survey
HIPE	Herschel Interactive Processing Environment
HST	Hubble Space Telescope
HzRGs	High Redshift Radio Galaxies
ICM	IntraCluster Medium

IDL	Interactive Data Language
IFS	Integral Field Spectroscopy
IFU	Integral Field Unit
IGM	InterGalactic Medium
IMF	Initial Mass Function
IR	InfraRed
IRAF	Image Reduction and Analysis Facility
IRAM	Institut de Radioastronomie Millimetrique
IRAS	InfraRed Astronomical Satellite
ISM	InterStellar Medium
JVLA	(Karl G.) Jansky Very Large Array
JWST	James Webb Space Telescope
KMOS	K-band Multi-Object Spectrograph
LINER	Low-Ionization Nuclear Emission-line Region
LIRG	Luminous InfraRed Galaxy
LSST	Large Synoptic Survey Telescope
MDO	Massive Dark Object
MIR	Mid Infrared
MMIRS	MMT Magellan Infrared Spectrograph
MMT	Multiple Mirror Telescope
MOSFIRE	Multi-Object Spectrometer For Infra-Red Exploration
MS	Main Sequence
NFW	Navarro-Frenk-White
NICMOS	Near Infrared Camera and Multi-Object Spectrometer
NIFS	Near Infrared Integral Field Spectrometer
NIR	Near InfraRed
NLR	Narrow Line Region
NRAO	National Radio Astronomy Observatory
NVSS	NRAO VLA Sky Survey
PA	Position Angle
PdBI	Plateau de Bure Interferometer
PSF	Point Spread Function
QSO	Quasi-Stellar Object
SB	StarBurst
SCANPI	SCAN Processing and Integration
SDSS	Sloan Digital Sky Survey
SED	Spectral Energy Distribution
SF	Star Formation
SFR	Star Formation Rate
SINFONI	Spectrograph for Integral Field Observations in the Near Infrared
SKA	Square Kilometre Array
SMBH	Super Massive Black Hole
SMG	SubMillimetre Galaxy
SPICA	SPace Infrared telescope for Cosmology and Astrophysics
SPIRE	Spectral and Photometric Imaging REceiver
sSFR	Specific Star Formation Rate

UDS	Ultra Deep Survey
ULIRG	Ultra-Luminous Infrared Galaxy
VIMOS	Visible Multi-Object Spectrograph
VLA	Very Large Array
VLT	Very Large Telescope
WISE	Wide-field Infrared Survey Explorer
XMM	X-ray Multi-Mirror Mission